TECHNISCHE
UNIVERSITÄT
DARMSTADT

Substoichiometric Phases of Hafnium Oxide with Semiconducting Properties

Zur Erlangung des Grades Doktor der Naturwissenschaften (Dr. rer. nat.)

genehmigte Dissertation von M.Sc. Nico Kaiser aus Erbach im Odenwald, Deutschland

Fachbereich Material- und Geowissenschaften

Tag der Einreichung: 24.04.2023

Darmstadt 2023

1. Gutachten: Prof. Dr. Lambert Alff

2. Gutachten: Prof. Dr. Leopoldo Molina-Luna

“Substoichiometric Phases of Hafnium Oxide with Semiconducting Properties“

Vom Fachbereich Material- und Geowissenschaften

der Technischen Universität Darmstadt

zur Erlangung des Grades Doktor der Naturwissenschaften (Dr. rer. nat.)

genehmigte Dissertation von M.Sc. Nico Kaiser aus Erbach im Odenwald, Deutschland

1. Gutachten: Prof. Dr. Lambert Alff

2. Gutachten: Prof. Dr. Leopoldo Molina-Luna

Darmstadt 2023

Kaiser, Nico : Substoichiometric Phases of Hafnium Oxide with Semiconducting Properties

Darmstadt, Technische Universität Darmstadt,

Jahr der Veröffentlichung der Dissertation auf TUprints: 2023

URN: urn:nbn:de:tuda-tuprints-242178

URI: https://tuprints.ulb.tu-darmstadt.de/id/eprint/24217

Tag der Einreichung: 24.04.2023

Tag der mündlichen Prüfung: 06.06.2023

Thesis Statement - Erklärung zur Dissertation

Thesis Statement pursuant to § 22 paragraph 7 of APB TU Darmstadt

I herewith formally declare that I, Nico Kaiser, have written the submitted thesis independently pursuant to § 22 paragraph 7 of APB TU Darmstadt. I did not use any outside support except for the quoted literature and other sources mentioned. I clearly marked and separately listed all of the literature and all of the other sources which I employed when producing this academic work, either literally or in content. I state that all passages which have been taken from publications of all means or unpublished material either whole or in part, in words or ideas, have been marked as quotations. This thesis has not been handed in or published before in the same or similar form.

In the submitted thesis the written copies and the electronic version for archiving are pursuant to § 23 paragraph 7 APB identical in content.

Darmstadt, ____

(Nico Kaiser, M.Sc.)

Abstract

Since the dawn of the information age, all developments that provided a significant improvement in information processing and data transmission have been considered as key technologies. The impact of ever new data processing innovations on the economy and almost all areas of our daily lives is unprecedented and a departure from this trend is unimaginable in the near future. Even though the end of Moore's Law has been predicted all too often, the steady exponential growth of computing capacity remains unaffected to this day, due to tremendous commercial pressure. While the minimum physical size of the transistor architecture is a serious constraint, the steady evolution of computing effectiveness is not limited in the predictable future. However, the focus of development will have to expand more strongly to other technological aspects of information processing. For example, the development of new computer paradigms which mark a departure from the digitally dominated van Neumann architecture will play an increasingly significant role. The category of so-called next-generation non-volatile memory technologies, based on various physical principles such as phase transformation, magnetic or ferroelectric properties or ion diffusion, could play a central role here. These memory technologies promise in part strongly pronounced multi-bit properties up to quasi-analog switching behavior. These attributes are of fundamental importance especially for new promising concepts of information processing like in-memory computing and neuromorphic processing. In addition, many next-generation non-volatile memory technologies already show advantages over conventional media such as Flash memory. For example, their application promises significantly reduced energy consumption and their write and especially read speeds are in some cases far superior to conventional technology and could therefore already contribute significant technological improvements to the existing memory hierarchy. However, these alternative concepts are currently still limited in terms of their statistical reliability, among other things. Even though phase change memory in the form of the 3D XPoint, for example, has already been commercialized, the developments have not yet been able to compete due to the enormous commercial pressure in Flash memory research. Nevertheless, the further development of alternative concepts for the next and beyond memory generations is essential and the in-depth research on next-generation non-volatile memory technologies is therefore a hot and extremely important scientific topic.

This work focuses on hafnium oxide, a key material in next-generation non-volatile memory research. Hafnium oxide is very well known in the semiconductor industry, as it generated a lot of attention in the course of high-*k* research due to its excellent dielectric properties and established CMOS compatibility. However, since the growing interest in so-called memristive memory, research efforts have primarily focused on the value of hafnium oxide in the form of resistive random-access memory (RRAM) and, with the discovery of ferroelectricity in HfO_2, ferroelectric resistive random-access memory (FeRAM). RRAM is a next-generation non-volatile memory technology that features a simple metal-insulator-metal (MIM) structure, excellent scalability, and potential 3D integration. In particular, the aforementioned gradual to quasi-continuous switching behavior has been demonstrated on a variety of RRAM systems. A significant change of the switching properties is achievable, for example, by the choice of top and bottom electrodes, the introduction of doping elements, or by designated oxygen deficiency. In particular, the last point is based on the basic physical principle of the hafnium oxide-based RRAM mechanism, in which local oxygen ions are stimulated to diffuse by applying an electrical potential, and a so-called conducting filament is formed by the remaining vacancies, which electrically connects the two electrode sides. The process is characterized by

the reversibility of the conducting filament which can be dissolved by a suitable I-V programming (e.g., reversal of the voltage direction).

In the literature there are some predictions of sub-stoichiometric hafnium oxide phases, such as Hf_2O_3, HfO or Hf_6O, which could be considered as conducting filament phases, but there is a lack of conclusive experimental results. While there are studies that assign supposed structures in oxygen-deficient hafnium oxide thin films, these assignments are mostly based on references from various stoichiometric hafnium oxide high-temperature phases such as tetragonal *t*-HfO_2 (*P*4_2/*nmc*) or cubic *c*-HfO_2 (*Fm*-3*m*), or high-pressure phases such as orthorhombic *o*-HfO_2 (*Pbca*).

Furthermore, the structural identification of such thin films proves to be difficult, as they are susceptible to arbitrary texturing and reflection broadening in X-ray diffraction. In addition, such thin films are usually synthesized as phase mixtures with monoclinic hafnium oxide. A further challenge in property determination is given by their usual arrangement in MIM configuration, which is determined by the quality of top and bottom electrodes and their interfaces to the active material. It is therefore a non-trivial task to draw conclusions on individual material properties such as electrical conductivity in such (e.g., oxygen-deficient) RRAM devices.

To answer these open questions, this work is primarily devoted to material properties of oxygen-deficient hafnium oxide phases. Therefore, in the first comprehensive study of this work, Molecular-Beam Epitaxy (MBE) was used to synthesize hafnium oxide phases over a wide oxidation range from monoclinic to hexagonal hafnium oxide. The hafnium oxide films were deposited on c-cut sapphire to achieve effective phase selection and identification by epitaxial growth, taking into account the position of relative lattice planes. In addition, the choice of a substrate with a high band gap and optical transparency enabled the direct investigation of both optical and electrical properties by means of UV/Vis transmission spectroscopy and Hall effect measurements. With additional measurements via X-ray diffraction (XRD), X-ray reflectometry (XRR), X-ray photoelectron spectroscopy (XPS) and high-resolution transmission electron microscopy (HRTEM), the oxygen content-dependent changes in crystal as well as band structure could be correlated with electrical properties. Based on these results, a comprehensive band structure model over the entire oxidation range from insulating HfO_2 to metallic Hf was established, highlighting the discovered intermediate key structures of rhombohedral *r*-$HfO_{1.7}$ and hexagonal *hcp*-$HfO_{0.7}$.

In the second topic of this work, the phase transition from stoichiometric monoclinic to oxygen-deficient rhombohedral hafnium oxide was complemented by DFT calculations in collaboration with the theory group of Prof. Valentí (Frankfurt am Main). A detailed comparison between experimental results and DFT calculations confirms previously assumed mechanisms for phase stabilization. In addition, the comparison shows a remarkable agreement between experimental and theoretical results on the crystal- and band stucture. The calculations allowed to predict the positions of oxygen ions in oxygen-deficient hafnium oxide as well as the associated space group. Also, the investigations provide information on the thermodynamic stability of the corresponding phases. Finally, the orbital-resolved hybridization of valence states influenced by oxygen vacancies is discussed.

Another experimental study deals with the reproduction and investigation, of the aforementioned substoichiometric hafnium oxide phases in MIM configuration which is typical for RRAM devices. Special attention was given to the influence of surface oxidation effects. Here, it was found that the oxygen-deficient phases *r*-$HfO_{1.7}$ and *hcp*-$HfO_{0.7}$ exhibit high ohmic conductivity as expected, but stable bipolar switching behavior as a result of oxidation in air. Here, the mechanism of this behavior was discussed and the role of the *r*-$HfO_{1.7}$ and *hcp*-$HfO_{0.7}$ phases as novel electrode materials in hafnium oxide-based RRAM in particular.

In collaboration with the electron microscopy group of Prof. Molina Luna, the studied phases, which have been characterized by rather macroscopic techniques so far, have been analyzed by wide-ranging TEM methodology. The strong oxygen deficiency in combination with the verified electrical conductivity of *r*-$HfO_{1.7}$ and *hcp*-$HfO_{0.7}$ shows the importance of the identification of these phases on the nanoscale. Such abilities are essential for the planned characterization of the "conducting-filament" mechanism. Here, the ability to distinguish *m*-HfO_2, *r*-$HfO_{1.7}$, and *hcp*-$HfO_{0.7}$ using high-resolution transmission electron microscopy (HRTEM), Automated Crystal Orientation and Phase Mapping (ACOM), and Electron Energy Loss Spectroscopy (EELS), is demonstrated and the necessity of combined measurements for reliable phase identification was discussed.

Finally, a series of monoclinic to rhombohedral hafnium oxide was investigated in a cooperative study with FZ Jülich using scanning probe microscopy. Since recent studies in particular highlight the significance of the microstructure in stoichiometric hafnium oxide-based RRAM, the topological microstructure in the region of the phase transition to strongly oxygen deficient rhombohedral hafnium oxide was investigated. Special attention was given to the correlation of microstructure and conductivity. In particular, the influences of grain boundaries on electrical properties were discussed.

In summary, this work provides comprehensive insights into the nature and properties of sub-stoichiometric hafnium oxide phases and their implications on the research of hafnium oxide-based RRAM technology. Taking into account a wide range of scientific perspectives, both, the validity of obtained results and the wide range of their application is demonstrated. Thus, this dissertation provides a detailed scientific base to the understanding of hafnium oxide-based electronics.

Zusammenfassung

Seit dem Beginn des Informationszeitalters sind alle entwickelten Technologien, welche eine signifikante Verbesserung der Informationsverarbeitung und Datenübertragung gewährleisteten, als zentrales technologisches Fortschrittselement anzusehen. Die Auswirkungen immer neuer Datenverarbeitungs-Innovationen auf die Wirtschaft und nahezu alle Bereiche unseres täglichen Lebens sind beispiellos und eine Abkehr von diesem Trend ist in naher Zukunft unvorstellbar. Auch wenn das Ende des Mooreschen Gesetzes schon allzu oft vorhergesagt wurde, ist das stetige exponentielle Wachstum der Rechenkapazitäten bis zum heutigen Zeitpunkt – sicherlich aufgrund des enormen kommerziellen Drucks - unbeeinflusst. Während die minimale physikalische Größe der Transistor-Architektur ein ernstzunehmendes Hindernis darstellt, ist die stetige Weiterentwicklung der Computer-Effektivität in absehbarer Zeit nicht limitiert. Der Fokus der Entwicklung wird sich jedoch stärker auf andere technologische Aspekte der Informationsverarbeitung ausweiten müssen. Die Entwicklung neuer Computerparadigmen welche eine Abkehr von der digital dominierten Von-Neumann Architektur verzeichnen, werden beispielsweise eine immer bedeutsamere Rolle einnehmen. Eine zentrale Bedeutung könnte hier der Kategorie der sogenannten Next-Generation non-volatile Memory Technologien, basierend auf verschiedenen physikalischen Prinzipien, wie Phasen-Umwandlung, magnetischen oder ferroelektrischen Eigenschaften oder Ionendiffusion zukommen. Diese Speichertechnologien versprechen zum Teil ausgeprägte Multi-Bit Eigenschaften bis hin zu quasi-analogem Schaltverhalten. Diese Attribute sind insbesondere für neue vielversprechende Konzepte der Informationsverarbeitung wie In-Memory Computing und neuromorphe Systeme von elementarer Bedeutung. Zusätzlich weisen viele Next-Generation non-volatile Memory Technologien, eine Vielzahl an Vorzügen gegenüber konventionellen Speichermedien wie FLASH auf. So verspricht deren Anwendung einen wesentlich reduzierten Energieverbrauch und auch deren Schreib- und besonders Lesegeschwindigkeit sind der konventionellen Technologie teils stark überlegen und könnten so bereits in der bestehenden Speicherhirachie signifikante technologische Verbesserungen bewirken. Jedoch sind diese alternativen Konzepte zurzeit noch unter anderem in ihrer statistischen Zuverlässigkeit limitiert. Auch wenn es zwischenzeitlich schon zur Vermarktung von beispielsweise Phasenwechselspeicher (engl. Phase Change Memory) in Form des 3D XPoint kam, kann sich die Entwicklungen aufgrund des enormen kommerziellen Drucks in der FLASH Forschung noch nicht durchsetzen. Nichtsdestotrotz ist die Weiterentwicklung alternativer Konzepte für die nächsten und übernächsten Speichergenerationen unabdingbar und die vertiefende Forschung an Next-Generation non-volatile Memory Technologien ist daher ein aktuelles und extrem bedeutendes wissenschaftliches Thema.

Diese Arbeit fokussiert sich hierbei mit Hafniumoxid auf ein zentrales Material der Next-Generation non-volatile Memory Forschung. Hafniumoxid ist sehr bekannt in der Halbleiterindustrie, da es durch seine exzellenten dielektrischen Eigenschaften und etablierten CMOS Kompatibilität im Zuge der high-*k* Forschung viel Aufmerksamkeit generierte. Seit dem wachsenden Interesse an sogenannten memristiven Speichermedien haben sich die Forschungsbemühungen jedoch primär auf den Nutzen von Hafniumoxid in Form von Resistive Random-Access Memory (RRAM) und mit der Entdeckung von Ferroelektrizität in HfO_2 auf Ferroelectric Resistive Random-Access Memory (FeRAM) konzentriert. RRAM ist eine Next-Generation non-volatile Memory Technologie, welche durch ihre simple Metal-Insulator-Metal (MIM) Struktur, exzellente Skalierbarkeit und potenzielle 3D Integration besticht. Insbesondere ist an einer Vielzahl von RRAM Systemen das zuvor erwähnte graduelle, bis hin zu quasi-

kontinuierlichem Schaltverhalten nachgewiesen. Eine signifikante Veränderung der Schalteigenschaften ist beispielsweise durch die Wahl der oberen und unteren Elektroden, das Einbringen von Dotierungselementen, oder durch gezielte Sauerstoffdefizienz möglich. Insbesondere der letztere Punkt setzt am physikalischen Grundprinzip des Hafniumoxid basierten RRAM Mechanismus an, bei dem durch das Anlegen eines elektrischen Potenzials lokale Sauerstoff-Ionen zur Diffusion angeregt werden, und durch zurückbleibende Vakanzen ein sogenanntes „Conducting Filament“ entsteht, welches die beiden Elektrodenseiten elektrisch verbindet. Der Prozess ist durch die Reversibilität des Filaments gekennzeichnet, welches sich durch die Anwendung einer geeigneten I-V Programmierung (z.B. Umkehr der Spannungsrichtung) wieder (teilweise) auflösen lässt.

In der Literatur gibt es einige Vorhersagen zu substöchiometrischen Hafniumoxid Phasen, wie beispielsweise Hf_2O_3, HfO oder Hf_6O, welche als „Conducting Filament“ Phasen in Frage kommen könnten, jedoch sind die Ergebnisse nicht durch experimentelle Ergebnisse bestätigt. Es gibt zwar Studien, welche die vermeintlichen Strukturen von sauerstoff-defizienten Hafniumoxid Dünnschichten zuordnen, jedoch basieren diese Zuweisungen meist auf Referenzen von verschiedenen stöchiometrischen Hafniumoxid Hochtemperaturphasen wie tetragonalem t-HfO_2 ($P4_2/nmc$) oder kubischem c-HfO_2 (Fm-3m) oder auf Hochdruckphasen wie orthorombischem o-HfO_2 ($Pbca$). Zudem erweist sich die strukturelle Identifikation dünner Schichten als schwierig, da diese anfällig für willkürliche Texturierung und Reflex-Verbreiterung z.B. bei der Röntgenbeugung sind. Zusätzlich liegen entsprechende Dünnschichten meist als Phasengemisch mit monoklinem Hafniumoxid vor. Eine weitere Herausforderung bei der Eigenschaftsbestimmung ist durch ihre übliche Anordnung in MIM Konfiguration gegeben, welche durch die Qualität der Elektroden und deren Grenzflächen zum aktiven Material bestimmt ist. Es ist daher kein triviales Unterfangen in solchen (z.B. sauerstoffdefizienten) RRAM-Bauelementen Rückschlüsse auf individuelle Materialeigenschaften wie die elektrische Leitfähigkeit zu schließen.

Um diese offenen Fragen zu beantworten, beschäftigt sich diese Arbeit primär mit Materialeigenschaften von sauerstoff-defizienten Hafniumoxid Phasen. Zur ersten umfangreichen Studie dieser Arbeit wurden daher mithilfe von Molekularstrahl Epitaxie, Hafniumoxid Phasen über einen breiten Oxidationsbereich von monoklinem hin zu hexagonalem Hafniumoxid synthetisiert. Die Hafniumoxid Schichten wurden dabei auf einkristallinen Saphirsubstraten abgeschieden, um mittels epitaktischem Wachstum eine effektive Phasen-Auswahl und Identifikation unter Berücksichtigung der Position relativer Netzebenenabstände zu erreichen. Zudem wurde durch die Wahl eines Substrates mit hoher Bandlücke und optischer Transparenz die direkte Untersuchung sowohl optischer als auch elektrischer Eigenschaften mittels UV/Vis-Transmissionsspektroskopie und Hall-Effekt Messungen ermöglicht. Mit weiteren Messungen via Röntgenbeugung (XRD), Röntgenreflektometrie (XRR), Röntgen-Photoelektronenspektroskopie (XPS) und hochauflösende Transmissionselektronenmikroskopie (HRTEM), konnten die vom Sauerstoffgehalt abhängigen Veränderungen an Kristall-, als auch Bandstruktur mit den elektrischen Eigenschaften korreliert werden. Basierend auf diesen Ergebnissen wurde ein umfangreiches Bandstrukturmodell über den gesamten Oxidationsbereich von isolierendem HfO_2 hin zu metallischem Hf erstellt, welches besonders die entdeckten dazwischenliegenden Schlüsselstrukturen von rhomboedrischem r-$HfO_{1.7}$ und hexagonalen hcp-$HfO_{0.7}$ beschreibt.

Im zweiten Themen-Komplex dieser Arbeit wurde im Speziellen der Phasenübergang von stöchiometrisch monoklinem zu saustoff-defizientem rhomboedrischem Hafniumoxid durch DFT Berechnungen in Zusammenarbeit mit der Theorie-Gruppe von Prof. Valentí (Frankfurt am Main) ergänzt. Ein detaillierter Vergleich zwischen experimentellen Ergebnissen und DFT Berechnungen, bestätigt hierbei zuvor angenommene Mechanismen zur Phasenstabilisierung. Zudem zeichnet sich die Gegenüberstellung durch eine bemerkenswerte Übereinstimmung der experimentellen und theoretischen Ergebnisse zur Kristall- als auch der Bandstruktur aus. Die Berechnungen erlauben Rückschlüsse auf die Positionen der Sauerstoffionen in Sauerstoff-Defizienten Hafniumoxid und der damit verbundenen Raumgruppe. Auch liefern die Untersuchungen Hinweise auf die thermodynamische Stabilität der entsprechenden Phasen. Schließlich wird die durch Sauerstoff-Vakanzen beeinflusste Orbital-aufgelöste Hybridisierung der Valenzzustände diskutiert.

Eine weitere experimentelle Studie beschäftigt sich mit der Reproduktion und Untersuchung, der zuvor genannten substöchiometrischen Hafniumoxid Phasen in für RRAM typischer MIM Konfiguration. Besonderes Augenmerk liegt hierbei auf dem Einfluss von Effekten der Oberflächenoxidation. Hierbei zeigt sich, dass die sauerstoff-defizienten Phasen *r*-$HfO_{1.7}$ und *hcp*-$HfO_{0.7}$ wie erwartet eine hohe ohmische Leitfähigkeit aufweisen, jedoch durch die Oxidation an Luft stabiles bipolares Schaltverhalten entwickeln. Hierbei werden die Ursachen dieses Verhaltens und insbesondere die Rolle der Phasen *r*-$HfO_{1.7}$ und *hcp*-$HfO_{0.7}$ als neuartige Elektrodenmaterialien in Hafniumoxid-basiertem RRAM diskutiert.

In Zusammenarbeit mit der Elektronenmikroskopie-Gruppe von Prof. Molina Luna wurden die entsprechend synthetisierten und charakterisierten Phasen mittels weitrechender TEM-Methodik analysiert. Die ausgeprägte Sauerstoffdefizienz im Zusammenspiel mit der nachgewiesenen elektrischen Leitfähigkeit von *r*-$HfO_{1.7}$ und *hcp*-$HfO_{0.7}$ zeigt wie wichtig die Identifikation dieser Phasen im nanoskaligen Bereich bei einer geplanten Charakterisierung des „Conducting-Filament“ Mechanismus sein können. Hierbei wurde unter anderem die Unterscheidbarkeit von *m*-HfO_2, *r*-$HfO_{1.7}$ und *hcp*-$HfO_{0.7}$ mittels hochauflösender Transmissionselektronenmikroskopie, automatisierter Kristallorientierung und Phasenzuordnung (ACOM) und Elektronenenergieverlustspektroskopie (EELS) demonstriert und die Notwendigkeit kombinierter Messungen für eine zuverlässige Phasenidentifikation diskutiert.

Letztendlich wird eine Serie von monoklinem zu rhomboedrischen Hafniumoxid in einer kooperativen Studie mit dem Forschungszentrum Jülich mittels Rastersondenmikroskopie untersucht. Da insbesondere kürzlich Studien die Signifikanz der Mikrostruktur in stöchiometrischem Hafniumoxid basiertem RRAM hervorheben, wurde hier die topologische Mikrostruktur im Bereich des Phasenübergangs zu stark Sauersoff-defizientem rhomboedrischen Hafniumoxid untersucht. Besonderes Augenmerk galt hierbei der Korrelation von Mikrostruktur und elektrischer Leitfähigkeit. Hierbei wurden insbesondere die Einflüsse der Korngrenzen auf die elektrischen Eigenschaften diskutiert.

Zusammenfassend liefert diese Arbeit umfassende Einblicke in die Beschaffenheit und die Eigenschaften substöchiometrischer Hafniumoxid Phasen sowie deren Implikationen für die Forschung an Hafniumoxid-basierten RRAM Technologie. Unter Berücksichtigung zahlreicher wissenschaftlicher Perspektiven zeigt sich hierbei sowohl die Belastbarkeit als auch der breite Anwendungsraum der gewonnenen Erkenntnisse. Damit liefert diese Dissertation eine grundlagenwissenschaftliche Basis zum Verständnis Hafniumoxid-basierender Elektronik.

Abbreviations

μ	Chemical potential
A	Ampere
ABF	Annular Bright Field
ACOM	Automated Crystal Orientation Mapping
ADF	Annular Dark Field
AFM	Atomic Force Microscopy
ALD	Atomic Layer Deposition
B3LYP	Becke, 3-parameter, Lee–Yang–Parr hybrid functional
BF	Bright Field
BRS	Bipolar Resistive Switching
c-AFM	Conducting Atomic Force Microscopy
CBM	Conduction Band Minima
CF	Conducting filament
Cf8	Counter-figure-eight (wise switching)
CTF	Contrast transfer function
DFT	Density Functional Theory
d_{hkl}	Lattice plane spacing corresponding to Miller indices
DOS	Density of States
DOSs	Density of States (plural)
DRAM	Dynamic Random Access Memory
EDX	Energy Dispersive X-ray spectroscopy
EELS	Electron Energy Loss Spectroscopy
E_F	Fermi-Level
EM	Electron Microscopy
eV	Electron Volts
F8	Figure-eight (wise switching)
FeRAM	Ferroelectric Random Access Memory
FIB	Focused Ion Beam
G_0	Conductance Quantum
GGA	General Gradient Approximation
HAADF	High Angle Annular Dark Field
HRS	High Resistance State
HRTEM	High Resolution Transmission Electron Microscopy
HSE06	Heyd, Scuseria and Ernzerhof hybrid functional
HZO	Hafnium-Zirconium Oxide
I	Current
I_c	Compliance current
$I_{leakage}$	Leakage-Current
I-V	Current-Voltage
LDA	Local Density Approximation
LRS	Low Resistance State
MBE	Molecular-Beam Epitaxy
MIM	Metal-Insulator-Metal
MRAM	Magnetic Resistive Memory
n-type	electron-type conduction
NVM	Non-volutile memory
OTF	Optical transfer function
OxRAM	Metal Oxide Resistive Memory
PBE0	Perdew–Burke-Ernzerhof hybrid functional
PBEsol	Perdew, Burke and Ernzerhof General Gradient Approximation
PCM	Phase Change Memory

PDF	Powder Diffraction File
PLD	Pulsed Laser Deposition
p-type	hole-type conduction
PVD	Physical Vapor Deposition
QC	Quantized Conductance
QCM	Quartz Crystal Microbalance
R	roughness
RHEED	Reflection High-Energy Electron Diffraction
RMS	Root-mean-square roughness
RRAM	Resistive Random Access Memory
RT	Room temperature
sccm	Standard cubic centimeters per minute
SCLD	Space Charge Limited Conduction
SPM	Scanning Probe Microscopy
SRAM	Static Random Access Memory
STEM	Scanning Transmission Electron Microscopy
STT-MRAM	Spin Transfer Torque Magnetic Resistive Memory
t	thickness
TEM	Transmission Electron Microscopy
U	Voltage
URS	Unipolar Resistive Switching
V	Volt
VB	Valence Band
VBM	Valence Band Maxima
VCM	Valence Change Memory
VF	Forming Voltage
VH	Hall Voltage
V_{Reset}	Reset-Voltage
V_{Set}	Set-Voltage
XPS	X-ray Photoelectron Spectroscopy
XRD	X-ray diffraction
XRR	X-ray Reflectometry
ρ	electrical resistivity or density

Index

Thesis Statement - Erklärung zur Dissertation II

Abstract IV

Zusammenfassung VIII

Abbreviations XII

Index XIV

1. ……Introduction 1
1.1. Next generation nonvolatile memory 2
1.2. Next Generation NVM as Storage Class Memory and Beyond 5
1.3. Emerging Memory Technologies Connected to Next Generation NVM 6
1.4. Switching in filament based OxRAM 7
1.5. High Pressure and High Temperature HfO_2 polymorphs 9
1.6. Ferroelectric Hafnium Oxide 10
1.7. Oxygen Deficient Phases of Hafnium Oxide 11
1.8. Conduction Mechanisms in Resistive Memories 13

2. ……Methods 15
2.1. X-ray Investigations with a Universal Goniometer 15
2.1.1. X-ray Reflectometry 15
2.1.2. Bragg-Diffraction & Rocking Curve 16
2.1.3. Pole Figures & Geometric Relations in Single Crystals 20
2.2. Transmission Electron Microscopy 22
2.3. X-ray Photoelectron Spectroscopy 25
2.4. Bandgap Estimation via UV/Vis-Spectroscopy 29
2.5. Hall Effect in Semiconductors & Van der Pauw Geometry 33
2.6. Density Functional Theory 36

3. ……Sample Synthesis & Preparation Methods 39
3.1. Molecular-Beam Epitaxy 39
3.2. Hafnium Oxide Synthesis via MBE 40
3.3. Titanium Nitride Synthesis via MBE 41
3.4. Photolithography 43
3.5. Ion Beam Etching & Optimization for In-Vacuo Grown Devices 45
3.6. Optimization of Electrode Thicknesses for operando TEM 48

4. ……Results & Discussion 50
4.1. Physical Properties of Oxygen Defect Stabilized Hafnium Oxide Phases 51
4.1.1. Novel Structures *r*-HfO_{2-x} and *hcp*-HfO_{2-x} between Hafnia and Hafnium 52
4.1.2. Identification of Rhombohedral Hafnium Oxide *r*-HfO_{2-x} 55
4.1.3. Electronic Environment and Composition of *r*-HfO_{2-x} and *hcp*-HfO_{2-x} 61
4.1.4. Oxygen Vacancy Induced P-Type Conduction 66
4.1.5. Optical Absorption and Bandgap Properties 69
4.1.6. Microstructure and Homogeneity of the Crystal Phases 73
4.1.7. Band Structure Model from Hafnia to Hafnium 74
4.2. Ab-Initio Simulations on Substoichiometric Hafnium Oxide Compared to Experimental Results 77
4.2.1. DFT Simulations on the Formation of Rhombohedral Hafnium Oxide *r*-HfO_{2-x} 77
4.2.2. DFT Calculated Crystal Structure of Rhombohedral Hafnium Oxide Compared to XRD Measurement's 81

4.2.3. Density of States and Bandgap of Rhombohedral Hafnium Oxide from Hybrid Functional Calculations, Photoelectron Spectroscopy and Optical Transmission 83
4.2.4. Analysis of the Band Structure and Orbital Hybridization within HSE06 85
4.3. Substoichiometric Phases of Hafnium Oxide as Novel Electrodes for RRAM Applications 87
4.3.1. Reproduction of Substoichiometric Hafnium Oxide Phases on Epitaxial TiN Electrodes 88
4.3.2. Preparation of TiN/HfO_{2-x}/Pt Stacks In-Vacuo and In-Atmosphere 91
4.3.3. Electrical Properties of Substoichiometric Devices prepared In-Air and In-Vacuo 93
4.3.4. Surface Oxidation and Substoichiometric Hafnium Oxide Phases as Ohmic Electrodes in RRAM 94
4.3.5. Electric Behavior of Substoichiometric Hafnium Oxide-based Devices without Surface Oxidation 97
4.3.6. Conduction Mechanisms in *m*-HfO_2, *r*-$HfO_{1.7}$ and *hcp*-$HfO_{0.7}$ based MIM devices 98
4.3.7. OxRAM with Conventional 35nm Compared to 200 nm TiN Bottom Electrodes for Operando TEM 100
4.4. Transmission Electron Microscopic Nanoscale Identification of Substoichiometric Hafnium Oxide Phases 103
4.4.1. HRTEM and HAADF-STEM identification of *m*-HfO_2, *r*-HfO_{2-x} and *hcp*-HfO_{2-x} 104
4.4.2. EELS Fingerprinting of *m*-HfO_2, *r*-HfO_{2-x} and *hcp*-HfO_{2-x} 106
4.4.3. Automated Crystal Orientation Mapping for *m*-HfO_2 and *r*-HfO_{2-x} Phase Separation 107
4.5. Scanning Probe Microscopy Analysis of Microstructure and Local Conduction 109
4.5.1. Reproduction of Substoichiometric Hafnium Oxide on Collaborative Sample Holders and Grain Size Effects 110
4.5.2. In-Vacuo Scanning Probe Microscopy 112
5. …… Conclusion & Outlook 116
Appendix XVI
List of figures XVIII
List of Table XXVIII
Bibliography XXIX
Curriculum Vitae XL
List of publications, scientific contributions and supervision of students XLI
Acknowledgement XLVI

1. Introduction

Modern computing systems feature several kinds of different memory classes. As the speed of the memory is directly connected to its cost, the memory technologies are ordered with fastest read and write times and smallest memory size close to the central processing unit (CPU). This arrangement is called memory hierarchy and displayed in Figure 1.

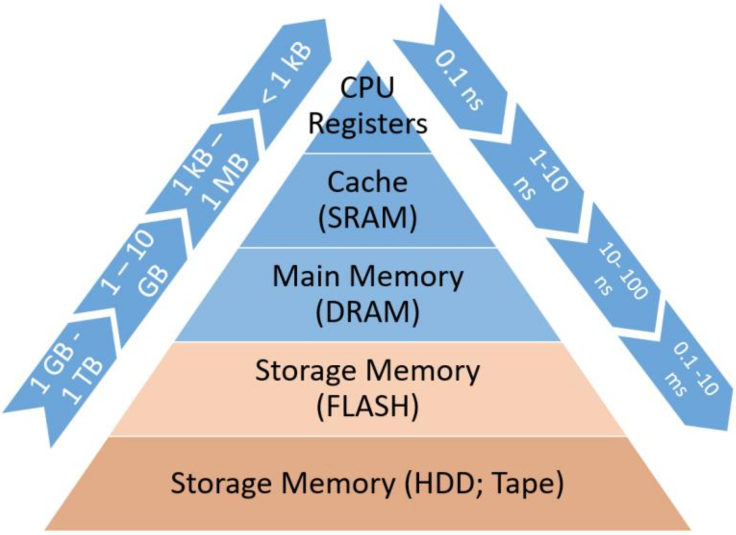

Figure 1: Classical memory hierarchy with fastest memories close to the CPU. The corresponding approximate speed and storage capacities are indicated on the sides of the pyramid and run in opposite directions. Note that the high speed memory types (Registers, Cache and Main Memory) which are shown in blue are all volatile while the storage memory (shown in orange) are the only non-volatile memory types.

The fastest types of memory are the registers which need to directly hold up with the CPU speed, therefore providing response in the order of one processing cycle. Following are the Cache consisting of static random-access memory (SRAM) and main memory which is made up from dynamic random-access memory (DRAM). Both SRAM and DRAM are established as an essential part of the memory hierarchy for over 30 years by now.[1, 2] While DRAM is significantly more compact, the SRAM architecture allows for one order of magnitude lower latency. Only after DRAM the first non-volatile memory (NVM) technologies are used. Therefore, up until DRAM all stored information is volatile and is effectively lost after the system is shut from the power supply. In case of DRAM the memory state even needs to be refreshed, which means it needs to be read and rewritten permanently. The non-volatile memory on the other hand which is also referred to as storage saves information independent of continuous power supply, and is therefore much better suited for permanent data storage. It is striking that in the realm of digital storage, we relied more than half a century on the magnetic Hard Disc Drive, a mechanically operated system with a head moving over a spinning disc for data manipulation. Also, magnetic tape storage – while extremely slow - is still used as a cost effective medium for data archiving.[3] Memory technology based on moving parts however (HDD ad especially tape) suffer obviously from extremely limited latency times. The invention of non-volatile NAND FLASH storage in 1984 paved the way for its suggestive development and became an important milestone in the attempt to lower the performance gap between the volatile main memory (DRAM) and storage in the memory hierarchy. From FLASHs commercial success starting from 1989 the technology was continuously upgraded and miniaturized, surpassing the 20 nm node, and therefore becoming more and more economically feasible.[4] Later due to physical miniaturization limitations the development of 3D integration was established.[5] In the context of the data hierarchy, the development of FLASH promotes the next technological steps towards more aggressive miniaturization the one hand and further closing the performance gap between storage and memory on the other hand. Several concepts have been proposed to overcome these limitations and many of them rely on the change of the resistance between two electrodes in a sandwich-type structure. Strikingly, those concepts, often summarized under the term “next generation non-volatile memory” rely on various physical phenomena like magnetism, ferroelectricity, phase-transitions, electronic effects or the diffusion of anion or cation species. Another important feature of those concepts in the context of the memory hierarchy is their non-volatile nature. First, energy expensive refresh cycles (as necessary for DRAM) are avoided, second it allows for faster or even instantaneous boot up times as non-volatile information can be fed faster into the main memory or even directly into the cache (or the registers). In the next chapter the most important next generation nonvolatile memory concepts and their fundamental working principles are explained.

1.1. Next generation nonvolatile memory

As already implied in the previous chapter, there are many concepts which allow for non-volatile resistive switching and are seen as potential successors for current memory technologies like FLASH. Often those technologies are summarized under the term “Next generation non-volatile memory”. There are many ways on how to categorize those concepts, which partially leads to contradicting statements in literature. One of the most useful descriptions however is by their basic physical principle as shown in Figure 2.

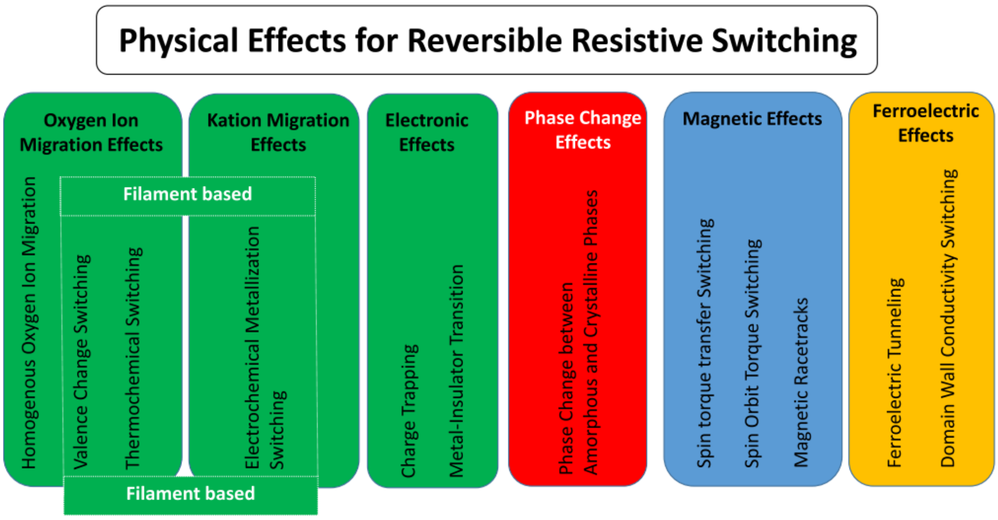

Figure 2: Categorization of next generation nonvolatile memory by their basic physical principles. Content reprinted from reference [6] https://doi.org/10.1088/1361-6528/ab2084 © IOP Publishing. Reproduced with permission. All rights reserved.

As evident from the figure, there are resistive switching principles based on ionic movements like oxygen ions (e.g. Metal Oxide Resistive Memory or OxRAM) or cations (e.g. conducting bridge memory or CBRAM), from which the majority is filament based.[6-8] This means that a conducting filament is induced on the basis of ion migration in an otherwise insulating layer. Such technologies which rely on the migration of anion or cation species are often summarized under the term Resistive Random Access Memory (ReRAM or RRAM).[7] Phase Change Memory (PCRAM) is another famous technology which is based on the change of the resistance of a layer via amorphization and (re)crystallization.[9-11] Further there is MRAM or Magnetic Resistive Memory which relies on mechanisms such as the megnetoresistive effect.[12] Amongst the most prominent MRAM concepts the Spin transfer torque (STT) mechanism is utilized, where the orientation of a magnetic layer (e.g. in a tunnel junction) may be changed via spin polarized current.[13] As the last example in Figure 2, ferroelectric effects are mentioned giving rise to Ferroelectric Random Access Memory (FeRAM) where for example the effect of ferroelectric tunneling is exploited.[14, 15] This concept works straight forward via the change of the polarization of the ferroelectric layer which in turn modifies the tunnel barrier in a device.[16]

Figure 3 shows how the fundamental architectures of selected memory technologies are designed. Starting from a) a SRAM circuit is shown, highlighting the complexity and size of one element, consisting of multiple (typically six) capacitors.[17] Figure 3b) shows the working principle of a DRAM cell only yielding one capacitor with volatile capacitance in a metal oxide semiconductor (MOS) configuration.[17] Compared to SRAM the device size for DRAM is reduced by a factor of about 10. Figure 3c) shows the principle of FLASH memory where a floating gate is implemented as a vital component to store charge, and therefore the state of the device in a non-volatile manner.[18, 19]

While all of the above mentioned memory types a-c) are already implemented in state of the art computing systems, the remaining devices d-i) belong to the next generation non-volatile memory category. Note that all of those architectures consist mainly of a simple sandwich structure, which allows for significantly reduced feature sizes.

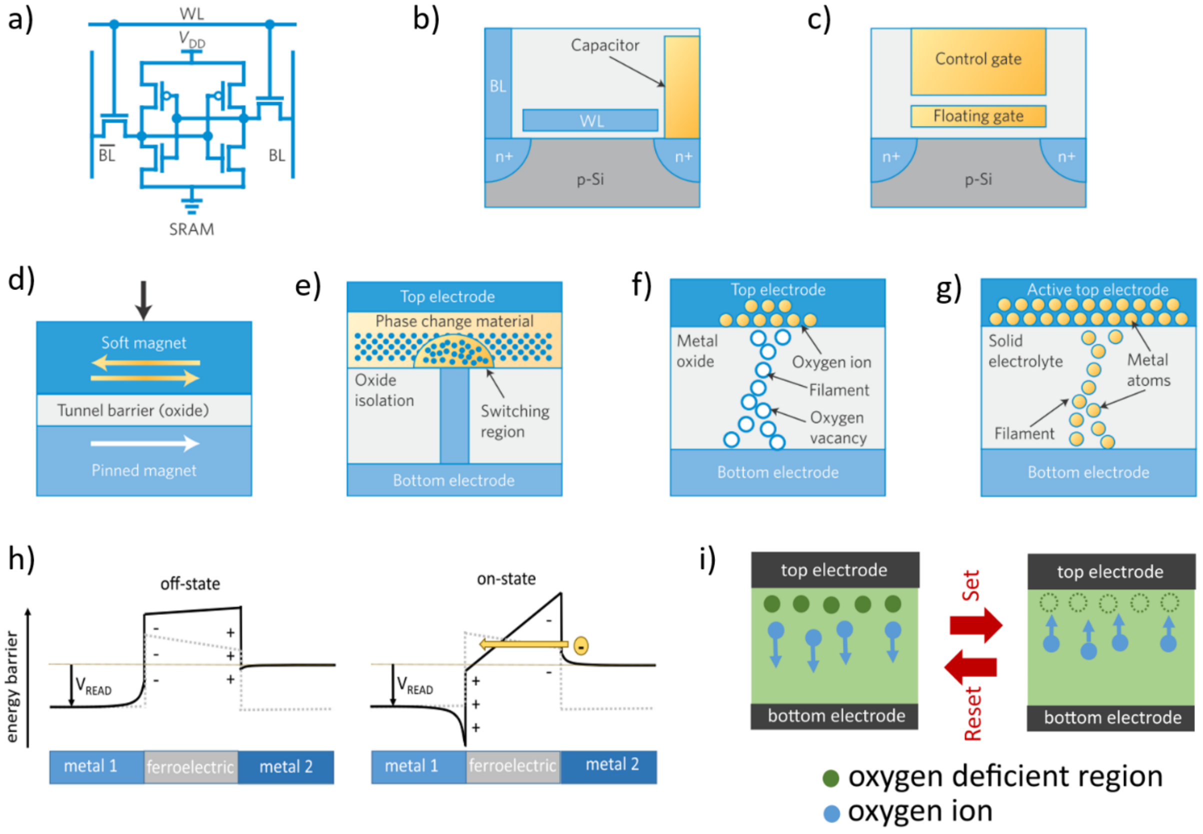

Figure 3: Memory technologies and their fundamental architectures with a) SRAM, b) DRAM, c) FLASH, d) STT-MRAM, e) PCRAM, f) Filament based OxRAM, e) CBRAM, h) FeRAM and i) Interface based OxRAM. Content a) - g) reprinted from reference [1] https://doi.org/10.1038/nnano.2015.29 with permission of Springer Nature BV. © 2015 Macmillan Publishers Limited. All rights reserved. Content h) & i) is reprinted from reference [16] https://doi.org/10.1088/1361-6528/ab2084 © IOP Publishing. Reproduced with permission. All rights reserved.

Figure 3d) shows a STT-MRAM design consisting of a pinned magnet and a soft magnet. Depending on weather the spin of the soft magnet is aligned with the pinned magnet, there is a magnetoresistance across the tunnel barrier (opposite spin direction) or not (same spin direction). This two nonvolatile states can be switched if a suitable current is driven through the device.[12, 13] As in this type of memory no change in the material (but only in magnetic domains) is induced, MRAM gives rise to significant endurance.

Figure 3e) shows a PCRAM cell consisting of a phase change material, separating the electrodes. Note that the bottom electrode is laterally defined, allowing to control the location of the switching region. By passing a high current in a short time through the device, the material is locally amorphisized. By passing a smaller current over a longer time, the material recrystallizes again. This type of phase change mechanism is usually utilized by the use of chalcogenides like (most commonly) $Ge_2Sb_2Te_5$ (GST) or GeTe. Switching between these two nonvolatile states translates to high (amorphous) and low electrical resistance (crystalline).[9-11]

Figure 3f) shows a OxRAM device, where an insulating material is simply sandwiched between two inert electrodes. For this purpose, mostly transition metal oxides are used. Prominent examples are Ta_2O_5, HfO_2 or Al_2O_3. By applying a suitable current, a conducting filament is formed via the migration of oxygen ions which leave oxygen vacancies behind. This conducting filament can be locally ruptured again by e.g. applying a current in the opposite direction. In this way the device can be set to a high resistance or low resistance state.

Figure 3g) shows a CBRAM device which works similar to an OxRAM device, by the creation of a conducting filament between two electrodes. In case of CBRAM however, the movement of a cation species is induced from an active electrode side (often Cu or Ag is used) which results in a metallic filament penetrating the insulating layer. Also this type of conducting filament can be ruptured again allowing to switch the device. The unique feature of filament based memories is, that the switching properties are (theoretically) independent of the device feature size, down to the size of the nm-sized filament.

Figure 3h) shows an FeRAM tunnel junction. Similarly, to the STT-MRAM device, the material is not affected during the switching and only the orientation of (in this case) ferroelectric domains is changed. As can be seen from the figure, by changing the polarization of the ferroelectric layer, the energetic barrier can be reduced from an insulating barrier to a conducting tunnel barrier and vice versa.[16] So far, an obstacle for FeRAM was the utilization of complex perovskite structures. The discovery of ferroelectricity in hafnia promoted the research interest in the technology as hafnia’s CMOS compatibility allows for industry friendly integration.

Figure 3i) shows an RRAM device working on the principle of homogeneous oxygen ion movement (also often referred to as interface-type switching). While similarly to the filament based OxRAM, the mechanism depends on the movement of oxygen ions, in this case, the effect is not localized but happens across the whole device interface area. By moving oxygen ions, the interface is transformed in an insulation region by filling up oxygen vacancy sites. The other way around, if oxygen ions are moved from the insulating region, vacancy sites emerge again, allowing for electrical conduction. Interface type against filament type switching in RRAM devices can be particularly hard to differentiate as both switching mechanisms can be inherent to transition metal oxides. Also the electric I-V behavior can be very similar. A typical approach would be to check if the switching behavior is effected by the device area. As mentioned before, in filament based devices, no significant difference is expected in dependence of the device area, while there is an area dependent influence on the low resistance state in case of homogeneous (interfacial) switching.

1.2. Next Generation NVM as Storage Class Memory and Beyond

The previous chapter gave an overview with an attempt to categorize selected technologies in next generation non-volatile memory. It is important to mention that there are many different variations of those architectures including different choices for the active switching materials as well as the type of electrodes that are used.[7, 20] Therefore, it is not an easy task to pinpoint the specific performances of individual technologies. However, there are various review articles which make an attempt to highlight trends and unique features of certain types of memory categories.[20, 21] As already mentioned in chapter 1.1, there is an significant performance gap between state of the art FLASH memory and the Main Memory (DRAM). For technologies to bridge this performance gap the term “Storage Class Memory” (SCM) has been established as displayed in Figure 4.

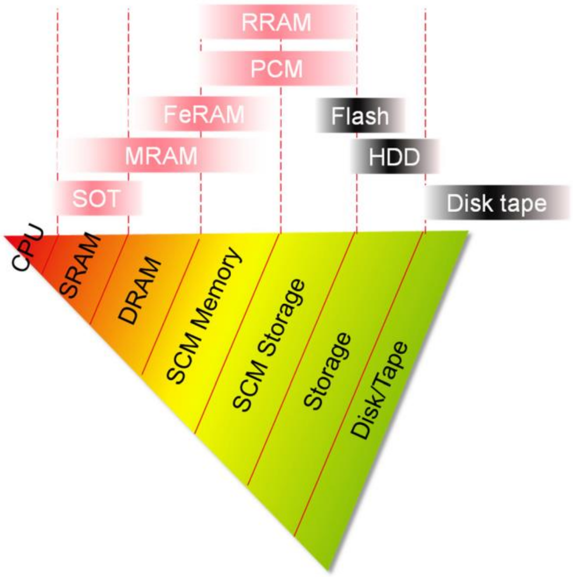

Figure 4: Next generation nonvolatile memories and their possible implementation in the memory hierarchy. Reprinted from reference [20] https://doi.org/10.3390/app112311254 which is published under a Creative Commons Attribution 4.0 International License. © 2021 by the authors. Licensee MDPI, Basel, Switzerland.

Considering the speed, all relevant candidates of next generation non-volatile have drastically reduced latency times with $\sim$ 1-1000 ns as compared to FLASH ($\sim$ 100μs). However, the requirements regarding endurance and read/write times are becoming more and more demanding, the closer the memory application gets to the CPU. Therefore, at the moment MRAM and specifically Spin Orbit Torque SOT-MRAM seems especially suitable for competing for applications in the Cache (currently SRAM) region with endurances up to $\sim 10^{15}$ and latency times of $\sim$ 10 ns to even >1 ns. [20, 21] Also FeRAM shows excellent latency of <20 ns and endurance $\sim 10^{11}$ and can therefore be considered for applications in the Main Memory (currently DRAM). [20] For both RRAM and PCRAM the endurance in only in the regime of $\sim 10^{7}$ however, both technologies are suitable for 3d integration [22, 23] and are therefore ideal candidates for storage class memory applications to bridge the gap between storage and main memory. [20]

1.3. Emerging Memory Technologies Connected to Next Generation NVM

A major limitation of state of the art computing is the van Neumann bottleneck. The vast majority of computing systems today use the van Neumann architecture, of which the key advantage is to follow a strict deterministic approach of single instruction, single operation (SISO). While this architecture allows for easy programmability, all of the data transfer between memory and processing unit is conducted over a shared bus system. By this strict separation of the memory and the computing unit significant time and energy is spent. This is called the van Neumann bottleneck. [20, 23] To overcome this problem emerging memory technologies such as In- or Near Memory Computing as well as neuromorphic processing attract more and more attention. Both emerging technologies are especially promoted through the potential which is seen in next generation non-volatile memory. This is highlighted in the web of science search results for RRAM as displayed in Figure 5. Note the steady increase in interest for both emerging fields within the research topic of RRAM. For in-memory computing high endurance and remarkably quick read and write cycles are ideal. While e.g. also RRAM and PCRAM are seen as competitors for specific in-memory computing tasks MRAM seems especially suitable for main computing by offering highest endurance and lowest latencies (compare chapter 1.2).[20] For this purpose however MRAM needs to improve upon its scalability.[24] Here PCRAM and RRAM show advantages due to their 3d integratability. [22, 23]

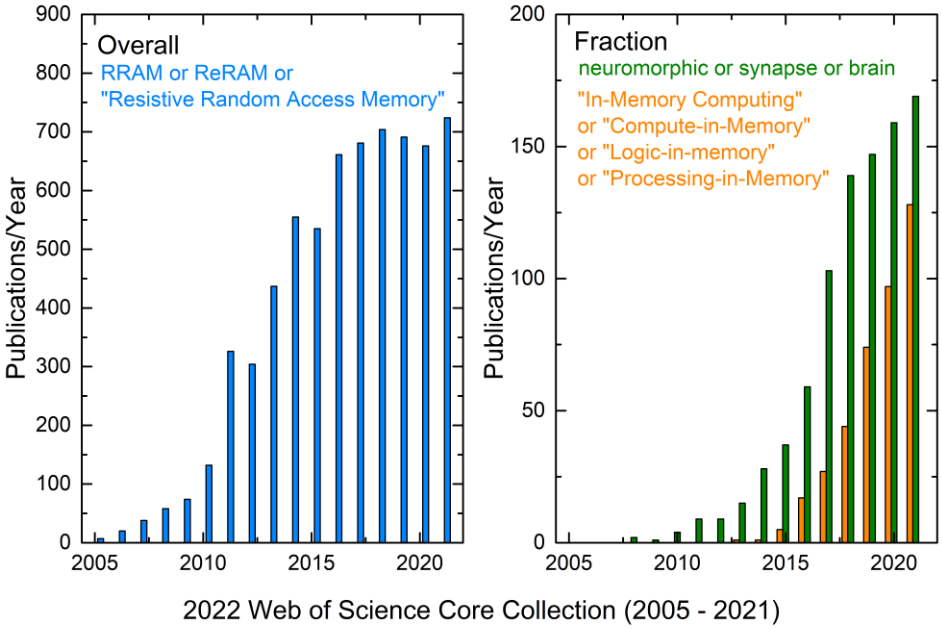

Figure 5: Search results for papers published in the web of science core collection with keywords on RRAM in general (left) and fractions of those publications using keywords regarding the emerging memory fields of "neuromorphic processing" and "In-Memory Computing" (right). Note the steady increase in interest for both emerging fields within the research topic of RRAM.

"Neuromorphic processing" or "brain inspired computing" is also a big topic regarding emerging memory technology. Those technologies can be considered as a form of in-memory computing. The future potential of such computing systems becomes obvious by comparing the power needed to run a human brain against the power needed for computing systems which run top level AI algorithms today. The program of AlphaGo for example was running on 1202 CPUs and 172 GPUs to compete against humans.[25] Assuming about 100 W per CPU and 200 W per

GPU, AlphaGo required about 154 kW to beat Lee Se-dol – his brain can be assumed to be running at a human average of about 20 W [26, 27]- in a match of Go.

For some neuromorphic approaches even simple binary NVM are sufficient (even MRAM), however for many applications synaptic weighting is required.[28] For this purpose, more continuous switching mechanisms are fundamental perquisites. In filamentary switching (OxRAM & CBRAM) the state can in principle be continuously controlled via the diameter of the conducting filament (often mainly in the reset direction). In OxRAM many systems have been demonstrated to show gradual behavior (also partially in the set direction), which can for example be controlled via doping or oxygen deficiency (via scavenging layer or homogeneous oxygen deficient deposition).[28-30] Also in PCRAM gradual switching is possible, but only in the set direction by gradually crystallizing the material via pulses, as high currents are required to amorphize the material again.[28]

1.4. Switching in filament based OxRAM

While the switching mechanism in OxRAM devices is fundamentally based on the formation and rupture of a so called "conducting filament" (CF) through the movement of oxygen ions, different switching modes can be observed in such devices. Before the devices can be switched an initial forming step is necessary.

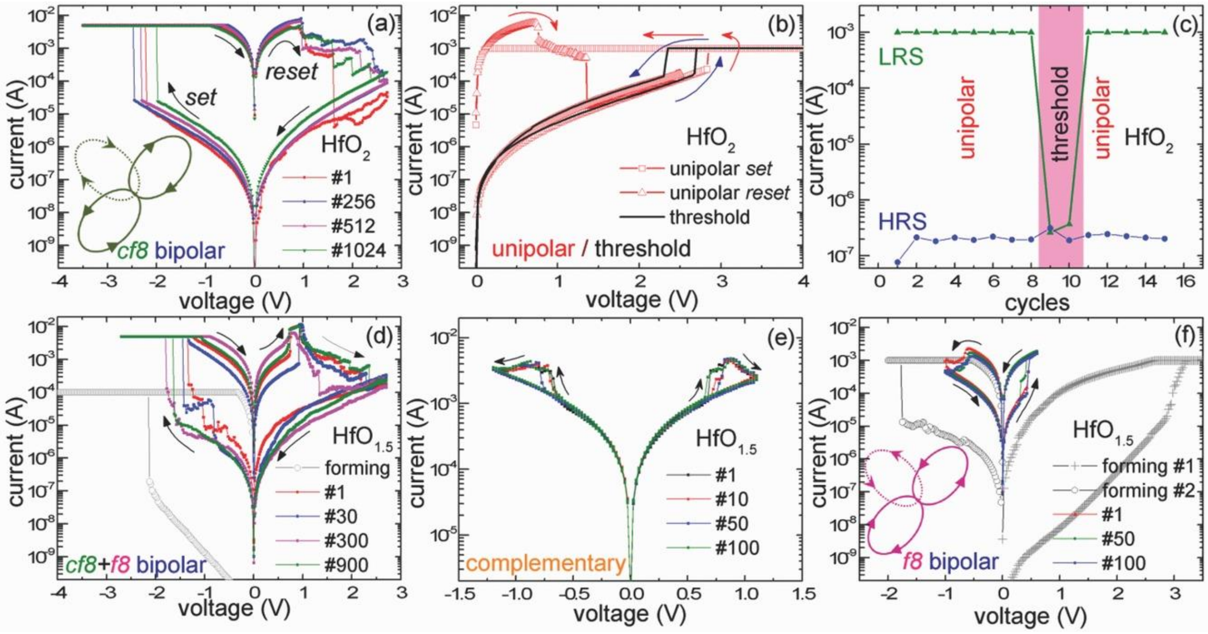

Figure 6: Switching modes of in HfO2-x based RRAM with all switching modes known for OXRAM with a) counter figure eight bipolar switching b) & c) unipolar and threshold switching for stochiometric HfO_2. In oxygen deficient $HfO_{1.5}$ the author could show combined counter figure eight + figure eight switching, e) complementary switching as well as f) figure eight switching. Reprinted after reference [31] https://doi.org/10.1002/adfm.201700432 with permission from John Wiley & Sons – Books. Copyright © 2017 WILEY-VCH Verlag GmbH & Co. KGaA, Weinheim.

In this initial forming step, the oxygen ions are diffusing locally away from a local filamentary region, in which the bandstucture is subsequently changed into an electrically conducting state, connecting both, the top and the bottom electrode. This process is partially reversible and can be repeated through switching by suitable I-V programming. During the formation of the conducting filament (but also during switching) it is necessary to limit the current (current compliance) to limit the size of the created filament, which would otherwise lead to an irreversible hard breakdown of the device. Fundamentally OxRAM devices can be operated in bipolar and unipolar resistive switching as shown in Figure 6 a) & b).

While bipolar resistive switching requires an asymmetry in the device structure (like two different electrodes) the unipolar switching mode is also possible in symmetric devices (with same electrode material). The bipolar resistive switching is usually referred to a valence change mechanism (VCM) in which the ionic movement is believed to be mostly driven by the electric field.[32, 33] In one voltage direction, the conducting filament is formed, while it is ruptured in the other direction. In contrary the unipolar switching happens in only one direction and is usually referred to the therochemical mechanism (TCM) which is believed to be governed mainly by competing concentration driven Fick diffusion and temperature dependent Soret effect.[32, 33] By applying a sufficiently high voltage an initial current is induced, which will lead to local joule heating inside the device. The local region with higher temperature promotes the diffusion of oxygen out of this region by the Soret effect and therefore a conducting filament is formed. By applying a current at lower voltages, the Fick diffusion is promoted, which leads to the recombination of vacancies and oxygen ions, rupturing the filament again. As can be seen in Figure 6 b) & c) threshold switching can coexist with unipolar switching. For this mechanism, after the formation of the filament a certain threshold voltage V required to maintain the on-state. Therefore, this switching mechanism is non-volatile. One explanation for this is improper heat dissipation which prevents the stable formation of a filament after the current is reduced.[34] It is referred to as a purely thermal effect.[35] Figure 6 d) shows the combined counter figure eight (cf8) and figure eight (f8) switching which also indicates a filament formation in the reset regime and gives rise to competing locations of filament formation and rupture for example at opposing electrode interfaces. The complementary switching as shown in Figure 6 e) shows another non-volatile switching mechanism which is symmetric in both polarities. Also this mechanism can be explained by competing regions in which the filament is formed and ruptured. By applying a suitable voltage, a conducting filament is formed, which is ruptured again e.g. at the opposite electrode side if the voltage is further increased and via versa in the opposite voltage direction.[31, 36] Figure 6 f) shows a bipolar switching mechanism in the figure eight (f8) direction. In this case it is reasonable to assume an inverse mechanism to the cf8 switching, where both the filament formation and rupture happen at the opposite electrode interface as for the cf8 switching.[31, 36]

An important characteristic in bipolar resistive switching in OxRAM is the rather abrupt set, in which the conducting filament is formed, while the reset shows some gradual reduction in the reset. The gradual reset can be understood in terms of a gradual reduction of the conducting filament diameter. This gradual behavior especially qualifies RRAM for neuromorphic applications and is responsible for the recent research interest in RRAM for brain inspired computing.[16] It was shown that the controlled introduction of oxygen vacancies via e.g. Molecular-Beam Epitaxy allows to promote the gradual behavior in transition metal oxides in the reset but even in the set direction.[29, 30]

All of the above mentioned mechanisms highlight the complexity of filamentary formation and rupture. Although in the last year's significant process was made towards the understanding of filamentary switching in RRAM, the precise processes, potential phase formations and the atomistic behavior during filamentary formation and switching remain a central matter of debate. A brief review on published nanoscale investigations on hafnia based RRAM is given at the introduction of chapter 4.4.

1.5. High Pressure and High Temperature HfO_2 polymorphs

Hafnium oxide is a polymorph material which shows several crystalline structures depending on temperature and pressure. It is noteworthy that the system of hafnium oxide behaves very similar to zirconium oxide, by showing very similar high pressure and high temperature structures. The ambient pressure, room temperature phase of stoichiometric hafnium oxide is of a monoclinic structure ($P2_1/c$). Via heating, the structure transforms into a tetragonal ($P4_2/nmc$) structure at around 1700 °C.[37] This monoclinic-tetragonal phase transformation does not occur at a specific point but gradually over a temperature range (from 0% - 100% phase transformation) and is fully reversible after cooling down. For both hafnium oxide and zirconium oxide it is known that these structures cannot be quenched. [38] Upon further heating, another phase transformation to a cubic ($Fm\text{-}3m$) structure takes place at around 2600 °C.[38, 39] Further annealing finally leads to the solid-liquid phase transformation which is observed around 2800 °C. All mentioned temperature dependent transformations are summarized in the following line after [38]

$$monoclinic \underset{1720\,°C}{\overset{1700°C}{\rightleftarrows}} tetragonal \underset{2600\,°C}{\overset{2600°C}{\rightleftarrows}} cubic \underset{2800\,°C}{\overset{2800°C}{\rightleftarrows}} liquid \qquad (1)$$

It is noteworthy that the coordination of hafnium to oxygen changes from the monoclinic to the cubic structure. While in monoclinic hafnium oxide the coordination of hafnium is seven fold, the coordination of oxygen is either three or four fold, resulting in an overall composition of HfO_2. For the case of stoichiometric cubic hafnium oxide hafnium oxide is eight fold coordinated to solely four fold coordinated oxygen (in a fluorite type arrangement), also resulting in the stoichiometric composition of HfO_2.[38, 40]

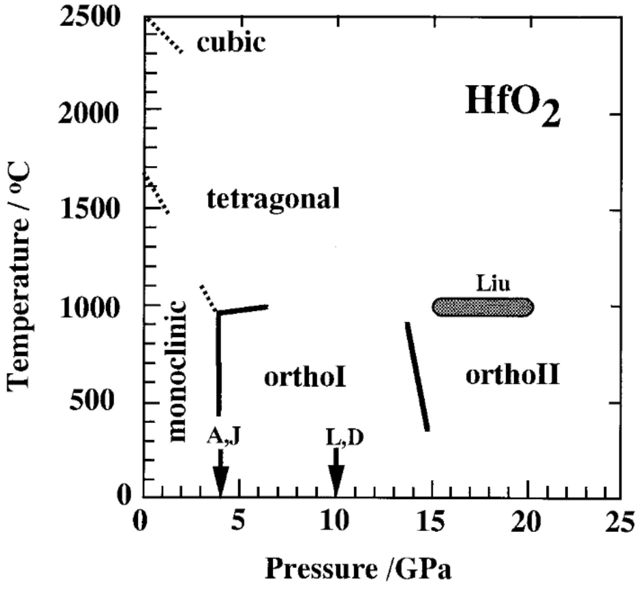

Figure 7: Experimentally verified polymorphism in stoichiometric HfO_2 showing five distinct phases with the monoclinic structure (*$P2_1/c$*) as the ambient pressure/temperature phase, the tetragonal (*$P4_2/nmc$*) and cubic (Fm-3m) structures as high temperature phases and the orthorhombic I (*Pbca*) and orthorhombic II (*Pmnb*) phase. Content reprinted from reference [39] https://doi.org/10.1111/j.1151-2916.2001.tb00843.x with permission of John Wiley & Sons - Books. Copyright © 2004 The American Ceramic Society, all rights reserved.

Additionally, to temperature studies, there is a vast number of investigations in the high pressure regime where two prominent orthorhombic structures could be identified. The first transformation occurs at about 14.5 GPa to the orthorhombic I structure (*Pbca*) and appears as a modification of the monoclinic structure, yielding seven-fold hafnium coordination. At even higher pressures of around 30 GPa a further transformation to a cottunite type structure (*Pmnb*) with nine-fold coordinated hafnium occurs. Those pressure induced transformations are summarized in the following line after [39]

$$\mathit{monoclinic} \underset{14.5\,GPa}{\overset{14.5\,GPa}{\rightleftarrows}} \mathit{orthorombic\ I} \underset{30.0\,GPa}{\overset{30.0\,GPa}{\rightleftarrows}} \mathit{orthorombic\ II} \qquad (2)$$

Interestingly for even higher pressures up to 50 GPa a further transformation to another tetragonal phase was reported. [41]

Figure 7 gives a rough phase diagram of the most relevant polymorphs of stoichiometric hafnium oxide as reported in literature. The phase boundaries noted in this figure are estimated from the results of multiple authors as mentioned in reference. [39]

It is important to mention that the phases of monoclinic, orthorhombic I and tetragonal hafnium oxide can be seen as distortions from the fluorite type cubic structure. In this sense all those phases are strongly interrelated. Especially the structures of cubic, tetragonal and orthorhombic I hafnium oxide show high similarities which can complicate definite phase allocations.

1.6. Ferroelectric Hafnium Oxide

The discovery of ferroelectricity in hafnium oxide promises a comparably easy to use ferroelectric material for the semiconductor industry. This is first and foremost due to its established CMOS compatibility.[42] Hafnium oxide is in contrast to the majority of known ferroelectric materials an easy binary compound and does not require high temperatures to be synthesized. [42] Therefore, in the recent years a great number of publications emerged on the topic of hafnia based ferroelectricity. With the discovery of ferroelectric behavior in hafnium oxide the scientific community proposed the existence of a polar orthorhombic phase. [43-46] Most commonly ferroelectricity was found in doped (Si, Zr, Y, Al, or Gd) [47] but also undoped hafnium oxide.[48, 49] As can be seen from Figure 8, the most prominent structures of hafnium oxide (compare chapter 1.5) including the high temperature structures of cubic and tetragonal hafnium oxide as well as the high pressure orthorhombic structures show non-polar symmetries, which disqualifies all of those structures for ferroelectricity.

In Figure 8 various hypothetical polar phases of hafnium oxide are proposed in decreasing symmetry order. The author proposes the two polar structures yielding the highest symmetry, namely orthorhombic $Pca2_1$ and $Pmn2_1$ as the most likely structures following a total energy argument.[47] Especially the orthorhombic $Pca2_1$ (equivalent to $Pbc2_1$) is proposed as ferroelectric phase by many publications.[43-46] While many authors find features similar to known hafnium oxide polymorphs in ferroelectric thin films, so far there is no clear picture of the exact crystal structures and lattice parameters of ferroelectric phases in hafnium oxide. This can be accounted to the high similarities of known and proposed crystal structures. Further, it is difficult to archive phase purity and often thin films are only synthesized as phase mixtures which complicates the assignment of individual reflexes. [43-48] Finally it is important to mention that polar behavior was identified in a (non-orthorhombic) rhombohedral structure of hafnium-zircon oxide (HZO).[50-52] For such rhombohedral structures polar space groups such as the R3 or R3M are discussed. [50-52] Generally, (as previously mentioned) a ferroelectric phase needs to be of a polar structure. A list of all available polar space groups is given in crystallographic books of reference such as the “International Tables of Crystallography”.[53]

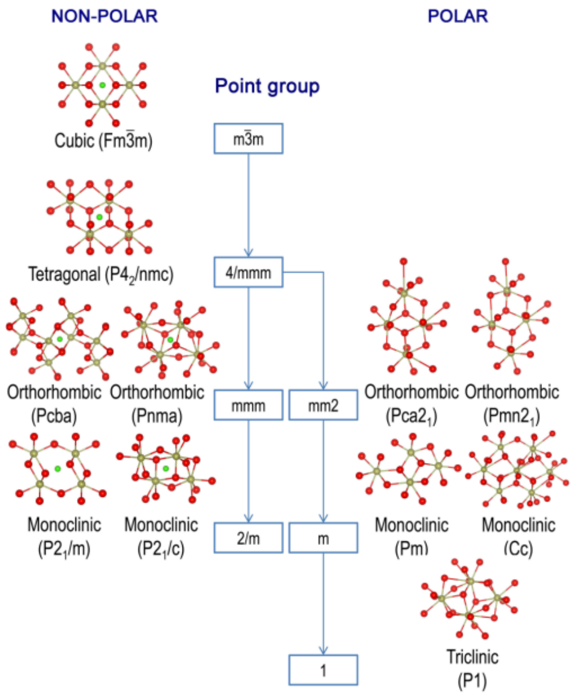

Figure 8: Known and hypothetical hafnium oxide symmetries as proposed by [47]. All verified phases of HfO_2 appear non-polar, while the proposed polar phases yielding the lowest total energy are of orthorhombic symmetry, including the most suggested symmetry $Pca2_1$ for ferroelectric hafnia. Content reprinted from reference [47] https://doi.org/10.1103/physrevb.90.064111 with permission of the American Physical Society. ©2014 American Physical Society.

1.7. Oxygen Deficient Phases of Hafnium Oxide

Oxygen deficiency in transition metal oxides is known to introduce defects which reduce the electrical resistance and can finally lead to a transition from an insulating to a conducting regime. Some of the first publications on the influence of oxygen defects in hafnium oxide investigate the electrical resistivity of polycrystalline specimens as a function of temperature and oxygen partial pressure.[54, 55] However, for those cases no structural investigation was included. On the other hand, there are several publications on hafnium oxide thin films grown under reducing conditions, including structural measurements (but without considering electrical properties). The structural features for such deficient hafnium oxide thin films are mostly indexed via the high temperature or high pressure phases of hafnium oxide (typically cubic *Fm*-3*m*, tetragonal $P4_2/nmc$ and orthorhombic I *Pbca*; compare chapter 1.5). [49, 56-60] However, as such oxygen deficient structures are almost exclusively synthesized in form of thin films, the measurements are susceptible to peak broadening and arbitrary texture. Furthermore, such thin films are typically obtained in form of phase mixtures (mostly together with a monoclinic phase fraction). All of the above mentioned issues together with the strongly interrelated nature of hafnium oxide polymorphs complicate a definite structural identification of the observed phases. One of the most rigorous investigations in the regime of oxygen deficient hafnium oxide was performed by E. Hildebrandt et al. by growing thin films over a broad range of oxidation conditions. [61-63] By applying a growth temperature of ~ 700 °C utilizing Molecular-Beam Epitaxy the author was able to show that the monoclinic structure can be maintained even after significant oxygen vacancy induced changes to the band structure as highlighted by the appearance of electrical conduction and the visual change from transparent to an apparent golden shine.[61-63] Another important finding in the Hf-O regime is the identification of *hcp*-Hf (the phase of metallic hafnium) with oxygen interstitials close to a composition of Hf_6O by Hiradiyashi at al. The authors found that the oxygen interstitials occupy the octahedral positions in the hcp Hf lattice in an ordered fashion.[64, 65] By heating above 430 °C an order-disorder transition for the interstitial positions could be identified. [64, 65]

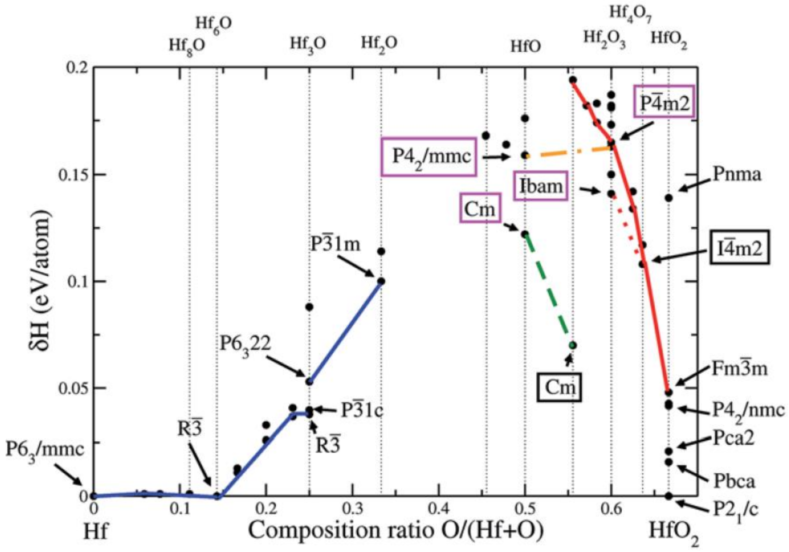

Figure 9: Fitness plot of hafnium oxide structures with different oxygen content predicted via evolutionary algorithm. At low oxygen contents oxygen is found to occupy octahedral positions in the (previously metallic) hexagonal lattice (blue line), the dashed green line shows an crossover of hexagonal and fluorite type structures while the red line indicates fluorite type structures and the doted red line, fluorite type structures with one dimensional vacancy chains [66, 67]. Content reprinted from reference [67] https://doi.org/10.1039/C8FD00104A with permission of the Royal Society of Chemistry. © The Royal Society of Chemistry 2019.

So far only experimental findings have been discussed, however there are many relevant theoretical publications on oxygen deficient hafnium oxide. One of the first rigorous DFT investigations of oxygen vacancies and interstitials in hafnium oxide was performed by Foster et al.[68] In addition, many more publications followed providing total energy, and defect energy level estimations on isolated oxygen defects in hafnium oxides. [69-73] Those publications, considering mostly insulated vacancies have been promoted through the discovery of hafnium oxide as an attractive high k solution for semiconductor applications. Later, with increasing research interest in RRAM, higher levels of oxygen deficiency have been considered and substoichiometric hafnium oxide phases like Hf_2O_3, HfO or Hf_6O have been proposed as possible phases in the formation of the conducting filament in RRAM.[66, 67, 74-77] A famous example is the prediction of a semi-metallic tetragonal phase of Hf_2O_3 by Xue et al.[76] Other interesting theoretical publications propose various sub-oxide phases over the whole oxidation range from HfO_2 to Hf. An important example is the work from Rushchanskii et al. [66, 67] who predicted via evolutionary algorithm various structures. As can be seen from Figure 9, phases at low oxygen concentrations are connected with a blue line, assigning them to modifications of the hcp-Hf lattice, where oxygen interstitials occupy octahedral positions. Similar results have been obtained from other authors.[74, 77, 78] In a more recent work from Schmidt et al. where hafnium oxide nanoislands where deposited by PLD, Rushchanskii showed simulations of "Hf_mO_n(:C) clusters (m = 3 to 10; n = 3 to 22)" with smaller coordination numbers than stoichiometric bulk hafnia.[79] In a publication from McKenna et al., it was even concluded that oxygen deficient hafnia should separate into m-HfO_2 and h-$HfO_{0.2}$.[74] Rushchanskii predicted HfO_x phases with monoclinic structure $1 < x < 1.25$ and fluorite-like structures for $1.5 < x < 1.75$. [74, 78] More recently Li L.-H., Xue K.-H. et al presented a study covering structure models from hafnia to hafnium, including monoclinic HfO_x cells roughly from 2 to -1.5, tetragonal cells from ~ 1.5 to 1.0 followed (in accordance with the previous publications) by hexagonal structures for the most oxygen deficient conditions.[77] As mentioned, many of such publications directly motivated with the perspective of finding candidate phases for the conducting filament in hafnium oxide based RRAM. [66, 67, 74-77]

1.8. Conduction Mechanisms in Resistive Memories

Conduction mechanisms are generally divided into interface dominated versus bulk dominated mechanisms.[80] Interface limited conduction mechanisms such as Schottky-emission, Fowler-Northeim tunneling, thermionic emission and direct tunneling depend e.g. on the interface barrier height and the type of charge carriers. Such interface limited conduction (attributed to electrode/dielectric interface) often shows rectifying behavior, meaning that the I-V dependence shows an asymmetry in the negative as compared to the positive direction of polarity. On the other hand, symmetric I-V behavior is expected for bulk limited conduction mechanisms such as Poole-Frenkel emission, Ohmic conduction, Space charge limited conduction (SCLC), ionic conduction, nearest neighbor- & variable range hopping conduction, trap assisted tunneling and grain-boundary-limited conduction.[80] In contrast to interface related mechanisms, bulk limited conduction is determined by properties of the (dielectric) material itself, such as the carrier mobility, density of states, trap density and the trap energy levels.[32] To identify a certain conduction mechanism, fitting to known mathematical expressions of the corresponding electric field or temperature dependence are the most popular approaches (See Table 1). Further, as previously mentioned many articles also investigate the symmetry of the corresponding I-V curves to separate e.g. bulk limited from interface limited conduction (like Poole-Frenkel emission from Schottky conduction).

For resistive switching memories there is no broad agreement on dominant conduction mechanisms in these devices. However, amongst often observed mechanisms are Poole-Frenkel emission, Schottky emission, SCLC, trap assistant tunneling and hopping conduction.[32] Also, between the high resistance state and the low resistance state, the conduction mechanism often (but not always) changes. In many cases the low resistance state corresponds to ohmic conduction. This non-uniform appearance of conduction mechanisms is even given for devices which are made from the same material, which highlights the complexity of these systems which are potentially susceptible to thickness, electrode materials (and therefore different interfaces) and fabrication process (therefore different material qualities). Also different conduction mechanisms may be dominant at different temperatures and/or contributing simultaneously to the total current.

For hafnium oxide based devices the following conduction mechanisms have been reported: Poole-Frenkel emission [81], Schottky emission [82, 83], SCLC [84], Trap assisted tunneling [85, 86], hopping conduction [87] and ohmic conduction (often in the LRS) [31].

Table 1: Survey of relevant conduction mechanisms with corresponding current density expression and electric field and temperature dependency. Adopted after reference [32] https://doi.org/10.3390/electronics4030586 which is published under Attribution 4.0 International (CC BY 4.0) License.

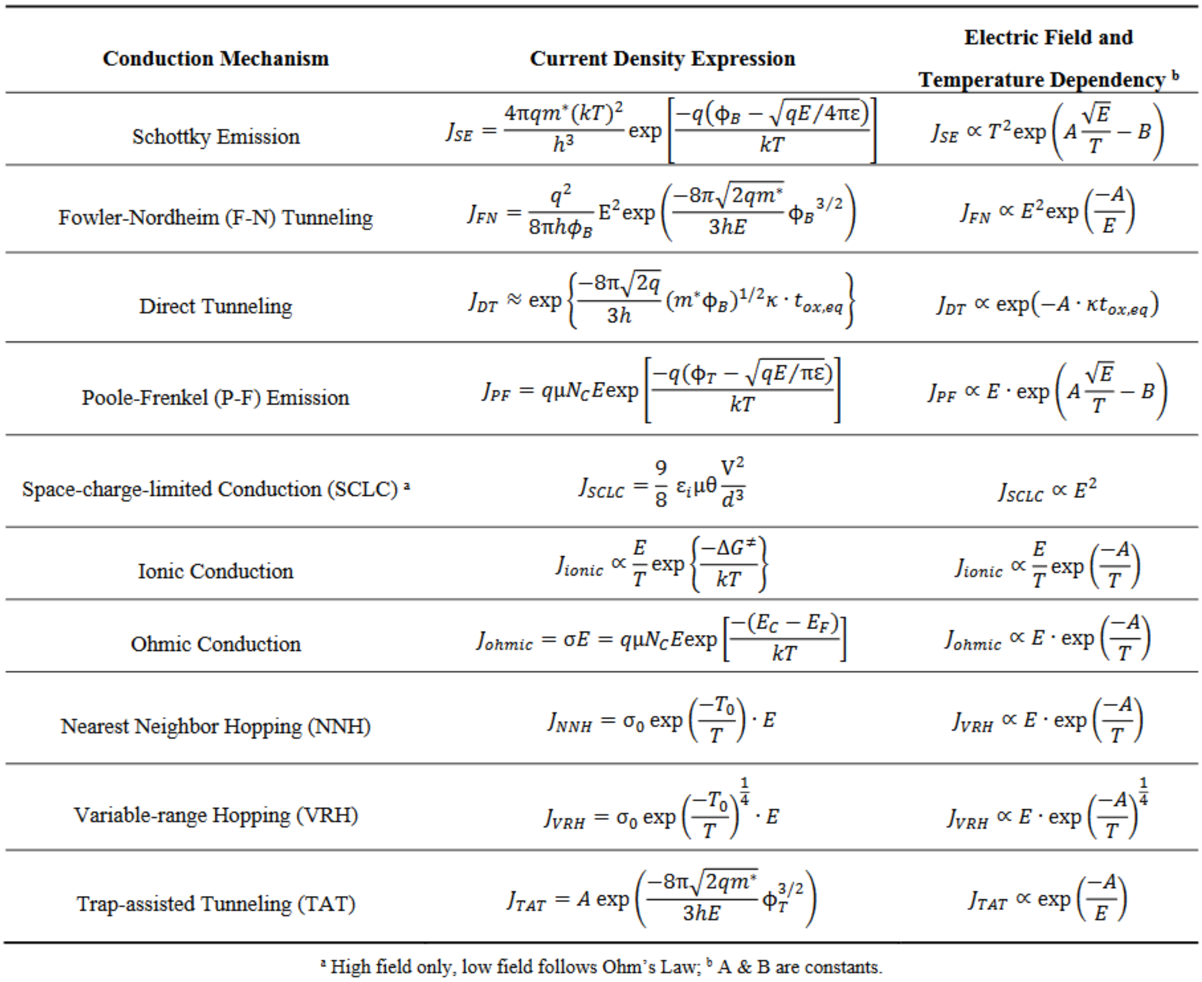

Conduction Mechanism	**Current Density Expression**	**Electric Field and Temperature Dependency** [b]
Schottky Emission	$J_{SE} = \frac{4\pi q m^*(kT)^2}{h^3} \exp\left[\frac{-q\left(\phi_B - \sqrt{qE/4\pi\varepsilon}\right)}{kT}\right]$	$J_{SE} \propto T^2 \exp\left(A\frac{\sqrt{E}}{T} - B\right)$
Fowler-Nordheim (F-N) Tunneling	$J_{FN} = \frac{q^2}{8\pi h \phi_B} \mathrm{E}^2 \exp\left(\frac{-8\pi\sqrt{2qm^*}}{3hE} {\phi_B}^{3/2}\right)$	$J_{FN} \propto E^2 \exp\left(\frac{-A}{E}\right)$
Direct Tunneling	$J_{DT} \approx \exp\left\{\frac{-8\pi\sqrt{2q}}{3h}(m^*\phi_B)^{1/2}\kappa \cdot t_{ox,eq}\right\}$	$J_{DT} \propto \exp(-A \cdot \kappa t_{ox,eq})$
Poole-Frenkel (P-F) Emission	$J_{PF} = q\mu N_C E \exp\left[\frac{-q(\phi_T - \sqrt{qE/\pi\varepsilon})}{kT}\right]$	$J_{PF} \propto E \cdot \exp\left(A\frac{\sqrt{E}}{T} - B\right)$
Space-charge-limited Conduction (SCLC) [a]	$J_{SCLC} = \frac{9}{8}\, \varepsilon_i \mu \theta \frac{\mathrm{V}^2}{d^3}$	$J_{SCLC} \propto E^2$
Ionic Conduction	$J_{ionic} \propto \frac{E}{T} \exp\left\{\frac{-\Delta G^{\neq}}{kT}\right\}$	$J_{ionic} \propto \frac{E}{T} \exp\left(\frac{-A}{T}\right)$
Ohmic Conduction	$J_{ohmic} = \sigma E = q\mu N_C E \exp\left[\frac{-(E_C - E_F)}{kT}\right]$	$J_{ohmic} \propto E \cdot \exp\left(\frac{-A}{T}\right)$
Nearest Neighbor Hopping (NNH)	$J_{NNH} = \sigma_0 \exp\left(\frac{-T_0}{T}\right) \cdot E$	$J_{VRH} \propto E \cdot \exp\left(\frac{-A}{T}\right)$
Variable-range Hopping (VRH)	$J_{VRH} = \sigma_0 \exp\left(\frac{-T_0}{T}\right)^{\frac{1}{4}} \cdot E$	$J_{VRH} \propto E \cdot \exp\left(\frac{-A}{T}\right)^{\frac{1}{4}}$
Trap-assisted Tunneling (TAT)	$J_{TAT} = A \exp\left(\frac{-8\pi\sqrt{2qm^*}}{3hE} \phi_T^{3/2}\right)$	$J_{TAT} \propto \exp\left(\frac{-A}{E}\right)$

[a] High field only, low field follows Ohm's Law; [b] A & B are constants.

2. Methods

2.1. X-ray Investigations with a Universal Goniometer

X-ray analysis provides a non-destructive tool for the characterization of solid matter. With a four-circle goniometer it is possible to apply a wide range of measurement techniques which are mostly characterized by the relative angles between the X-ray source (Incident beam), the sample and the detector. Figure 10 shows the according arrangement of the goniometer setup with the relevant angles θ, ω, ϕ and χ. In the following chapters, different measurement techniques and physical principles which are relevant to this goniometer arrangement will be discussed.

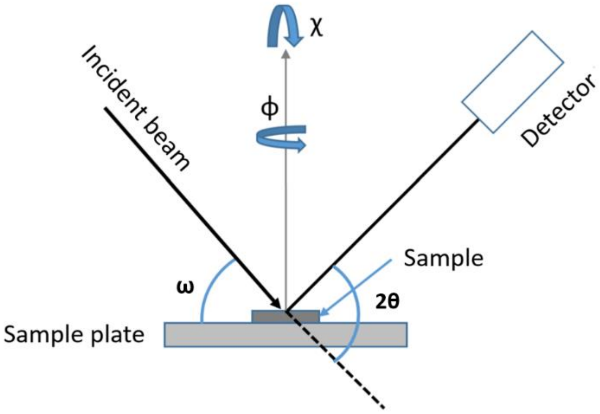

Figure 10: Four cycle with all associated degrees of freedom in θ, ω, ϕ and χ.

2.1.1. X-ray Reflectometry

X-ray reflectometry (XRR) is a characterization method that was developed ~ 1985 primarily for thin film analysis. The method is characterized by a monochromatic X-ray beam (e.g. Cu Kα) which is directed under low angles of typically 0 ° - 5 ° on the samples surface.[88] The X-ray signal, which is consequently reflected, is then detected at the opposing side under the same angle as the angle of incidence (specular reflectivity). Due to the simple geometry, sharing basically the same degrees of freedom necessary for basic 2θ/ω X-ray diffraction analysis, the measurement can be performed by most diffractometers and evolved into a standard method for thin film analysis.

XRR analysis allows extracting many properties inherent to thin films or in case of multilayer structures layer and interface properties. One of the most prominent characteristics being the thin film thickness, which can be obtained in the range of typically 3 - 300nm with sub-nm precision.

Figure 11 gives a comprehensive overview of the different features of a typical XRR graph and the corresponding properties. First, one can see the critical angle θ_c which determines, up to which angle the incident beam is completely reflected from the surface (assuming the ideal case with no absorption).[88, 89] By passing the critical angle, the X-ray beam will be transmitted through the thin film layer, leading to a drastic decline in reflectivity. The critical angle is directly associated with the electron density, indicating the total density ρ of the thin film material. Therefore, this value can be useful to e.g. verify stoichiometric or indicate defective compounds provided that the corresponding density is significantly affected.[90]

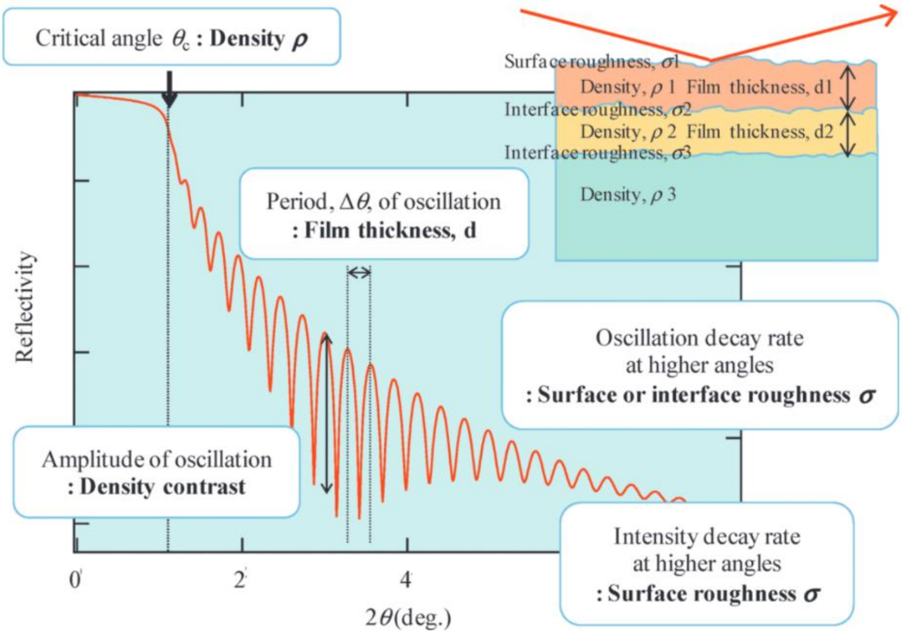

Figure 11: Typical XRR graph in which different features are correlated with various thin film properties. Content reprinted from reference [89].

By transmitting into the layer, a part of the X-ray signal is always reflected. This effect takes place at every interface, at least the air/thin-film and the thin-film/substrate interface.[88] The superposition of both reflected signals results in angle dependent oscillating interference fringes from which the thin film thickness can be deduced. Parratt [91] and Blanton [92] showed direct relations between the positions of interference maxima and the corresponding film thickness.

Further characteristics are the density contrast, which is associated with the amplitude, the initial intensity decay rate at higher angles, which correlates with the surface roughness and the oscillation decay rate at higher angles corresponding to both surface roughness and interface roughness. [89]

While the thin film thickness of a one-layer system can conveniently be extracted by simple equations [92], more information is usually extracted by the use of XRR simulation software which even allows to analyze multilayer systems and estimate individual layer thicknesses, densities and interface roughness. [93]

2.1.2. Bragg-Diffraction & Rocking Curve

One of the most prominent relations in the context of X-ray diffraction analysis is the famous Bragg law which was derived in 1912 by William Lawrence Bragg. The formula is based on the phenomena that an incident beam of wavelength λ which is diffracted of a crystalline sample leads to angle dependent constructive or destructive interference correlated to available lattice planes. Constructive interference is achieved, when the phase shift of the diffracted beam components is zero. The phase shift in turn is always zero if the path difference of beam fractions being diffracted of two lattice planes equals an integer value n of the wavelength λ. The total path difference is derived from simple geometric relations (see Figure 12) and dependent on both, the incidence angle θ as well as the lattice plane spacing d.

The full mathematical expression is then given by:

$$n \cdot \lambda = 2 \cdot d \cdot sin(\theta). \tag{3}$$

Alternatively by applying crystallographic formalism, the integer value n can mathematically be included by the use of Laue indices (hkl).

$$\lambda = 2 \cdot d_{hkl} \cdot sin(\theta) \tag{4}$$

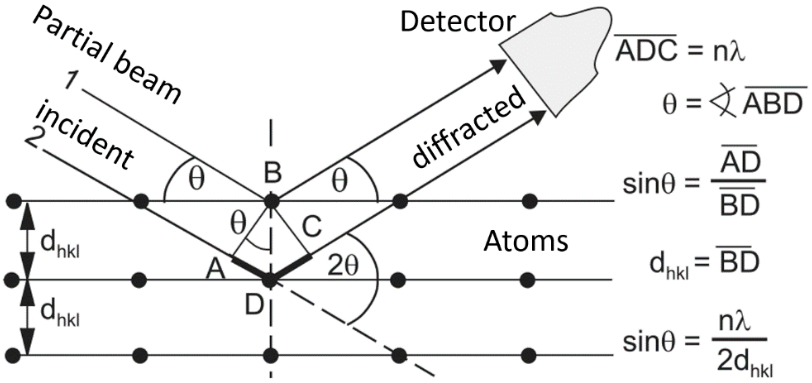

Figure 12: Bragg-Law and its geometric relations between d_{hkl}, λ and $sin(\theta)$. Content reprinted from reference [88] with permission of Springer.

Important tools to identify a certain phase are databases of powder diffraction files. The most important databases for crystallographic data are maintained by the International Centre for Diffraction Data (ICCD, PDF products), FIZ Karlsruhe (Inorganic Crystal Structure Database – ICSD) in cooperation with the National Institute of Standards and Technology (NIST); and the freely available Crystallography Open Database (COD). Every phase features a specific set of d_{hkl} values, which translate (as previously discussed) in certain 2θ positions.

The relative intensities depend on the atomic form factors and the superordinate structure factor which describe the scattering of isolated atoms and the whole crystal structure, respectively.

Standard database entries are given by so-called powder diffraction files (PDF) which are obtained from powder measurements or calculated. In any case the relative 2θ positions and intensities are listed as they would appear from a powder measurement. In the most ideal case all 2θ positions and relative intensities match with a database entry of an expected compound.

However, in case of thin films, the reflections are often subject to peak broadening (due to limited grain sizes and overall thickness), and epitaxial relations which can lead to preferred crystal orientations. Especially due to the texturization it is in many cases not possible to capture all relevant reflections in a single 2θ scan. This is discussed in further details in chapter 2.1.3 (see Figure 15). Also relative intensities in thin films cannot be translated into PDF data, as the multiplicity of lattice spacing's in a powder cannot be (directly) translated into oriented crystal structures. The intensities are then determined by the nature of epitaxy, potential multi-domain orientations and thin film geometry.

Nonetheless, PDF data remains an important point of reference. As already discussed in the previous chapter's hafnium oxide is a strongly polymorph material (See chapters 1.5, 1.6 and 1.7). Figure 13 shows XRD patterns from PDFs of relevant hafnium oxide phases. This comparison shows that the patterns of cubic (*Fm-3m*), tetragonal (*P42/nmc*) and orthorhombic I (*Pbca*) are similar and share a strong reflection around 30° in 2θ. Further around 35° in 2θ one can see symmetry dependent peak splitting, showing the strong interrelation of those phases. As evident from the diffraction patterns, the monoclinic ambient pressure phase and the high pressure orthorhombic phase can be discerned much more easily.

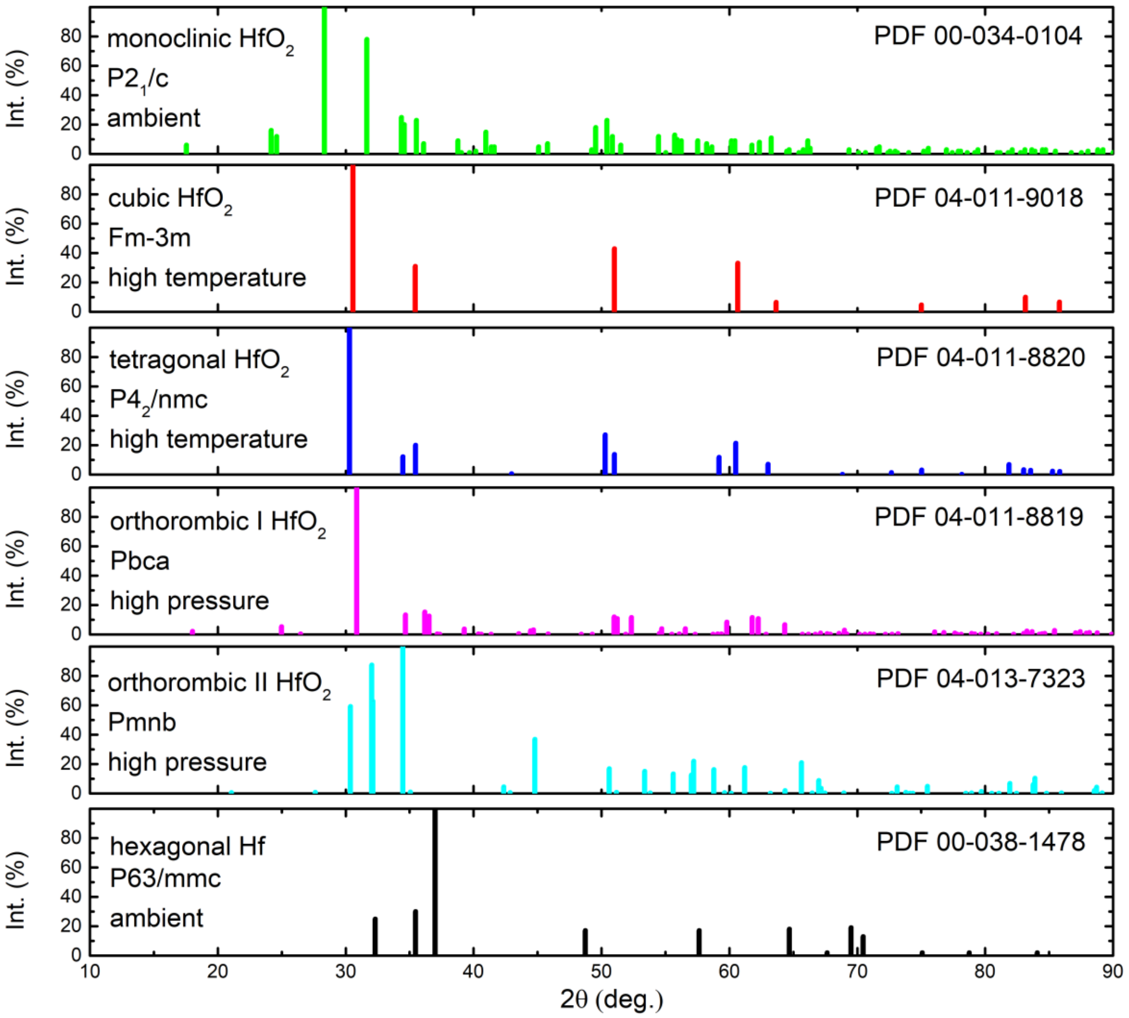

Figure 13: XRD patterns as obtained from powder diffraction files for relevant hafnium oxide and hafnium structures (Compare chapter 1.5). Note that especially the structures of cubic (*Fm-3m*), tetragonal (*$P4_2/nmc$*) and orthorhombic I (*Pbca*) show similar patterns where all structures share an intense reflection at about 30° in 2θ with peak splitting occurring in dependence of symmetry at about 35° 2θ. This highlights how the tetragonal and the orthorhombic phase are distorted from the cubic, fluorite type *Fm-3m* structure. In contrast, the ambient phase of monoclinic hafnia as well as the high-pressure orthorhombic II phase can be easily discerned. Further, the hexagonal phase of metallic hafnium shows significant differences to all hafnium oxides.

Further, the phase of metallic hexagonal hafnium shows definitely a distinct pattern from all displayed hafnium oxides.

As mentioned previously, thin films, which show an epitaxial relation, are often highly oriented. One method to probe the quality of the orientation of a thin film is to do a rocking-curve measurement. Figure 14 shows the basic principle of such a measurement. First the 2θ angle is set to the value of plane d_{hkl}. Then the ω angle is tilted in positive and negative direction relative to the alignment position (compare Figure 10). Figure 14 shows exemplary how a typical thin film measurement looks like in relation to its substrate. In most cases, the thin film shows a more significant peak broadening than the single crystalline substrate. This full width half maximum (FWHM) of the obtained peak is a measure of the relative spread of crystal planes which is called mosaicity. If a rocking-curve peak is observed a strong texture can be assumed in any case. If there is an additional background under the actual peak, this can serve as an indication of interfacial defects, like misfit dislocations which are often induced as a consequence of epitaxial strain.[94]

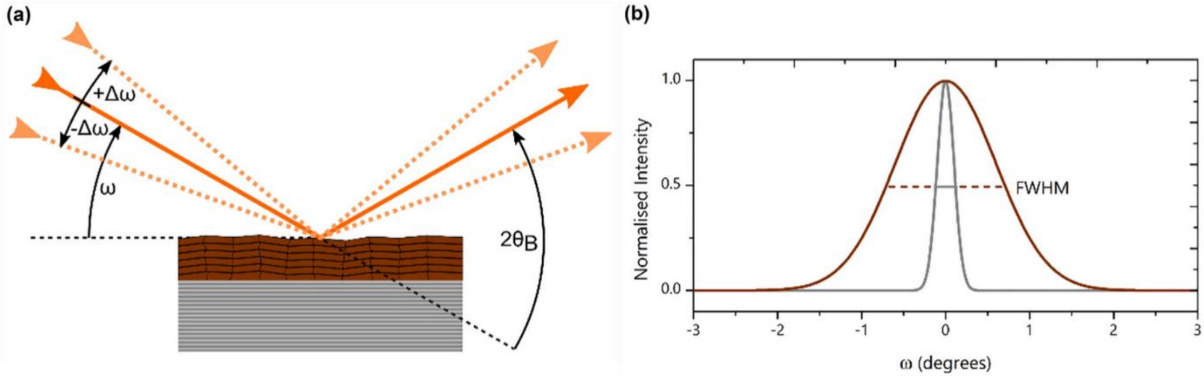

Figure 14: a) Basic Rocking-curve principle with the 2θ angle being set to a defined lattice plane reflection while the ω angle is scanned in a positive and negative direction with respect to the aligned starting positon. b) Shows how the highly oriented substrate (as shown in a) shows a significantly reduced FWHM as compared to the less oriented thin film. Content reprinted from reference [95] https://doi.org/10.1007/s10832-021-00263-6 with permission of Springer Nature BV. © The Author(s), under exclusive licence to Springer Science+Business Media, LLC, part of Springer Nature 2021.

2.1.3. Pole Figures & Geometric Relations in Single Crystals

Pole figure measurements are characterized by scanning ψ and φ angles while maintaining the 2θ angle (compare Figure 15).

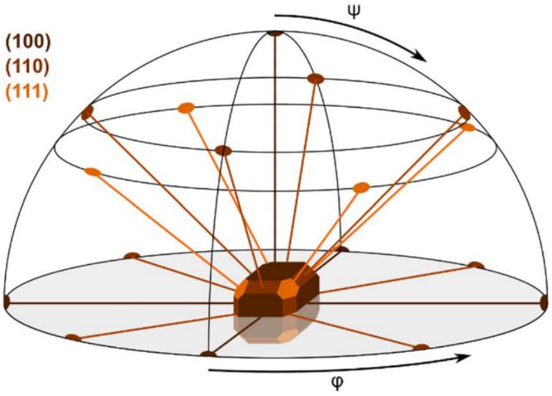

Figure 15: Exemplary pole figure dome showing on an cubic single crystal at which ψ and φ angles the specific lattice planes (100), (110) and (111) show up. For a measurement the 2θ angle is set to a defined value which matches a feature (e.g. the (111) lattice plane) while ψ and φ angles are mapped (covering the displayed dome). The obtained intensity distribution is projected on a 2D plane, showing at which positions the mapped feature shows up. Content reprinted from reference [95] https://doi.org/10.1007/s10832-021-00263-6 with permission of Springer Nature BV. © The Author(s), under exclusive licence to Springer Science+Business Media, LLC, part of Springer Nature 2021.

In this way one can detect at which geometrical positions a certain lattice plane is arranged. Therefore, this kind of measurement is relevant for samples where preferential crystallographic orientations are expected like in forged or rolled metals, single crystals or thin films where epitaxy to the substrate often enables strongly textured growth. By choosing a measurement range of 0 – 90 ° in ψ and 0-360 ° in φ results in a typical complete hemispherical scan around the sample.

An practical example of a pole figure data-set of thin films in given in Figure 16. While those images are a result of Electron scattering via Electron Backscatterd Diffraction (EBSD) the information is complementary to pole figures obtained via X-ray scattering. The figure shows at which angles the (10-11) lattice planes are oriented. Interestingly, in dependence of the growth temperature different orientations of the graphite layer with respect to the substrate can be identified. Note that the different multi-domain characteristics (as indicated by red and yellow dotted lines) can be easily distinguished from such a pole figure dataset.

To verify a certain crystallographic structure in a strongly textured system, it can be useful to evaluate the geometrical angles between lattice planes.

The equations for a triclinic system include all possible degrees of freedom for the lattice parameters a, b, c as well as α, β, γ. Here the angle between two lattice planes is given as a general solution via:

$$\cos(\delta) = \frac{d_{h1k1l1} \cdot d_{h2k2l2}}{{V_{UC}}^2} \cdot A_A \tag{5}$$

with

$$A_A = s_{11}h_1h_2 + s_{22}k_1k_2 + s_{33}l_1l_2 + s_{23}(k_1l_2 + k_2l_1) + s_{13}(l_1h_2 + l_2h_1) + s_{12}(h_1k_2 + h_2k_1)$$

and

$$s_{11} = b^2c^2sin^2(\alpha) \qquad s_{12} = abc^2(cos(\alpha)\cos(\beta) - \cos(\gamma))$$

$$s_{22} = a^2c^2sin^2(\beta) \qquad s_{23} = bca^2(cos(\beta)\cos(\gamma) - \cos(\alpha))$$

$$s_{33} = a^2b^2sin^2(\gamma) \qquad s_{13} = acb^2(cos(\gamma)\cos(\alpha) - \cos(\beta))$$

Here $h_1k_1l_1$ and $h_2k_2l_2$ as well as d_{h1k1l1} and d_{h2k2l2} are the Miller indices and the lattice plane spacing's of the two relevant lattice planes. Further V_{UC} is the volume of the unit cell.

Lattice plane spacing's d_{hkl} are generally obtained via the following formula:

$$\frac{1}{d_{hkl}^2} = \frac{Q}{a^2b^2c^2(1 - cos^2(\alpha) - cos^2(\beta) - cos^2(\gamma) + 2\cos(\alpha)\cos(\beta)\cos(\gamma))} \qquad (6)$$

with

$$\mathrm{Q} = b^2c^2h^2sin^2(\alpha) + c^2a^2k^2sin^2(\beta) + a^2b^2l^2sin^2(\gamma) + 2abc^2hk(\cos(\alpha)\cos(\beta) - \cos(\gamma)) + 2ab^2chl(\cos(\alpha)\cos(\gamma) - \cos(\beta)) + 2ba^2ckl(\cos(\beta)\cos(\gamma) - \cos(\alpha)).$$

The unit cell volume V_{UC} can be deduced from the following relation:

$$V_{UC} = a \cdot b \cdot c\sqrt{1 - cos^2(\alpha) - cos^2(\beta) - cos^2(\gamma) + 2\cos(\alpha)\cos(\beta)\cos(\gamma)}\,. \qquad (7)$$

By applying such calculations, it is easy to determine e.g. a certain ψ angle for a φ measurement with respect to the out of plane lattice parameter. Further ψ and φ dependent 2θ variations can be verified.

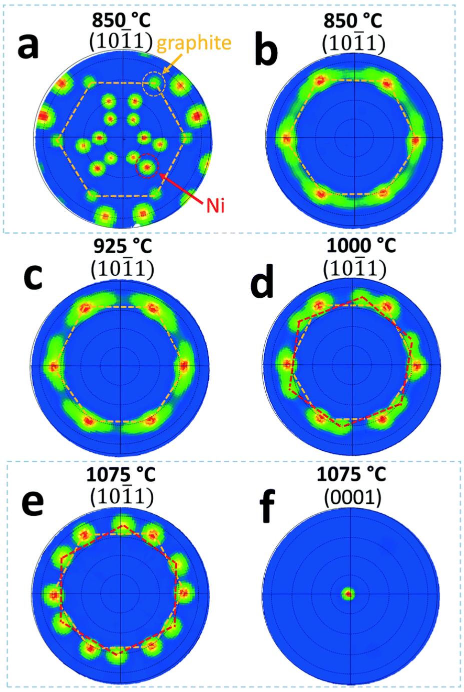

Figure 16: Exemplary EBSD pole figures tracking the (10-11) lattice plane of graphite on (a) Ni substrate and (b)-(e) after transfer to SiO_2/Si showing varying alignment with respect to the substrate in dependence of their growth temperature. Especially the different multi-domain characteristics (yellow and red dotted lines) can easily be identified by the pole figure analysis. (f) Further analysis of the (0001) plane shows its perpendicular alignment to the substrate. Content reprinted from reference [96] https://doi.org/10.1039/C9CE01515A with permission of the Royal Society of Chemistry. © The Royal Society of Chemistry 2020.

2.2. Transmission Electron Microscopy

Transmission electron microcopy (TEM) is a technique in which a thin specimen is exposed to an electron beam and transmitted electrons are detected in order to achieve a magnified image. In its basic TEM mode, many processes in an electron microscope work analog to an optical microscope, the terminologies are very similar. The electron beam is generated in an electron gun with high acceleration voltages of a few 10 to several 100 kV.[97] Consequently the beam is directed through a series of apertures and lenses as well as the specimen and projected onto a screen or recorded via different detectors. Two distinct setups are presented in Figure 17 showing a) a transmission electron microscope setup (TEM) and b) a scanning transmission electron microscopy configuration (STEM).

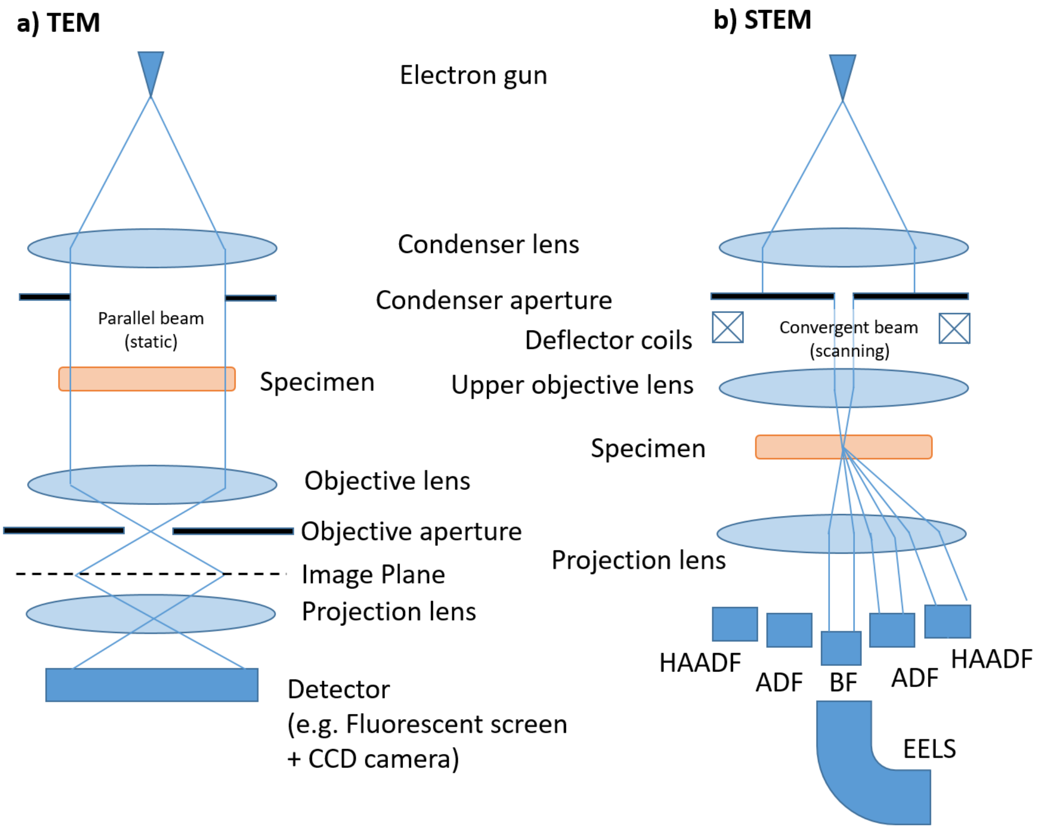

Figure 17: Simplified beam path and fundamental working principle of a) transmission electron microscopy (TEM) and b) scanning transmission electron microscopy (STEM). Note that for the TEM sketch the incident beam is parallelized before hitting the specimen, while for the STEM configuration a convergent beam is locally directed onto the sample. This convergent beam is consequently scanned across the sample surface. After interaction with the sample, the beam may be recorded by different detectors like the bright field (BF), annular dark field (ADF) or high angle annular dark field detector (HAADF) detector. Alternatively, to BF imaging the beam may be analyzed by electron energy loss spectroscopy (EELS).

In case of the TEM setup the electron beam is first parallelized, before being transmitted through the specimen. When passing through the sample, the electrons interact with the specimen and a number of different interaction types can be used to form an image. Typical modes for TEM are the diffraction mode, in which crystallographic diffraction patterns are captured, or the bright field mode in which both, amplitude and phase contrast can play a role. The final image is then recorded by a CCD screen.

A given optical system can be described including its optical properties in the contrast transfer function (CTF) shown in Figure 18 a), which shows the relative contrast which is delivered for each spatial frequency at a given defocus. In TEM the CTF is especially important for high resolution imaging. As can be seen, the function follows a sinusoidal-like dependence oscillating around zero. Those frequencies close to zero are therefore not delivered and lost in the final image. Also, the phase contrast is oscillating between positive and negative values which can complicate the interpretation of the measured image. Therefore, for many cases (especially in materials science) the Scherzer focus as displayed in Figure 18 a) as the blue line is considered the optimal focus, as it allows to image a broad band of special frequencies over a comparable uniform phase contrast conditions.[98] However, if larger features need to be imaged (e.g. in the field of biology), it can be beneficial to choose a higher defocus (see green line in Figure 18 a), in order to shift the total value of the phase contrast to lower special frequencies, sacrificing resolution but allowing to image larger features with stronger contrast.

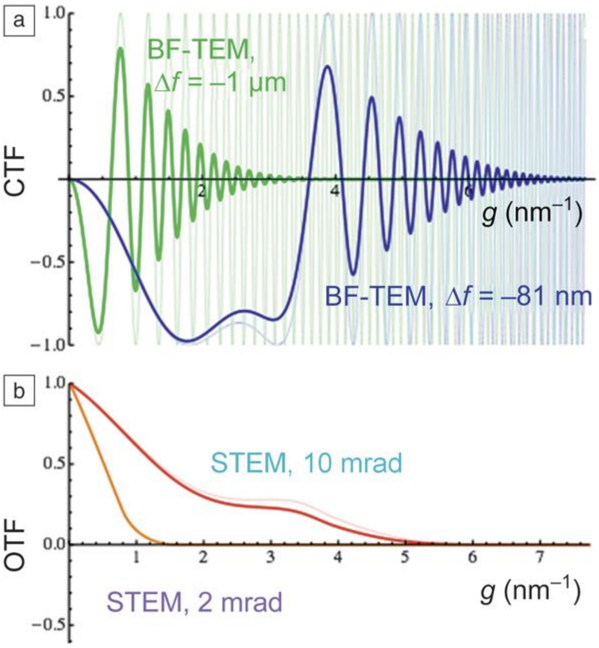

Figure 18: a) Simulated contrast transfer function (CTF) for TEM in Scherzer focus (blue), covering a broad spectrum of spatial frequencies with rather uniform contrast. The green line shows the CTF at a high defocus value, allowing better contrast for bigger feature sizes, but sacrificing resolution. The more transparent lines show the corresponding CTFs assuming an ideally coherent electron source, while the dampened functions represent CTFs assuming a real electron source. b) Shows simulated optical transfer functions (OTF) which are relevant for STEM. The red line corresponds to the Scherzer focus, offering good contrast at high resolution. The orange line corresponds to a smaller beam convergence, which sacrifices resolution for enhanced depth of focus. Content reprinted from reference [99] https://doi.org/10.1557/mrs.2016.136 with permission of Springer. Copyright © Materials Research Society 2016.

While in a typical TEM setup the beam passes through the sample in a parallelized fashion (Figure 17 a), in STEM (Figure 17 b) the electron beam is converged to probe a local area on the specimen und consequently scanned across the samples surface. In this way each signal which is captured from the transmitted electron beam can be directly assigned to a specific location on the sample. For a typical STEM setup, there is a variety of different detectors to capture different signals of the transmitted electron beam. First, there is the bright field (BF) detector, which allows to capture images similar to (BF) TEM. Other detectors are the annular dark field detector, which captures electrons which have been scattered at a larger angle. In contrast to conventional dark field TEM the scattered electrons do not need to pass through an objective aperture. Therefore, by collecting all scattered electrons with an ADF angle with an annular ring detector, one can achieve much higher count rates. For STEM it is also common to have the possibility to detect high angle annular dark field (HAADF) images with a corresponding annular detector. The advantage of this technique is its Z-contrast sensitivity which allows to obtain an element weight specific contrast which can be e.g. beneficial to monitor interfaces of heterostructures in materials science.

In STEM the contrast transfer function does not apply. Instead the optical transfer function (OTF) as shown in Figure 18 b) needs to be considered which is especially important for high resolution imaging. Other than the CTF, the OTF is not oscillating. In Figure 18 b) simulated OFTs are shown where the red line corresponds to the Scherzer focus (optimal resolution) while the line in orange shows a function for a smaller beam convergence, allowing for an increased depth of focus, but sacrificing resolution.

A further advantage of the STEM setup is the possibility to use either the bright field detector or an electron energy loss spectroscopy (EELS) unit while doing dark field imaging to capture signals simultaneously.

While the methods discussed so far are not energy dispersive (relying on elastically scattered signals), the previously mentioned technique of EELS allows to detect inelastically scattered electrons in dependence of their kinetic energy.[100] The detected electron-energies therefore allow to identify specific elements in the sample, but can also provide information about the chemical environment of the investigated species (core spectra). Further, in the low loss region (<50 eV) it is possible to extract features of the valence band region. Therefore, EELS shows similarities to X-ray photoelectron spectroscopy which is discussed in chapter 2.3.

Another important method is called 4D-STEM. For this technique a pixelated detector is used, which allows to generate a 2D image for every 2D raster position on the samples surface (therefore being referred to as 4D). One method associated with 4D-STEM is automated crystal orientation mapping (ACOM). For ACOM, for every electron beam raster-position an 2D diffraction pattern is obtained. Those diffraction patterns are then processed by an algorithm to assign a phase and crystal orientation for every pixel of the 2D sample surface. This technique is especially useful to identify e.g. the orientation of different domains in a sample or to discriminate between different phases in a phase mixture.

2.3. X-ray Photoelectron Spectroscopy

X-ray Photoelectron Spectroscopy (XPS) is a surface sensitive, nondestructive analysis technique which uses the photoelectric effect to investigate the chemical properties of a material from a qualitative and quantitative perspective.

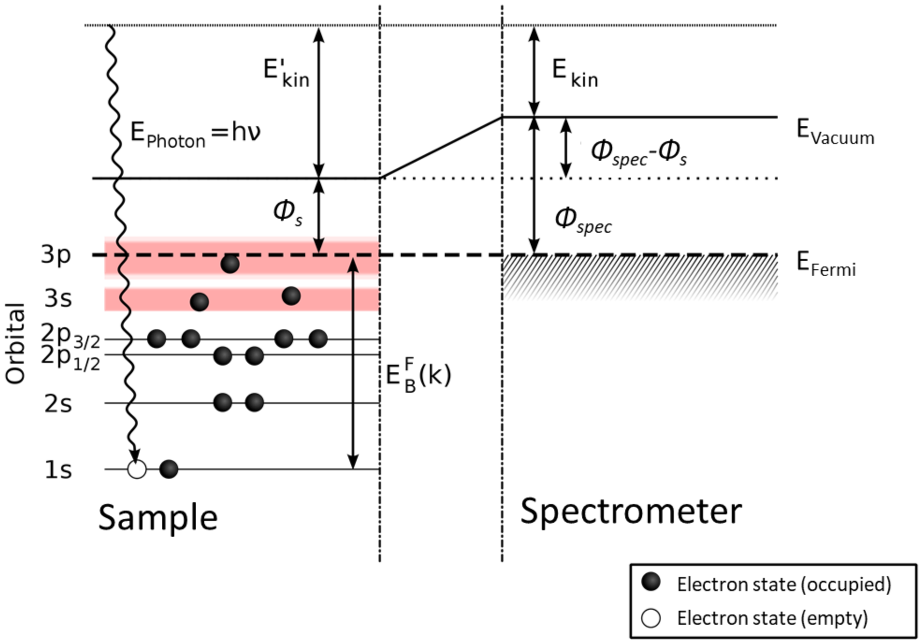

Figure 19: Energy scheme for emission and detection in X-ray Photoelectron spectroscopy. Modified after https://de.wikipedia.org/wiki/Datei:XPS_-_Energy_levels_%28schematic%29_DE.svg (2023) which is published under Attribution-ShareAlike 3.0 Unported (CC BY-SA 3.0) Creative-Commons-License.

The analysis technique works by irradiating a sample by an X-ray source (for example Al Kα). By the incident photons electrons are excited from the valence band and core states. The process is illustrated in Figure 19. In order to escape to the vacuum level the electrons needs to overcome their orbital-specific binding energy E_B^F with respect to the fermi level as well as the material specific work function of the sample ϕ_s. After subtracting both contributions, the remaining energy that was transferred by the photon $h\nu$ is carried by the excited electron via kinetic energy E'_{kin} after the following relation

$$E'_{kin} = h\nu - \phi_s - E_B^F \tag{8}$$

The binding energy E_B^F (with respect to E_F =0) is the quantity over which XPS spectra are typically plotted. It is obtained as follows:

$$E_B^F = h\nu - \phi_s - E'_{kin} \tag{9}$$

By grounding both the sample and spectrometer, their fermi levels are aligned and a contact potential $\phi_{spec} - \phi_s$ is formed (Compare Figure 19). As a consequence, by entering the spectrometer, the kinetic energy is modified by the energy difference of the contact potential after

$$E_{kin} = E'_{kin} + (\phi_{spec} - \phi_s) \tag{10}$$

By combining equation 9 and equation 10 one obtains:

$$E_B^F = h\nu - E_{kin} - \phi_s - (\phi_{spec} - \phi_s) = h\nu - E_{kin} - \phi_{spec} \qquad (11)$$

As obvious from the relation the work function of the sample ϕ_s cancels out and only the spectrometer potential ϕ_{spec} remains relevant. The spectrometer work function is then calibrated for the specific XPS instrument. This is typically achieved by recording reference spectra of common metals like gold, silver or copper. For such calibration measurements usually highly intense and well defined features are selected like the $Au\ 4f_{7/2}$ emission line in case of gold.

As clear from the discussion above, the calibration can only be achieved if both, the sample and spectrometer are electrically grounded, so that their fermi levels can align. Nonetheless sometimes grounding might not be possible. This is the case if a sample or thin film substrate shows insulating properties. Then the electrons which are excited from the material cannot be properly compensated and consequently charging effects can have severe influence on the measurement like (charging) time dependent shifts of the binding energy or peak broadening.[101, 102]

To overcome such distorting effects, it is possible to apply charge compensation measures like low energy electron beam and/or ion charge neutralization. By applying charge neutralization time dependent energy shifts can be avoided and the overall shape of the spectra will be conserved, nonetheless the calibration via metal standards is still not applicable. [103]

Alternatively, the C 1s signal is commonly used as a reference signal as it is also typically found as a contamination by-product for samples that have been exposed to atmosphere. Specifically, the C-C binding energy can be set to a value of ~ 284.8 eV. While in some cases the carbon binding energy can vary and caution is advised by using this method it is commonly accepted to as a procedure to directly calibrate an obtained spectrum if reference metal calibration is not possible.[104, 105]

Next to the C 1s signal there are other potential features inherent to specific materials that may provide a binding energy reference.[103] If there is no carbon signal (e.g. in case of in-vacuo transferred samples) and no binding energy reference is applicable it is reasonable to align spectra to a common feature like the valence band maximum for better comparison. Then it should be clarified that no binding energy calibration was possible. While in such a case it is not possible to directly assign binding energies it is nonetheless valid to do fitting and determine e.g. the energetic difference between features like different oxidation states in one spectra. This is justified as the overall shape (or relative positions of binding energies) of the spectra is independent from the samples potential if it is kept at a constant value by e.g. providing charge neutralization.

As every change of an elemental oxidation state is associated with a change in its binding energy XPS is an excellent tool to investigate the chemical environment of a samples species. For this purpose, usually highly intense and well defined spectra of core level orbitals are selected. In hafnium oxide typically the Hf 4f orbital is analyzed. Figure 20 shows one of the first published results on the oxidation behavior of hafnium after Morant et al. While for low oxidation conditions the majority of the emission spectra is attributed to the metallic Hf^0 (Hf^m) doublet, for Hf^{4+} a clear energy shift of several eV is visible. As additional doublets are needed to achieve satisfying fitting the presence of (not clearly identified) sub oxide signals must be assumed. While up until now no clear picture of the oxidation behavior of hafnium oxide is established the appearance of additional signals in the transition between Hf^{4+} and Hf^0 is verified in a multitude of publications, therefore confirming the existence of sub oxide states in hafnium oxide.

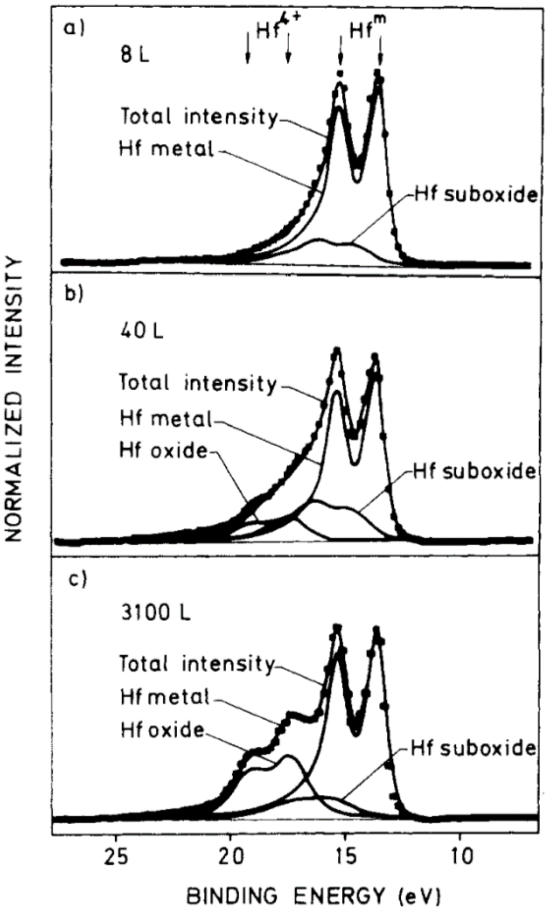

Figure 20: Hf 4f orbital of hafnium metal exposed by a) 8L, b) 40 L and c) 3100 L of oxygen at room temperature showing oxidation dependent Hf^{4+} and Hf^{x+} "suboxide" contributions with clear energy shifts from metallic Hf^0 (Hf^m). Content reprinted from reference [106] https://doi.org/10.1002/sia.740160163 with permission of John Wiley & Sons – Books. Copyright © 1990 John Wiley & Sons Ltd. All rights reserved.

As each element shows a unique set of inherent binding energies, it is a straight forward approach to assign emission lines to specific elements. For this purpose, element specific binding energies are listed in common XPS databases and books of reference. By comparing the integrated intensity of selected emission lines it is possible to estimate the chemical composition of a material from the quantitative perspective. However, the resulting intensities are not only influenced by the relative amounts of elements present in the sample. The photoelectron – current I_A for an element A at a specific kinetic energy E_A is given by[107]:

$$I_A = \sigma_A^X D(E_A) \int_{\gamma=0}^{\pi} \int_{\phi=0}^{2\pi} L_A(\gamma) \times \int_{y=-\infty}^{\infty} \int_{x=-\infty}^{\infty} J_0(xy) T(xy\gamma\phi E_A) \times \int_{z=0}^{\infty} N_A(xyz) \times \exp\left(\frac{-z}{\lambda_M(E_A)\, cos\, \theta}\right) dz\, dx\, dy\, d\phi\, d\gamma \qquad (12)$$

Where σ_A^X is the emission cross section of a photoelectron from the corresponding shell per atom, $D(E_A)$ the detection probability for each excited photoelectron, γ, ϕ, x, y and z are parameters describing the geometrical properties including the relative positions of X-ray source, sample and spectrometer. $L_A(\gamma)$ is the angular asymmetry for the photoelectron-emission rate, $J_0(xy)$ the X-Ray characteristic flux intensity at a given point (x, y) on the sample, $T(xy\gamma\phi E_A)$ the analyzer transmission, $N_A(xyz)$ the atom density at (x, y, z) in the sample, $\lambda_M(E_A)$ the photoelectron inelastic free mean path and θ the angle of emission of the photoelectron from the sample surface normal.[107]

This relation highlights the complex origin and wide ranging dependencies of photoelectron currents at any given E_A. In order to achieve a practical approximation, integrated intensities are typically divided by element-specific photoionization cross sections (PICS) or by atomic sensitivity factors (ASFs). While PICS are theoretically calculated probabilities for photoelectron excitation (which requires additional mathematical expressions such as spectrometer specific detection probabilities), ASFs are determined from real measurements. One of the most used ASF references are the ones of Wagner.[108] Considering ASFs for a binary compound the ratio between two species can be written as:

$$\frac{N_A}{N_B} = \frac{I_A \cdot ASF_B}{I_B \cdot ASF_A} \tag{13}$$

For the concentration c_A of element, A in a multicomponent system the following relation is valid:

$$c_A = \frac{I_A \cdot {ASF_A}^{-1}}{\sum_n (I_n \cdot {ASF_n}^{-1})} \tag{14}$$

However, as the ASF factors originate from a specific spectrometer, a correction factor is needed if a different setup is used. Due to all above mentioned uncertainties, literature emphasizes the use of reference samples with known composition, to normalize the obtained intensities respectively in order to obtain the best possible stoichiometry estimate.[109]

2.4. Bandgap Estimation via UV/Vis-Spectroscopy

One of the most important characteristics for semiconductors and insulators is the nature of their band gap properties. While large bandgaps effectively prevent charge transport, therefore being characteristic for insulating materials (e.g. $\sim$ 5eV for diamond), rather small bandgaps (e.g. $\sim$1 eV for silicon) allow the thermal excitation of a significant amount of charge carriers, namely electrons from the valence band to the conduction band while leaving behind hole-type charge carriers, which themselves contribute to the flow of current.

The nature of bandgaps is not limited to the difference of the energetic difference between valence band maximum (VBM) and conduction band minimum (CBM). The individual bands show various modulated parabolic shapes that are directly associated with the materials chemistry. There are materials where the VBM and the CBM are located at the same crystal momentum (hk) positions and such where they appear at different (hk) positions.

In the first case a transition from VBM to CBM is directly possible without a change in the electrons crystal momentum. A material with such a band structure is called direct band gap semiconductor (e.g. GaAs). In the second case however, the electrons crystal momentum needs to change by the difference of the wave vector in order to allow the transition. Materials which show such non-coinciding VBM and CBM are called indirect bandgap semiconductors (e.g. silicon). The difference between direct and indirect bandgaps yields important implications for optoelectronic properties and associated applications like solar cell technology.

However, the precise nature of the bandgap is only accessible via demanding methodology like advanced photoelectron-spectroscopic methods or on basis of modelling via e.g. density functional theory (DFT) calculations.

A comparably straight forward analysis of the bandgap value is possible with UV/VIs spectroscopy namely transmission and/or reflectivity measurements in the ultraviolet and optical range. Such measurements allow to analyze photon interactions in the energetic range of valence band to conduction band transitions. By deducing a wavelength dependent absorption coefficient from the obtained spectra, the band-gap value can be estimated by comparably simple analysis. Therefore, UV/VIs spectroscopy remains one of the most prominent methods for bandgap estimation.

For estimating the absorption coefficient from an obtained spectrum it is possible to incorporate both transmitted and reflected fractions from the total intensity via the following formula. Note that the logarithmic nature of the function is due to the thickness dependency of the absorption after Beer and Lambert (Beer-Lambert law [110]).

$$\alpha = \frac{1}{d} \ln\left(\frac{(1-R)^2}{T}\right) \tag{15}$$

Where α is the absorption coefficient, d the sample thickness, R the reflectance and T the transmittance. If the band gap appears in the UV-range the reflection part can be neglected in most cases. This can be useful if the reflectance cannot be measured with the instrumentation provided or if only the transmission configuration of a spectrometer yields sufficient intensity. In this case the absorption is directly deduced from the transmission spectra.

$$\alpha = \frac{1}{d} \ln(T) \tag{16}$$

To deduce a bandgap value from an absorption spectrum, the near-absorption-edge part is commonly plotted after the following famous relation, commonly referred to as Tauc plot (Tauc et al., Phys. Status Solidi 15, 627 (1966)[111]).

$$(\alpha h\nu)^{1/n} = A(h\nu - E_g) \tag{17}$$

Where $h\nu$ is the photon energy, E_g the bandgap and A is the slope of the Tauc plot in the linear region. While this equation was originally developed for amorphous semiconductors, empirical data suggests its applicability also for crystalline solids. [112, 113]

The value in the exponent is determined by the nature of the transition (see previous introduction on indirect & direct semiconductors) with:

$n = 1/2$ for direct, allowed transitions

$n = 3/2$ for direct, forbidden transitions

$n = 2$ for indirect, allowed transitions

$n = 3$ for indirect forbidden transitions

By plotting $(\alpha h\nu)^{1/n}$ over $h\nu$, a linear slope is expected for either case. Commonly different n values are plotted, usually with $(\alpha h\nu)^{1/2}$ or $(\alpha h\nu)^2$ on the abscissa to see how the best linear fit for the absorption edge can be obtained. [112, 113] By applying the original theory the slope is then directly extrapolated to the ordinate, yielding the band gap value at $(\alpha h\nu)^{1/n} = 0$.

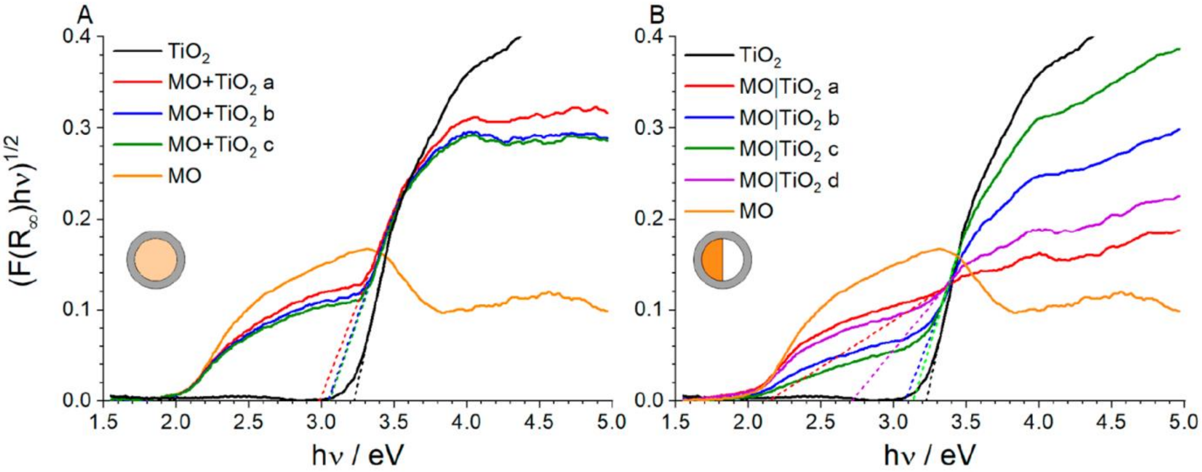

Figure 21: Tauc-Plots showing isolated as well as combined spectra of methyl orange (MO) and Titanium Dioxide (TiO₂) for A) mixtures and B) samples that were placed side by side in the spectrometer beam. In both cases the combined spectra lead to an underestimation of the original TiO2 bandgap. This effect is especially prominent in B) and highlights the necessity for appropriate bandgap-correction. Reprinted with permission from reference [114]. https://doi.org/10.1021/acs.jpclett.8b02892 Copyright © 2018 American Chemical Society.

However, many material systems require adaptations from the ideal theory. The often referred Urbach tail is for example a rather prominent phenomena - being associated with e.g. defect states - that is identified by a logarithmic tail, attached to the actual absorption edge (with slope A). There are theories directly translating such absorption phenomena to modified band gap features.

While such non-ideal absorption spectra (being intrinsic to many materials) are widespread in literature, one of the most applied analysis techniques remains the direct extrapolation of the absorption slope to the abscissa. However, depending on the intensity of additional absorption phenomena (e.g. Urbach tail) or in case of significant contributions from unexpected scattering or reflection processes (e.g. at Interfaces), this direct extrapolation partially leads to drastic underestimations of investigated bandgaps.

A reliable, straight forward approach to extract bandgap values from non-ideal absorption spectra is given by extrapolating the baseline signal against the extrapolation of the slope A of the actual absorption edge. The bandgap value is then read from the intersect point.

This analysis method is rigorously exploited by P. Makuła who highlights the reliability of the method from several perspectives. By measuring samples containing the distinct absorption spectra of TiO_2 and methyl orange (MO) it is shown that the additional spectra of MO distorts any extrapolation of the TiO_2 absorption edge to the abscissa, leading to an (partially drastic) underestimation of the bandgap value for classical Tauc analysis in any case (see Figure 21). This observation is shown for two scenarios, where the MO is either directly mixed with TiO_2 (Figure 21 a) or where MO and TiO_2 samples are placed next to each other in the beam path (Figure 21 b).

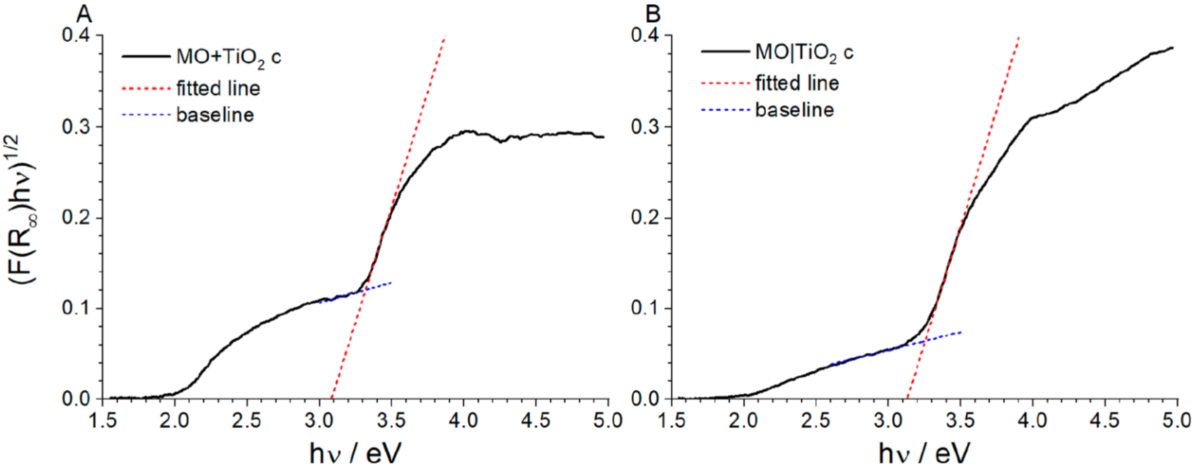

Figure 22: Tauc-Plots showing how an appropriate baseline-correction is carried out. The baseline, which is considered to be independent from the investigated bandgap feature should be extrapolated so that it cuts the original bandgap extrapolation. The bandgap estimate is then read from the intercept point. While a baseline extrapolation is always connected to an uncertainty, the method is shown to produce accurate results in many cases and therefore serves as one of the best analysis strategies. Reprinted with permission from reference [114]. https://doi.org/10.1021/acs.jpclett.8b02892 Copyright © 2018 American Chemical Society.

P. Makuła shows that via extrapolating the baseline (in this case a consequence of MO absorption) to the absorption slope of TiO_2 as shown in Figure 22, comparable bandgap values, very close to the original TiO_2 absorption can be observed in all cases, qualifying this approach as one of the best analysis strategies for systems with multiple absorption functions.

This approach is not limited to a specific scenario as for the Beer-Lambert law any mixture or contribution may be considered as separate parts of a linear superposition. It should be noted that e.g. two different chemicals might react in a way that the original absorption-functions are modified. Nonetheless, in the context of a semiconductor with an additional independent baseline part (e.g. Urbach tail) following formula applies

$$\alpha(h\nu) = \alpha_s(h\nu) + \alpha_b(h\nu) \qquad (18)$$

With $\alpha_s(h\nu)$ being the semiconductor part and $\alpha_b(h\nu)$ being the baseline part. When applying this function to the Tauc-equation one yields:

$$((\alpha_s(h\nu) + \alpha_b(h\nu)) \cdot h\nu)^{1/n} = A(h\nu - E_g) \qquad (19)$$

For $n = 1/2$ (direct bandgap) with:

$$(\alpha_s(h\nu)h\nu)^2 + 2\alpha_s(h\nu)\alpha_b(h\nu)(h\nu)^2 + (\alpha_b(h\nu)h\nu)^2 = A(h\nu - E_g) \qquad (20)$$

For $n = 2$ (indirect bandgap) after Taylor series expansion:

$$(\,(\alpha_s(h\nu)^{\frac{1}{2}} + \frac{1}{2}\alpha_b(h\nu) \cdot \left(\frac{1}{\alpha_s(h\nu)}\right)^{\frac{1}{2}} + \frac{1}{8}\alpha_b(h\nu)^2 \cdot \left(\frac{1}{\alpha_s(h\nu)}\right)^{\frac{3}{2}}$$

$$+\frac{1}{16}\alpha_b(h\nu)^3 \cdot \left(\frac{1}{\alpha_s(h\nu)}\right)^{\frac{5}{2}} + \cdots) \cdot (h\nu)^{\frac{1}{2}} = A\big(h\nu - E_g\big) \qquad (21)$$

For the photon energy $h\nu$ close to the bandgap the baseline absorption α_b is > 0, therefore influencing the bandgap E_g as can be seen from the equations above. However, as obvious from equation 20 and 21, if the baseline absorption $\alpha_b = 0$, all baseline-containing terms are eliminated and the original Tauc-formula is restored with $(\alpha_s(h\nu) \cdot h\nu)^{1/n} = A(h\nu - E_g)$. In the Tauc plot this can approximately be achieved by defining the (extrapolated) baseline intersection as zero, consequently reading the bandgap from this point. Therefore, this approach allows accurate bandgap estimations, even when the widespread conventional Tauc-approach can indeed not be applied.

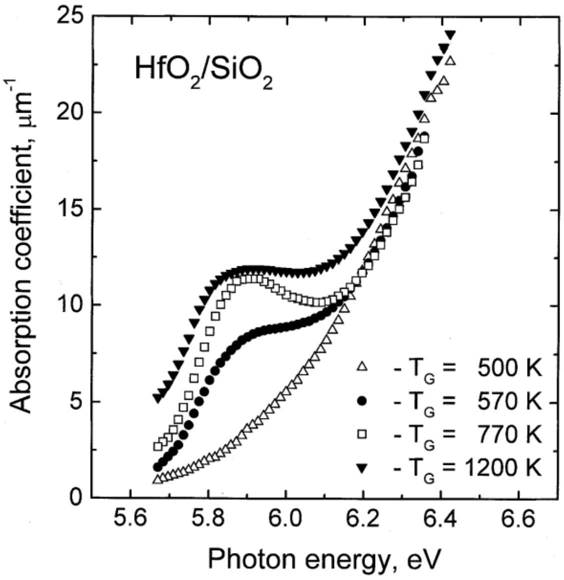

Figure 23: Shows the evolution of the double-absorption feature in hafnia thin films in dependence of substrate temperature. Content reprinted from reference [115] https://doi.org/10.1016/j.tsf.2004.01.110 with permission of Elsevier Science & Technology Journals. Copyright © 2004 Elsevier B.V. All rights reserved.

For hafnium oxide optical absorption and ellipsometry investigations yield band gap values close to ~5.6 eV. [115, 116, 118, 119] While DTF calculations suggest monoclinic stoichiometric hafnium oxide to have an indirect bandgap, indirect and direct bandgaps are found to be almost degenerate in energy. [40, 120, 121]

Interestingly, in hafnia there are several reports of a second absorption shoulder. [115-117, 119, 122] Figure 23 shows that the shoulder appears at higher substrate temperatures, while other publications also show a dependence on film thicknesses [116] and after annealing [117].. In all cases the appearance of the second absorption shoulder corresponds to higher levels of monoclinic crystallinity. Therefore, the feature is discussed to be a consequence of long range order effects in the monoclinic crystal structure. Further it has been shown by Hildebrandt *et al.* that this double absorption feature can also be found in substoichiometric monoclinic hafnium oxide with significant oxygen deficiency.[63]

2.5. Hall Effect in Semiconductors & Van der Pauw Geometry

The Hall effect was named after Edwin Herbert Hall who discovered the Lorenz-Force driven phenomena in 1879. The Hall effect is associated with a so called Hall voltage, which appears if a conducting material is subjected to a magnetic field in perpendicular direction to an applied current. The direction in which the Hall voltage is obtained is in turn defined in perpendicular relation to both, current and magnetic field. The Hall voltage U_H is directly associated with the Hall coefficient A_H via the following relation.

$$U_H = A_H \frac{I_p \cdot B}{d} \tag{22}$$

Where I_p is the current and d the thickness of the layer which is perpendicularly permeated by the magnetic field B. From this relation, the material specific nature of charge transport can be derived. Most strikingly, the sign of the Hall coefficient indicates the type of dominant charge carries.

In semiconducting materials, it is generally known that, if an electron is excited in the conduction band, it leaves behind a so called hole which is a change carrier with an inverse charge sign. In intrinsic semiconductors (where the fermi level is located exactly between valence and conduction band) there is a perfect balance between both electron- and hole concentrations. In defective semiconductors however the relation of mobile holes to electrons may be modified depending on the nature of doping.

In the classical frame of acceptor vs donator type doping, acceptor defects result in p-type doping, where the fermi level is shifted towards the valence band, giving rise to an access of hole charge carries. Donor type defects on the other hand shift the fermi level in the opposite direction towards the conduction band, therefore promoting an access of electron charge carriers.

The Hall coefficient is directly associated with the type and number of charge carriers via the following relation.

$$A_H = \frac{p\mu_h^2 - n\mu_e^2}{e(p\mu_h + n\mu_e)^2} \tag{23}$$

Here e is the elementary charge while n and p are the electron and hole concentrations. Further, the relation gives rise to additional important quantities namely μ_e and μ_h the mobilities for both electrons and holes respectively. This relation highlights how the sign of the Hall coefficient directly shows which type of conduction, either electron ($e\mu_e$), or hole conduction

($h\mu_h$) is dominant in a given case. However, this equation alone does not allow to derive specific charge carrier concentrations or mobilities.

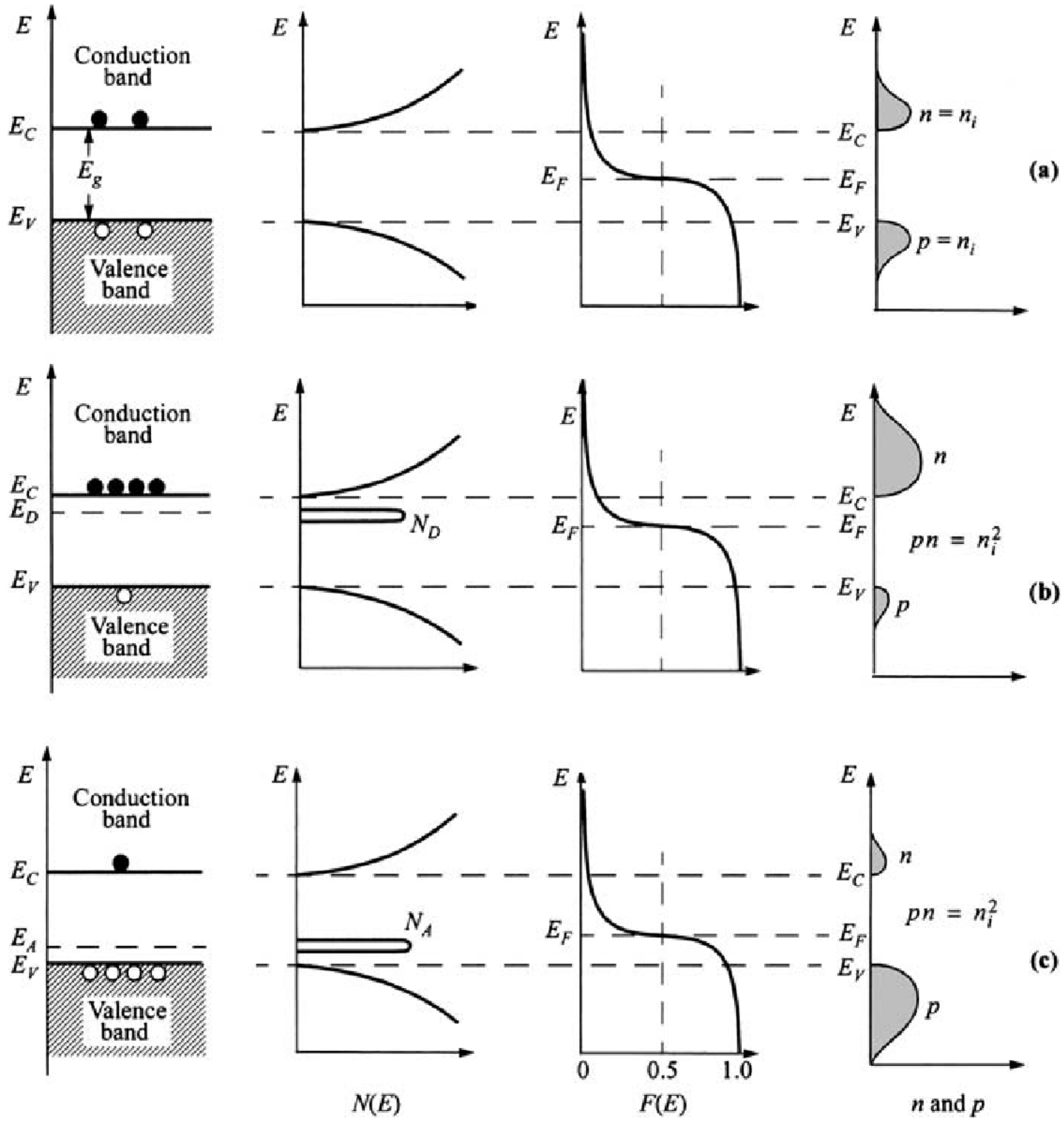

Figure 24: Charge carrier densities in dependence of the fermi-level position. The fermi–level position is modified from the intrinsic position (a) a by donor (b) or acceptor (c) type defects. Content reprinted from reference [123] with permission from John Wiley & Sons – Books. Copyright © 2007 John Wiley & Sons, Inc. All rights reserved.

To further characterize the nature of charge transport via Hall effect methodology it is generally assumed - as true for the majority of relevant cases – that the measured mobilities are in good approximation with the mobilities of the dominant charge carriers as extracted from the sign of the Hall coefficient. In this context it is possible to derive the mobilities if the conductivity of the investigated sample is known.

$$\mu_{h/e} = R_H \cdot \sigma = \frac{R_H}{\rho} \qquad (24)$$

Further the charge carrier concentration can then be derived using:

$$n = \frac{\sigma}{e\mu_e};\ p = \frac{\sigma}{e\mu_h} \qquad (25)$$

To measure the conductivity of a sample the famous four-probe method is commonly used by which the probing current is injected by a pair of electrodes separate from the electrodes used to detect the voltage drop along the conduction path. By applying such a configuration were the voltage is measured over a large resistance, the effect of contact resistance is eliminated and – by applying the measurement geometry – the measured values directly reveal the samples resistivity.

Another geometry for resistivity analysis which is commonly used in thin film research is the van der Pauw geometry. Similar to the four-probe method, four electrodes are utilized with two for injecting a probing current and two for measuring the corresponding voltage. However, in this case, small (approximately point-sized) pairs of electrodes are placed directly on adjacent edges of the sample. Leo J. van der Pauw first described the measuring method 1958 showing that the method can be used on any arbitrarily shaped layer of homogeneous resistivity and thickness following the equation:

$$\exp\left(-\frac{\pi d}{\rho}\cdot R_{12,34}\right)+\exp\left(-\frac{\pi d}{\rho}\cdot R_{23,41}\right)=1 \qquad (26)$$

ρ can then be extracted numerically or by using the following approximation:

$$\rho=\frac{\pi d}{\ln 2}\cdot\frac{R_{12,34}+\ R_{23,41}}{2}\cdot f$$

Where f is a known geometry factor, which can be extracted from literature for any given case. If the geometry is defined by a symmetrical square shape with contacts on the corners and the values for $R_{12,34}$ and $R_{23,41}$ are identical the relation is simplified to:

$$\rho=\frac{\pi d}{\ln 2}\cdot R_{12,34} \qquad (27)$$

Further, it is possible to apply an offset correction for Hall voltages.

The square geometry yields several practical advantages and enabled next to resistivity measurements also Hall effect measurements to develop into a standard measurement routine. The main reason for this is found is the sheer simplicity of the geometry, allowing to directly deposit electrodes onto square samples without the need to apply lithographic procedures.

To measure the Hall effect in van der Pauw geometry, a current is simply injected diagonally over adjacent corners of the square. While the Magnetic field is applied perpendicularly to the square surface, the Hall voltage is measured over the remaining corners, also diagonally and therefore perpendicular to both, the direction of the applied current and the magnetic field.

2.6. Density Functional Theory

Density functional theory is a basic theory for the modern ab initio calculation methods which can theoretically evaluate the ground state of the electronic structure of many body systems of nuclei and electrons and is widely used for molecular or solid state modelling in chemistry or materials science. Fundamentally, a many-body system can be described by the time-dependent Schrödinger equation,

$$i\hbar\frac{\partial}{\partial t}\Psi = \boldsymbol{H}\Psi \tag{28}$$

In order to deal with ground state properties of the system, it is sufficient to consider the **stationary Schrödinger equation**.:

$$\boldsymbol{H}\Psi_i = E_i\Psi_i \tag{29}$$

The equation consists of a Hamiltonian $\boldsymbol{H}$, which is a mathematical operator acting upon the wave functions $\psi_i(\vec{x})$, which describe the quantum mechanical system. In turn the equation provides Eigenvalues E_i, which represent the energy levels of the corresponding wave functions $\psi_i(\vec{x})$. The state with the lowest energy $\psi_0(\vec{x})$ is considered the ground state of the system.

The basic principle of DFT is based on the **Hohenberg Kohn theorem** which states that the potential V of a system of electrons can be determined by its electron-density, which is the sum of the probability densities of all electrons.

$$\boldsymbol{\rho}(\vec{x}) = \sum_i |\Psi_i|^2 = \sum_i \Psi_i\Psi_i^* \tag{30}$$

According to DFT, the ground state energy can be obtained with the ground state density ρ_0.

Now, the expressions which connect the above discussed electron density with the Schrödinger equation are the **Kohn-Sham functions[124]** after:

$$\boldsymbol{H}\psi_i(\vec{x}) = (\boldsymbol{H_{kin}} + \boldsymbol{V_{ext}} + \boldsymbol{V_{coul}} + \boldsymbol{V_{xc}})\,\psi_i(\vec{x}) \tag{31}$$

With $\boldsymbol{H_{kin}}$ being the kinetic part of non-interacting electrons.

$$\boldsymbol{H_{kin}} = -\frac{1}{2}\nabla^2 \tag{32}$$

$\boldsymbol{V_{ext}}$ accounting for a static external potential.

$$\boldsymbol{V_{ext}} = \sum_n \frac{Z_n}{|\vec{x} - \vec{R}_n|} \tag{33}$$

For DFT the this is given by the interaction of nuclei and electrons with Z_n being the charge and $\vec{R}_n$ the position of the nuclei. In the context of the Born Oppenheimer approximation, the nuclei are considered as stationary objects as their velocity is very small against the electrons velocity.

$\boldsymbol{V_{Coul}}$ Being the electron-electron interaction, but without interaction effects between wave functions.

$$\boldsymbol{V_{Coul}} = \int \frac{\rho(\vec{x}')}{\vec{x}-\vec{x}'} d\vec{x}' \tag{34}$$

While all of the above mentioned potentials are connected to single electron wave functions, the interaction between these wave functions is handled by the so called exchange correlation potential $\boldsymbol{V_{xc}}$ with

$$\boldsymbol{V_{xc}} = \frac{\delta E_{xc}}{\delta \rho} \tag{35}$$

While all other potentials are exact, the exchange correlation potential cannot be derived analytically yet and is dependent on approximations. The exchange correlation potential $\boldsymbol{V_{xc}}$ is dependent on the exchange correlation energy $\boldsymbol{E_{xc}}$ with

$$\boldsymbol{E_{xc}} = \int \rho \epsilon_{xc} d\vec{x}' \tag{36}$$

Where ϵ_{xc} is the exchange correlation functional density. A large number of correlation energy $\boldsymbol{E_{xc}}$ approximations are available in literature and the selection of the right problem-relevant approach is an important part in DFT analysis.

In order to verify a valid solution to the eigenvalue problem one has to ensure that the density ρ is consistant with the kohn sham potential $H_{KS} = (H_{kin} + V_{ext} + V_{coul} + V_{xc})$. This is commonly achieved in DFT by applying the **self-consistent field cycle (SCF)** [125] algorithm displayed in Figure 25.

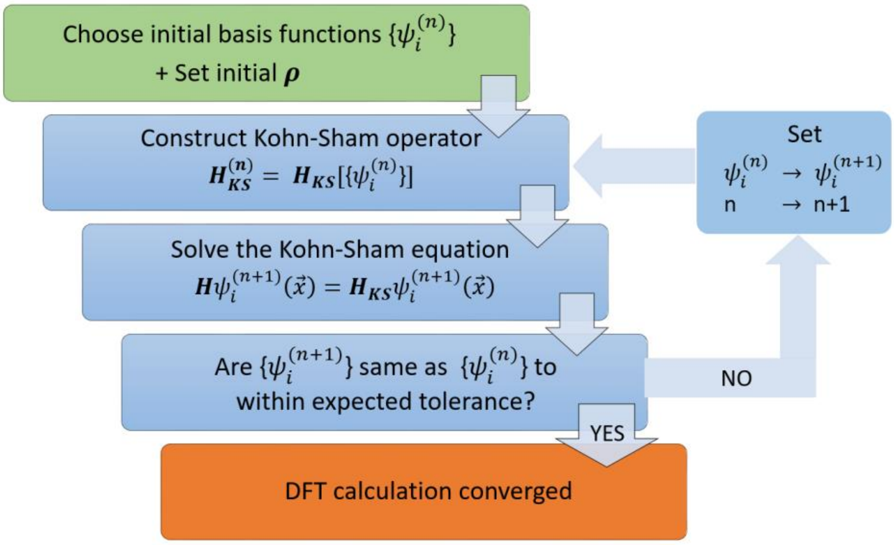

Figure 25: Self Consist Field (SCF) Cycle algorithm for eigenvalue determination in DFT.

As a starting point an initial electron density ρ and a set of basis functionals is selected. In case of solid state/materials investigations the basis functionals are often based of spherical harmonics.[126] With the initial guess of the density ρ the Kohn-Sham operator is constructed. Next the Kohn Sham equation is solved and it is checked if the obtained eigenfunctions are within the expected tolerance to the initial (or previous) wavefuntions. This process is then repeated with the aim of reaching the corresponding tolerance. Once fulfilled the DFT calculation is converged and can be considered self-consistent, however depending on initial conditions or restrains a DFT approach is not guaranteed to converge.

As previously mentioned the exchange correlation energy $\boldsymbol{E_{xc}}$ approximation plays a fundamental role in DFT. Kohn and Sham [124] first introduced the **Local Density Approximation (LDA)**:

$$\boldsymbol{E_{xc}^{LDA}} = \int \rho \epsilon_{xc}(\rho)\, d\vec{x} \tag{37}$$

This is the simplest approximation is useful if the density is almost constant or at high densities where the kinetic energy is big against the exchange correlation terms.[124, 127] In materials science this functional gives reasonable results for atomic positions in equilibrium structures, however is a bad approximation for the surface and overlap of atoms. [124]

By incorporating spin-dependencies one arrives at the next more complicated approximation namely the **local spin density approximation (LSDA)** which allows to evaluate non-symmetric, spin-polarized systems [128]:

$$\boldsymbol{E_{xc}^{LSDA}} = \int \rho \epsilon_{xc}(\rho \uparrow, \rho \downarrow)\, d\vec{x} \tag{38}$$

Better results could be achieved with the first **generalized gradient approximations (GGA)**. [129] This kind of approximation which also takes the local gradient of the density into account is the most commonly used exchange-correlation functional in DFT today.

$$\boldsymbol{E_{xc}^{GGA}} = \int \rho \epsilon_{xc}(\rho \uparrow, \rho \downarrow, \Delta\rho \uparrow, \Delta\rho \downarrow)\, d\vec{x} \tag{39}$$

One of the most prominent GGA approaches is PBE approximation after Perdew, Burke and Ernzerhof [129] and a famous modification for densely packed solids is called PBEsol.[130]

Following the LDA or GGA approach hybrid functionals have been developed which include a Hartree-Fock-like exchange component leading to further improvements in the prediction of molecular or materials properties. While standard LDA or GGA calculations still tend to significantly under- or overestimate e.g. bandgap values, the hybrid functional approach paved the way for achieving a high level of agreement with experimental bandgap values in many cases. Here B3LYP of Lee, Yang and Parr is still one of the most commonly used functionals.[131] Later, the hybrid functional HSE after Heyd, Scuseria and Ernzerhof, which is based on a screened Coloumb potential was demonstrated to be more computationally effective while offering comparable precision to other well established hybrid functionals like B3LYP or PBE0.[132] The most commonly used variant of HSE approximations is HSE06 showing good results in many cases using a standard parameter set.

3. Sample Synthesis & Preparation Methods

3.1. Molecular-Beam Epitaxy

Molecular-Beam Epitaxy (MBE) is a Physical Vapor Deposition method for the epitaxial growth of thin films. The method is characterized by the use of one or multiple thermal molecular beams which react with a substrate surface in an ultra-high vacuum environment.[133] A typical MBE setup features a substrate manipulator, evaporation sources (mostly for metallic materials) and quartz crystal microbalance units for elemental rate control.

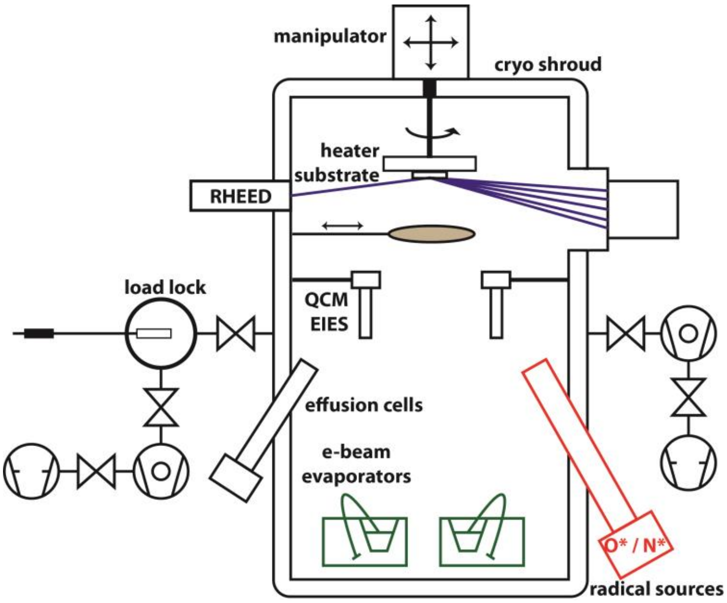

Figure 26: MBE unit featuring e-beam evaporators in an UHV body, corresponding QCM units, radical sources for O* and N* incorporation, a substrate manipulator with a heating unit and a RHEED system for in-situ growth control.

The evaporation sources are often resistively heated effusion cells or electron beam evaporators. Many units also incorporate RF-plasma sources for gaseous species and corresponding mass flow control units to set a defined fraction of standard cubic centimeters per minute. The substrate manipulator allows to control the substrate temperature by IR or resistive heating (and for some setups even N_2 or He cooling). By controlling all corresponding parameters of evaporation rates, gas flows and substrate temperature an abundance of deposition conditions becomes available which allows to control the thermodynamic and kinetic growth conditions, and therefore the stoichiometry, crystalline or amorphous structure, microstructure of thin films and their epitaxial relation to the substrate. With the help of the QCM units it is not only possible to determine the rate of individual molecular streams, but also estimate the total film thickness via calibration. By the use of a shutter system the deposition of atomic species on the substrate can be blocked at any time, which is vital while ramping up evaporation rates and starting the gas plasma during setup. Further, the shutter control is useful to temporarily block the molecular beams if the rate control shows spontaneous fluctuations which is typical for evaporation sources. Finally, the shutter blocks the deposition stream once the desired film thickness is reached after which the sources may be ramped down.

3.2. Hafnium Oxide Synthesis via MBE

As hafnium oxide is a binary compound, there are two possibilities on how to control the relative stoichiometry utilizing an MBE setup. First, the elemental evaporation of hafnium can be controlled over the relative power output of the evaporation source and the evaporation rate checked via the QCM units (compare chapter 3.2).

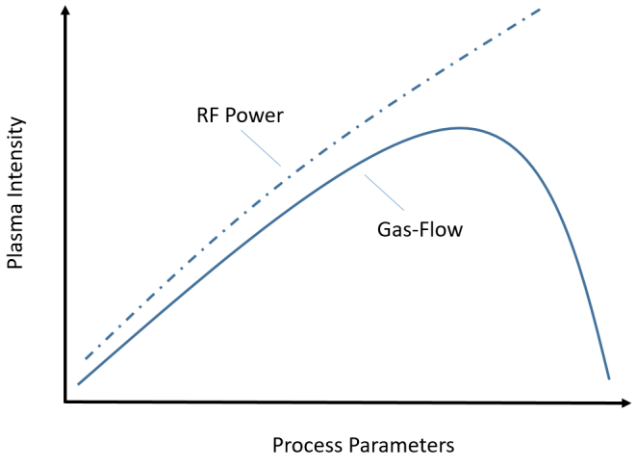

Figure 27: Schematic on the plasma intensity in dependence of RF Power and Gas-Flow conditions. Note that a gas flow exceeding a certain threshold will lead to a reduced plasma intensity. Redrawn with information from [134].

Second the rate of RF activated oxygen radicals can be controlled over the gas flow and the RF Power. Usually, for oxides, the gas flow rate is changed to achieve a more significant change in the systems partial pressure and oxidation conditions. However, as can be seen from Figure 27, once a certain gas-flow threshold is exceeded, the plasma intensity is reduced again. Therefore, in order to achieve a continuous increase in oxidation conditions with increasing gas flow, the flow rate must not exceed the highest point of the curve. Further, as this gas-flow curvature is dependent on the plasma energy, the range of oxidation conditions can be further controlled by checking the gas-flow dependent plasma intensity at different radio frequency powers.

Other ways to change the crystal phase, microstructure and epitaxy of hafnium oxides are given by the type of substrate and the substrate temperature. While Hildebrandt et al. [61-63] demonstrated purely monoclinic growth at elevated temperatures of ~ 700 °C, and amorphous growth is expected for low temperatures[135], the data discussed in the results & discussion part of this work show the formation of *r*-HfO_{2-x} and *hcp*-$HfO_{0.7}$ as intermediate phases between stoichiometric hafnia and metallic hafnium for growth around 320 °C.

3.3. Titanium Nitride Synthesis via MBE

The synthesis of TiN via MBE is achieved via evaporation of metallic titanium together with a RF-activated gas flow of nitrogen. Figure 28 a) shows three exemplary samples of TiN thin films on c-cut sapphire. The conditions chosen for the sample in blue and red appear optimal, as can be seen by the position of the (111) reflection, which is very close to the reference line from the bulk compound. Further, the pronounced Laue oscillations show highly coherent lattice planes (compare chapter 2.1.2) which shows highly oriented growth and is associated with high crystal quality. On the other hand, the sample shown in black shows no signs of Laue oscillations, but further shows a significant shift to higher angles from the reference line, indicating smaller lattice constants and therefore nitrogen deficiency from the stoichiometric composition. This is further supported by the deposition conditions which have an increased Titanium rate as compared to the other samples. This indication of the (111) TiN reflection shift appeared as a useful indication for TiN quality.

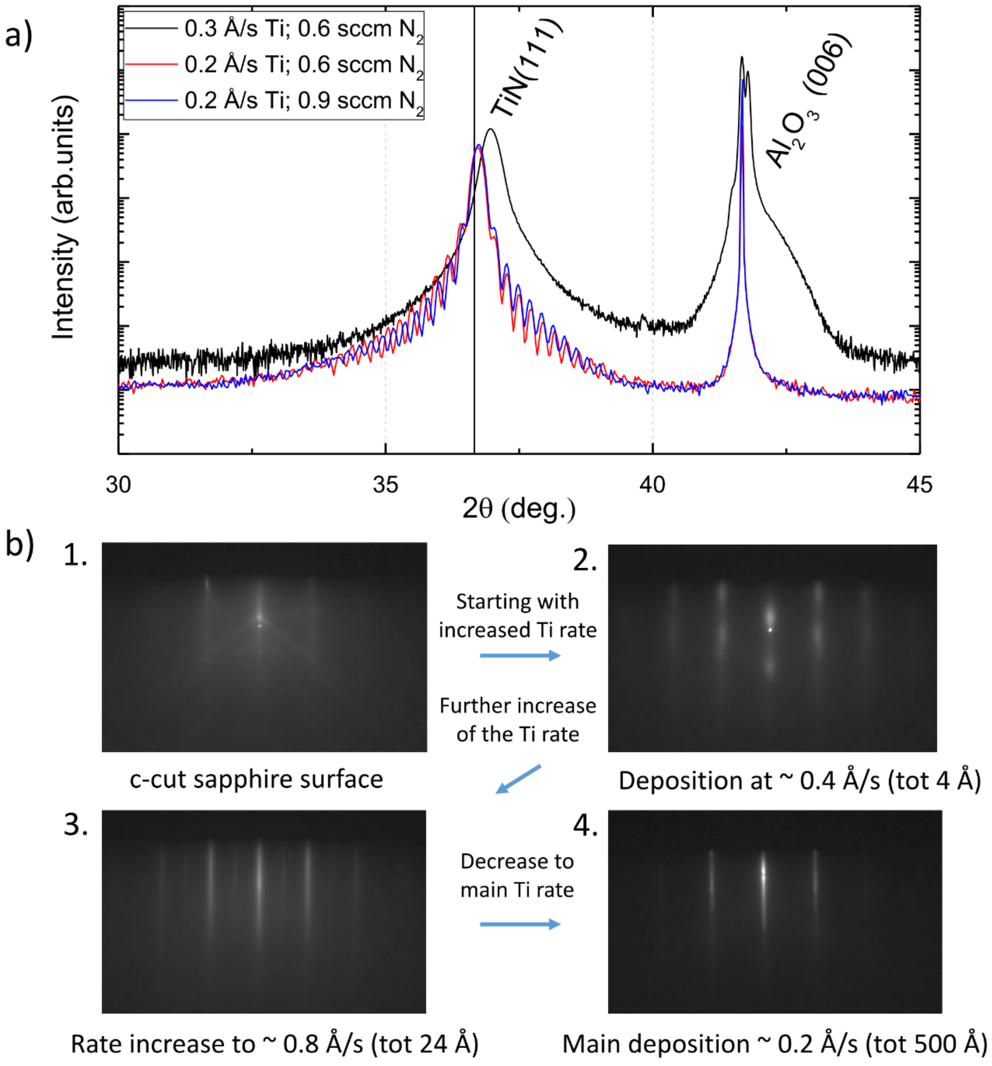

Figure 28: a) shows TiN films grown at 800 °C for different conditions shows optima growth conditions (red and blue) while the sample shown in black shows TiN grown under reduced conditions as indicated by the shift of the (111) reflection. The substrate reflection appears different due to different monochromator settings (graphite instead of Ge(220) monochromator). b) shows RHEED patterns of the different stages during growth from 1 to 4.

As part of this work, TiN was, after initial optimization, grown using constant parameters to assure a reproducible bottom electrode quality throughout different growth studies (In which mostly the hafnium stoichiometry was changed). However, a Molecular-Beam Epitaxy system is further subject of changes which cannot be fully controlled. An example is the flow cross-section of the aperture of the nitrogen plasma tube which can be further and further reduced due to undesired adsorption during deposition. As the cross-section shrinks, the pressure in the plasma tube changes (with constant gas flow), which affects the plasma intensity. This can be checked by tracking the change of the optical power output, which is a measure of the plasma intensity. As observed during this work, the plasma intensity may be reduced to a critical point, where the stoichiometry of the thin film is significantly changed. An indication for this is, as discussed previously, the shift in the (111) TiN maxima. During maintenance it turned out that, once the plasma conditions have changed critically, the boron-nitride aperture of the nitrogen plasma tube could be cleaned successful in aqua regia, which also effectively dissolves e.g. TiN adsorbents.

Figure 28b shows the RHEED patterns of different stages during the growth. First there is a streaky pattern with additional Kikuchi lines indicates a flat, single-crystalline surface. The second pattern is captured after 4 Å of TiN growth starting from an elevated Ti evaporation rate. This pattern shows a modulated streaky pattern, which indicates a multilevel stepped surface which is non ideal. A better surface quality is subsequently achieved by further increasing the Ti rate, until a sharp streaky pattern is obtained as can be seen in the third pattern. Note that in the monitored case even additional streaks appear between the main streaks, which indicate a further long-range order reflection. This pattern therefore indicates a flat, highly crystalline surface. The last pattern was captured after Ti rate reduction to the main parameter and deposition until 500 Å (As displayed by the quartz crystal microbalance). While the additional streaks vanished, a sharp, streaky pattern remained, also indicating a flat surface of high crystalline quality.

Especially the elevated Ti deposition rate increase at the beginning turned out to be a crucial component to achieve the above mentioned surface quality, which can be explained by the reduction of strain at the interface by a density gradient. In contrast, by not using a higher Ti rate at the beginning a less streaky pattern, towards island growth can be observed. While the exact deposition parameters and overall thickness may vary for all TiN thin films mentioned in this work (used as bottom electrode), the overall routine (Figure 28b) to achieve a high surface quality has been applied to all grown TiN bottom electrodes.

3.4. Photolithography

All discussed lithographic procedures have been optimized for the cleanroom equipment as available in the L2|07 M^3 laboratory building.

For the standard liftoff procedure to obtain 30 x 30 μm^2 square features (for the top contact of RRAM devices) negative ma-N1420 Photoresist from micro resist technology GmbH (Berlin, Germany) was used. The following recipe was elaborated for this purpose.

First the sample is coated by the photoresist via spin coating at 6000 rpm for 40 s. Then the edge bead (accumulation of photoresist at the edges) is removed via scratching with a razor blade, followed by a heating procedure at 105 °C for 2 min. After that the photoresist is exposed via a MJB4 Mask-Aligner from SÜSS MICROTEC SE (Garching, Germany). For this purpose, the pressure for the wedge error compensation (WEC) is set to 1.5 – 1.6 bar with a 3 second delay in soft contact mode. The exposure time is set to achieve a dose of ~ 385.2 mJ/cm^2 (I line). Subsequently the sample is developed in ma-D 533 from micro resist technology GmbH for 80 s.

Table 2: Optimized lithographic routines for corresponding square features.

Process	**30 x 30 μm^2**	**3 x 3 μm^2**
Resist	ma-N1420 (negative)	AZ ECI 3012 (positive)
Developer	ma-D 533	AZ 300 MIF
Spin coating	6000 rpm, 40 s	6000 rpm, 40 s
Baking	105 °C, 120 s	90 °C, 60 s
UV Exposure (edge beard)	-	1254 mJ/cm^2; I line Soft contact
Developing (edge beard)	-	60 s
UV Exposure (main)	385.2 mJ/cm^2; I line Soft contact	167.2 mJ/cm^2; I line Vacuum contact
Developing (main)	80 s (liftoff); 60 s (IBE)	60 s

The top electrode may be subsequently deposited via sputtering but must not exceed a total of ~ 400 nm as thicker deposition might prevent an effective separation of deposited material on the photoresist and on the sample surface. For the here investigated devices ~ 100 nm Pt followed by ~ 250 nm Au have been deposited. The rather large electrode thickness is needed in order to prevent accidental penetration of the devices upon placing the contacting pins on top of the electrodes. After deposition the lift off procedure is achieved by immersing the sample in acetone.

While the 30 x 30 μm^2 routine works reliably, such feature sizes are considered large, even for UV-Lithography. Therefore, an alternative routine was established to reduce the feature sizes down to 6 x 6 μm^2 and 3 x 3 μm^2.

For the previously mentioned routine, a clean edge beard removal proved difficult utilizing standard laboratory techniques like a razor blade or a cotton-tip with acetone (especially on the limited sample sizes of 5 x 5 mm^2). This resulted in the incorrect pattern-transfer because of undesired beam path and/or interference (square features translated into diamond shapes). While such effects do not have a serious impact on the previously discussed 30 x 30 μm^2 process, for 6 x 6 μm^2 and especially 3 x 3 μm^2 it appeared crucial. In order to improve the contact quality between mask and sample for smaller feature sizes, the etch beard was removed via UV-exposure with subsequent developing. For this purpose, a mask was used, which only exposes the edges of the sample. While this procedure is not possible with negative photoresist, positive AZ ECI 3012 photoresist from MicroChemicals GmbH (Ulm, Germany) was utilized. To ensure a complete removal of the edge beard a high exposure dose of i.e. 1254 mJ/cm² was applied to achieve total dissolution of the edge region after developing in AZ 300 MIF developer for 60 seconds.

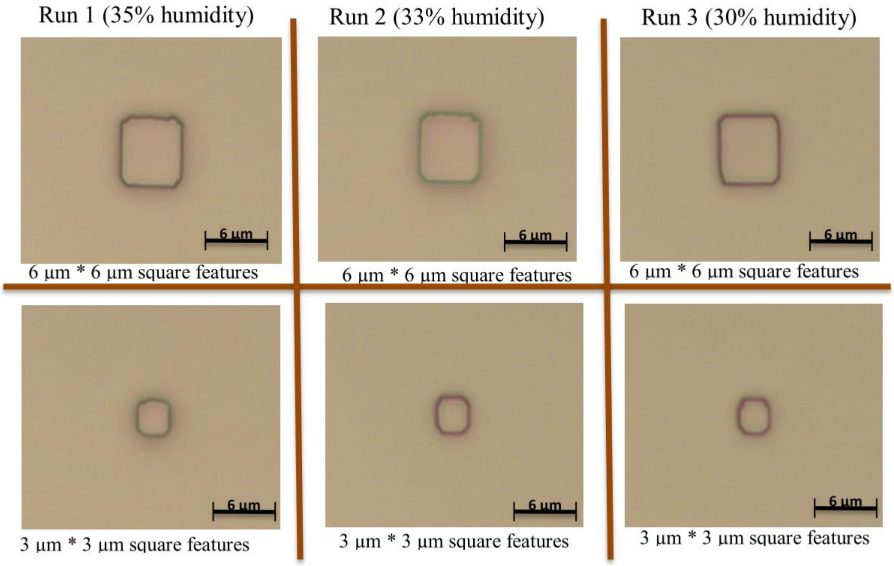

Figure 29 Optical microscope images of 6 x 6 µm² and 3 x 3 µm² features at three different days on gold, showing high reproducibility. As the cleanroom is not equipped with air conditioning the corresponding humidity is shown for every day respectively. After the Advanced Research Lab from Nitin Malik (supervised by Nico Kaiser).

The final procedure was obtained after optimization of baking and UV-exposure from the guideline recipe from MicroChemicals GmbH. For this procedure the AZ ECI 3012 photoresist is spin-coated onto the sample at 6000 rpm for 40 s. This is followed by a soft baking step at 90 ° C for 60 s. Then the sample is exposed in a first step in order to remove the edge beard (see above). Then the main exposure is carried out with 167.2 mJ/cm² by applying vacuum contact (to further reduce potential contact gaps). Finally, the sample is developed in AZ 300 MIF for 60 s. This recipe has been tested for reproducibility, where 6 x 6 μm² and 3 x 3 μm² square features have been obtained at three different days with close to no deviation as can be seen in Figure 29.

3.5. Ion Beam Etching & Optimization for In-Vacuo Grown Devices

The micro patterning of RRAM stacks is a vital component of the electrical characterization routine and can have significant influence of the quality and nature of the devices that are created in the process. An easy method is the application of top electrodes with a simple lift-off procedure. In this case a stack of switching material (e.g. hafnium oxide) which is deposited onto a bottom electrode (e.g. titanium nitride) is covered with photoresist, to cover the areas in which no top electrode material should be deposited (compare previous chapter 3.4). After the deposition of the top electrode, the photoresist is simply dissolved in a suitable solvent (e.g. Acetone), which removes the top electrode access areas from the stack and only leaves designated electrode-patches behind.

While this procedure is rather straight forward, it has some disadvantages as it is necessary to expose the active switching material to the atmosphere. In consequence, the material is directly exposed to the standard impurity levels present in the facilities including deposition labs and clean room equipment. Also, the atmospheric partial pressures are prone to change the active material e.g. via oxidation which is especially critical for oxygen deficient thin films.

In order to overcome the above mentioned problems a routine with the implementation of ion beam etching (IBE) - which allows to ablate designated thin film layers – was elaborated. Together with this technique it is possible to deposit the top electrode material in-vacuo, which can then act as a protective barrier against atmospheric exposure. In this case the photoresist is applied after the deposition of the top electrode material and acts as shielding against the IBE bombardment. Therefore, the layer is applied in negative layout as compared to the lift-off procedure. Table 3 shows a list of parameters which have been used for preparing hafnium oxide based RRAM stacks in this work.

Table 3: Ion Beam Etching Parameters used for Pt/HfO_{2-x}/TiN stacks. All etching has been performed with liquid nitrogen cooling of the sample holder.

Plasma RF Power	Argon gas flow	Distance from ion source	Focusing Potential	Acceleration Potential	Ion current
150 W	2.5 sccm	200 mm	200 V	500 V	9-13 μA

In order to track which layers of the stack are currently etched, and to stop the procedure at the desired layer, the IBE unit is equipped with a secondary mass spectrometer from Hiden Analytical Ltd. (Warrington, U.K.). To track a species a defined m/z (mass/atomic number) ratio and quadrupole potential needs to be selected. Specifically, for Ti (as part of the TiN bottom electrode) and Hf (as part of the hafnium oxide dielectric) m/z ratios of 48 and 179.6 respectively in conjunction with an analyzing potential of -2 V have been identified as effective tracking parameters. Figure 30 contains mass spectrometry data, which has been tracked during IBE of a typical hafnium oxide stack with Figure 30 a) showing how first a strong Au signal (the top electrode buffer) is ablated, then a small rise in the subsequent Pt top electrode layer. After $\sim$ 300 s etching the Hf signal of the hafnium oxide layer rises and vanishes after additional $\sim$ 50 s, accompanied by a rise in the Ti signal from the TiN bottom electrode. As can be seen from this plot the Au, Hf and Ti signals can easily be identified, while the change in the Pt signal appears comparably weak. The reason for the bad peak to noise ratio of the Pt signal is given by the overlap by the signal from two-ion particles of ^{98}Mo and ^{97}Mo isotopes that are etched incidentally from the sample stage material. In contrast to Figure 30 a), which shows the complete etching through the top electrode materials and the hafnium oxide layer, stopping after 10 s etching into TiN, Figure 30 b) shows a second procedure, where the etching stops after ~ 10 s etching into hafnium oxide, leaving the hafnia layer mostly intact. Figure 30 c) shows the corresponding arrangement of layers which is not true to scale as different materials show different etch rates.

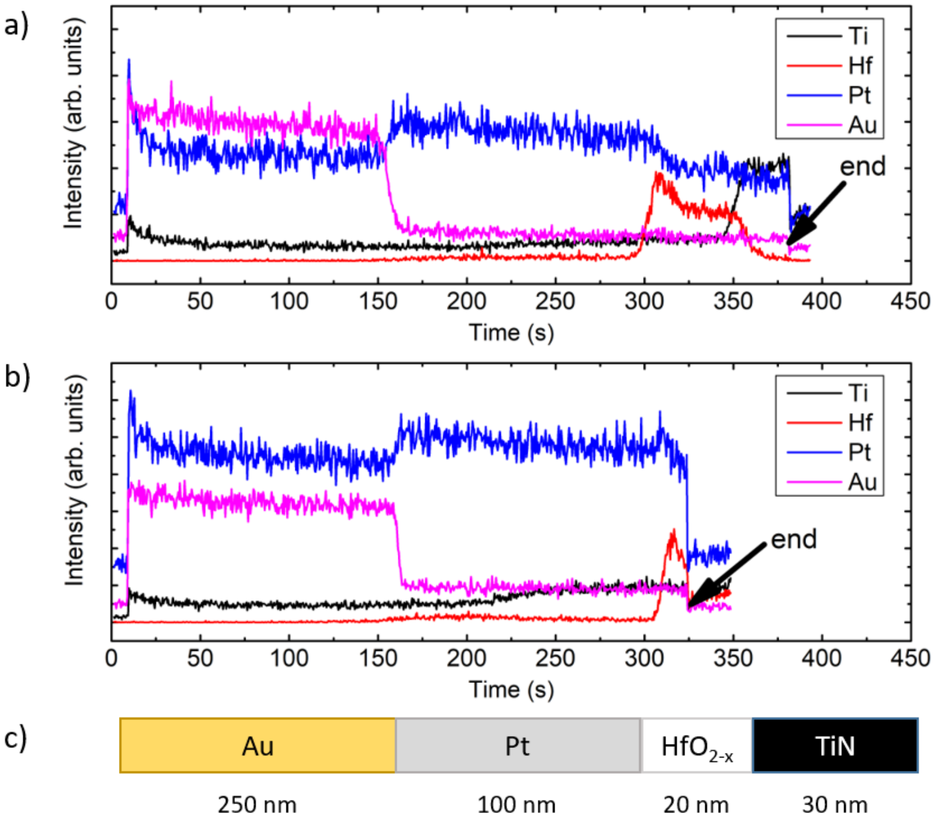

Figure 30: End point detection with a mass spectrometer during IBE procedures for a typical hafnium oxide based RRAM stack. a) complete etching through top electrode materials and hafnium oxide with stop at the HfO_{2-x}/TiN interface b) only etching through the top electrode with stop at the Pt/HfO_{2-x} interface. c) shows the structure of the stack in relation to the mass spectrometer signal above. Note that the actual thicknesses are not true to scale, as e.g. gold (~ 80 nm/min) shows a significantly faster etch rate than platinum (40 nm/min).

An important aspect of the IBE procedure is the subsequent removal of the photoresist, which turned out to be challenging. After IBE treatment a dissolution simple dissolution in acetone proofed to be impossible. Also other conventional solvents inter alia DSMO, NMP or Dichlormethane showed no impact via simple immersion over 12 h at room temperature. Even the treatment with strongly basic NaOH solutions in the range from pH 10 to pH 14 was only partially successful. A common explanation for the high chemical resistance occurring in photo resist is cross-linking of the photo resist molecules. While this problem can occur due to heat accumulation on the samples surface it can be considered unlikely as all samples have been actively cooled indirect with liquid nitrogen during etching. A more likely scenario is the cross-linking due to UV-emission of the Argon plasma. In any case a reproducible and clean removal of photoresist remains could be achieved via the following recipe:

- Use of photoresist specific solvents mr-Rem 500 or mr-Rem 700 (pH ~ 8) from micro resist technology GmbH
- Heating of solvents below boiling point
- Immersion of samples for ~ 30 min under continuous heating

- Ultrasonic treatment for 1 min at 60% power output
- Rinsing of samples with acetone and isopropanol

In order to investigate the influence of the in-vacuo capping as well as different etching routines as displayed in Figure 30, four samples, grown in the same deposition process have been systematically prepared and their leakage current has been investigated. The stack arrangement of Au/Pt/HfO_2/TiN is therefore identical for all samples together with a close to stoichiometric hafnium oxide layer. While two samples have been capped in-vacuo, two samples have been exposed to atmosphere. Also, while two samples have been etched through the hafnium layer to the bottom electrode (BE), two samples have an intact hafnium oxide layer either through lift of or through etching-stop at the top electrode (TE) -hafnia interface.

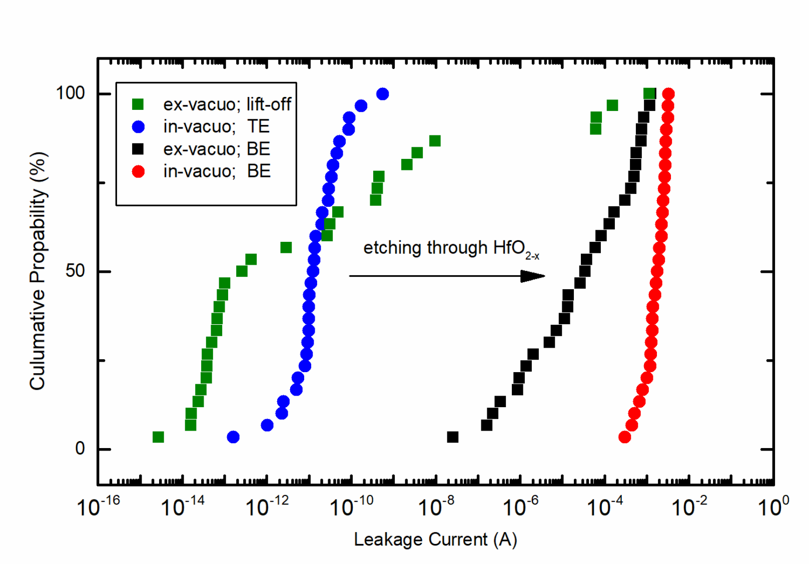

Figure 31: Leakage current distribution of four Au/Pt/HfO_2/TiN stacks with an identical hafnium oxide layer. The samples are separated in the way the top electrode was deposited (in-vacuo vs. ex-vacuo/after atmospheric exposure) and weather the hafnia layer is etched through or not (etching to BE or to TE/lift-off). Note that etching through the hafnia layer leads to a significant increase in leakage current while the statistical spread is reduced for samples which received the top electrode deposition in-vacuo.

The results from leakage current measurements are shown in Figure 31. The first big difference which strikes is the difference in leakage current between two groups (green and blue) with intact hafnia layer and (black and red) with etched hafnia layer. This difference indicates that etching through the hafnia layer (to the BE) significantly increases the leakage current. One explanation for this occurrence is the redeposition of e.g. bottom electrode material like titanium onto the sidewalls of the devices. In this way a shortcut from top to bottom electrode would be created, increasing the overall leakage current. Another explanation is given by the fact that the argon bombardment of hafnia is known to induce defects in the material, which can also promote electrical conduction. If the defects cannot be sufficiently re-oxidized via atmosphere it can be assumed that the hafnia sidewalls would be conducting, similarly creating a shortcut between both electrodes.

The second difference can be seen in the statistical spread of the measurements. While the samples which have been capped in-vacuo show a narrower distribution (blue and red), samples of which the hafnia layer was exposed to atmosphere (green and black) show more wide spread leakage currents. This effect can be explained by the resilience of in-vacuo capped stacks against contaminations from e.g. regular impurity levels from the facilities, which would otherwise spread the statistical distribution.

From this investigation it can be concluded, that the in-vacuo deposition of the top electrode layer is beneficial, not only due to the prevention of oxidation, but also to reduce potential statistical spread. Further, it was found that etching through the hafnia layer should be prevented, as it induces significant leakage currents. While effects like re-sputtering or defect-induction on device sidewalls might be reduced by e.g. applying a reduced acceleration voltage, it is a straight forward approach to just stop ~ 10 s after the Hf signal is picked up as the total time for 20 nm etching is ~ 50 s (compare Figure 30 a & b).

3.6. Optimization of Electrode Thicknesses for operando TEM

An important aspect of the here discussed project was the anticipated TEM operando experiment in which the cross-section of a functional RRAM stack of Pt/HfO_{2-x}/TiN is prepared and subsequently connected onto a chip, which allows electric control over the sample while guaranteeing electron transparency.

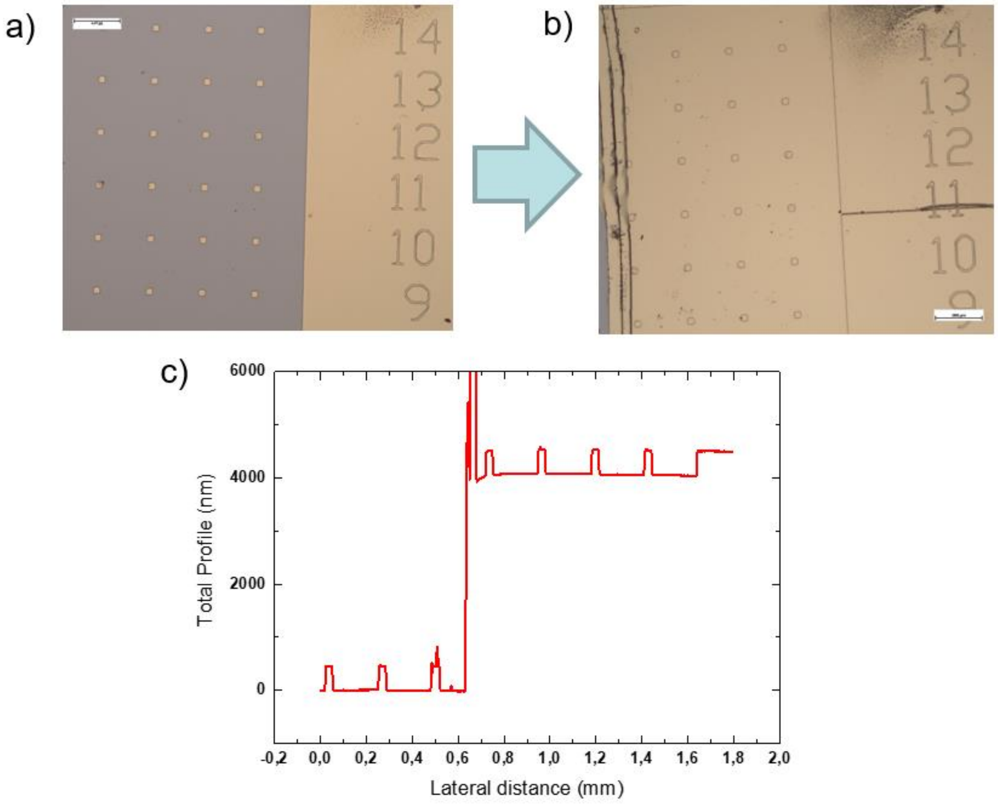

Figure 32: Optimal miscopy a) before and b) after sputtering of 4 µm gold on one half of the sample with 30 x 30 µm square electrodes showing that designated devices are still visible for TEM lamellae preparation c) profilometer measurement confirming 4000 nm thickness after 8,000 s (133.3 min) deposition at 30 mA, also showing that the total height of the electrodes ~ 350 nm is still conserved after the significant gold layer deposition.

Depending on the exact preparation technique a certain thickness of top and bottom electrode is required. While at least several 100 nm are required for a successful connection of either electrode to the corresponding ports on the chip. Another important issue is the buildup of joule heating during electrical switching which can be a serious threat to the lamellae. The rather violent, high voltage electroforming as necessary for many pristine oxides (including stoichiometric hafnia) results in elevated temperatures, which is crucial for operando TEM where nm-sized lamellae are prepared and switched. Especially such delicate, low volume devices are susceptible for overshoot currents and significant joule heating.[136, 137] One way to deal with an abrupt raise in thermal energy is to use additional electrode martial which can act as a heat sink. For this purpose, a routine to achieve electrode thicknesses in the micrometer range has been established. Figure 23 shows how a stack with standard micropatterning and ∼ 350 nm top electrode a) before, and b) after the deposition of 4 μm gold deposition after sputtering under an optical microscope.

Clearly all 30 x 30 μm^2 square features and corresponding numbering are still clearly visible after the deposition. Figure 23 shows the corresponding profilometer measurement where the tip first runs over a previously covered half of the stack, measuring the ∼ 350 nm electrode patches, which is followed by the 4000 nm step of the deposited gold layer. Strikingly, the profile of the electrode patches is also still clearly preserved even after the deposition. The 4 μm deposition was achieved by utilizing a, Dual-Target-Sputter Coater Q300T from Quorum Technologies Ltd with a 54 (diameter) x 0.2 mm gold target by applying a sputtering current of 30 mA for 8000 s (133.3 min). Note that this time is exceeding the maximum indented deposition time of the system, so that multiple subsequent depositions are necessary. Further it should be considered that this extended deposition time takes away about ∼ 1/3 of a total 0.2 mm target. This method can be applied to any stack that has previously been patterned. However, as all devices in the deposited area are subsequently connected across the samples surface, a direct electrical characterization (with contacting pins via e.g. Kiteley characterization unit) is then irreversibly impossible. Nonetheless, this method offers a straight forward approach, if the devices in question have already been adequately characterized. In this case the devices can be easily located in a focused ion beam setup (with SEM) and a functioning lamellae with can be cut from the stack.

4. Results & Discussion

The results & discussion part is divided in four main chapters namely 4.1 "Physical Properties of Oxygen Defect Stabilized Hafnium Oxide Phases", 4.2 "Ab-Initio Simulations on Substoichiometric Hafnium Oxide Compared to Experimental Results", 4.3 "Substoichiometric Phases of Hafnium Oxide as Novel Electrodes for RRAM Applications", 4.4 "Transmission Electron Microscopic Nanoscale Identification of Substoichiometric Hafnium Oxide Phases" and 4.5 "Scanning Probe Microscopy Analysis of Microstructure and Local Conduction".

Many parts of the presented results and the corresponding discussion (particularly of chapters 4.1 and 4.2) have been published under

"Kaiser, N., Vogel, T., Zintler, A., Petzold, S., Arzumanov, A., Piros, E., Eilhardt, R., Molina-Luna, L., and Alff, L., Defect-Stabilized Substoichiometric Polymorphs of Hafnium Oxide with Semiconducting Properties. ACS Applied Materials and Interfaces, 2022. **14**(1): p. 1290-1303."

and "Kaiser, N., Song, Y.-J., Vogel, T., Piros, E., Kim, T., Schreyer, P., Petzold, S., Valentí, R., and Alff, L., Crystal and Electronic Structure of Oxygen Vacancy Stabilized Rhombohedral Hafnium Oxide. ACS Applied Electronic Materials, 2023. **5**(2): p.754–763"

The first chapter 4.1 is mostly discussing physical properties of substoichiometric hafnium oxide grown by Molecular-Beam Epitaxy and is concerned with in-detail structural identification, chemical characterization, electrical characterization and band structure analysis of the novel phases of rhombohedral *r*-HfO_{2-x} and hexagonal *hcp*-HfO_{2-x}. The gathered results of this first part are finally summarized in a band-structure model from stoichiometric hafnia to metallic hafnium.

The second main chapter 4.2 discusses the results of a close collaboration with Goethe-Universität Frankfurt am Main. Here DFT calculations for the phase stabilization of *r*-HfO_{2-x} by oxygen vacancies were examined and strong agreements with the experimental results such as the crystal and band structure are discussed. In particular, the results also indicate that *r*-HfO_{2-x} could be a thermodynamically stable bulk phase.

The next chapter 4.3 is concerned with the properties of the previously discussed hafnium oxide phases, but reproduced in a typical MIM configuration for RRAM applications. Special attention is paid to the electrical characterization and differentiation of samples that were produced entirely in a vacuum from those that were exposed to atmospheric oxidation. The discussed results allow conclusions that the substoichiometric phases can act as conductive electrodes in the form of effective oxygen reservoirs. The results also confirm that the discovered phases could play a vital role in the switching mechanism as part of the electrically conducting filament.

Chapter 4.4 discusses the nanoscale identification substoichiometric phases of hafnium oxide by means of electron microscopic methodology. This approach deserves special attention in the context of the identification of the conducting filament in RRAM. So far, there is no comprehensive picture on the nano level that takes both structural and chemical aspects into account. Therefore, this chapter demonstrates the possibility to identify the here discussed and comprehensively analyzed phases with electron microscopic methods such as high resolution imaging, electron energy loss spectroscopy and automated crystal orientation mapping.

Finally, chapter 4.5 shows the results of c-AFM characterization of substoichiometric hafnium oxide. The obtained results are the product of a close collaboration with FZ Jülich and demonstrate the functioning sample exchange from the synthesis at the TU Darmstadt with subsequent sample analysis in the FU Jülich with specially designed sample holders and vacuum suitcase. The chapter shows a reproduced series from m-HfO_2 to r-$HfO_{1.7}$ deposited on custom designed sample holders and discusses their corresponding characterization via scanning probe spectroscopic techniques. Special attention is given to the microstructure and their role for mediating electrical conduction specifically in oxygen deficient hafnium oxide.

4.1. Physical Properties of Oxygen Defect Stabilized Hafnium Oxide Phases

This chapter is discussing the physical properties of hafnium oxide thin films which have been grown under oxygen deficient conditions. Many of the discussed results and adapted figures are published particularly under "Kaiser, N., Vogel, T., Zintler, A., Petzold, S., Arzumanov, A., Piros, E., Eilhardt, R., Molina-Luna, L., and Alff, L., Defect-Stabilized Substoichiometric Polymorphs of Hafnium Oxide with Semiconducting Properties. ACS Applied Materials and Interfaces, 2022. **14**(1): p. 1290-1303.".

Hafnium oxide is a famous high-k dielectric solution for semiconductor applications. Following the increasing research interest in fast and energy efficient memristive systems hafnium oxide became a prominent material in RRAM research due to its excellent performance.[31, 138-141] Investigations in this material system were recently further promoted through the applicability of RRAM technology in neuromorphic computing where more gradual switching behavior is required. Next to doping, oxygen deficiency in transition metal oxides is known to crucially affect its properties and functionality. For hafnium oxide this is especially interesting as it is a high-k dielectric but even more so in its application as resistive random access memory. In hafnium oxide based (filamentary) OxRAM the switching mechanism is governed by oxygen movement, where a local region is derived from oxygen and forms a so called conducting filament. Therefore, it is clearly of interest which kind of oxygen deficient modifications exist for hafnium oxide and how their physical properties are characterized. However so far there are not many studies which investigate the effects of strong oxygen deficiency in hafnium oxide. There are several publications which suggest suboxide modifications such as Hf_2O_3, HfO or Hf_6O, there is however a lack of experimental evidence.[66, 67, 74, 76]

While oxygen deficient hafnium oxide is almost exclusively reported in form of thin films, the observed structures are often associated with high temperature or high pressure modifications of hafnium oxide which are strongly interrelated and considered to be stoichiometric (compare chapters 1.5 & 1.7). However, a clear structural identification is complicated due to phase mixtures, XRD peak broadening or arbitrary texturing in such films. Further, electrical properties of hafnium oxide are often investigated in form of metal-insulator-metal configurations with specific interfaces, which complicates conclusions on materials properties.[8, 142, 143] Such devices are prone to interfacial effects such as the surface oxidation of hafnium oxide (compare chapters 4.3.2 & 4.3.4) or the formation of TiO_xN_y at the interface of commonly used TiN as electrode material.[144, 145]

To answer such open questions this chapter is concerned with the comprehensive identification of substoichiometric hafnium oxide phases and their physical properties. Therefore, hafnium oxide is grown over a broad range of oxidation conditions on c-cut sapphire substrates via Molecular-Beam Epitaxy which allows to identify two intermediate phases between hafnia and hafnium as detailed in chapter 4.1.1. The deposition on c-cut sapphire enables growth of highly crystalline hafnium oxide under epitaxial conditions which allows for an effective analysis of symmetry and peak splitting which allows for a detailed structural identification of oxygen deficient *r*-HfO_{2-x} in chapter 4.1.2. The investigation is followed by in-vacuo XPS analysis in chapter 4.1.3 where the chemical environment as well as the oxygen content of *r*-HfO_{2-x} and *hcp*-HfO_{2-x} are discussed. By deposition on transparent, insulating sapphire the experiment was designed to enable the direct measurement optical bandgap and electrical properties. Chapter 4.1.4 and 4.1.5 discuss corresponding resistivity and Hall effect measurements as well as optical absorption spectroscopic results. Thereafter chapter 4.1.6 discusses the crystallinity and microstructure of observed phases via Transmission Electron Microscopy. Finally, all aforementioned results are summarized in chapter 4.1.7. Here a comprehensive band structure model from hafnia to hafnium is presented, discussing the development and interplay of midgap states as well as the valence- and conduction band in dependence of the oxygen content.

4.1.1. Novel Structures *r*-HfO_{2-x} and *hcp*-HfO_{2-x} between Hafnia and Hafnium

To investigate the structural and physical properties of oxygen deficient hafnium oxide, 13 samples of 20 nm thin films have been grown under varying oxidation conditions via Molecular-Beam Epitaxy. All samples have been synthesized under CMOS compatible substrate temperature of 320 °C. In order to achieve epitaxial growth, the thin films have been deposited on sapphire single crystals of 5 x 5 mm^2 (0.5 mm thickness) with c-cut orientation. Further sapphire was chosen as substrate material because of its wide bandgap and insulating properties, which allow a direct measurement of the thin films electrical properties and optical absorption. To achieve a broad range of oxidation conditions both the hafnium evaporation rate and the oxygen gas flow have been varied.

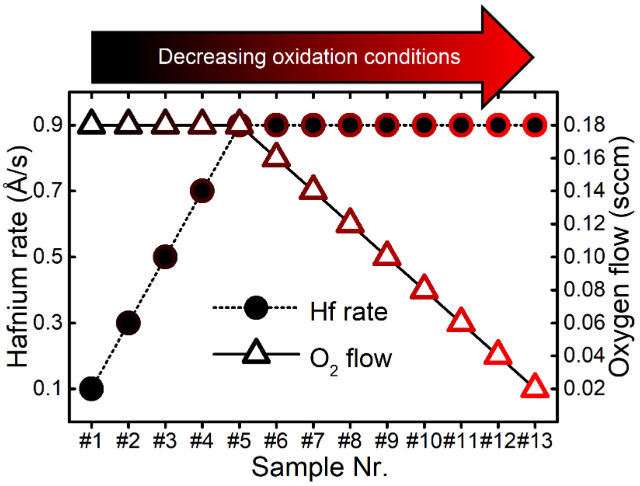

Figure 33: Deposition conditions for the discussed series of 13 samples following a consistent trend in oxidation conditions with most oxidizing conditions for #1 to more and more reduced oxidation conditions to #13. Note that the oxygen flow remains constant for varying hafnium evaporation rate and via versa. Reprinted with permission from reference [146]. https://doi.org/10.1021/acsami.1c09451 Copyright © 2021 American Chemical Society.

The main deposition parameters of the series are shown in Figure 33, showing an increase of the hafnium rate from 0.1 Å/s to 0.9 Å/s for samples #1 to #5 while maintaining a constant gas flow of 0.18 standard cubic centimeters per minute (sccm). For samples #5 to #13 the O_2 gas flow was varied from 0.18 sccm to 0.02 sccm at a constant hafnium evaporation rate of 0.9 Å/s. To promote the reaction of oxygen with the evaporated hafnium the O_2 flow was excited into a plasma by a constant radio frequency power of 200 W. Note that the trend from most oxidizing to most oxygen deficient conditions is highlighted in a color transition from black to red (for better clarity) which is also applied to all other graphs in this work.

Figure 34 shows the evolution of the crystal structure in dependence of the applied conditions as mentioned above. The XRD measurements have been conducted with a Rigaku SmartLab diffractometer in parallel beam configuration. A Ge (220) double bounce monochromator was used to select the Cu $K\alpha_1$ radiation. Vertical lines highlight literature reference values for specific reflexes of monoclinic (*m*-HfO_2; PDF 00-034-0104), cubic (*c*-HfO_2; PDF 04-011-9018) and metallic hexagonal (*hcp*-Hf; PDF 00-038-1478). For highest oxidation conditions the structure of monoclinic hafnium oxide is dominant, which is expected as it represents the ambient pressure phase of stoichiometric hafnia. [147] By gradually reducing the oxidation conditions, the monoclinic phase vanishes and a second phase shows up and becomes most prominent close to the reference line of stoichiometric cubic *c*-HfO_2. However, in chapter 4.1.2 the phase is comprehensively identified to be of a rhombohedral structure (*r*-HfO_{2-x}).

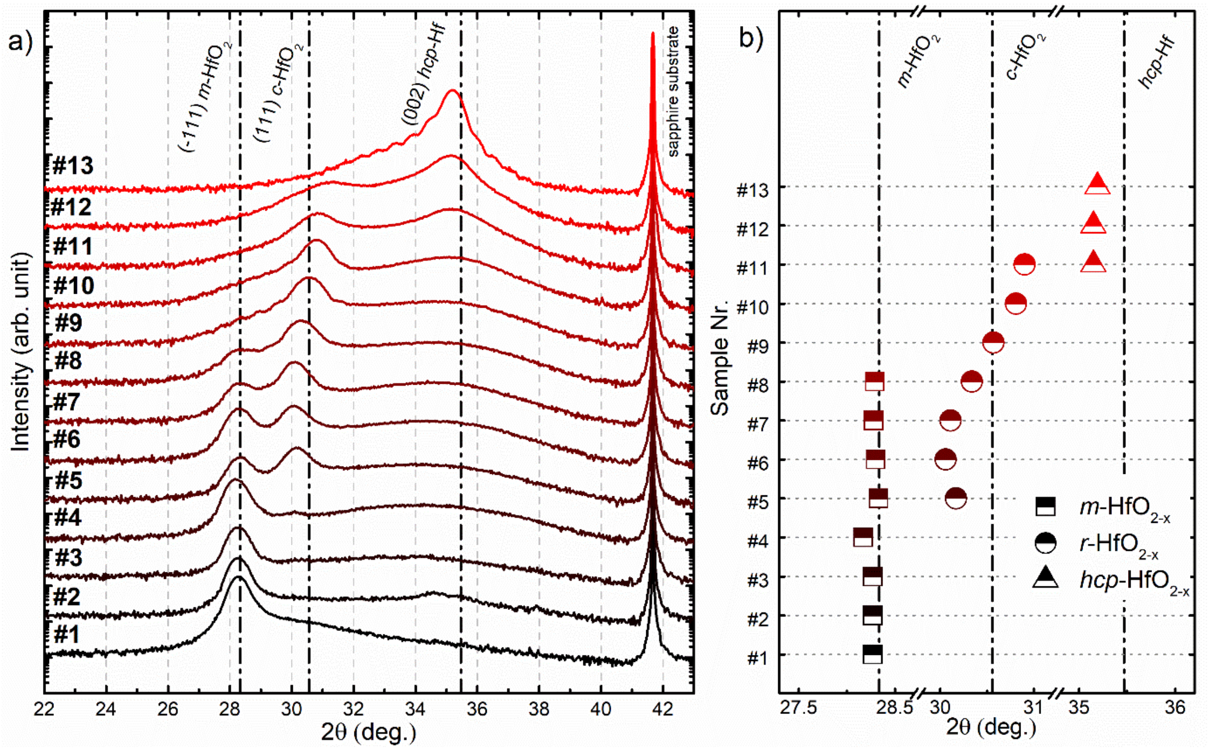

Figure 34: Oxidation depend evolution of the crystals structures a) and corresponding lattice planes b). The measurements show crystal structures with lattice parameters close to stoichiometric cubic hafnia (*c*-HfO_2) and close to hexagonal metallic hafnia (*hcp*-Hf) as transitional structures between stoichiometric monoclinic hafnia (*m*-HfO_2) and metallic hafnium. The transitional structures are identified as oxygen vacancy stabilized *r*-HfO_{2-x} and oxygen rich metallic hafnium with oxygen interstitials *hcp*-$HfO_{0.7}$ as will be discussed in the following chapters. Reprinted with minor changes with permission from reference [146]. https://doi.org/10.1021/acsami.1c09451 Copyright © 2021 American Chemical Society.

Interestingly, as can be seen in Figure 34 b), while the monoclinic (-111) reflection remains constantly at the corresponding reference line at ~28.3° in 2θ, the (111) reflection of *r*-HfO_{2-x} shifts from ~ 30.2° to 30.9° in 2θ corresponding to a change in the lattice constant from 2.92 Å to 2.89 Å and specifically 2.92 Å for the sample with the most pronounced out of plane intensity for *r*-HfO_{2-x} (#9).

By reducing the oxidation conditions further, a second transition to a hexagonal *hcp*-HfO_{2-x} phase can be observed.

Figure 35 a) shows how the critical angle in X-ray reflectometry changes in dependence of the oxidation conditions. As expected, less oxidizing conditions lead to an increase in the critical angle which translated into a higher electron density as the heavy Hf ions are less and less separated by light oxygen ions. An estimate on the XRR density is given in Figure 35 b) which was extracted through refinement via RCRefSim software. [93] The density of the most oxidized sample is close to the bulk density of stoichiometric hafnia with 9.68 g/cm³ as indexed by the dotted line. [148] The change in density shows a gradual trend over ~ 10.54 g/cm³ for *r*-HfO_{2-x} (#9) to up to a maximum of 11.25 g/cm³ for *hcp*-HfO_{2-x} (#13). Note that the density for metallic hafnium is about 13.25 g/cm³. [149] Therefore, the observed (rather low) density of 11.25 g/cm³ for *hcp*-HfO_{2-x} indicates a significant amount of oxygen interstitials.

Figure 35 c) shows the rocking curve measurements of the out of plane reflections from the most isolated key structures *m*-HfO_2 (#1), *r*-$HfO_{1.7}$ (#9) and *hcp*-$HfO_{0.7}$ (#13). In all cases a sharp reflection with full width at half maxima (FWHM) values between 0.05° and 0.06° are observed, showing highly oriented growth and low mosaicity. Further by looking at the 2θ scans in Figure 34 a), *r*-$HfO_{1.7}$ (#9) and *hcp*-$HfO_{0.7}$ (#13) show Laue oscillations, which result from a high coherence of parallel lattice planes indicating high crystalline quality.

Previously it was reported that growth of hafnium oxide at temperatures as high as 700 °C leads to the formation of the monoclinic structure only[63], and low temperature growth result in the amorphous thin films.[138] Therefore, it is notable that highly crystalline *r*-HfO_{2-x} can be isolated in a limited window of reduced oxidation conditions at 320 °C.

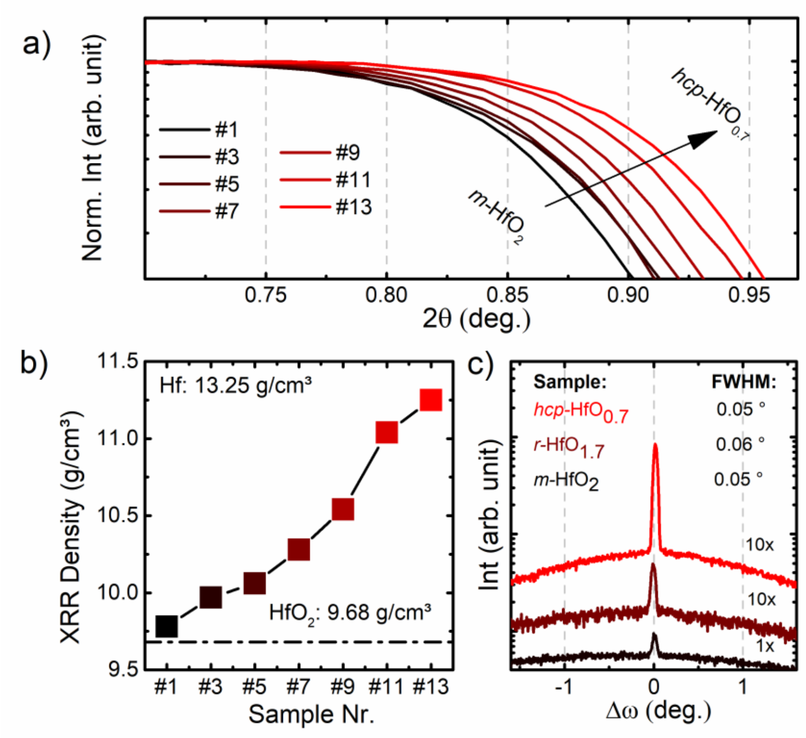

Figure 35: a) Increasing critical angle in dependence of decreasing oxidation conditions b) corresponding XRR density as extracted from RCRefSim c) Rocking curve measurements of the most isolated key structures *m*-HfO_2 (#1), *r*-$HfO_{1.7}$ (#9) and *hcp*-$HfO_{0.7}$ (#13). Reprinted with minor changes with permission from reference [146]. https://doi.org/10.1021/acsami.1c09451 Copyright © 2021 American Chemical Society.

In summary a series of hafnium oxide thin films under varying oxidation conditions was shown and their transformation in crystalline structure and XRR density was discussed. The smooth transition from one crystalline structure to another as apparent from Figure 34 reveals *r*-$HfO_{1.7}$ (#9) and *hcp*-$HfO_{0.7}$ (#13) as the links in a transition from monoclinic hafnia to purely metallic hafnium. Further the smooth trend in XRR density confirms the gradual variation in oxygen content.

4.1.2. Identification of Rhombohedral Hafnium Oxide *r*-HfO_{2-x}

In order to identify second phase, which shows up in oxygen deficient hafnium oxide (directly after the monoclinic structure) as discussed in chapter 4.1.1 additional XRD measurements have been performed on sample #9 with the most prominent reflection around ~ 31° in 2θ. For this purpose, pole figure and in plane measurements have been conducted which allow to analyze additional reflections from highly oriented films. As shown in Figure 36 a), the out-of-plane lattice constant fits several polymorphs like the cubic (*Fm*-3*m*), the tetragonal ($P4_2/nmc$) or orthorhombic 1 (*Pbca*) phase. [38, 41, 47]

As discussed in chapters 1.5 & 1.7 these phases are well known high temperature (cubic & tetragonal) and high pressure (orthorhombic I, orthorhombic II) polymorphs of HfO_2. However, these phases are also regularly associated with oxygen deficient hafnium oxide structures as they show similar features. [57, 138, 150] Although similar to the monoclinic phase, all those structures appear to be of a higher symmetry and are strongly interrelated [47], which impedes the unambiguous identification of this subset of phases. [56-58]

To identify the phase in question, the epitaxial growth conditions offers two advantages. First, due to the limited out of plane reflexes, it is easier to identify to most phase pure sample (see chapter 4.1.1) and second it allows identifying reflections in dependence of the ψ and the φ angle (compare chapter 2.1.3) which enables an effective analysis of peak splitting even in the presence of significant peak broadening. The verification of peak splitting is a conclusive strategy to discern between cubic, tetragonal or orthorhombic structures with similar dimensions.

Figure 36 a) shows the out plane reflection of the sample #9 together with exemplary patterns of powder diffraction files of previously discussed hafnia polymorphs which match with the reflection around 30.5 ° in 2θ, namely with the cubic (PDF 04-011-9018), tetragonal (PDF 04-011-8820) and orthorhombic (PDF 04-011-8819) phase (see Figure 13; chapter 2.1.2). The corresponding reflection matching the out of plane lattice constant are displayed in red with a normalized intensity of 100%. The reflections displayed in blue around 34°-37° in 2θ represent the relevant lattice planes indicating the effect of peak splitting with only one (200) reflection for the cubic phase with highest symmetry, two reflections (002) & (110) for tetragonal and three prominent reflections (002), (200) & (040) for the orthorhombic I phase (with the lowest symmetry of the three phases).

However, the reflections in Figure 36 a) which are displayed in blue do not appear in the out-of-plane 2θ/ω scan and are only accessible at specific ψ and the φ angles. Figure 36 b) lists all reflexes (as indicated in blue in Figure 36 a) which are relevant for peak splitting around 35.5° in 2θ with corresponding ψ angles. Those angles have been calculated as angles between the expected out of plane lattice parameter from each structure and the corresponding in plane angle (compare chapter 2.1.3). As the out of plane parameter appears perpendicular to the substrate, the angle directly translates into the geometrical ψ angle. In addition to the 2θ separation in peak splitting, this analysis also allows to identify the separation which is expected in ψ which is also listed in the corresponding table in Figure 36 b).

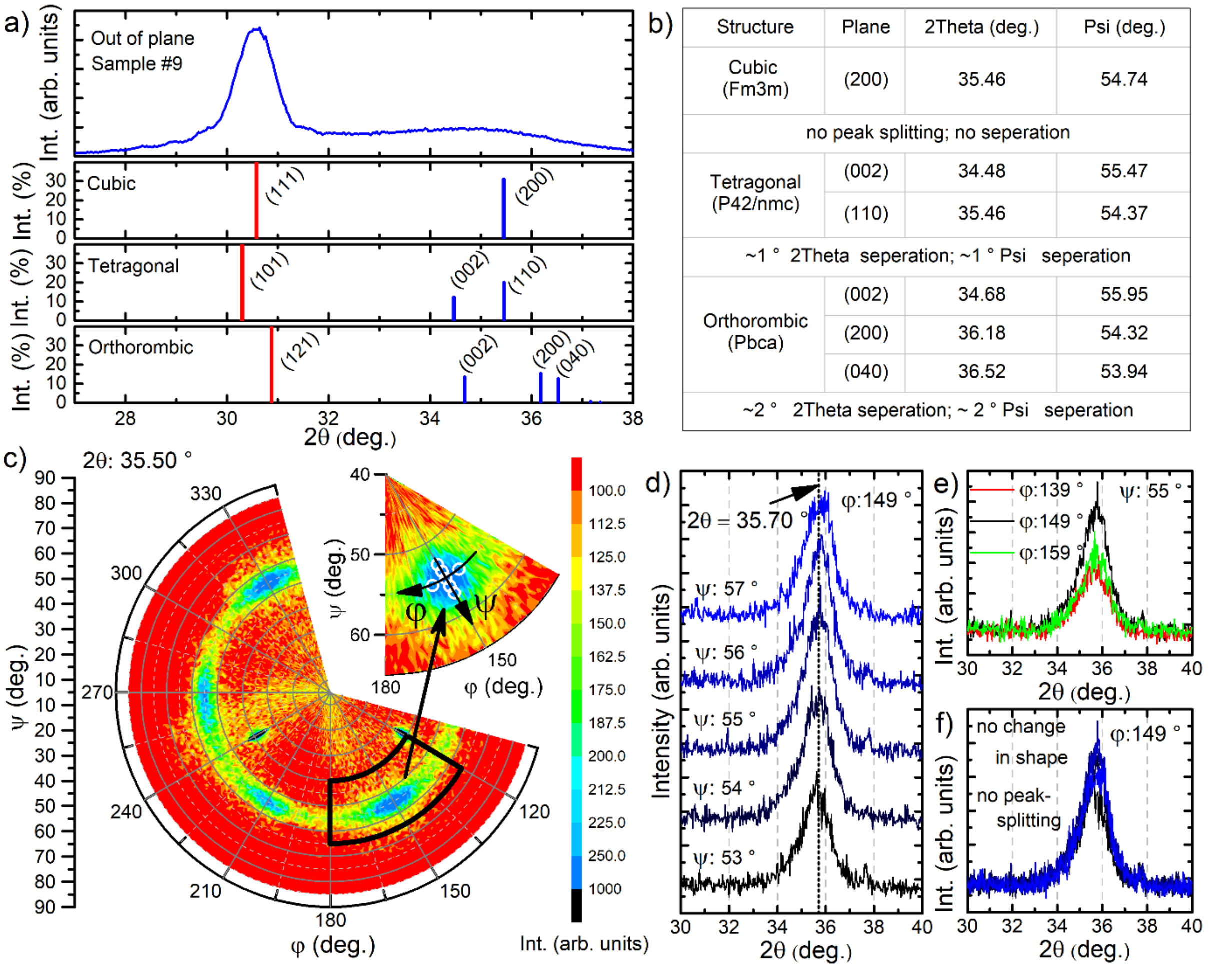

Structure	Plane	2Theta (deg.)	Psi (deg.)
Cubic (Fm3m)	(200)	35.46	54.74
no peak splitting; no seperation			
Tetragonal (P42/nmc)	(002)	34.48	55.47
	(110)	35.46	54.37
~1 ° 2Theta seperation; ~1 ° Psi seperation			
Orthorombic (Pbca)	(002)	34.68	55.95
	(200)	36.18	54.32
	(040)	36.52	53.94
~2 ° 2Theta seperation; ~ 2 ° Psi seperation			

Figure 36: a) shows the 2θ/ω scan of sample #9 in comparison with PDF references of known HfO_2 structures, highlighting that the out of plane lattice parameter fits all corresponding structures. b) shows a list of lattice planes relevant for phase identification around 35° in 2θ as well as their expected separation in 2θ and in ψ. c) shows the pole figure measurement with peudo-six-fold symmetry at ˜ 35.5 ° in 2θ and d), e) and f) confirm that the measured reflection spots show no indications of peak splitting, therefore confirming that the reflections originate from a single (002) lattice plane. As a consequence, the investigated phase corresponds most closely to the cubic reference. The identification is usually further hindered by the effects of peak broadening in thin films as well as the presence of different (usually monoclinic) phase fractions. As already discussed in chapter "Novel Structures *r-HfO2-x* and *hcp-HfO2-x* between Hafnia and Hafnium" 4.1.1, the isolation of an intermediate oxygen deficient phase is only possible in a limited window of growth conditions. Reprinted with permission from reference [146]. https://doi.org/10.1021/acsami.1c09451 Copyright © 2021 American Chemical Society.

In a first step to measure in plane reflections, pole figure measurements in the relevant range from 31.0° to 36.5° in 2θ have been performed in 0.5° steps. As can be seen from Figure 38 a) & b) at ∼ 70.5° in ψ reflections show up around 31.0° to 31.5° in 2θ which is expected for in plane-oriented variants of the out of plane reflection (reflection indicated in red in Figure 36 a). Note that the out of plane signal as shown in Figure 36 a) has a shoulder which stretches over several degree in 2θ. While initially it was believed to be part of a surface oxidation effect which is known to happen in deficient hafnium oxide[135], the reproduced growth on TiN discussed in chapter 4.3.1 (page 88) does not show such a feature. Further considering the TEM results discussed in chapter 4.1.6 which suggest continuous highly crystalline hafnium oxide phases, this contribution can likely be assigned to an interface effect in partial areas of the sapphire/HfO_{2-x} interface. The second set of thin film reflexes can be discerned in Figure 39 j & k) at 35.5° to 36.0° in 2θ as roughly expected from reflexes indicated in blue (Figure 36a). Both, Figure 38 a & b) as well as Figure 39 j & k) show the corresponding reflections in a pseudo-six fold symmetry which results from the defined orientation of domains. The relation of domains to the c-cut sapphire substrate becomes visible in Figure 39 j) where the three-fold (104) reflex around 35° in ψ appears 30° shifted in φ to the thin film reflections at ~ 55.0° in ψ.

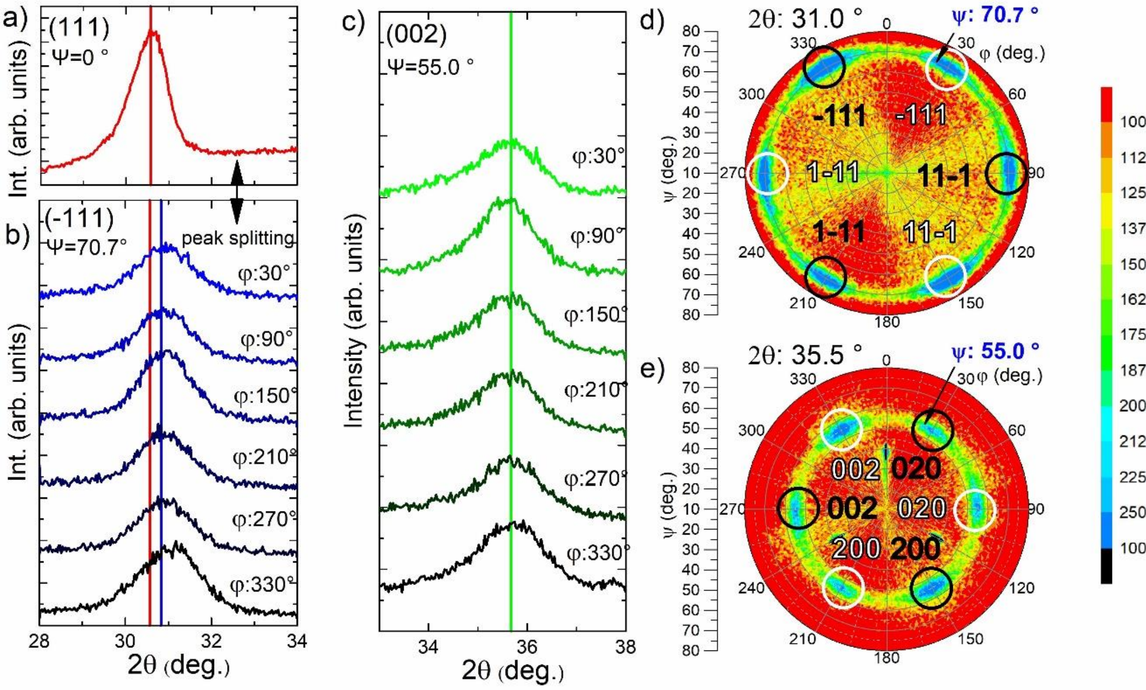

Figure 37: a), b) and c) show the 2θ scans on the corresponding (111), (-111) and (002) reflections with reference to the geometrical parameters ψ and φ. a) & b) show the peak splitting between (111) and (-111) verifying the rhombohedral nature of the phase. Note that the vertical lines, highlighting the peak maxima in a), b) and c) satisfy the mathematical relation for a rhombohedral structure. d) and e) show the corresbonding pole figures for the (-111) and (002) reflections. The pseudo-sixfold symmetry can be understood by the growth of multiple domains of threefold symmetry (highlighted in black and white) which are offset by 60° in φ. Reprinted with permission from reference [151]. https://doi.org/10.1021/acsaelm.2c01255 Copyright © 2023 American Chemical Society.

To further investigate if the second set of reflexes originate from one or multiple lattice planes (as for tetragonal or orthorhombic) or one lattice plane (for cubic) a series of 2θ scans has been performed in dependence of ψ and φ around one diffraction spot from the pole figure as shown in Figure 36c. In case of the tetragonal reference one would expect a separation of ~ 1° in 2θ and also ~1° in ψ. In case of the orthorombic reference one would even expect a separation of ~ 2° in 2θ and also ~ 2° in ψ (compare Figure 36b). However as can be seen from Figure 36 d-f) the reflection shows no significant changes in peak position or shape over the whole range of 53° to 57° in ψ and only a loss of overall intensity for measurements at 139° and 159° in φ. Therefore, the corresponding reflection is verified to originate from one lattice plane, which is (from the set of references) only true for the cubic case, which it best reassembles. As the obtained results show strongest similarities with the cubic phase of hafnium oxide (c-HfO_2) which is known to form from stoichiometric hafnium oxide at high temperatures of 2800 °C and higher (compare chapter 1.5) it was first designated low temperature phase of cubic hafnium oxide (LTP c-$HfO_{1.7}$).[146] This distinction was drawn as the investigated phase is formed at much lower temperatures (320 °C) and stabilized through oxygen vacancies, which is, amongst other things, reflected in a special XPS fingerprint (further details are provided in the following chapter 4.1.3). While the investigated phase appears to be similar to its high temperature cubic counterpart the measured (002) reflex (Figure 36 d) shows a slightly increased angle of 35.7° instead of 35.46° which would be expected for an ideal cubic structure. Therefore, the structure indicates a slight rhombohedral distorted cubic lattice, where the structure is elongated along the [111] out of plane direction. This slight rhombohedral distortion was already discussed in the publication, where the phase of LTP *c*-$HfO_{1.7}$ was first mentioned, but the exact rhombohedral nature (*r*-$HfO_{1.7}$) of this pseudocubic structure was described later.[151] The corresponding XRD measurements and conclusions are discussed below, while a further insides provided by DFT calculations are shown in chapter 4.2.2.

If the structure is elongated along the (111) plane (as compared to an ideal cubic structure), a rhombohedral peak splitting of the (111) and (-111) is expected. While the (111) lattice plane is assigned to the out of plane position of $\psi = 0°$, the (-111) direction is expected at $\psi \sim 70.5°$ (from geometric considerations assuming an approximate cubic structure). To directly identify the nature of peak splitting, 2θ scans of all (-111) reflection spots as shown in Figure 37 d) have been measured. Additional 2θ measurements were also carried out on all (002) reflections (see Figure 37 e) in order to obtain as complete a picture as possible. Figure 37 a-c) show the 2θ measurements on the (111), (-111) and (002) reflections with a corresponding reference to the geometric angles ψ and φ. In the plots between Figure 37 a) and Figure 37 b), the peak splitting between (111) and (-111) becomes obvious and corresponds to a shift of ~ 0.25° in 2θ. The vertical lines as indexed in Figure 37 a-c) highlight the corresponding peak maxima and satisfy the mathematical relation for a rhombohedral structure [88]:

$$\frac{1}{{d_{hkl}}^2} = \frac{(h^2+k^2+l^2)sin^2\alpha + 2(hk+kl+hl)(cos^2\alpha - \cos\alpha)}{a^2(1-3cos^2\alpha + 2cos^3\alpha)} \qquad (40)$$

with $\alpha = \beta = \gamma = 89.66°$, confirming the rhombohedral nature of the phase. A slight deviation of ~ 0.2° is found in the (-111) reflection at $\varphi = 330°$ which is likely a second contribution overlaying the (-111) signal which is discussed in the supporting information of the original publication.[151] The corresponding unit cell parameters are listed in Table 4, highlighting the differences to a reference of stoichiometric cubic hafnium oxide (PDF 04-011-9018) which is known to form at high temperatures. Further information and discussion about this recently identified phase can be found in chapters 4.2.1 and 4.2.2 where DFT calculations show, amongst other things, that this phase could exist as a thermodynamically stable bulk compound, and that the space group is likely of $R3m$ symmetry.

Table 4: Crystal structure of *r*-$HfO_{1.7}$ as extracted from the XRD measurements on sample #9 in comparison to the cubic reference (*c*-HfO_2; PDF 04-011-9018). Note that the main difference is given by the elongation in [111], resulting in α = β = γ = 89.66°.

Structure	a=b=c (Å)	α=β=γ (deg.)	Vol (Å³)	Plane	d(Å)	2θ (deg.)	ψ (deg.)
c-HfO_2	5.06	90	129.55	(111)	2.92	30.57	0
				(-111)	2.92	30.57	70.53
				(002)	2.53	35.45	54.74
r-$HfO_{1.7}$	5.03	89.66	122.54	(111)	2.92	30.57	0
				(-111)	2.90	30.83	70.69
				(002)	2.48	36.14	55.17

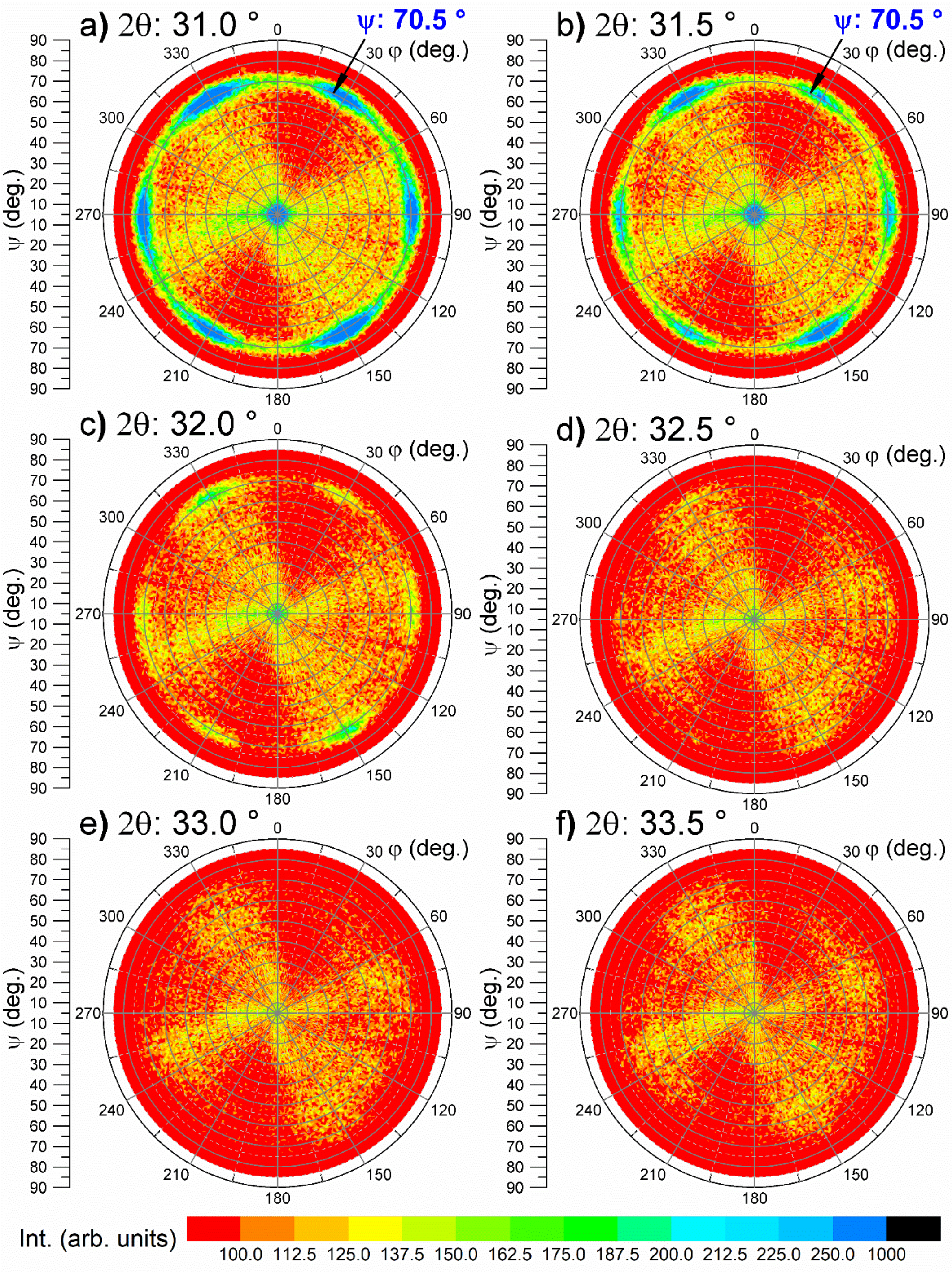

Figure 38: Pole figure measurements on sample #9 (*r*-HfO$_{1.7}$) from a) to f) at 2θ values from 31.0° to 33.5° in 0.5° steps. Displayed scans cover ψ = 5 ° to 80 ° and φ = 0 ° to 360 °.

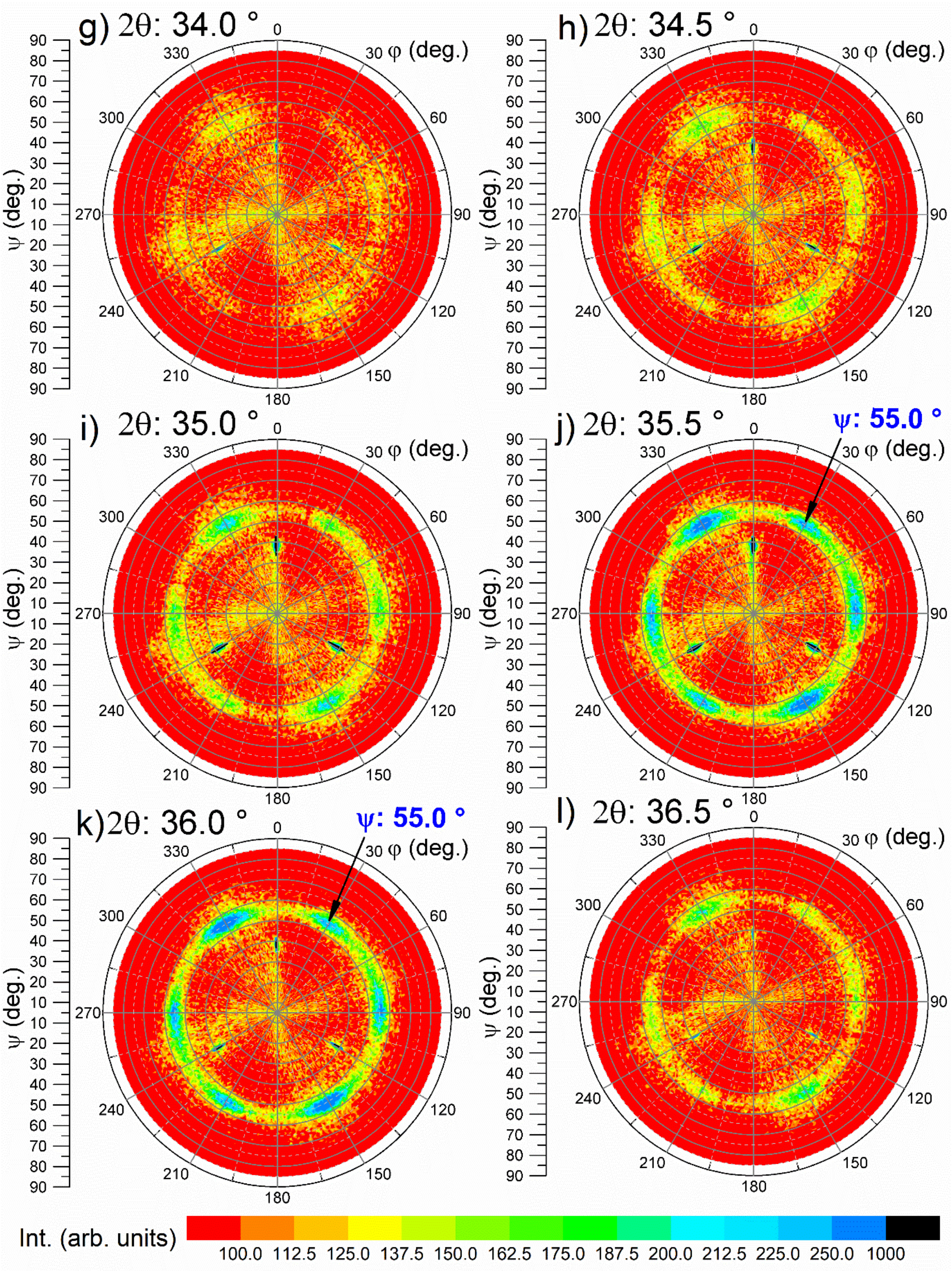

Figure 39: Pole figure measurements on sample #9 (r-HfO$_{1.7}$) from g) to l) at 2θ values from 34.0° to 36.5° in 0.5° steps. Displayed scans cover ψ = 5 ° to 80 ° and φ = 0 ° to 360 °.

4.1.3. Electronic Environment and Composition of *r*-HfO_{2-x} and *hcp*-HfO_{2-x}

In order to investigate the influence of oxygen engineering on the chemical environment, electronic structure and elemental composition of HfO_{2-x} X-ray photoelectron spectroscopy (XPS) measurements have been performed. Special thanks to Tobias Vogel assisted with the fitting of the discussed spectra. As oxygen-deficient hafnium oxide is known to develop an oxidation layer of several nanometers if exposed to atmosphere[135], all samples have been measured in-vacuo. This was possible by transferring the samples in a custom vacuum suitcase, equipped with an ion-getter pump and an ion-gauge to guarantee a strict continuity of ultra-high vacuum conditions.

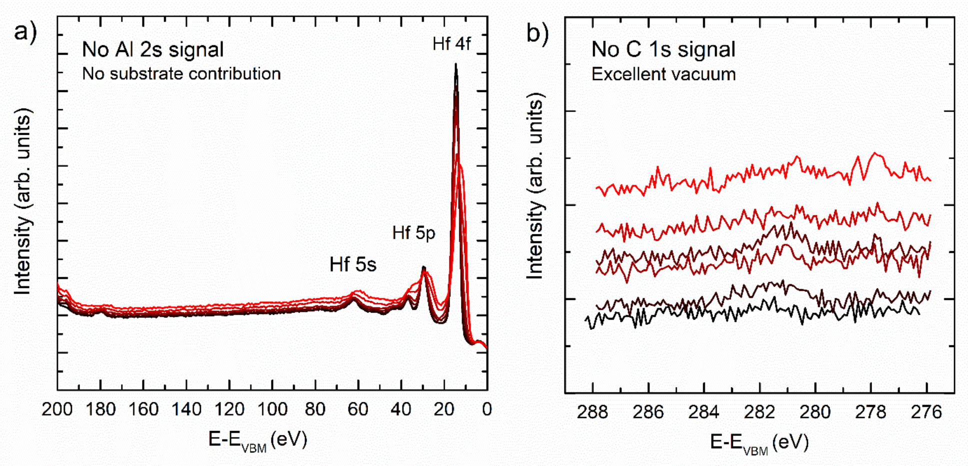

Figure 40: a) Evidence from survey scans that no Al 2s signal is detected (around 120 eV), ruling out contributions from the substrate b) shows designated scans around the energy window where a C 1s signal would be expected. As can be seen, almost no deviation from the noise can be identified, which shows that besides minimal potential traces no carbon is present in the thin films or even at the surface. While at least carbon adsorbates are a common feature in XPS spectra, these scans highlight the excellent vacuum-conditions for both, synthesis and in-vacuo transfer.

All spectra have been measured by utilizing a standard X-ray gun providing Al K_α radiation. Therefore, a typical mean free path of six nanometers can be assumed, which is significantly exceeded by the thin film thickness of 20 ± 2 nm. Consequently, no contribution from the substrate is expected. This is confirmed in Figure 40 a) where no signal from the Al 2s (most intense Al line which is a vital component of the sapphire substrates) orbital can be seen. Photoelectrons have been capured under an escape angle of 75°. As the thin films have been deposited onto insulating sapphire substrates, dual beem charge neutralization was allpied during all measurements. Due to the insulating nature of the substrates and the absence of a detectable C 1s signal (See Figure 40 b; because of excellent in-vacuo conditions), all spectrra have been alligned to the energy of the valence band maximum E_{VBM}. By the reference measurement on a gold-calibrated deficient hafnium oxide thin film on a conducting TiN/Si stack, the energetic difference between E_F and E_{VBM} is estimated to be ~ 4.3 eV which sould be added to the $E\text{-}E_{VBM}$ indicated abcissa in all spectra to receive an bidning energy approximation.

Further, as can be seen in Figure 41, the survey spectra of all investigated samples show no indication of unexpected elemental contributions, as all significant features can be assigned to either hafnium with Hf 4f, Hf 5p, Hf 5s, Hf 4d, Hf 4p and the auger feature Hf NNN or oxygen with O 1s and the auger feature O KLL.

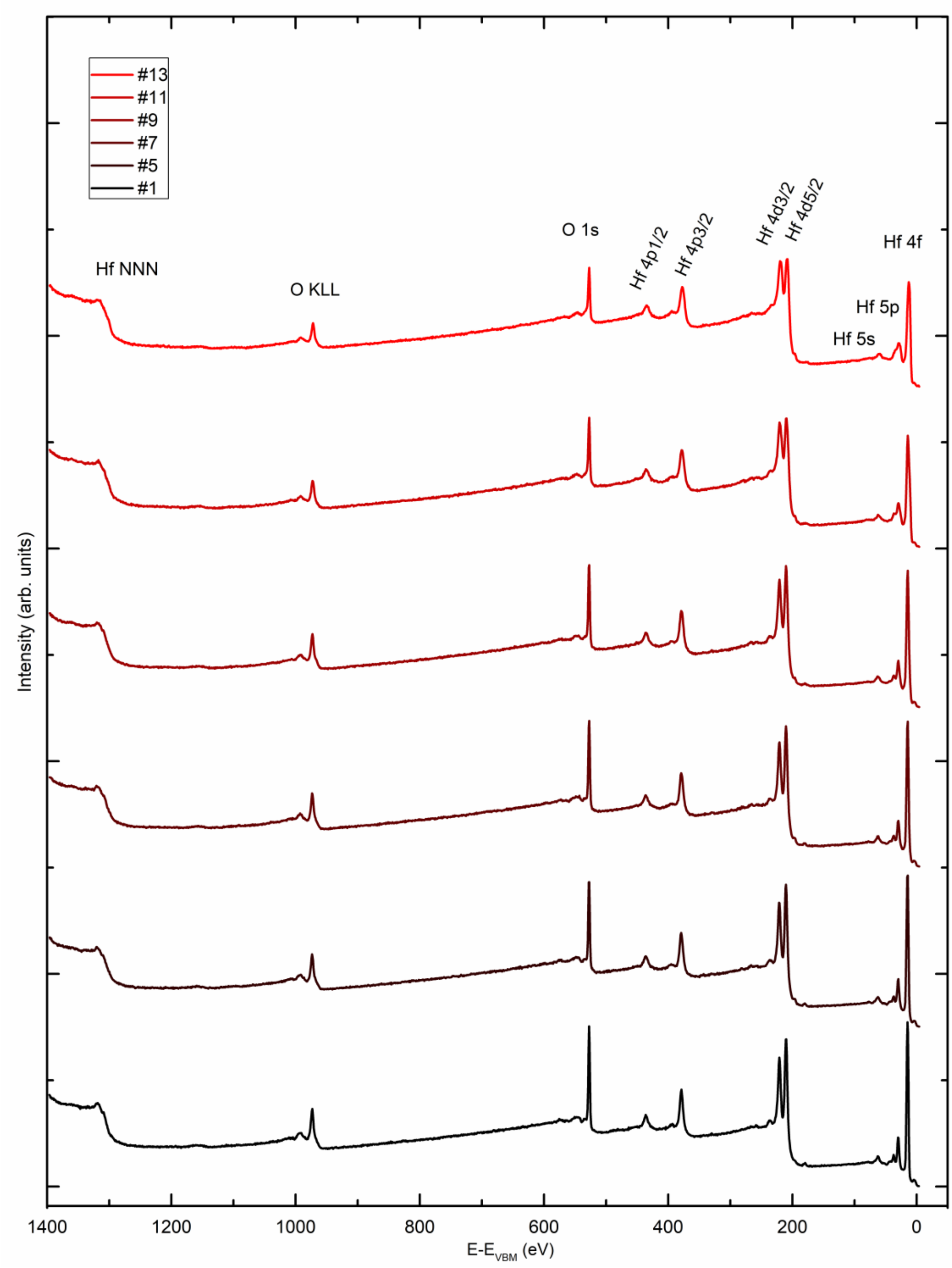

Figure 41: XPS surveys on all samples indexed after the Handbook of X-ray Photoelectron Spectroscopy. The orbital emission lines of Hf 4f, Hf 5p, Hf 5s, Hf 4d, Hf 4p as well as O 1s can be clearly identified. Further the auger signals of O KLL and Hf NNN are present in the spectra. Note that all relevant lines are indexed with the expected species of hafnium and oxygen but no additional or unexpected features.

Figure 42 a) shows the Hf 4f emission lines of the series in dependence of oxidation conditions and oxygen content (from #1 to #13). A Shirley type background was subtracted from all spectra and the fit constrains are based in Morant *et al.* [106] with peak splitting of 1.71 eV and an area ratio of 0.72 for doublets of Hf^{4+} and sub oxide contributions Hf^{x+}. Further, all Hf^{4+} and Hf^{x+} peaks have been fitted by a Gaussian-Lorentzian function. For the Hf^{0} contributions a Doniac-Sunjic function was used with a relative area of 0.75. Besides sample #5, where the Hf^{x+} contributions could be fitted with only one doublet, the rest was fitted with two Hf^{x+}

doublets. Sample #1 could be fitted with one single Hf^{4+} doublet which is expected for a stoichiometric monoclinic structure and in good agreement with the high oxidation conditions. For strongly deficient conditions, the energetic difference between Hf^0 and Hf^{4+} was set contribution was set to an energy difference of 3.4 eV to 4.1 eV which is in accordance with literature. [106, 135, 152, 153] Note that the investigated series covers an extremely broad range of oxidation conditions, which also involves complete structural transformations. This highlights that minor variations between the energetic difference of Hf^0 and Hf^{4+} are expected.

Comparing the Hf 4f spectra in Figure 42 a), the samples grown under most oxidizing conditions namely #1 (monoclinic) up to #9 (rhombohedral) show the highest possible oxidation state of Hf^{4+} as the predominant fraction. As all samples have been transferred and measured under excellent vacuum conditions (compare Figure 40b) the Hf^{4+} signal can be directly attributed to the thin film lattice and not merely to surface oxidation. The observation of Hf^{4+} states as the main oxidation state is consistent with the atomistic description of cubic or similar phases, since many theoretical models explain not just m-HfO_2 but also higher symmetry polymorphs such as cubic hafnia in Hf^{4+} configuration. [150, 154, 155] Note that cubic hafnia, as explained in chapter 3.2, is generally only accessible and stable at high temperatures. [38, 41]

With the use of DFT calculations, Lee et al. proposed that cubic (or tetragonal) HfO_2 phases are stabilized in the ambient environment by doping and subsequent compensation by charged oxygen vacancy defects.[155] Two specific explanations are provided to support this mechanism. First, m-HfO_2 hafnium atoms are seven-fold coordinated, whereas cubic hafnia hafnium atoms are eight-fold coordinated. The desired seven-fold coordination of hafnium can be met by introducing charged oxygen vacancies into the cubic matrix. Second, charged defects can cause lattice relaxations, which lower the relative energy of the cubic or tetragonal phases in comparison to the monoclinic phase.[155]

Also in this study, the transformation from a monoclinic structure to a pseudocubic structure is facilitated by the simultaneous incorporation of oxygen vacancies, similarly to the observations of Lee et al. [155]. The findings mentioned in 4.1.2 highlight specifically the similarity of the rhombohedral phase to a cubic reference. However, in this work oxygen vacancy defects are incorporated into a non-doped crystal lattice, necessitating the conservation of charge neutrality in absence of dopants. Therefore, observed generation of Hf^{x+} ($x < 4$) sub-oxides as illustrated in Figure 42 a) are in good agreement with the hypothesis of oxygen vacancy stabilization.

Other theoretical hypotheses for oxygen-deficient hafnia encourage the separation of deficient HfO_{2-x} in phases of m-HfO_2 and hcp-$HfO_{0.2}$ or the production of distinct sub-oxide phases such semi-metallic Hf_2O_3, HfO, or Hf_2O.[66, 67, 76] First, as the XRD results (see Figure 34) clearly show an almost exclusive formation of r-HfO_{2-x} (see Figure 34), which is different from the monoclinic and hexagonal phase, our study first establishes that the phase separation in monoclinic and hexagonal fractions can be excluded for the investigated system.

Also, the rhombohedral phase was measured again after three years, and it was discovered to remain stable for at least this period of time. Second, as the number of sub-oxide signals Hf^{x+} (perhaps Hf^{3+}, Hf^{2+}, or Hf^{1+}) is small in comparison to the amount of Hf^{4+} states, the production of a crystalline sub-oxide phase with a single oxidation state can likely be ruled out for r-HfO_{2-x}. If the intrinsic oxidation state was drastically transformed from Hf^{4+} (HfO_2) to, say, Hf^{3+} (as for the example Hf_2O_3), one would expect a significant shift towards lower binding energies for the majority of the Hf 4f signal.

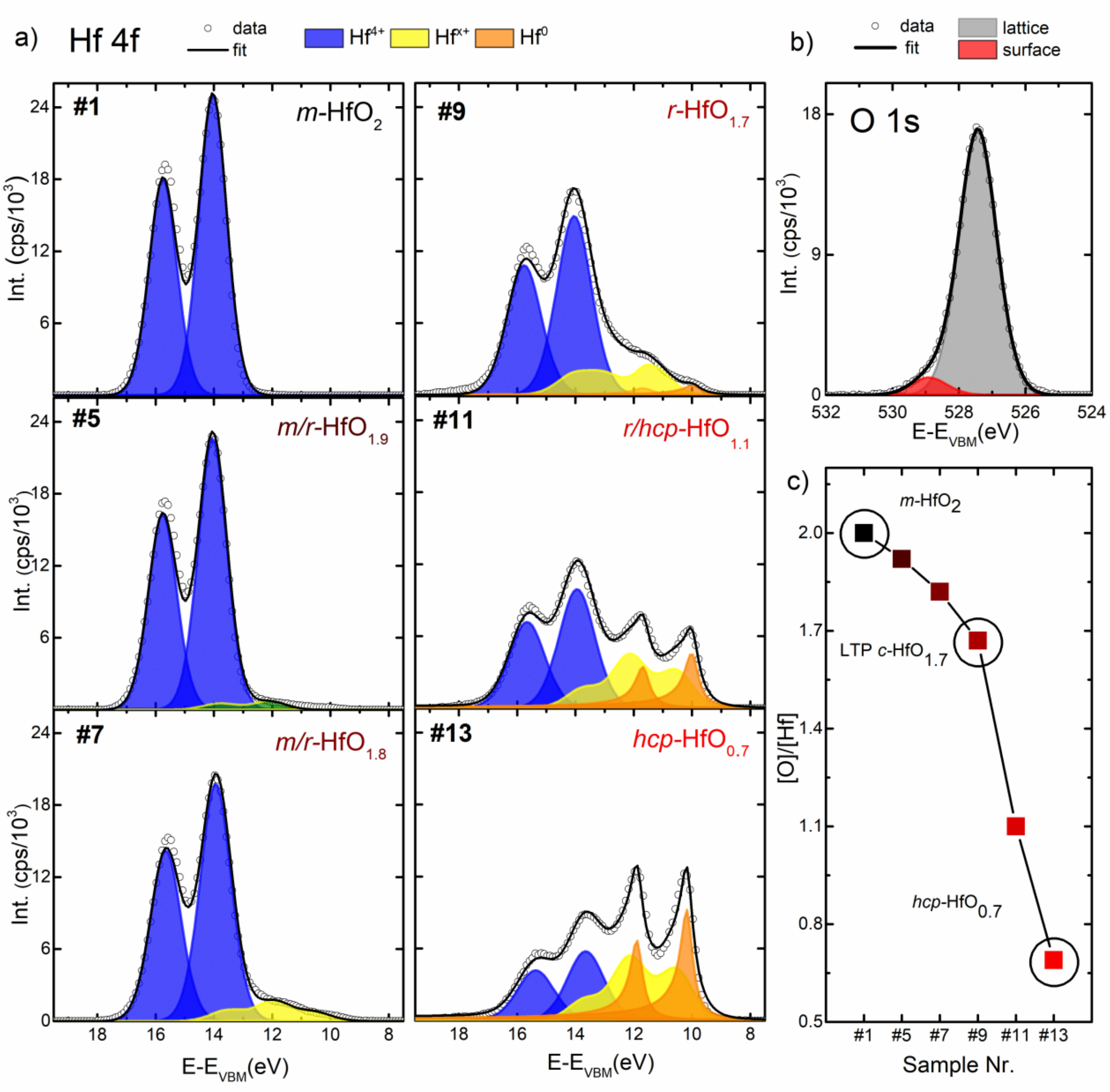

Figure 42: In-vacuo XPS spectra of selected oxygen deficient hafnium oxide thin films in dependence of their oxidation conditions over the complete series (from #1 to #13). a) shows the Hf 4f emission lines where sample #1 could be fitted with a single Hf^{4+} doublet showing close to stoichiometric composition. With decreasing oxidation conditions additional Hf^{x+} signals show up while for most deficient samples clear Hf^{0} contributions show up. b) shows a O 1s spectra of sample #9 which is representative for the whole series with a clear main contribution from lattice oxygen and a small shoulder indicating traces of surface adsorbates e.g. in form of residual water in the load lock. C) shows the stoichiometry estimate of the corresponding samples as obtained from area matching of the Hf 4f lines and the O 1s lattice contribution. Reprinted with minor changes with permission from reference [146]. https://doi.org/10.1021/acsami.1c09451 Copyright © 2021 American Chemical Society.

As an alternative, one may expect a substantial transformation of the O 2p valence band, which appears to be almost identical between *m*-HfO$_2$ #1 and *r*-HfO$_{1.7}$ #9. (see chapter 3.6). Instead, the similarity of the Hf 4f core and O 2p valence band signals between the two structures emphasizes their chemical similarity and supports the stabilization of *r*-HfO$_{1.7}$ #9 as a related symmetry variation of the monoclinic structure.

As is clear from the discussion up to this point, oxygen vacancy defects stabilize the *r*-HfO$_{2\text{-}x}$ phase. To identify the ideal oxygen vacancy defect density for the phase stabilization and to give absolute values of oxygen content for the analyzed series, area matching of the Hf 4f and

O 1s (lattice) emission lines has been conducted. Figure 42 b) shows an O 1s spectra which is representative for all samples from *r*-$HfO_{1.7}$ #9. For all corresponding spectra, two Gaussian-Lorentzian functions were necessary to fit the O 1s profile, with the low-energy component being attributed to traces of surface oxygen, such as hydroxyl groups from traces of leftover water in the vacuum transfer or load lock.[156] Therefore, just the lattice oxygen component has been taken into account for stoichiometry estimation. Figure 42 c) displays the sample series' estimated oxygen content plotted against the oxidation conditions. It reveals a steady trend in the atomic ratio, which ranges from [O]/[Hf] = 2 for *m*-HfO_2 (#1) to 1.7 for *r*-$HfO_{1.7}$ (#9) to 0.7 for *hcp*-$HfO_{0.7}$ (#13).Additionally, the development of the XRR density illustrated in Figure 35 b) (page 54) coincides with the oxygen content. While there is a correlation between the oxygen concentration and XRR density from the most oxidized *m*-HfO_2 sample #1 to *r*-$HfO_{1.7}$ #9, the transition to hexagonal *hcp*-$HfO_{0.7}$ #13 shows a more rapid shift for both parameters. This incremental dependency can be explained by two mechanisms. First, defect induced lattice relaxations and second, the proportional transformation to a higher density bravais lattice. For both scenarios the average distance between the heavy cations would be gradually reduced.

The oxygen concentration of the most-pure rhombohedral phase (LTP *c*-$HfO_{1.7}$, sample #9) is calculated to be [O]/[Hf] = 1.7. (see Figure 4c). This translates to around 1.2 oxygen vacancies per unit cell for a (pseudo-)cubic structure with four hafnium- and eight oxygen-ions. From this a defect density of 9.8×10^{21} cm^{-3} can be computed by assuming the unit cell volume of 122.54 $Å^3$ as determined from the XRD investigation in 4.1.2. The most deficient sample *hcp*-$HfO_{0.7}$ (#13) has a significant quantity of oxygen for the hexagonal structure with a composition [O]/[Hf] = 0.7. Only experimental evidence of hexagonal structures with compositions up to Hf_6O have been published so far. [65] Nonetheless, in the case of Hf_6O, oxygen is estimated to occupy just one-fifth of the hexagonal matrix's available octahedral sites. [74] As a result, the hexagonal structure would still provide enough octahedral sites to accommodate all of the oxygen observed for *hcp*-$HfO_{0.7}$ (sample #13). Modeling predicts hexagonal structures as the most likely metastable phases up to at least [O]/[Hf] = 0.5 via oxygen intercalation at octahedral locations, which supports this. [66, 67, 74] The experimental results given here demonstrate that the hexagonal structure of HfO_{2-x} can truly accommodate such large quantities of oxygen.

4.1.4. Oxygen Vacancy Induced P-Type Conduction

As significant oxygen deficiency is known to promote conduction in transition metal oxides, the studied materials have been investigated by means of resistivity and Hall effect measurements. Special thanks to Dr. Alexey Arzumanov who assisted with the electrical measurements and performed the Hall effect measurements with corresponding data analysis. In order to eliminate contact resistances, the resistivity of the samples under investigation was measured in van der Pauw geometry and is shown in Figure 43. The samples #1 through #3, which are the most oxidized, have large resistivity's and could not be measured due to a limit of 10^{-2} Ωm, however samples #4 through #13 exhibit a steady decline in resistivity over an order of magnitude. Therefore, as a result of oxygen engineering, the overall resistivity changes dramatically from 10^{10} Ωm for stoichiometric *m*-HfO_2 #1 [63] over 10^{-4} Ωm for *r*-HfO_{2-x} to $7.3*10^{-6}$ Ωm for *hcp*-$HfO_{0.7}$ #13.

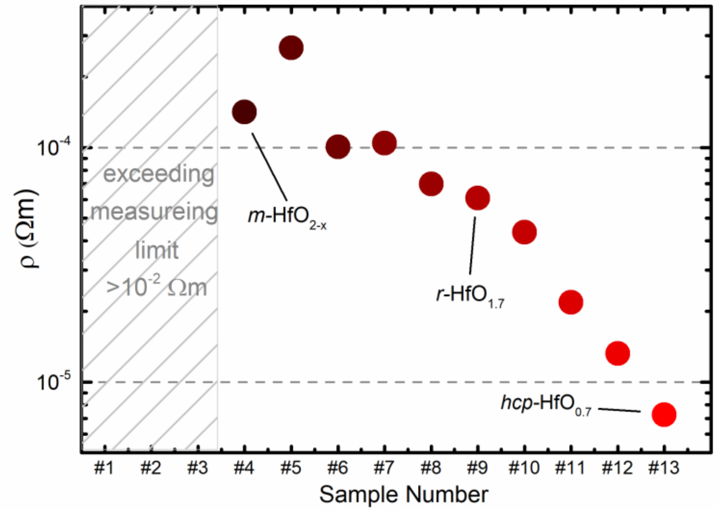

Figure 43: Van der Paw resistivity of the hafnium oxide series in dependence of oxidation conditions (from most oxidized sample #1 to most deficient sample #13) . Note that the monoclinic samples #1 to #3 grown under most oxidizing conditions could not be measured which is expected for close to stoichiometric hafnia. However, in the vicinity of the phase transition from monoclinic to rhombohedral structure the samples show significant conductivity with a measureable decline of about one order of magnitude between *r*-$HfO_{1.7}$ and *hcp*-$HfO_{0.7}$. Reprinted with minor changes with permission from reference [146]. https://doi.org/10.1021/acsami.1c09451 Copyright © 2021 American Chemical Society.

While all *r*-HfO_{2-x}-containing thin films (samples #5 - #11) exhibit conducting behavior, even *m*-HfO_{2-x} #4 with no obvious *r*-HfO_{2-x} contributions (see Figure 34, page 53) shows a similar resistivity. This shows that the drop in resistivity is mostly caused by defects rather than a change in crystal structure. The reported conductivity for *m*-HfO_{2-x} is consistent with previous research on MBE produced HfO_{2-x} at elevated temperatures (700 °C), where similar variations in resistivity in dependence of oxidation conditions were shown for monoclinic thin films only. [62, 63]

Figure 44 depicts the charge carrier characteristics derived from Hall effect measurements. All of the studied *r*-HfO_{2-x}, *r/hcp*-HfO_{2-x} and *hcp*-HfO_{2-x} samples have positive Hall coefficients, indicating, that holes are the majority charge carriers. The charge carrier concentration for *r*-HfO_{2-x} #9 is 5.8×10^{21} cm^{-3} with a charge carrier mobility of 0.18 $cm^2V^{-1}s^{-1}$. It is worth noting that the XPS estimated defect density of 9.8×10^{21} cm^{-3} (see previous chapter 4.1.3) for *r*-HfO_{2-x} #9 is within the charge carrier concentration range, implying 0.6 free charge carriers per oxygen vacancy.

The measured values correspond well with previous Hall effect studies on deficient monoclinic HfO_{2-x} samples. Hildebrand et al. [62, 63] discovered *p*-type conductivity with charge carrier concentrations of 6×10^{21} cm^{-3} and mobilities of $2\ cm^2V^{-1}s^{-1}$,, whereas Hadacek et al. [157] reported *p*-type charge carriers with concentrations of $10^{22}\ cm^{-3}$ and $1\ cm^2V^{-1}s^{-1}$, respectively. It is worth noting that the charge carrier density is about one to two orders of magnitude greater than in other p-type semiconductors such as (Ga,Mn)As or (Zn,Mn)Te with normal doping concentrations. [157, 158] At the same time, charge carrier mobilities in semiconductors are substantially lower (by two to three orders of magnitude) than normal hole mobilities.

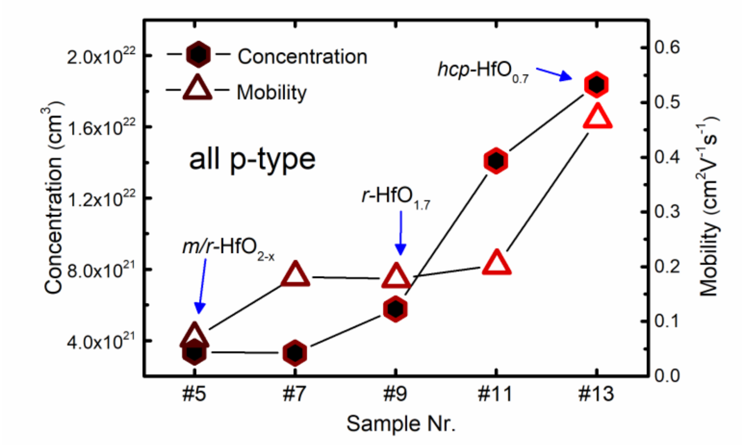

Figure 44: All measured samples show positive Hall coefficients, indicating holes as majority-charge carriers. Note that the measurements reveal consistent trends with oxygen content for both, charge charrier concentrations and mobilities. Reprinted with minor changes with permission from reference [146]. https://doi.org/10.1021/acsami.1c09451 Copyright © 2021 American Chemical Society.

The resistivity-temperature dependencies of the samples *r*-$HfO_{1.7}$ #9 and *hcp*-$HfO_{0.7}$ #13 are shown in Figure 45. Both samples exhibit semiconducting characteristics. Notably, even the sample with the least oxygen content in the series, *hcp*-$HfO_{0.7}$ #13, which has a hexagonal crystal structure comparable to metallic Hf (see Figure 34, page 53), does not exhibit metallic behavior. Additionally, the resistivity of *hcp*-$HfO_{0.7}$ #13 at room temperature is about 20 times greater than that of metallic Hf ($3.2\times10^{-7}\ \Omega m$ [159]), measuring $7.3\cdot10^{-6}\ \Omega m$. Because *hcp*-$HfO_{0.7}$ contains a considerable amount of oxygen, as revealed by XPS (compare Figure 42, page 64) and verified by the low XRR density (see Figure 35, page 54), the formation of a continuous metallic 5d band is likely prevented. The Hf 4f spectra (see Figure 42, page 64), which do not only display metallic Hf^0 states, but also significant levels of Hf^{4+} and sub-oxide Hf^{x+} oxidation states, provide additional support for this argument.

As both, *r*-$HfO_{1.7}$ as well as *hcp*-$HfO_{0.7}$ show significant electrical conductivity, those phases need to be considered as potential candidates to be formed as the conducting filament in RRAM. Especially as the conductivity is induced through oxygen deficiency, those findings correspond well with the famous model of the valence change mechanism. Further as the significant conduction is induced in the vicinity of the phase transition from *m*-HfO_2 to *r*-$HfO_{1.7}$, it is reasonable to assume forming free devices in this transitional region between sample #1 and #4 (compare Figure 43).

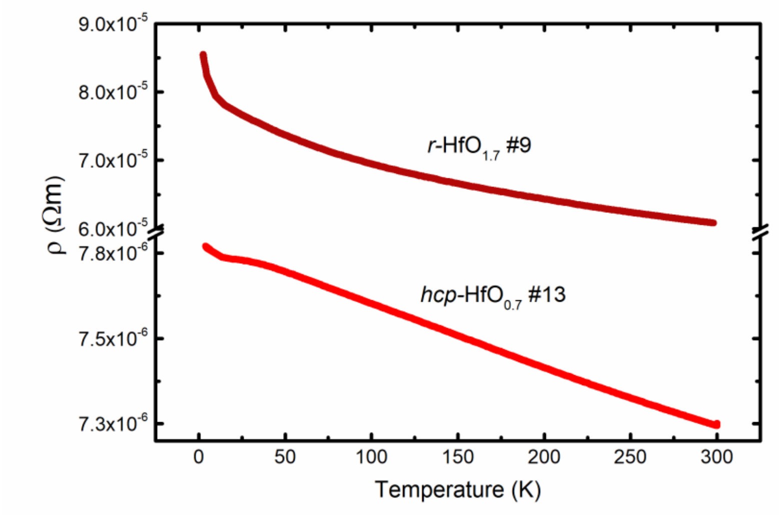

Figure 45: Resistivity of the conducting key phases *r*-$HfO_{1.7}$ and *hcp*-$HfO_{0.7}$ measured in dependence of the thin film temperature. Note that both show increasing resistivity at lower temperatures, following semiconducting behavior. The curves do not indicate metallic properties, even for the most deficient *hcp*-$HfO_{0.7}$ phase. Reprinted with minor changes with permission from reference [146]. https://doi.org/10.1021/acsami.1c09451 Copyright © 2021 American Chemical Society.

4.1.5. Optical Absorption and Bandgap Properties

UV/Vis transmission and XPS valence band measurements were performed on the samples to gain a better understanding of the band structure and electrical characteristics. All samples studied by XPS were subjected to transmission spectroscopy experiments ranging from ~ 800 nm to 190 nm as displayed in Figure 46. An Agilent Carry 7000 UV-Vis system was used for the optical measurements. The samples were tested in transmission and single beam mode. The overall spectrum as depicted in Figure 46 a) already shows a clear trend of decreased transmission with decreasing oxidation conditions. Further, Figure 46 a) shows the low wavelength (high energy) region in which the absorption slopes can be seen. Take note of the twofold absorption property, which is only seen in monoclinic hafnia (compare chapter 2.4; specifically Figure 23, page 32).

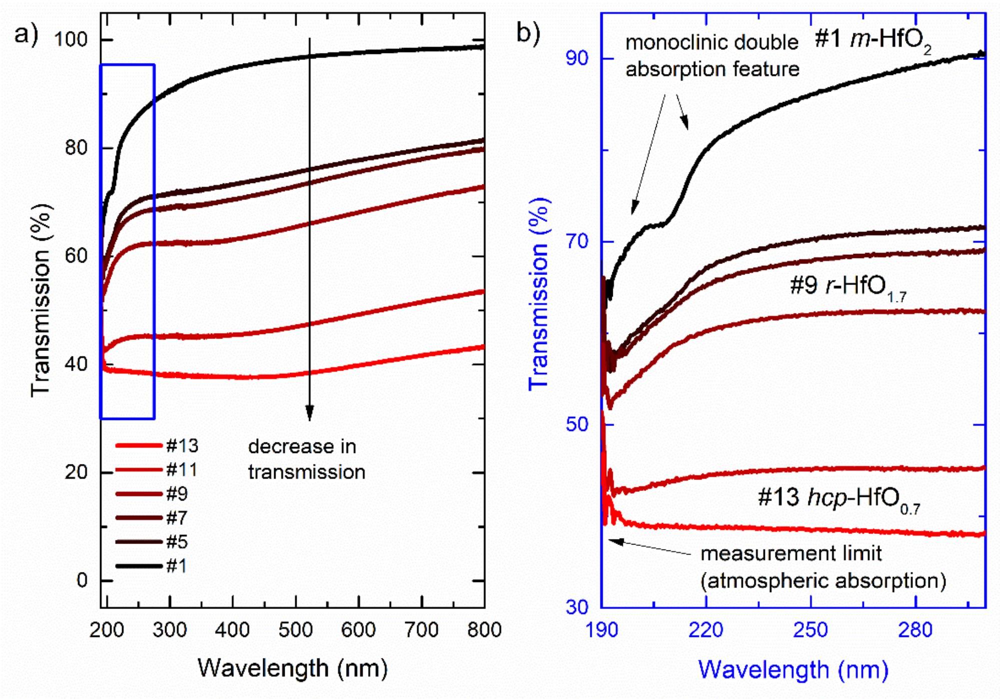

Figure 46: Transmission spectroscopy raw data on the oxidation dependent hafnium oxide series on sapphire with a) showing the complete range, clearly demonstrating a decrease in the overall transmission for lower oxygen content and b) showing the region of interest for occurring absorption slopes. Note of the twofold absorption feature, which appears exclusively in monoclinic hafnia. The measurement is limit to around 190 nm due to atmospheric absorption as indicated by the noise appearing below 200 nm.

In order to obtain a better approximation for the isolated thin film spectra, the substrate transmission was measured individually and subtracted. Also, the absorption coefficient was calculated directly from the transmission spectra (without reflection) by considering the individual film thickness of 20 ± 2 nm. The famous method of bandgap evaluation via Tauc-plot, represents the well-known relation between absorption α, energy hν, bandgap E_g and corresponding slope A which reads as follows:

$$(\alpha h\nu)^{1/n} = A \cdot (h\nu - E_g) \qquad (41)$$

With n = ½ allowed direct and n = 2 for allowed indirect transitions. Several DFT models demonstrate that stoichiometric monoclinic hafnium oxide is an indirect semiconductor by definition, while at the same time showing an insignificant energetic degeneracy between direct and indirect transitions. [40, 120, 121] Also, for calculated cubic and tetragonal phases of hafnium oxide a similar energetic degeneracy was observed. [40, 120, 121] Therefore, in Figure 47 both plots, considering a) indirect, but also for direct b) transitions are displayed.

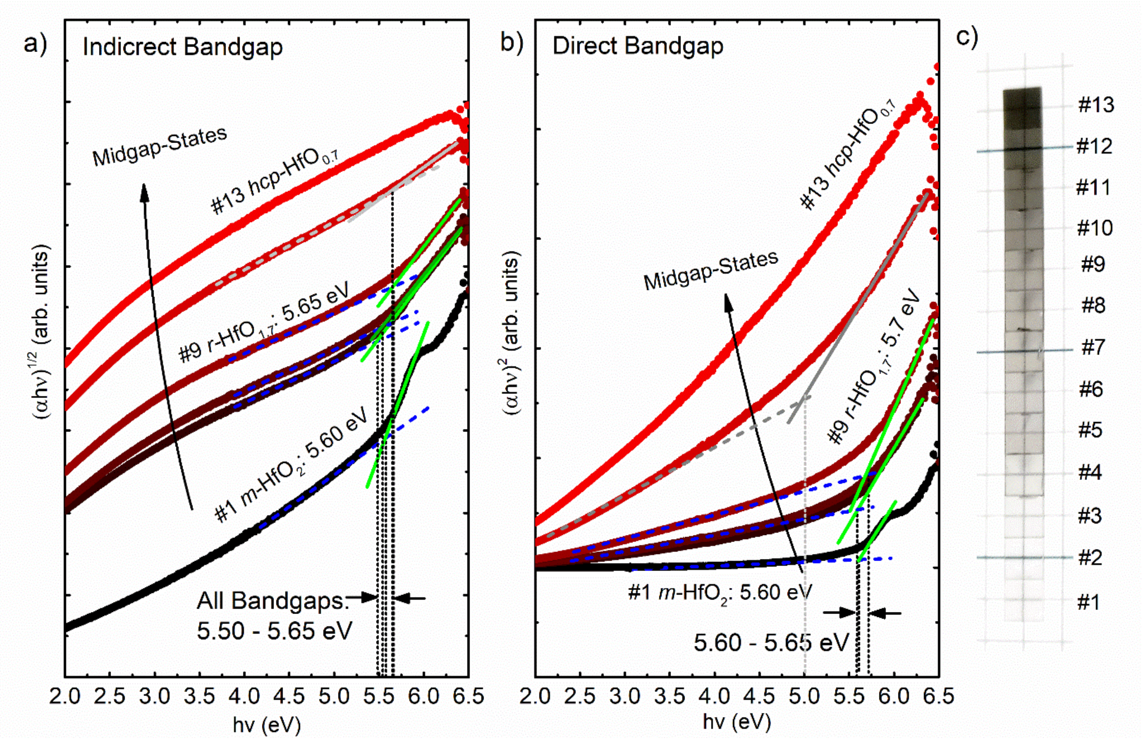

Figure 47: Bandgap estimation via Tauc plot in representation for a) indirect and b) direct bandgap. Both show similar bandgap values for *m*-HfO_2 as well as *r*-$HfO_{1.7}$ c) shows the gradual visual darkening of the sample series. Reprinted in parts with permission from reference [146]. https://doi.org/10.1021/acsami.1c09451 Copyright © 2021 American Chemical Society.

All of the deficient samples that have been studied have at most a single, recognizable optical absorption edge, whereas *m*-HfO_2 (#1) has a second absorption shoulder at higher energies which clearly translates from the transmission spectra into both plots. Although there are several theories concerning the precise origin of this characteristic, it is attributed to the monoclinic structure since it only manifests when amorphous hafnium oxide crystallizes in this structure (compare chapter 2.4).[117, 119, 122] The findings of the presented series support the notion that this twofold absorption property is in fact an inherent long-range order effect of the monoclinic structure. This is due to the observation, that other examined samples that aren't monoclinic, namely mixtures of monoclinic-rhombohedral, rhombohedral and rhombohedral-hexagonal structures, exhibit only one absorption slope.

After subtracting substrate contributions, a baseline below the relevant absorption edge is clearly visible in all spectra. The definite increase in baseline absorption can be assigned to the continuous increase of oxygen vacancy induced defect states in the bandgap region as will be discussed later (compare Figure 48). This conclusion is further supported by the samples' visual appearance, which is shown in Figure 47 c). As the oxygen deficiency increases, the samples gradually darken, going from seeming transparent for *m*-HfO_2 #1 to virtually opaque with *hcp*-$HfO_{0.7}$ #13. For *m*-HfO_2 #1 however, no defect states are visible in the bandgap region as monitored by XPS. Therefore, the baseline is most likely the consequence of a change in the reflection or scattering of the sapphire substrate when it is covered by the hafnia thin film. [160] In any case, it is vital to consider how each baseline contributes. Thus, underestimating bandgaps in the presence of a baseline by immediately extending the linear absorption slope to the abscissa is a typical error which can lead to large deviations from the real value. More information on consistent bandgap analysis is provided in chapter 2.4. Figure 47 a & b) illustrate a correct approach for estimating the bandgap by extrapolating the bandgap slope (green) to the extrapolated baseline (blue), which takes the effects of the baseline into account.[160, 161] When this approach is applied to optical spectra, bandgaps in the range of 5.5 eV to 5.65 eV are discovered for all materials, assuming indirect bandgaps, while 5.0 eV to 5.65 eV are found assuming direct bandgaps. Please keep in mind that the presence of a baseline is always associated with higher uncertainty. While the plot for indirect transitions allows for a better distinction of the baseline versus the absorption slope (and therefore higher accuracy), the representation for direct bandgap absorption exhibits a less defined transition.

The bandgap of 5.6 eV for stoichiometric sample *m*-HfO_2 #1 which is the same in both the indirect and direct Tauc representation is in good accordance with literature. [115, 116, 118, 119] Similarly a bandgap of 5.65 eV in indirect representation (5.7 eV for assuming a direct bandgap) may be derived from the most isolated rhombohedral sample *r*-$HfO_{1.7}$ #9, which is near to the bandgap of stoichiometric hafnia. It is worth noting that the energy degeneracy between direct and indirect bandgaps is in good agreement with the previously described theoretical predictions, indicating that direct and indirect transitions in hafnium oxides are almost equivalent. [40, 120, 121] Note that the bandgap shows hardly any change from *m*-HfO_2 #1 to *r*-$HfO_{1.7}$ #9 (and in indirect representation even towards *hcp*-$HfO_{0.7}$). This shows that the energetic differences of the main optical transitions are not significantly influenced by the additional defect states that are introduced by oxygen deficiency.

Furthermore, the morphology of the valence band (predominantly O 2p), as shown in Figure 48, appears to be unaltered from *m*-HfO_2 #1 to *r*-$HfO_{1.7}$ #9. This similarity in band gap and the O 2p band likely reflects the similarities of both crystal structures, and it further supports the hypothesis of oxygen vacancy stabilization of rhombohedral hafnium oxide (as discussed in the previous chapter 4.1.3). The intensity and shape of the O 2p band only begin to alter clearly toward *hcp*-$HfO_{0.7}$ due to increasing oxygen deprivation and more drastic crystalline modifications.

A more significant change over the whole series can be seen in the dramatic change of the midgap states which clearly increase already in the vicinity between monoclinic and rhombohedral transformation. Figure 48 indicates the reference position of the valence band maximum (E_{VBM}) to the conduction band minimum (E_{CBM}) which is separated by about 5.65 eV for the rhombohedral structure (5.6 eV for the monoclinic phase) as estimated from the Tauc plot analysis. While no defect states are observed in the bandgap region for the most oxidized sample #1 (further confirming the stoichiometric composition of sample #1), midgap states begin to arise and steadily grow in the bandgap region beginning with sample #5. These findings are quite consistent with the results obtained on amorphous systems by Perevalov et al., who reported via XPS that Ar^+ bombardment of HfO_2 promotes the development of such states roughly 3 eV above the valence band. [162] Because ion etching of hafnia preferentially ablates oxygen, the presence of oxygen vacancies as the source of these observations is supported.

However, in this energy region, instead of a vacancy defect band, the creation of a metallic 5d represents an alternative scenario. [163, 164] Nonetheless, because the metallic Hf^0 contribution in *r*-$HfO_{1.7}$ #9 is small in comparison to the Hf^{4+} and Hf^{x+} suboxide contributions, the bulk of midgap-states up to the *r*-$HfO_{1.7}$ phase may be ascribed to oxygen vacancy defects.

Indeed, numerous simulations on HfO_2 demonstrate that the existence of vacancies is followed with the development of such states deep in the band gap like 3 eV above the VBM. [68, 71, 72] Nonetheless, these estimates are almost entirely predicated assuming low oxygen vacancy densities. Higher defect concentrations, such as 1.2 vacancies per cubic unit cell seen in sample *r*-$HfO_{1.7}$ #9 (see chapter 3.3), necessitate the consideration of defect interactions. [162] The incremental increase and evident spread of states over the midgap-region implies the establishment of a wide oxygen-vacancy defect band.

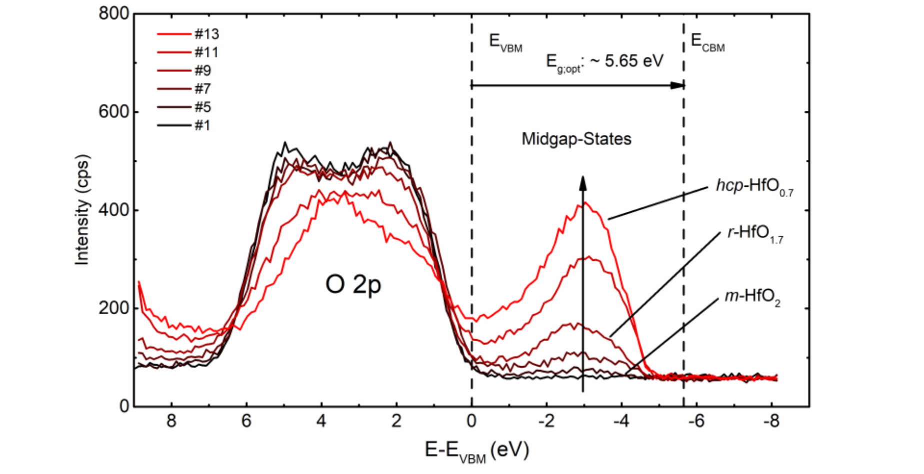

Figure 48: Valence band spectra of the oxidation dependent series with the indicated reference point of E_{VBM}. Note that the conduction band minimum reference E_{CBM} is placed above the E_{VBM} by 5.65 eV consistently with the observed bandgap od rhombohedral hafnium oxide (5.6 eV for monoclinic. Note that while there is a significant increase in midgap DOS over the whole series, the valence band appears almost unchanged from the monoclinic to rhombohedral transformation and only changes significantly towards *hcp*-$HfO_{0.7}$. Reprinted with permission from reference [146]. https://doi.org/10.1021/acsami.1c09451 Copyright © 2021 American Chemical Society.

The steady increase in the midgap density of states (DOS) for all deficient thin films, containing either *r*-HfO_{2-x} and/or *hcp*-HfO_{2-x}, is consistent with the scaling of charge carrier concentrations and conductivity for those phases (see chapter 4.1.4), identifying this defect band as the primary reason of emergent electrical conductivity. The presence of states in the area above the valence band and near to the Fermi-level, in particular, agrees well with the observed p-type conduction, as discussed in further detail in chapter 4.1.7.

4.1.6. Microstructure and Homogeneity of the Crystal Phases

While the homogeneous distribution of oxygen vacancy defect states in the crystalline matrix has been presumed as the origin of the emerging conductivity so far, other hypotheses that need to be considered include the possibility of the formation of an inhomogeneous percolation path for amorphous metallic or sub-oxide clusters. [62, 153] Metallic clusters in more oxidized materials (from monoclinic to rhombohedral hafnium oxide) may be ruled out since photoelectron spectroscopy reveals no significant metallic Hf^0 states in the Hf 4f spectra (see Figure 4 a). However, only microscopic techniques can confirm or rule out whether conducting amorphous sub-oxide phases are present. Figure 6 presents images of the key materials *m*-HfO_2 (a), *r*-$HfO_{1.7}$ (b) and *hcp*-$HfO_{0.7}$ (c) of the series taken via a high-resolution transmission electron microscope (HRTEM). For TEM preparation, the thin films are capped via a sputtered platinum layers (dark contrast, bottom right). The bright region on the top left shows the c-cut sapphire substrates.

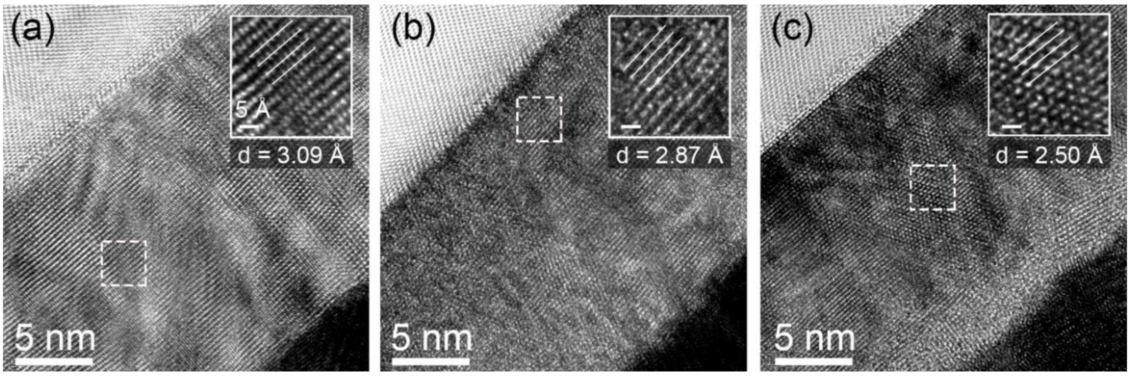

Figure 49: TEM phase contrast images of (a) *m*-HfO_2 #1 , (b) LTP *c*-$HfO_{1.7}$ #9 and (c) *hcp*-$Hf_{0.7}$with atomic resolution showing homogeneous crystallinity for all samples. The bright contrast represents the sapphire substrate, while the dark contrast is a platinum capping layer for TEM preparation. The insets (showing blow ups of the regions marked by dashed boxes) show the FFT extracted lattice parameters of the hafnium oxide thin films which are in good agreement to the XRD measured out of plane lattice constants for any crystal structure respectively. Reprinted with permission from reference [146]. https://doi.org/10.1021/acsami.1c09451 Copyright © 2021 American Chemical Society.

Fast Fourier Transformation (FFT) analysis was used to extract the out-of-plane lattice parameters of the samples, which are marked in the insets of Figure 49 (a), (b), and (c) with 3.09 Å, 2.87 Å and 2.50 Å for *m*-HfO_2 #1, *r*-$HfO_{1.7}$ #9 and *hcp*-$HfO_{0.7}$ #13, respectively. The FFT derived values correlate well with the lattice parameters retrieved from the XRD reflections (3.15 Å, 2.92 Å and 2.55 Å), confirming the highly textured nature of the thin films. More specifically, the observed HRTEM images resemble the XRD estimated growth directions of [-111] for *m*-HfO_2 #1, [111] for *r*-$HfO_{1.7}$ #9, and [002] for *hcp*-$HfO_{0.7}$ #13. (compare Figure 34, page 53).

Further, regarding the microstructure, Figure 49 depicts single crystalline domains with diameters of many tens of nanometers. Note that for *hcp*-$HfO_{0.7}$ a ~ 4 nm layer appears amorphous on the surface of the HfO_{2-x} layer. This can be explained by the effect of surface oxidation (as the Pt-layer was deposited after exposure to atmosphere). Besides this effect, high resolution contrast found across the layers, verifies the homogeneous crystallinity of all hafnium oxide thin films, ruling out amorphous metallic or sub-oxide clusters. In this context the data shows no indication for a percolation path and suggests a homogenous distribution of oxygen vacancy defects in the observed crystalline structures. Therefore, the appearance of conductivity can be understood as a material property of *r*-$HfO_{1.7}$ and *hcp*-$HfO_{0.7}$.

4.1.7. Band Structure Model from Hafnia to Hafnium

On the basis of all previously presented data from XRD (chapter 4.1.1 & 4.1.2), XPS (chapter 4.1.3 & 4.1.5), electrical and Hall effect measurements (chapter 4.1.4), UV/Vis transmission measurements (chapter 4.1.5) and HRTEM imaging (chapter 4.1.6) a simplified band structure model over the whole oxidation range from stoichiometric monoclinic hafnia to metallic hafnium is summarized in Figure 50 and will be discussed in the following. VESTA [165] was used to model the key structures for *m*-HfO$_2$, *r*-HfO$_{1.7}$ and *hcp*-Hf, which are based on powder diffraction data for monoclinic and cubic hafnium oxide, as well as hexagonal hafnium, as indicated in chapter 4.1.1. As the rhombohedral structure is of a pseudocubic form, the cubic powder diffraction file was taken as reference. As described in chapter 3.3, the structure of *hcp*-HfO$_{0.7}$ is modeled using the *hcp*-Hf structure with oxygen occupying octahedral sites. Note that the atomic positions of oxygen are assigned to occupation fractions in accordance to the atomic ratio estimated via XPS.

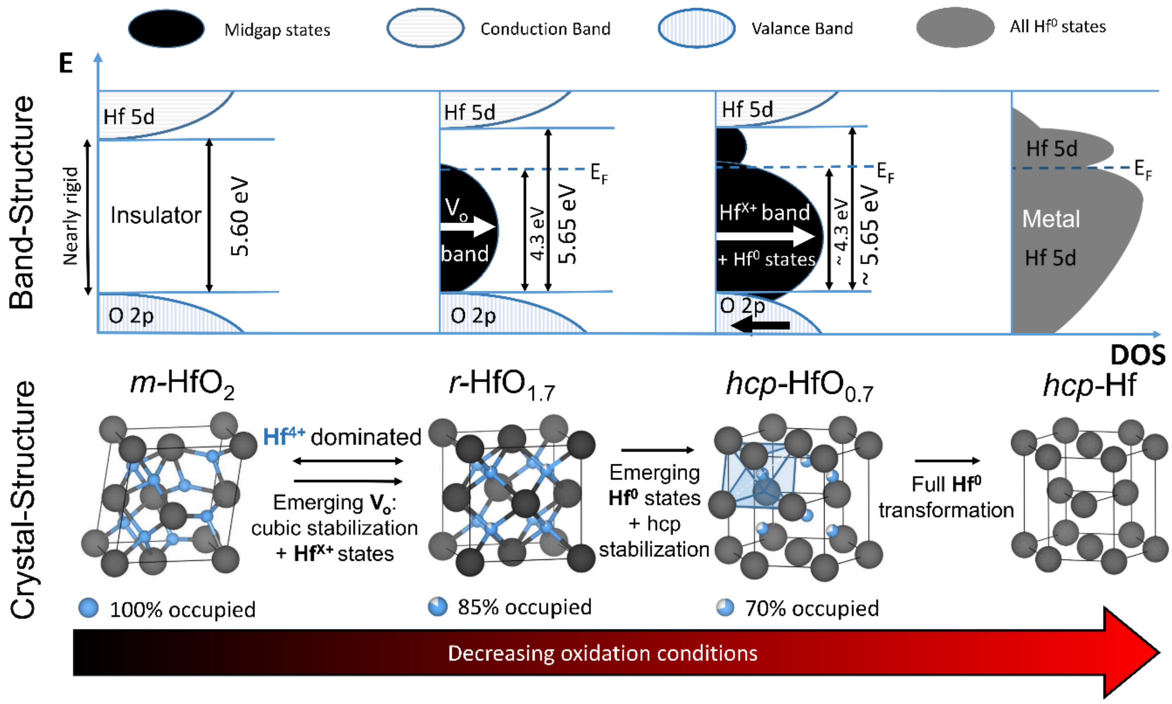

Figure 50: Model of the electronic structure for the whole oxidation range, from stoichiometric hafnia to metallic hafnium. As representative phases, the synthesized key structures of *m*-HfO2, *r*-HfO$_{1.7}$, and *hcp*-HfO$_{0.7}$ are shown. The development of a midgap defect band between O 2p and Hf 5d states, mainly below the Fermi level, is revealed as the key mechanism for emergent *p*-type conductivity throughout the series. Note that the band gaps between the O 2p valence states and the Hf 5d conduction band remain virtually unchanged especially from *m*-HfO$_2$ to r-HfO$_{1.7}$ and only change dramatically towards *hcp*-Hf. Reprinted with minor changes with permission from reference [146]. Copyright © 2021 https://doi.org/10.1021/acsami.1c09451 American Chemical Society.

m-HfO$_2$ is well known to be a transparent insulator with a bandgap of approximately 5.6 eV. [115, 116, 118, 119] For stoichiometric monoclinic hafnia the valence band is dominated by localized oxygen 2p orbitals, whereas the conduction band is governed by Hf 5d states. [40] Oxygen vacancies are induced into the crystalline matrix when oxidation conditions decrease, resulting in the creation of oxygen vacancy (Vo) defect states (followed by the emergence of Hf^{x+} signals) and the subsequent stabilization of *r*-HfO$_{1.7}$ (see chapter 4.1.3). The formation of a continuous defect band for *r*-HfO$_{1.7}$ is implied from XPS valence spectra and since the required defect density for complete stabilization is estimated as high as 1.2 vacancies per unit cell (or 9.6×10^{21} cm^{-3}; compare chapter 4.1.3).

While the Vo defect band is forming, the shape of the O 2p band and the optical bandgap between O 2p and Hf 5d remain practically unchanged (compare Figure 47 & Figure 48). This high likeness can be considered a consequence from the similarity of the monoclinic and the (pseudocubic) rhombohedral structure (see Figure 50).

The oxygen vacancy defect band (Vo) reaches from the O 2p valence band to at least the fermi level position (see Figure 48). Note that the fermi level position for *r*-$HfO_{1.7}$ was taken from a gold calibrated measurement on reference sample which was grown on a conducting TiN/Si substrate as the insulating nature of the used sapphire substrates does not allow for a reliable calibration (even with dual beam charge neutralization). The assumption that not many defect-states exist at energies greater than the Fermi level is hypothetical (since photoelectron spectroscopy is confined to states below the Fermi level) and is based on the samples' p-type conducting nature. Given that holes are the majority charge carriers, it is plausible to expect at least less defect states to be present in this energy region.[123]

The development of the Vo defect band in the energy area between the O 2p band and the Fermi level overcomes two major causes for the scarcity of p-type conditions in oxides: On the one hand, the valence band's generally lower energy position, [166] on the other hand, localized O 2p orbitals as valence band maximum (VBM). Most oxides have flat O 2p bands, which result in high effective hole masses and disqualify them as p-type conductors. [166, 167] In this series, the midgap band functions almost as a quasi-valence band, moving its VBM near to the Fermi level. Furthermore, the V_o band, which is likely associated to a non-metallic Hf 5d[163], basically replaces the O 2p band, which should provide larger hole mobilities.

When the oxidation conditions are reduced further, a large quantity of metallic Hf^0 states arise, stabilizing the structure of *hcp*-$HfO_{0.7}$. Despite the fact that the phase still contains Hf^{x+} ($0 < x < 4$) and even Hf^{4+} contributions, the HRTEM phase contrast supports its homogeneous crystallinity. This is supported by several publications, which predicted the existence of oxygen-rich hexagonal hafnium oxide. [66, 67, 74] When the valence band spectra of *hcp*-$HfO_{0.7}$ are compared to spectra of simply metallic *hcp*-Hf, it becomes clear that this phase shows indeed different properties than plain hafnium.

While the value of the "bandgap" between O 2p and the conduction band can only be hypothesized for *hcp*-$HfO_{0.7}$ (due to the intensity of the optical baseline signal), the trend of the other samples supports a consistent value of about 5.6 eV (or 5.0 eV for the direct bandgap of *r/hcp*-HfO_{2-x}). In any case, the similarities in the XPS valence spectra (see Figure 48) suggest a comparable value of 4.3 eV above the O 2p band for the Fermi level location. Further, *hcp*-$HfO_{0.7}$ still exhibits no metallic temperature dependency but also p-type conductivity (see Figure 44 & Figure 45). Therefore, it is plausible to anticipate a similar band structure as *r*-$HfO_{1.7}$ with rising, but still low DOS around the fermi level when compared to purely metallic Hf.

Because a large amount of Hf^0 states are found in the *hcp*-$HfO_{0.7}$ Hf 4f spectra (see Figure 42), the rising amount of midgap states (see Figure 48) would be partially provided by metallic (Hf^0) Hf 5d states. In conjunction the O 2p states are considerably reduced. As the transition to *hcp*-Hf is not fully facilitated, the conducting characteristics of *hcp*-$HfO_{0.7}$ are still highly influenced by oxygen, occupying the octahedral positions in the hexagonal close packed matrix of hafnium (compare chapter 4.1.3). [66, 67, 74] When the valence band spectra of *hcp*-$HfO_{0.7}$ are compared to spectra of simply metallic *hcp*-Hf, it is further supported that this phase shows indeed different properties than plain hafnium. Figure 8 depicts the band structure of metallic *hcp*-Hf based on XPS valence spectra and DFT calculations from the literature. [163, 164] The O 2p band noticeably disappeared, the valence band's maximum intensity is pushed towards the Fermi level, and the bandgap is completely filled by metallic Hf^0 states (mostly Hf 5d [163]).

To summarize, a complete band structure model that takes the gradual formation of defect bands between localized O 2p and Hf 5d orbitals in consideration was described. While the midgap states between *m*-HfO_2 and *r*-$HfO_{1.7}$ were associated to an oxygen vacancy band, additional Hf^0 states were suggested to contribute to the midgap states towards *hcp*-Hf. According to this model, the steady growth of these midgap states below the fermi level and the O 2p states is identified as the cause of increasing p-type conductivity, as these defect bands replace the low-energy and low-mobility O 2p orbitals as the effective valence band.

4.2. Ab-Initio Simulations on Substoichiometric Hafnium Oxide Compared to Experimental Results

This chapter is discussing the comparison of experimental and density functional theory based results on oxygen deficient hafnium oxide. Many of the discussed results and adapted figures are published particularly under "Kaiser, N., Song, Y.-J., Vogel, T., Piros, E., Kim, T., Schreyer, P., Petzold, S., Valentí, R., and Alff, L., Crystal and Electronic Structure of Oxygen Vacancy Stabilized Rhombohedral Hafnium Oxide. ACS Applied Electronic Materials, 2023. **5**(2): p.754-763"

While the previous chapter was exclusively discussing experimental results, this section is about the comparison of DFT based results with measurements. This work is a result of a close collaboration between TU Darmstadt and Goethe Universität Frankfurt and specifically between the work group of Prof. Valentí (Frankfurt, Institute for Theoretical Physics) and Prof. Alff (Darmstadt, Institute of Materials science). Special thanks to Young-Joon Song who performed the DFT calculations.

As mentioned in previous chapters, there are many DFT models of substoichiometric hafnium oxide such as Hf_2O_3, HfO, Hf_6O, [66, 67, 74, 76] however, there is no significant experimental evidence which could verify their crystal and/or bandstucture. As discussed in chapter 4.1, the phases r-$HfO_{1.7}$ and hcp-$HfO_{0.7}$ have been identified as intermediate phases between hafnia and hafnium. Here specifically the oxygen-content dependent phase transformation from the stoichiometric monoclinic to oxygen deficient rhombohedral hafnium oxide is further investigated via ab-initio methodology. In 4.2.1 total energy calculations further verify the previously proposed model that introduction of oxygen vacancies in the monoclinic structure leads to the stabilization of r-HfO_{2-x}. The following chapter 4.2.2 discusses the similarities between the calculated and the experimentally measured rhombohedral unit cell. In chapter 4.2.3 the calculated density of states of the valence band region of r-$HfO_{1.5}$ are compared to XPS and optical absorption measurements. And finally in 4.2.4 a more in detailed discussion on the calculated band structure including the orbital hybridization is presented.

4.2.1. DFT Simulations on the Formation of Rhombohedral Hafnium Oxide r-HfO_{2-x}

In order to compare the experimental results on the structural transformation from m-HfO_2 to r-$HfO_{1.7}$ with DFT simulations, total energy calculations have been conducted. For this purpose, structure relaxations on the monoclinic $P2_1/c$ and cubic reference structure $Fm\text{-}3m$ have been performed via generalized gradient approximation (GGA) [129, 130], using lattice parameters close to the experimental results. Since monoclinic and cubic HfO_2 unit cells contain of four hafnium cations and eight oxygen anions, it is straightforward to simulate compositions of $HfO_{1.75}$ and $HfO_{1.5}$ by removing one or two oxygen ions respectively. While there are eight ways to remove one oxygen ion for $HfO_{1.75,}$ due to symmetry reasons, the possibilities are reduced to one for the cubic and two for the monoclinic structure. For $HfO_{1.5}$ there are 28 oxygen vacancy combinations which are reduced to ten, considering the monoclinic symmetry and three for the cubic case. In order to relax the structures, volume, atomic positions as well as the shape of the cell have been iterated. Those calculations have been performed, using the projector augmented wave method [126] from the Vienna Ab Initio Simulation Package (VASP)[168]. Structural relaxations were conducted via GGA considering a 12 x 12 x 12 k-mesh until the Hellmann-Feyman forces fell below a threshold of 1 meV/Å.

Strikingly, the oxygen vacancies in the initial cubic unit cell induce a small rhombohedral transformation after full relaxation. As a consequence, the space groups of the deficient cubic structures c-$HfO_{1.75}$ and c-$HfO_{1.5}$ turn into the rhombohedral space group $R3m$. Also, due to small transformations deficient monoclinic structures m-$HfO_{1.75}$ and m-$HfO_{1.5}$ relax into lower symmetry triclinic structures (P1). To avoid confusion, the triclinic deformed unit cells will be referred to as "monoclinic" in the following since the differences between the monoclinic and triclinic structures are minimal (the exact structural parameters of all calculated phases are listed in

Table 5 at the end of this section). A direct comparison between the calculated and experimentally synthesized rhombohedral structure is given in chapter 4.2.2.

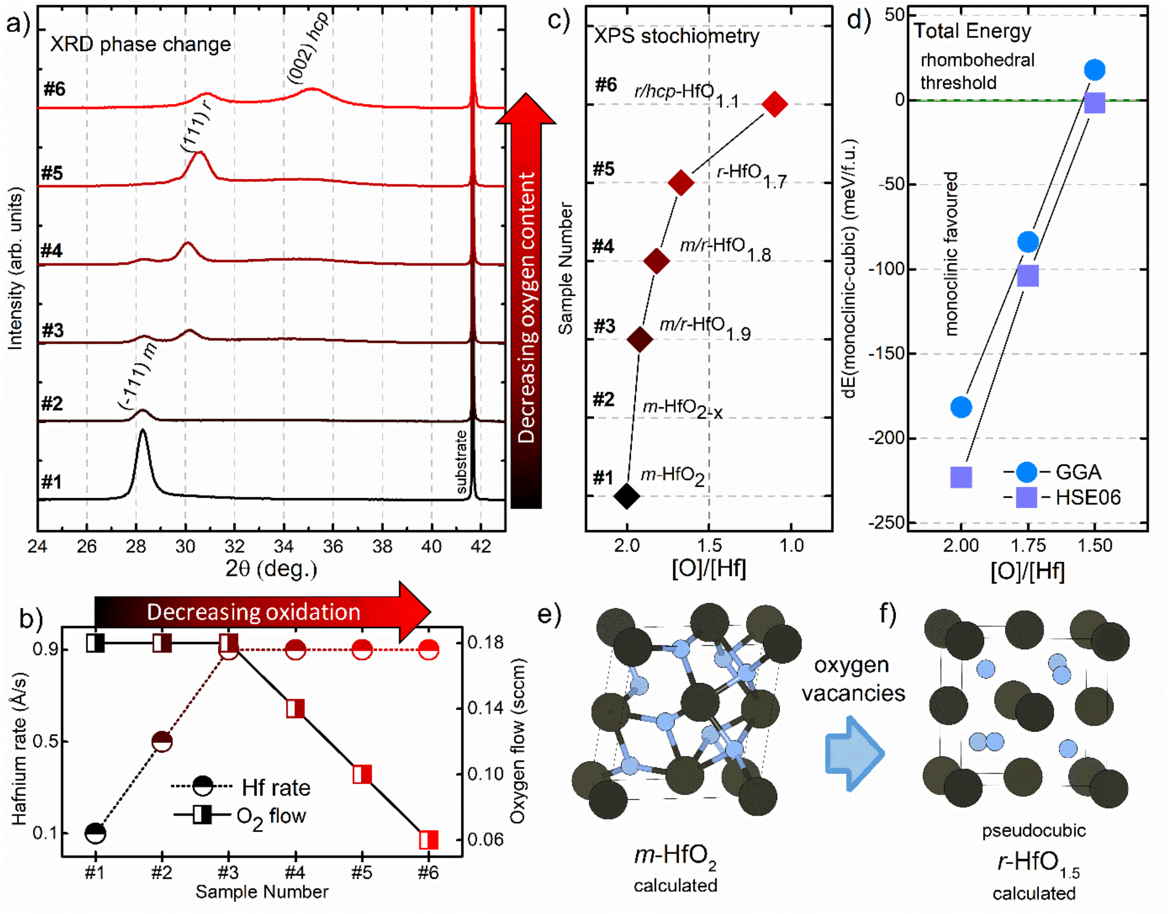

Figure 51: Comparison of experimental vs theoretical data on the phase transformation from monoclinic to rhombohedral structure. a) shows the phase transformation from 2θ/ω XRD scans with b) the corresponding deposition conditions which result in a consistent trend in the atomic ratio as displayed in c). d) shows the energetic difference between the discussed monoclinic and pseudocubic relaxed structures, confirming a consistent trend with more energetic stability towards the pseudocubic rhombohedral structure. Note that the rhombohedral structure is crossing the energetic threshold for its stabilization over the monoclinic reference at a ratio of [O]/[Hf] = 1.5, which is close to the experimental value of [O]/[Hf] = 1.7 as determined via XPS. E) and f) show the calculated stable structures of m-HfO_2 and r-$HfO_{1.5}$. Reprinted with permission from reference [151]. https://doi.org/10.1021/acsaelm.2c01255 Copyright © 2023 American Chemical Society.

Figure 51 directly compares the structural transformation via a) XRD as well as the atomic composition as estimated by c) XPS against the total energy calculations as obtained from the above-mentioned DFT calculated structures d). Note that the results shown in a) and b) are identical to the already discussed experimental data from chapters 4.1.1 & 4.1.3 respectively, while their numbering was matched to the XPS investigated samples. The corresponding MBE conditions are shown in Figure 51 b). Note that there is a steady decline in oxygen content from the monoclinic to the rhombohedral transformation where the most pronounced reflection of the rhombohedral structure appears at an oxygen content of [O]/[Hf] = 1.7. From this point a further transformation occurs to a hexagonal hafnium phase with oxygen interstitials. This transition shows a more dramatic change in the oxygen content over [O]/[Hf] = 1.1 for a phase mixture of rhombohedral and hexagonal to sole *hcp*-$HfO_{0.7}$ with [O]/[Hf] = 0.7 as discussed in in chapters 4.1.1 & 4.1.3.

The total energy difference between monoclinic and pseudocubic structures in dependence of their oxygen content is displayed in Figure 51 d). This graph confirms the experimental oxygen content dependent trend of relative phase stabilities by DFT for GGA but also HSE06 exchange correlation functionals. For stoichiometric HfO_2 the monoclinic phase is obviously energetically favored, however for a composition of $HfO_{1.5}$ the total energy difference between both structures is either crossed or very close to the threshold for the transformation to a rhombohedral unit cell. The ratio of [O]/[Hf] = 1.5 is in good agreement with the experimental estimate of [O]/[Hf] = 1.7 for the most prominent rhombohedral sample, especially as the next deficient sample with a rhombohedral/hexagonal phase mixture shows a rapid decline to [O]/[Hf] = 1.1.

McKenna et al. also conducted total energy calculations on oxygen dependent phase transitions in hafnium oxide and discovered that the monoclinic phase was preferred over a tetragonal phase up to a reduction of [O]/[Hf] = 1.3. Following the calculations, a phase separation between monoclinic and hexagonal hafnium oxide was concluded to be the most likely scenario oxygen-deficient hafnium oxide. [74]

However, as was already mentioned in this section, our findings from both an experimental and theoretical standpoint demonstrate that a rhombohedral structure (*r*-HfO_{2-x}) is clearly formed as an intermediate phase. Additionally, this phase's considerable stability was confirmed as it was re-measured using XRD three years after synthesis and showed no signs of degradation.

Table 5: Calculated crystal structures and atomic positions of relaxed stoichiometric and oxygen deficient hafnium oxide structures. Reprinted with permission from reference [151]. https://doi.org/10.1021/acsaelm.2c01255 Copyright © 2023 American Chemical Society.

$m-\mathbf{HfO_2}$ $(P2_1/c)$

a	b	c	α	β	γ
5.07849	5.16438	5.23505	90	99.6675	90

Atom	Positions	Site
Hf	(0.22231, 0.04278, 0.79287)	(4e)
O1	(0.42691, 0.34104, 0.66244)	(4e)
O2	(0.05327, 0.75862, 0.51760)	(4e)

$c-\mathbf{HfO_2}$ $(Fm\text{-}3m)$

a
5.01691

Atom	Positions	Site
Hf	(0.00000, 0.00000, 0.00000)	(4a)
O	(0.75000, 0.25000, 0.25000)	(8c)

$m-\mathbf{HfO_{1.75}}$ $(P1)$

a	b	c	α	β	γ
5.03468	5.11268	5.19333	90.2094	90.0281	98.8509

Atom	Positions	Site
Hf1	(0.99340, 0.50010, 0.41363)	(1a)
Hf2	(0.44093, 0.08184, 0.50281)	(1a)
Hf3	(0.44261, 0.58047, 0.91722)	(1a)
Hf4	(0.00000, 0.00000, 0.00000)	(1a)
O1	(0.80645, 0.60789, 0.09245)	(1a)
O2	(0.64076, 0.97266, 0.81588)	(1a)
O3	(0.63208, 0.47155, 0.59542)	(1a)
O4	(0.80632, 0.11288, 0.32068)	(1a)
O5	(0.16405, 0.77434, 0.69848)	(1a)
O6	(0.27468, 0.80463, 0.21886)	(1a)
O7	(0.27202, 0.30409, 0.19115)	(1a)

$r-\mathbf{HfO_{1.75}}$ $(R3m)$

a	α
5.02028	90.5356

Atom	Positions	Site
Hf1	(0.49017, 0.49017, 0.49017)	(1a)
Hf2	(0.00000, 0.00000, 0.50716)	(3b)
O1	(0.78418, 0.78418, 0.78418)	(1a)
O2	(0.27350, 0.72777, 0.72777)	(3b)
O3	(0.22536, 0.78739, 0.22536)	(3b)

$m-\mathbf{HfO_{1.5}}$ $(P1)$

a	b	c	α	β	γ
4.99658	5.10462	5.15127	89.4642	89.3485	81.4499

Atom	Positions	Site
Hf1	(0.98651, 0.50475, 0.58696)	(1a)
Hf2	(0.43559, 0.92500, 0.49065)	(1a)
Hf3	(0.43192, 0.43086, 0.07895)	(1a)
Hf4	(0.00000, 0.00000, 0.00000)	(1a)
O1	(0.64059, 0.04991, 0.18027)	(1a)
O2	(0.63561, 0.53833, 0.38867)	(1a)
O3	(0.80263, 0.88392, 0.68165)	(1a)
O4	(0.15896, 0.22810, 0.29851)	(1a)
O5	(0.26490, 0.20362, 0.77751)	(1a)
O6	(0.27749, 0.69810, 0.79573)	(1a)

$r-\mathbf{HfO_{1.5}}$ $(R3m)$

a	α
4.96722	89.3739

Atom	Positions	Site
Hf1	(0.98226, 0.98226, 0.98226)	(1a)
Hf2	(0.50232, 0.50232, 0.01942)	(3b)
O1	(0.23521, 0.23521, 0.77455)	(3b)
O2	(0.73280, 0.73280, 0.27712)	(3b)

4.2.2. DFT Calculated Crystal Structure of Rhombohedral Hafnium Oxide Compared to XRD Measurement's

While the experimental phase identification of *r*-HfO_{2-x} is covered in chapter 4.1.2, this section discusses the similarities between the measured and the calculated rhombohedral structure. In addition, the calculated oxygen positions, the resulting space group and consequent implications are subject to this chapter. Figure 52 compares the experimental results from Figure 37 (chapter 4.1.2) with the calculated structure. Specifically Figure 52 a-c) show the 2θ measurements, together with the vertical lines which indicate the peak maxima for the corresponding (111), (-111) and (002) lattice planes. Those 2θ values are transferred into Figure 52 d), in order to directly compare the reflex positions to a powder diffraction file of a cubic reference (*c*-HfO_2; PDF 04-011-9018) and the calculated phase. From this comparison, one can clearly see that while the (111) plane of the stoichiometric cubic reference and the (experimentally determined) deficient rhombohedral phase are practically identical, the rhombohedral phase is identified by a peak splitting between the (111) and (-111) planes. While this image highlights the similarities between both the calculated and experimental rhombohedral diffraction patterns it is noteworthy that this peak splitting is even stronger for the calculated rhombohedral structure (Find the exact comparison of the crystallographic data in Figure 52 e). This finding is striking, as the calculated structure was relaxed from a (perfectly) cubic lattice with two oxygen vacancies. Therefore, this observation serves as evidence that the rhombohedral modification is a consequence of the induced oxygen vacancies, and not merely an effect which is attributed to epitaxial strain. This is further underpinned by comparing the unit cell of the calculated rhombohedral cell to the cubic reference as displayed in Figure 52 h & i). While the cubic HfO_2 cell is characterized by a *Fm-3m* space group, which is realized by the symmetric ordering of oxygen ions, this symmetry is reduced by the induction of oxygen vacancies, and upon relaxation, results in a rhombohedral distortion yielding a *R*3*m* symmetry. Figure 52 j & k) show the same calculated rhombohedral cell in (111) growth direction in side view and top view respectively. This representation highlights that the pseudo-six-fold symmetry which is evident in the pole figure plots in Figure 52 f & g) can be understood as two crystalline domains of three-fold symmetry which show an offset of 60 ° in φ. The corresponding crystalline directions are therefore highlighted in black and white (representing two separate domains). In order to show how the arrangement of crystalline orientations is compatible with the recorded pole figures all relative (-111) and (002) directions have been assigned.

To our knowledge, this phase is the first rhombohedral phase of pure hafnium oxide to be observed thus far. However, it is important to point out that a variety of comparable rhombohedral structures have recently been found in thin films of hafnium zirconium oxide (HZO), which have also been grown epitaxial. Strikingly, those reported HZO phases showed ferroelectric characteristics. The high conductivity of the thin films discussed in this work however makes it impossible to verify polar P-E loops, which is a crucial test for ferroelectric characteristics. Another indication for potential ferroelectric behavior is the symmetry of the space group, as a polar symmetry is a vital requirement for ferroelectric materials. While the experimental determination of the space group requires identifying the oxygen sub lattice, it is practically impossible to measure with X-ray diffraction in thin films (due to the limited volume), the DFT simulation considers all ions, including oxygen. From those calculations the polar *R*3*m* space group is determined (compare Table 5, page 80). Therefore, the here discussed results are in good agreement with the reported ferroelectricity in rhombohedral HZO phases and suggests that the structure can be stabilized in hafnium oxide either through ionic substitution by zirconium or by the introduction of oxygen vacancies.

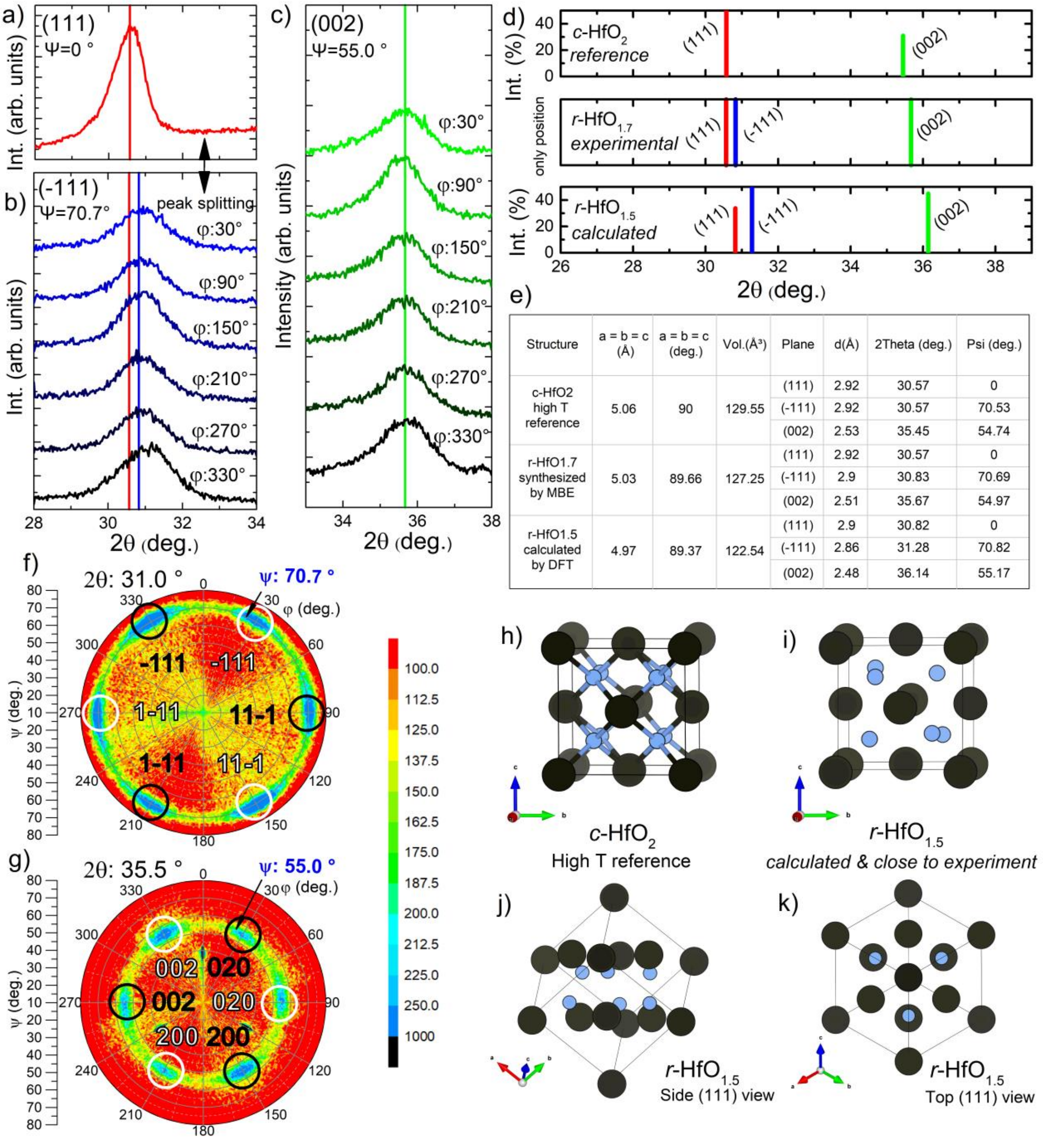

Structure	a = b = c (Å)	a = b = c (deg.)	Vol.(Å³)	Plane	d(Å)	2Theta (deg.)	Psi (deg.)
c-HfO2 high T reference	5.06	90	129.55	(111)	2.92	30.57	0
				(-111)	2.92	30.57	70.53
				(002)	2.53	35.45	54.74
r-HfO1.7 synthesized by MBE	5.03	89.66	127.25	(111)	2.92	30.57	0
				(-111)	2.9	30.83	70.69
				(002)	2.51	35.67	54.97
r-HfO1.5 calculated by DFT	4.97	89.37	122.54	(111)	2.9	30.82	0
				(-111)	2.86	31.28	70.82
				(002)	2.48	36.14	55.17

Figure 52: a), b) and c) showing the corresponding (111), (-111) and (002) reflections which are transferred in d) where a comparison between a cubic reference and the calculated rhombohedral phase is shown. Note that the rhombohedral peak splitting between (111) and (-111) is even more pronounced for the calculated as for the measured case. e) displays the corresponding lattice parameters of all discussed phases. f) & g) showing pole figure measurements which reflect the set of (-111) and (002) lattice planes. Note that the lattice planes are represented in white and black, indicating the multi-domain nature of the thin film. h) & i) show a comparison between a stoichiometric cubic phase yielding the highly symmetric *Fm*-3*m* space group and the calculated rhombohedral phase with two oxygen vacancies, yielding a polar *R*3*m* symmetry. j) and k) show the rhombohedral phase in (111) growth direction from the side and top view respectively. Reprinted with permission from reference [151]. https://doi.org/10.1021/acsaelm.2c01255 Copyright © 2023 American Chemical Society.

4.2.3. Density of States and Bandgap of Rhombohedral Hafnium Oxide from Hybrid Functional Calculations, Photoelectron Spectroscopy and Optical Transmission

While in chapter 4.1.5 & 4.1.7 the experimental results of the oxygen dependent evolution from *m*-HfO_2 to *hcp*-$HfO_{0.7}$ of the bandgap and ingap states has been discussed, this section compares (analogous to the crystal structure discussion in the previous chapter 4.2.2) the results of the stoichiometric monoclinic case and specifically the deficient rhombohedral structure to theoretical calculations. For the deficient rhombohedral phase, [O]/[Hf]=1.7 (sample #5; Figure 51, page 78) according to XPS estimation and [O]/[Hf]=1.5 for the DFT simulation apply, while [O]/[Hf]=2 (sample #1) applies for the monoclinic stoichiometric case. As was noted in chapter 4.2.1, the critical composition for the change from monoclinic to rhombohedral structure was found to be $HfO_{1.5}$, which is close to the experimental estimate of $HfO_{1.7}$.

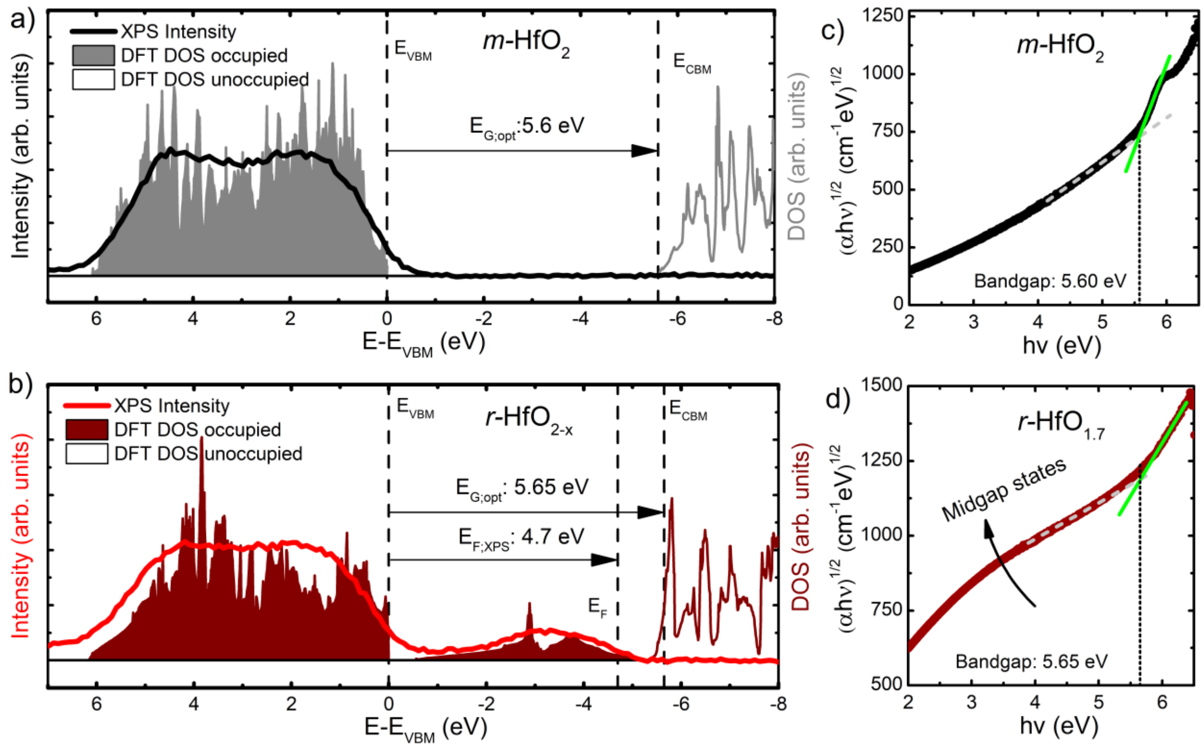

Figure 53: a) and b) compare XPS valence spectra and optical bandgap values to calculated DOS for m-HfO_2 as well as r-$HfO_{1.7}$ from measurement and r-$HfO_{1.5}$ from calculation respectively. c) & d) show the corresponding Tauc plots for bandgap estimation. Note the close resemblance of XPS spectroscopic data with the calculated DOS as well as the close agreement with the optical bandgap between the most pronounced occupied and unoccupied DOS. Reprinted with permission from reference [151]. https://doi.org/10.1021/acsaelm.2c01255 Copyright © 2023 American Chemical Society.

The computed total DOSs are depicted in Figure 53 with the occupied and unoccupied states of monoclinic HfO_2 separated by an insulating bandgap (as expected for stoichiometric hafnia). A high degree of consistency can be seen by showing the spectroscopic data and the computed total DOS together. Although the XPS data resembles the valence band states, XPS is limited to only capture states with positive binding energies beginning at the Fermi level. One can however determine the energy difference between the valence band maximum (VBM) and conduction band minimum (CBM) by determining the optical bandgap using UV-Vis measurements. The bandgap can be read straight from the abscissa because the estimated states are aligned to the VBM. Here, the optical bandgap (dashed line) at 5.60 eV agrees remarkably well with the predicted appearance of unoccupied DOS at 5.56 eV above the Fermi level as determined by DFT simulation. This is accomplished by using the hybrid functional HSE06, which, as detailed in section 4.2.4, enables a better estimate of band gaps than the common GGA functional.

The consistency between experimental results and DFT computations for rhombohedral *r*-HfO_{2-x} is very high, as illustrated in Figure 33 b). For this material, the spectroscopic data also closely approaches the estimated DOS. The DFT calculations, also explain specifically the development of dispersive states in the bandgap spanning many eV. Due to the relatively low DOS in the bandgap, the absorption edge for the matching optical bandgap could still be easily detected in the absorption spectra. This is represented in Figure 33b, where the optical bandgap of 5.65 eV agrees closely with the energy difference of the most conspicuous occupied vs unoccupied DOS, which is 5.41 eV.

Furthermore, the experimentally determined Fermi level ($E_{F,XPS}$, which corresponds to the temperature dependent chemical potential) is located above the great majority of midgap states. This observation is therefore consistent with the DFT results. The predicted Fermi level (for T = 0 K) is above all midgap states up to the conduction band, however the position of the (experimental) chemical potential rather cuts those defect bands at 4.7 eV with respect to the reference point E_{VBM}. Nonetheless, in each scenario, the Fermi level is located near oxygen vacancy-induced midgap states, supporting considerable electrical conduction of *r*-HfO_{2-x}, as shown by resistance and Hall effect studies in chapter 4.1.4.

For both, the monoclinic and the rhombohedral material, the corresponding Tauc plots (for indirect transitions) are displayed in Figure 33 c & d) respectively. Note that for both a visible absorption slope is recognized which is extrapolated to the extrapolated baseline absorption rather than the abscissa. This method is one of the most accurate estimations for the optical bandgap as it also considers additional baseline features. This is especially crucial in the presence of midgap states as determined by both XPS valence spectra as well as the discussed DFT predictions. More details on the method are given in chapter 2.4 while a detailed discussion on the badgap estimation for the whole oxidation range from monoclinic hafnia to hexagonal hafnium oxide is delivered in chapter 4.2.3. As previously stated, the extracted values of 5.6 eV (for both direct & indirect transition) and 5.65 eV (5.7 eV for a direct transition) for *m*-HfO_2 and *r*-$HfO_{1.7}$ are in good agreement with the aforementioned DFT band structure predictions of 5.56 eV for *m*-HfO_2 and 5.41 eV for *r*-$HfO_{1.5}$. Note, that the DFT calculations show excellent conformity with the proposed band structure model as discussed in chapter 4.1.7.

4.2.4. Analysis of the Band Structure and Orbital Hybridization within HSE06

As part of this chapter a comprehensive explanation of the estimated electronic structures in HfO_{2-x} is provided. While common exchange-correlation functionals like the local density approximation and the generalized gradient approximation, which are extensively used in DFT calculations, significantly underestimated the bandgap of monoclinic HfO_2 [40, 120, 169] it has already been demonstrated that the GW method, as well as hybrid functionals like B3LYP and PBE0, can produce consistent results.[71, 72, 121]

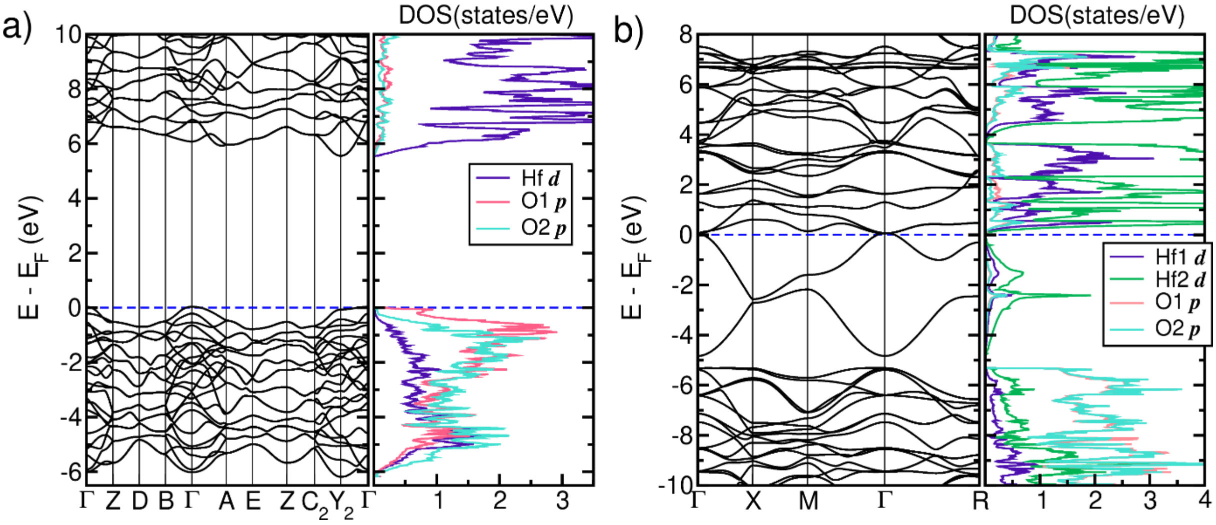

Figure 54: Band structure and orbital resolved DOS for the calculated structures of a) stoichiometric monoclinic *m*-HfO_2 and b) deficient rhombohedral *r*-$HfO_{1.5}$. Both predictions show a high level of agreement to the experimental results. Reprinted with permission from reference [151]. https://doi.org/10.1021/acsaelm.2c01255 Copyright © 2023 American Chemical Society.

As shown in the preceding chapter, the observed bandgap may be precisely approximated using the hybrid functional approach HSE06, as implemented in VASP. Figure 54 a) depicts predicted band structures and orbital resolved DOSs in HSE06 for monoclinic HfO_2. Fully occupied oxygen bands exhibit strong hybridization with Hf 5d states. Above 5.6 eV, the band structure is dominated by empty Hf 5d states. Figure 55 b) (next page) shows similar electrical structures in also stoichiometric *c*-HfO_2 with a bandgap of 5.46 eV. Due to the crystal field environment of Hf in a cube of adjacent O, unoccupied Hf 5d states are separated into lower *eg* and higher *t2g* levels in this scenario. Furthermore, the band width of completely occupied oxygen *2p* states in *c*-HfO_2 is roughly 1 eV wider than in *m*-HfO_2.

The CBM, emerges near the Y_2 point whereas the VBM in *m*-HfO_2 is located at both the Γ and the $Y_2(-\pi/a\ ,0,0)$ points, which are almost degenerate in energy. This finding gives rise to the possible combination of direct and indirect bandgaps which is in good agreement with the experimental results detailed in chapter 4.1.5. For so far discussed stoichiometric hafnium oxide we find – as expected - that *m*-HfO_2 is more energetically stable than *c*-HfO_2, namely by 181.5 meV within GGA and 223 meV within HSE06 (compare Figure 51 d).

Figure 54 b) depicts the band structure and orbital resolved DOSs within HSE06 of *r*-$HfO_{1.5}$, which appears in excellent agreement with the previously presented experimental results on oxygen deficient rhombohedral hafnium oxide. For direct comparison and as a benchmark the electronic structure of stoichiometric *m*-HfO_2 is shown in Figure 54 a). Two dispersive bands (HfO_{2-x}, x = 0.5; Hf $5d^{+\delta}$, $\delta = 1$) develop from 0 to -5 eV below the Fermi level due to oxygen deficiency. Each band has two spins, and the unit cell contains four Hf atoms for the simulations.

These midgap bands are made up of hybridized states of Hf 5d and O 2p orbitals. Notably, at the Γ point, the top of these midgap states touches the conduction Hf 5d states, making this system more metallic. However, there is still a slight gap between these midgap states and fully occupied O 2p bands, with a direct gap at the Γ point of around 482 meV, preventing this system from becoming completely metallic. This observation is in good agreement with the electrical results, which suggest semiconducting behavior as discussed in chapter 4.1.4.

In terms of bandgaps, both direct and indirect transitions appear to be viable, as illustrated in Figure 54 b), between the Γ or X point of the occupied O 2p bands maximum and the Γ point of the midgap states lowest. In contrast to *r*-$HfO_{1.5}$, the midgap states in *m*-$HfO_{1.5}$ (See Figure 55 a) are located between the occupied O 2p and empty Hf 5d states. These findings are consistent with prior measurements of resistivity on *r*-$HfO_{1.7}$, which is more conductive than *m*-HfO_{2-x}.

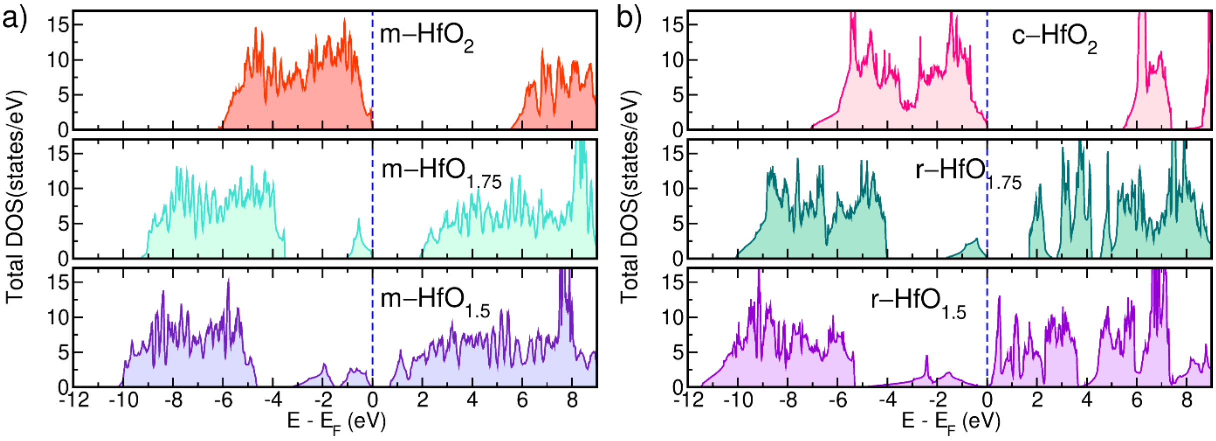

Figure 55: Predicted DOS of all structures as calculated for the energy comparison in chapter 4.1.3. The corresponding lattice parameters and atomic positions are found in Table 5. While $HfO_{1.5}$ is identified as a turning point from monoclinic to rhombohedral transformation, the rhombohedral structure shows more disperse defect states, with a significantly smaller gap to the CBM, therefore indicating higher conductivity as compared to the deficient monoclinic structure. Reprinted with permission from reference [151]. https://doi.org/10.1021/acsaelm.2c01255 Copyright © 2023 American Chemical Society.

Furthermore, the difference in total energies between *r*-$HfO_{1.5}$ and *m*-$HfO_{1.5}$ inside HSE06 is virtually overturned, as seen in Figure 51d. It is worth noting that the total energy of *m*-$HfO_{1.5}$ within HSE06 is still 1.6 meV lower than that of *r*-$HfO_{1.5}$, but the difference is minor and comparable with thermal effects (In the GGA data, *r*-$HfO_{1.5}$ is roughly 18 meV more energetically favorable than *m*-$HfO_{1.5}$). As a result, the presented DFT results strongly validate the previously discussed model (from experimental results) that oxygen vacancies support the rhombohedral structure of hafnium oxide and contribute to its high conductivity.

4.3. Substoichiometric Phases of Hafnium Oxide as Novel Electrodes for RRAM Applications

While so far in this work, oxygen deficient hafnium oxide was primarily investigated in terms of physical properties, another important view is the examination of discussed phases in a typical Metal-Insulator-Metal configuration. This kind of device configuration is the fundamental architecture for VCM RRAM and is characterized by the interfaces between the top-, as well as the bottom-electrode adjacent to the active material layer. As already discussed previously parts of this work, there are different interfacial effects, which can determine the charge transport characteristics in such systems. Further it is known that the exposure to oxygen can lead to the oxidation of specific interfacial layers. On the one hand even commonly used TiN which is known for its comparably inert characteristics is prone to (interfacial) oxidation which is also specifically discussed in the field of RRAM. On the other hand, there are strong indications that oxygen deficient hafnium oxide tends to form an oxidation layer.

Therefore, in order to further investigate the properties of discussed phases in MIM configuration, this chapter first discusses the reproduction of substoichiometric hafnium oxide phases *r*-HfO_{2-x} and *hcp*-HfO_{2-x} on epitaxial TiN electrodes in chapter 4.3.1. The following chapter 4.3.2 discusses the systematic preparation of hafnium oxide stacks where the platinum top electrode has been deposited in-vacuo or after exposure to air. Section 4.3.3 gives an overview of obtained I-V characteristics, showing strikingly that *r*-HfO_{2-x} and *hcp*-HfO_{2-x} show typical bipolar RRAM switching behavior if exposed to air, but conducting behavior if prepared in-vacuo. The following chapter 4.3.4 concludes based on switching properties and forming voltages that surface oxidation layers with similar properties form independent of the thin films' oxygen content on both *r*-HfO_{2-x} and *hcp*-HfO_{2-x}. Due to the confirmation of conducting behavior of these oxygen deficient phases if treated in-vacuo, special attention is given to the role of *r*-HfO_{2-x} and *hcp*-HfO_{2-x} as electrically conducting bottom electrodes. Consequently chapter 4.3.5 demonstrates the similarities between the leakage currents of hafnium oxide in MIM configuration and the resistivity of samples grown on sapphire where a transition of insulating to conducting behavior is found for both series. Finally, section 4.3.6 verifies the conduction mechanisms in switchable and conducting devices, further indicating *r*-HfO_{2-x} and *hcp*-HfO_{2-x} as potential phases which may form in the conducting filament. As this chapter is primarily about hafnium oxide in MIM configuration the additional section 4.3.7 shows a deposition routine to obtain thick 200 nm TiN bottom electrodes for operando TEM investigations.

4.3.1. Reproduction of Substoichiometric Hafnium Oxide Phases on Epitaxial TiN Electrodes

While so far in this work, oxygen deficient hafnium oxide was primarily investigated in terms of physical properties, this chapter will discuss the properties of the oxygen-dependent series in metal-insulator-metal configuration. In order to provide a good basis for literature comparability the stack configuration $Pt/HfO_{2-x}/TiN$ – which is known for its good performance – was chosen.[31, 170, 171] For this purpose, first the deposition conditions for a reproducible TiN layer as bottom electrode have been elaborated.

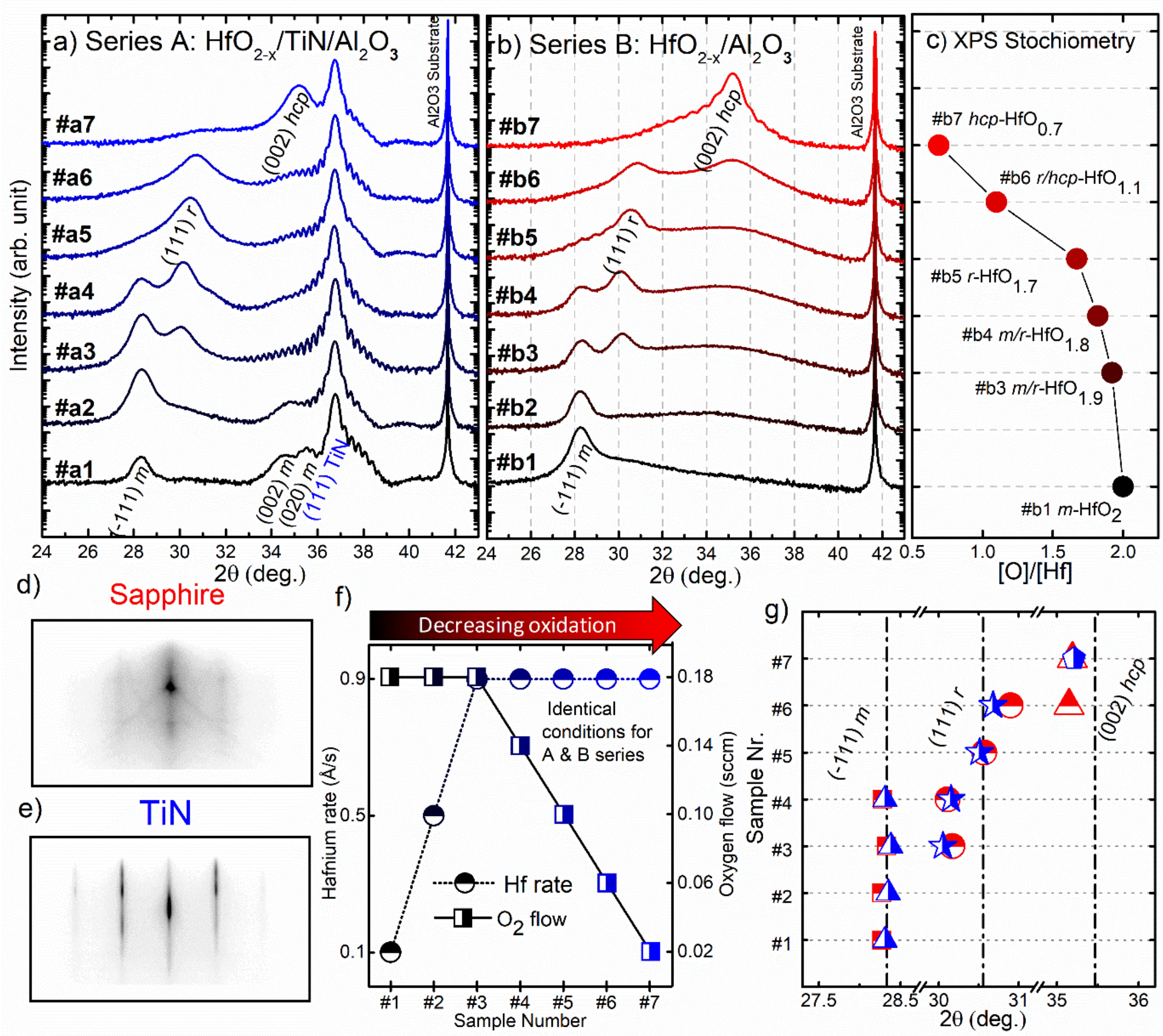

Figure 56: a-b) 2θ/ω XRD measurements of series A with additional 35 nm TiN layer on the sapphire substrate and of series B on plain sapphire. Note the high similarities of the hafnium oxide phases for both oxygen dependent series and the excellent reproducibility of epitaxial TiN for series A. c) shows the XPS estimated stoichiometry of series B for reference. d-e) shows the RHEED patterns of the c-cut sapphire substrate and the TiN layer, indicating good surface quality and epitaxial crystallinity. f) deposition conditions for both series in dependence of the sample number. g) comparison of the (-111) m-HfO_{2-x}, (111) r-HfO_{2-x} and (002) hcp-HfO_{2-x} reflections show the high level of agreement between both series also for the relative 2θ positions.

Following the procedure as detailed in chapter 3.3, high quality epitaxial TiN thin films of 35 nm have been achieved on c-cut sapphire substrates at a titanium rate of 0.2 Å/s. Further a nitrogen flow of 0.6 sccm at a RF power of 340 W was set and a substrate temperature of 800 °C was chosen for the growth. Figure 56 a) shows the oxygen dependent hafnium oxide series on TiN bottom electrodes. Note that for all samples the (111) TiN reflection appears virtually identical with respect to shape, peak maxima and Laue oscillations, indicating excellent reproducibility of high quality crystalline TiN layers. Figure 56 d, e) show the RHEED patterns of the sapphire substrate as compared to a fully grown 35 nm TiN bottom electrode. Note that black/white was inverted and the contrast/brightness was individually adjusted for better visibility. The sapphire pattern is characterized by vertical and Kikuchi lines, as expected from a single crystalline, flat surface. The TiN pattern also shows straight vertical lines, which appear slightly modulated. This pattern can be interpreted as a multilevel stepped surface (definitely not island growth) with good epitaxial surface quality.

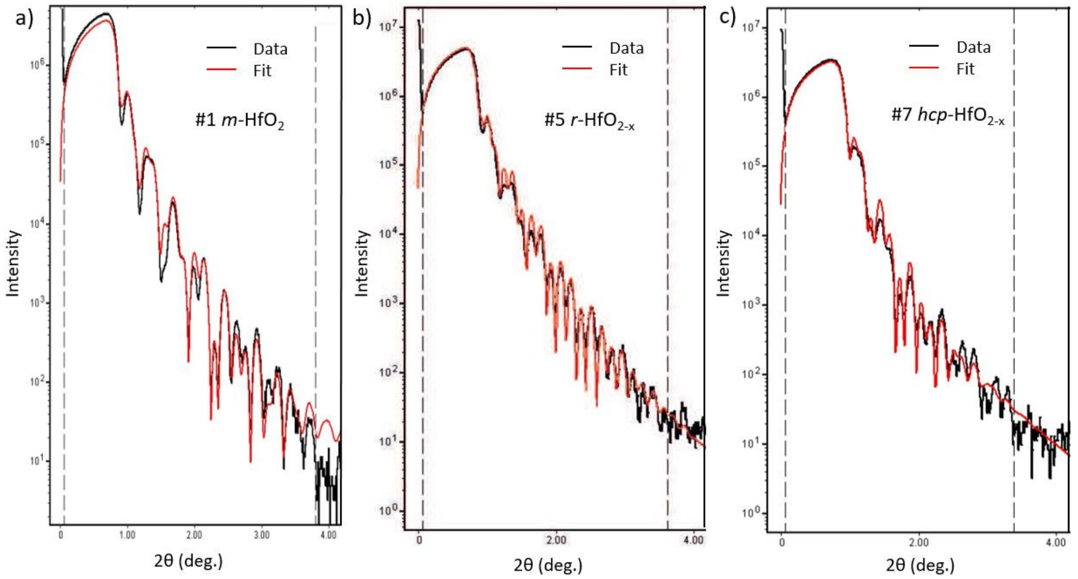

Sample	Layer	Thickness (nm)	Rel.Density	Roughness (nm)
#1b m-HfO$_2$	2 HfO$_2$	20.52	0.99	1.18
	1 TiN	33.80	0.92	0.88
#5b r-HfO$_{2-x}$	2 HfO$_2$	19.92	0.99 fix	1.27
	1 TiN	36.89	1.14	1.13
#7b hcp-HfO$_{2-x}$	2 HfO$_2$	18.18	1.18	1.61
	1 TiN	35.53	1.13	1.32

Figure 57: XRR data of the key samples a) #1a *m*-HfO$_2$, b) #5a *r*-HfO$_{2-x}$ and c) #7a *hcp*-HfO$_{2-x}$ with representative fitting via RCRefSim. Reasonable results could be obtained in any case using a two-layer model of hafnium oxide and titanium nitride on an aluminum oxide substrate. The vertical dashed lines show the range in which the fit is applied to the data. Below the corresponding fitting parameters are shown.

Figure 56 b) shows the equivalent series c-cut sapphire substrates (without TiN layer). The same thickness of 20 nm for the hafnium oxide layer was chosen for both series and identical deposition conditions have been applied as displayed in Figure 56 f) with 200 W forward power for the oxygen source and a substrate temperature of 320 °C. By comparing the XRD data from both series as displayed in Figure 56 a,b) one can see that the same oxygen dependent phase transitions take place, namely from monoclinic *m*-HfO$_2$ (as expected for stoichiometric hafnia) over rhombohedral *r*-HfO$_{1.7}$ to a modified metallic hexagonal lattice with oxygen interstitials *hcp*-HfO$_{0.7}$ (compare chapters 4.1.1, 4.1.2 & 4.1.3). While the overall phase transitions appear unchanged between both series, one significant difference is the texture orientation of the monoclinic phase. For the series B, #b1 *m*-HfO$_2$ appears strictly (-111) oriented while the growth on epitaxial TiN #a1 shows also the (002) and (020) reflection. Note that the (-111) orientation is reduced for the next sample on sapphire #a2, but appears stronger for #b2.

Previous studies have shown, that the epitaxial orientation of domains in monoclinic hafnia thin films can be controlled via the deposition parameters of substrate temperature and/or oxygen plasma.[139, 172] The here discussed results show that by solely reducing the hafnium rate (and therefore the oxidation conditions), the relative fraction of (-111), (002) and (020) out of plane orientations can be controlled on (111) TiN as can be seen between #a1 and #a2. Besides these discussed differences in domain orientation, the overall phase transformation appears virtually identical between both series. This finding is underpinned in Figure 56 g) where the reflection maxima of monoclinic (-111), rhombohedral (111) and hexagonal (002) are compared for series A & B in blue and red respectively.

Figure 57 shows the XRR data of the key samples of series A namely a) #1a *m*-HfO_2 , b) #5a *r*-HfO_{2-x} and c) #7a *hcp*-HfO_{2-x} with representative fitting via RCRefSim.[93] By using the expected two layer model of hafnium oxide on titanium nitride on a sapphire substrate namely $HfO_2/TiN/Al_2O_3$ a good fitting quality could be achieved for thickness estimations.

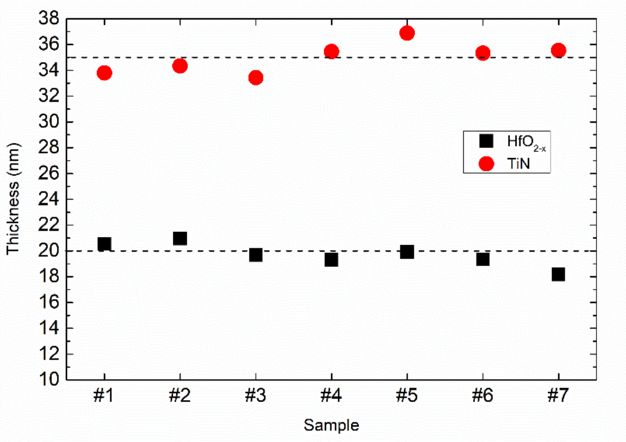

Figure 58: XRR thicknesses of the investigated samples HfO_{2-x} and TiN layers as extracted by fitting via RCRefSim. The graph shows uniform thickness of 35 ± 2 nm for the TiN bottom electrode and 20 ± 2 nm for the HfO_{2-x} layers which have been achieved via extensive calibration.

Figure 58 shows the extracted layer thicknesses for the whole series A. As can be seen a uniform thickness of 35 ± 2 nm for the TiN bottom electrode and 20 ± 2 nm for the HfO_{2-x} layers could be achieved. While the TiN thickness reproduced from one parameter set, the HfO_{2-x} thickness has been individually calibrated for each parameter set, as the density of hafnium oxide shows an oxygen content dependent density as shown in Figure 35, page 54.

4.3.2. Preparation of TiN/HfO_{2-x}/Pt Stacks In-Vacuo and In-Atmosphere

Surface oxidation can significantly change the interfacial properties of materials, which is especially of concern if an oxidized surface is embedded in multilayer structures. While RRAM stacks consist in their most fundamental form of comparably simple arrangement of an active, insulating material which is sandwiched between two conducting electrodes, any of the interfaces involved may potentially be subject to oxidation if treated in atmosphere or if a sufficiently high oxygen partial pressure is introduced in the growth chamber. In this work, stacks of Pt/HfO_{2-x}/TiN are investigated. While the HfO_{2-x}/TiN layers are grown under vacuum conditions, a potential oxidation of TiN cannot be avoided due to the subsequent growth of HfO_{2-x} which necessitates a predefined oxygen flow. At the HfO_{2-x}/Pt interface however, potential surface oxidation of hafnium oxide can be prevented and depends on the application route of the platinum top electrode. For the application via lift-off, photoresist is directly applied on the hafnium oxide layer, which requires the exposure to air. However, by utilizing Ion Beam Etching, the hafnium oxide layer can be shielded by direct deposition of platinum in-vacuo. In order to effectively investigate the potential effects of surface oxidation it is sensible to compare both cases.

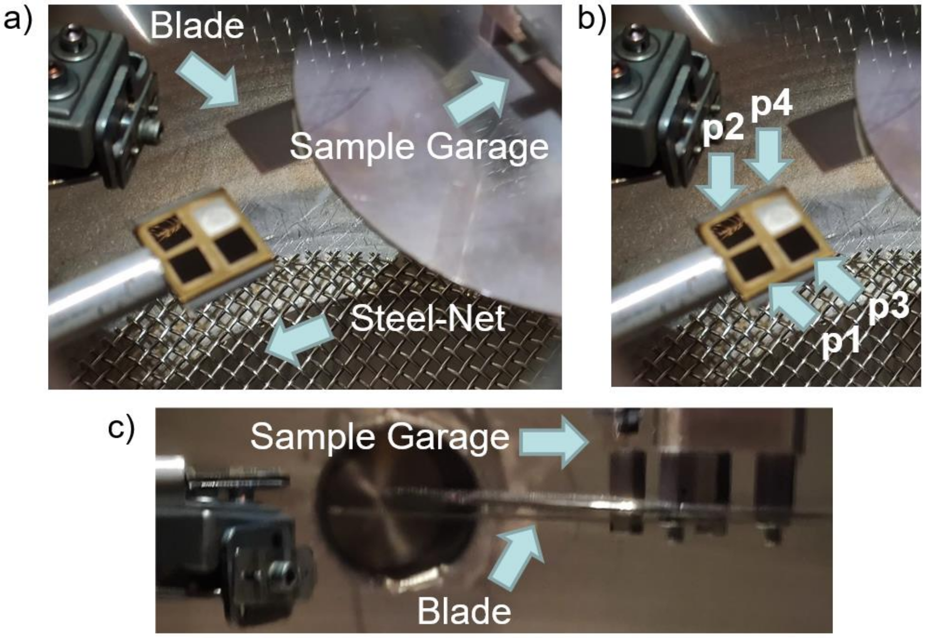

Figure 59: Loadlock setup for the removal of individual samples of TiN/HfO_{2-x} before platinum capping. a) Shows how a blade is connected below the sample garage, allowing samples to be detached from the holder, which can then fall into a steel net installed underneath. b) shows the four positions p1-p4 on which 5 x 5 mm substrates are glued on the sample holder. Note that that sample on p4 has already been detached by the blade. c) side view, showing how the blade is attached to the sample garage allowing to control height and rotation.

To achieve a high level of comparability between samples which have been treated in air vs. in-vacuo a setup was installed in the load lock of the MBE growth chamber which allowed to separate samples which have been grown in one deposition run. Figure 59 a,c) shows how a blade was attached below the sample garage, to scrape individual samples from the sample holder. Those can then be dropped on a steel net while the remaining samples on the sample holder can be directly deposited with platinum, without breaking UHV conditions. Figure 59 b) shows the four positions p1-p4 where the 5 x 5 mm substrates are attached (via silver glue) to the holder. Note that p4 was already detached after hafnium oxide deposition in Figure 59 b).

Generally, positions p2 and p4 have been removed for lift off preparation in air and p1 and p3 have been directly deposited with platinum to shield the hafnium oxide layer from atmosphere.

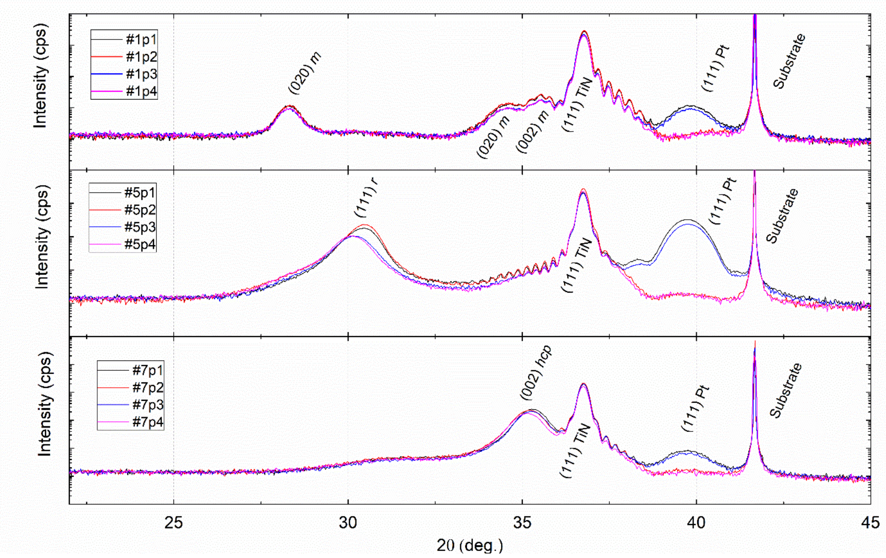

Figure 60: Comparison of the reproducibility of RRAM stacks with monoclinic (top), rhombohedral (middle) and hexagonal (bottom) hafnium oxide phases. Note that for every graph all four samples have been grown with the same settings simultaneously. Generally, the plots show a high level of reproducibility, with the biggest difference being a slight shift and higher signal intensity for the rhombohedral reflex (111). Note that samples at positions p1 and p3 which have been in-vacuo deposited with platinum show a corresponding Pt (111) reflex.

Figure 60 shows XRD measurements of four samples of monoclinic, rhombohedral and hexagonal hafnium oxide layers respectively. Note that for each synthesized phase all samples have been grown with the same deposition parameters simultaneously. The 2θ scans show good level of reproducibility, with the biggest difference being a slight shift and higher signal intensity of the rhombohedral (111) plane. As sample rotation with 10 rpm is used for all depositions, this is not a result of geometrical deposition conditions, but might be the result of a slight temperature gradient on the sample holder (which should remain constant even with rotation). In a nutshell, the approach of growing the samples simultaneously proves to achieve an excellent level of reproducibility, where all oxygen dependent phase transitions and relevant features are virtually identical. Note, that for the samples at positions p1 and p3 which have been directly deposited with platinum (in-vacuo) show a corresponding (111) Pt reflection. Further information on the methods used for micropatterning, including photoresist application and Ion Beam Etching procedures are detailed in chapters 3.4 & 3.5.

4.3.3. Electrical Properties of Substoichiometric Devices prepared In-Air and In-Vacuo

While the previous chapters 4.3.1 & 4.3.2 have described the preparation of devices with oxygen deficient hafnium oxide phases in stack configuration TiN/HfO_{2-x}/Pt and their structural properties, this chapter discusses their I-V-characteristics. Figure 61 gives an overview on the switching properties of devices with the hafnium oxide key structures a) *m*-HfO_2, b) *r*-$HfO_{1.7}$ and c) *hcp*-$HfO_{0.7}$ which correspond to the samples #1, #5 and #7 in Figure 56, page 88.

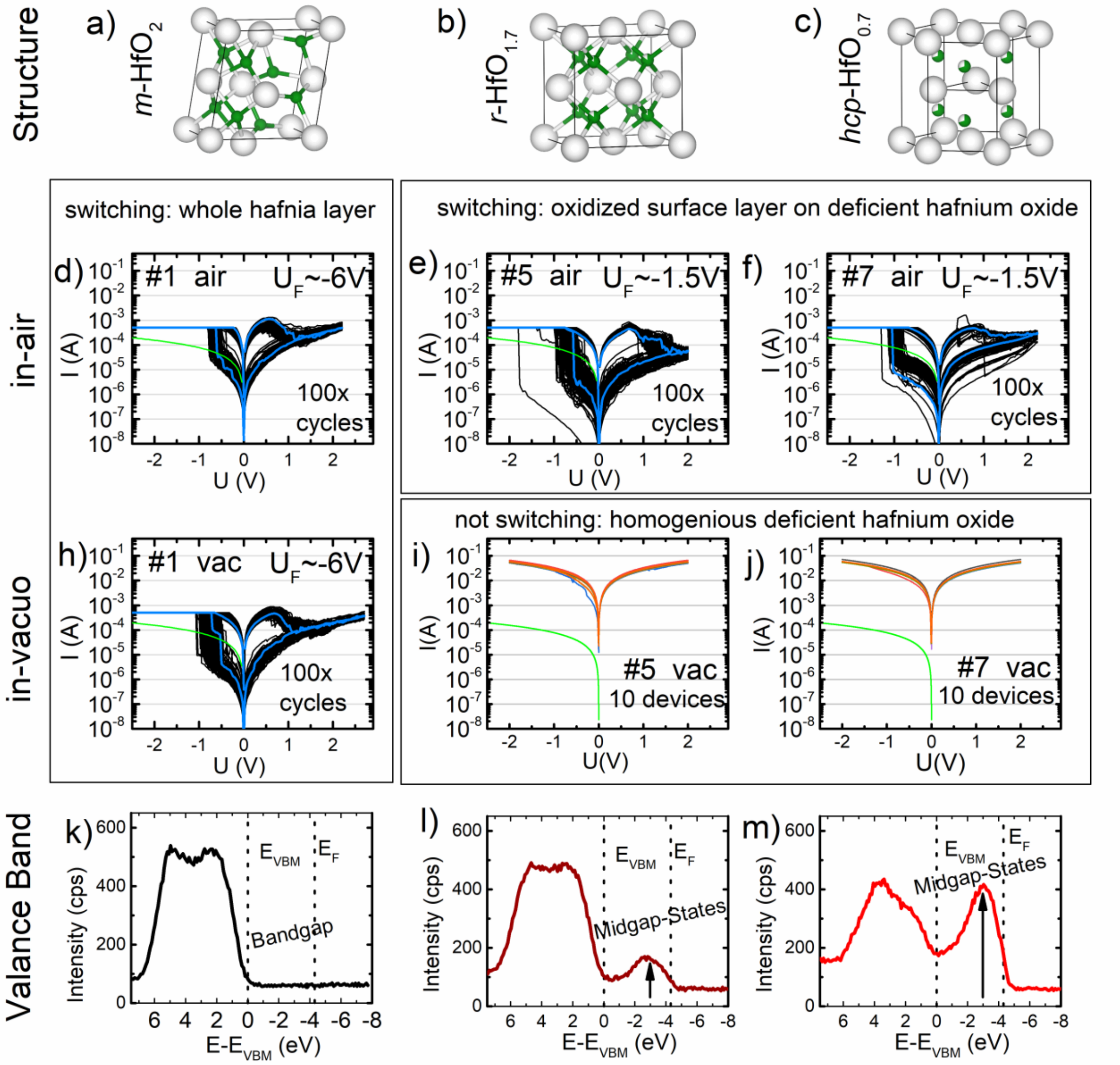

Figure 61: Overview of IV-characteristics for TiN/HfO_{2-x}/Pt stacks with the key phases a) *m*-HfO_2 b) *r*-$HfO_{1.7}$ and c) *hcp*-$HfO_{0.7}$. Note that stoichiometric, monoclinic devices d,h) show stable switching for at least 100x cycles independent of their preparation method (in-air or in-vacuo) which is expected. For deficient layers of hafnium oxide however there is a significant difference. For both, *r*-$HfO_{1.7}$ and *hcp*-$HfO_{0.7}$ stable switching can be observed if treated in-air e,f), however, if the same devices are prepared in-vacuo, they show a significant decrease in resistivity and no switching properties. Note that for all cases a G_0 reference is marked as a green line, showing the HRS is below or close to G_0 for all switching samples (as expected). For the conducting samples, the IV curves show even significantly higher conductivity than the LRS of all switching samples (up to the compliance current). k-l) show in-vacuo XPS valence spectra of reference measurements of corresponding hafnium oxide phases which show midgap states in the vicinity of the fermi level which is in good agreement with the observation of conducting, not switching samples if prepared in-vacuo.

The presented data specifically highlights the similarities and differences between samples that have been prepared in-air, meaning that the HfO_{2-x} layer has been exposed to air before the top Pt electrode has been deposited, and in-vacuo, meaning that the Pt top layer was deposited in vacuum, shielding the HfO_{2-x} layer from oxygen. For all switching devices a compliance current of 500 μA was chosen for the set. Electroforming was performed with a reduced compliance current of 10 μA. Both, electroforming and set are performed in the direction of the negative polarity with respect to the platinum top electrode (and grounded TiN bottom electrode). Therefore, for all switching cases a counter figure eight (cf8) kind of switching is shown (compare chapter 1.4).

Figure 61 d,h) shows that devices of stoichiometric monoclinic hafnium oxide show stable switching up to at least 100 cycles independent of the preparation in-air or in-vacuo, which is expected. Figure 61 e,f) shows for both deficient hafnium oxide phases *r*-$HfO_{1.7}$ and *hcp*-$HfO_{0.7}$ stable switching if exposed to air, however, if the same samples have been prepared in-vacuo as shown in Figure 61 i,j), they show no switching but conducting properties. For all graphs the conductance quantum (G_0) is plotted as a green line, which is typically a reference value to decide if at least a 1D conduction channel has been formed. [173-175] For the switching samples the high resistance state (HRS) is below or close to the value of the conductance quantization G_0. This is expected as the conducting filament is typically assumed to be either ruptured (therefore even preventing a 1D conduction path) or reduced to a very small diameter.[173-175] For the conducting samples in Figure 61 i,j) however the current is even significantly higher than for the LRS of the switching samples. This finding is in good agreement with in-vacuo XPS valence spectra Figure 61 k-m) of reference samples (HfO_{2-x} on sapphire; compare chapter 4.1.5, page 69) that show the appearance of midgap states in the vicinity of the fermi level.

4.3.4. Surface Oxidation and Substoichiometric Hafnium Oxide Phases as Ohmic Electrodes in RRAM

This chapter further discusses the effect of in-air oxidation on the oxygen deficient hafnium oxide phases. Figure 62 shows the forming voltage distribution off all switching samples from Figure 61. Note that the devices with stoichiometric monoclinic *m*-HfO_2 (in-air and in-vacuo) show high forming voltages of about 6.5 V, while the oxygen deficient samples *r*-HfO_{2-x} and *hcp*-HfO_{2-x} show an extremely narrow cumulative distribution with low forming voltages around 1.5 V. Low forming voltages are generally desirable as they are believed to result in a less violent electroforming process and therefore reduce the statistical device to device variability, which is still a key issue for the commercial viability of RRAM technology.[138, 139]

It is striking, that, although there is a significant difference in in the oxygen content between the deficient phases *r*-$HfO_{1.7}$ and *hcp*-$HfO_{0.7}$, their forming voltages as presented in Figure 62 are virtually identical (after exposure to air). In a previous publication it was already shown that oxygen deficient hafnium oxide will form an oxidation layer with a defined thickness of a view nm. This idea was supported by XPS findings and a thickness independent electroforming potential.[135] The here presented result is in good agreement with this finding and further suggests that a similar oxidation layer also forms independent of the hafnium oxide stoichiometry and structure from *r*-$HfO_{1.7}$ to *hcp*-$HfO_{0.7}$. The idea, that the oxygen deficient phases themselves have virtually no influence on the forming but only the oxidation layer, is further underpinned by the findings presented in Figure 61, where the IV-characteristics of in-air and in-vacuo preparation are compared. Indeed, both, *r*-$HfO_{1.7}$ to *hcp*-$HfO_{0.7}$ show significantly higher currents if prepared in the absence of oxygen.

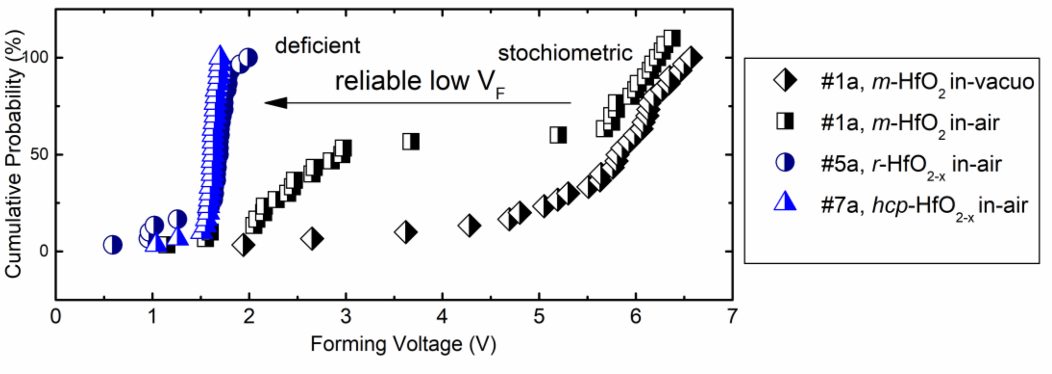

Figure 62: Forming Voltage characteristics of devices with stoichiometric monoclinic hafnium oxide as well as deficient rhombohedral and hexagonal hafnium oxide as prepared in-air. All forming steps have been performed with negative polarity from the Pt top electrode towards the grounded TiN bottom electrode. Note that the stoichiometric *m*-HfO_2 layers show high forming voltages up to -6.5 V (in-air and in-vacuo) while deficient devices (in-air) of *r*-$HfO_{1.7}$ and *hcp*-$HfO_{0.7}$ show a stoichiometry independent low forming voltage of about -1.5 V.

While the forming voltages are almost identical for both deficient phases, the leakage current measurements between *r*-$HfO_{1.7}$ and *hcp*-$HfO_{0.7}$ (not shown) still show about one order of magnitude difference (unexpectedly even lower leakage currents are measured for the more oxygen deficient *hcp*-$HfO_{0.7}$), which suggests that the surface oxidation is not completely identical. This is also supported by HRTEM measurements as discussed in chapter 4.1.6, where a ~ 4 nm amorphous top layer can be seen to form on top of *hcp*-$HfO_{0.7}$ which is a consequence of the exposure to air. For the *r*-HfO_{2-x} phase however, there is no obvious change to the crystalline structure. This suggests, that while the rhombohedral lattice (once formed) can remain in shape after oxidation, it is energetically unfavorable for the hexagonal lattice to stay crystalline and its structure is changed to an amorphous state.

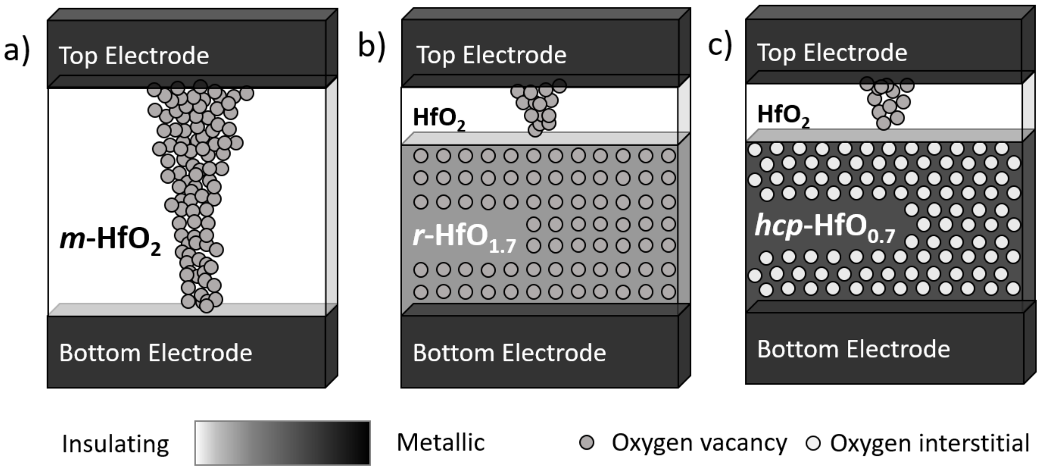

Figure 63: Simplified model of the filament formation in stoichiometric against oxygen deficient hafnium oxide after exposure to air. a) The stoichiometric sample requires the largest formation voltage as the filament forms through the whole hafnium oxide layer. b) and c) for both deficient *r*-$HfO_{1.7}$ and *hcp*-$HfO_{0.7}$ a surface oxidation layer of limited thickness evolves in air. As both *r*-$HfO_{1.7}$ and *hcp*-$HfO_{0.7}$ show conducting properties they act as the effective bottom electrodes and the formation voltage is only defined by the surface oxidation layers. This results in identical low formation voltages for both, *r*-$HfO_{1.7}$ and *hcp*-$HfO_{0.7}$.

In any case the presented (practically identical) forming voltage statistics support the likeness of both oxidation layers e.g. in form of similar thickness and suggests similar device to device variability and switching characteristics between *r*-$HfO_{1.7}$ and *hcp*-$HfO_{0.7}$. It would therefore be interesting to perform a more thorough investigation of the reproducibility of switching characteristics from oxidized *r*-$HfO_{1.7}$ to oxidized *hcp*-$HfO_{0.7}$. By assuming a general formation of surface oxidation layers with constant properties a broad parameter window of variable hafnium oxide compositions and thickness can lead to identical device characteristics. If this hypothesis would be further confirmed it could therefore lead to easily accessible, reproducible hafnium oxide based device fabrication with low forming voltages.

Following the model of surface oxidation *r*-$HfO_{1.7}$ and *hcp*-$HfO_{0.7}$ would act as effective bottom electrodes for the oxidized surface layer. This is especially underpinned by the conducting nature of both phases as shown previously from device properties but also from materials properties discussed in chapter 4.1.4 (p. 66). For both substoichiometric phases it can be assumed that they can host a considerable amount of oxygen. For r-HfO_{2-x} this is supported by oxygen dependent shift of the out of plane lattice plane as discussed in chapters 4.1.1 (p. 52) and 4.3.1 (p. 88). For *hcp*-HfO_{2-x}, oxygen is predicted to occupy the octahedral positions which allows for a maximum occupation of [O]/[Hf] =1.[66, 67, 74] Our results discussed in chapter 4.1.3 (p. 61) suggest occupation of 70% respectively [O]/[Hf] =0.7. Therefore, both phases qualify as reactive electrodes and potentially excellent oxygen reservoirs. The effect of “oxygen breathing” through an electrode site is generally believed to influence the endurance and retention of VCM memory as it can e.g. act as a diffusion barrier to stabilize the LRS. If there is no electrode that can host oxygen, the excess oxygen can only be “stored” as typically less stable interstitials [176, 177] or in form of oxygen gas accumulating at the interface which can lead to electrode delamination.[178-181] So far it was shown that interface layers with high diffusion barriers provide more reliable retention (as re-oxidation of the LRS is prevented).[181-183] For amorphous hafnium oxide it was shown by simulation that the diffusion is promoted by the free volume in low density HfO_{2-x}.[184] Gradually stronger diffusion barriers were observed in am-Al_2O_3, TiN, and Hf. [184] As shown in chapter 4.1.1 the density of *r*-HfO_{2-x} ~ 10.54 g/cm^3 is smaller than the estimated 11.25 g/cm^3 for *hcp*-HfO_{2-x} (which is still considerably lower than that of metallic Hf). Following this argument *r*-HfO_{2-x} would provide a lower diffusion barrier as compared to *hcp*-HfO_{2-x}. Therefore, it would be interesting to further investigate the devices with *r*-$HfO_{1.7}$ or *hcp*-$HfO_{0.7}$ electrodes with respect to endurance and retention properties.

4.3.5. Electric Behavior of Substoichiometric Hafnium Oxide-based Devices without Surface Oxidation

This chapter further discusses the electrical properties of substoichiometric hafnium oxide phases prepared in-vacuo (compare chapter 4.3.2). As capped devices of *r*-$HfO_{1.7}$ or *hcp*-$HfO_{0.7}$ not show switching properties (see chapter 4.3.3) Figure 64 compares a) the leakage current statistics of the whole series A in TiN/HfO_{2-x}/Pt configuration Figure 64 a,b) against the electrical Van der Paw characterization of series B (Al_2O_3/HfO_{2-x}) Figure 64 c,d). As discussed in chapter 4.3.1 for both series identical growth conditions were chosen for the hafnium oxide layer, with which the phase transitions from *m*-HfO_2 over *r*-HfO_{2-x} to *hcp*-HfO_{2-x} could be reproduced closely. Figure 64 b) shows the cumulative probabilities of the leakage current measurements and represents how the samples #1 and #2 (which are of monoclinic structure) show insulating properties while samples with rhombohedral or hexagonal phase fractions #3-#7 show rather conducting behavior. This observation is coinciding with the Van der Paw measurements displayed in Figure 64 d) where the first two samples could not be measured. For samples #3-#7 a gradual decline in resistivity is observed by the Van der Paw measurements which is further consistent with the gradual increase of midgap states as discussed in chapter 4.1.5.

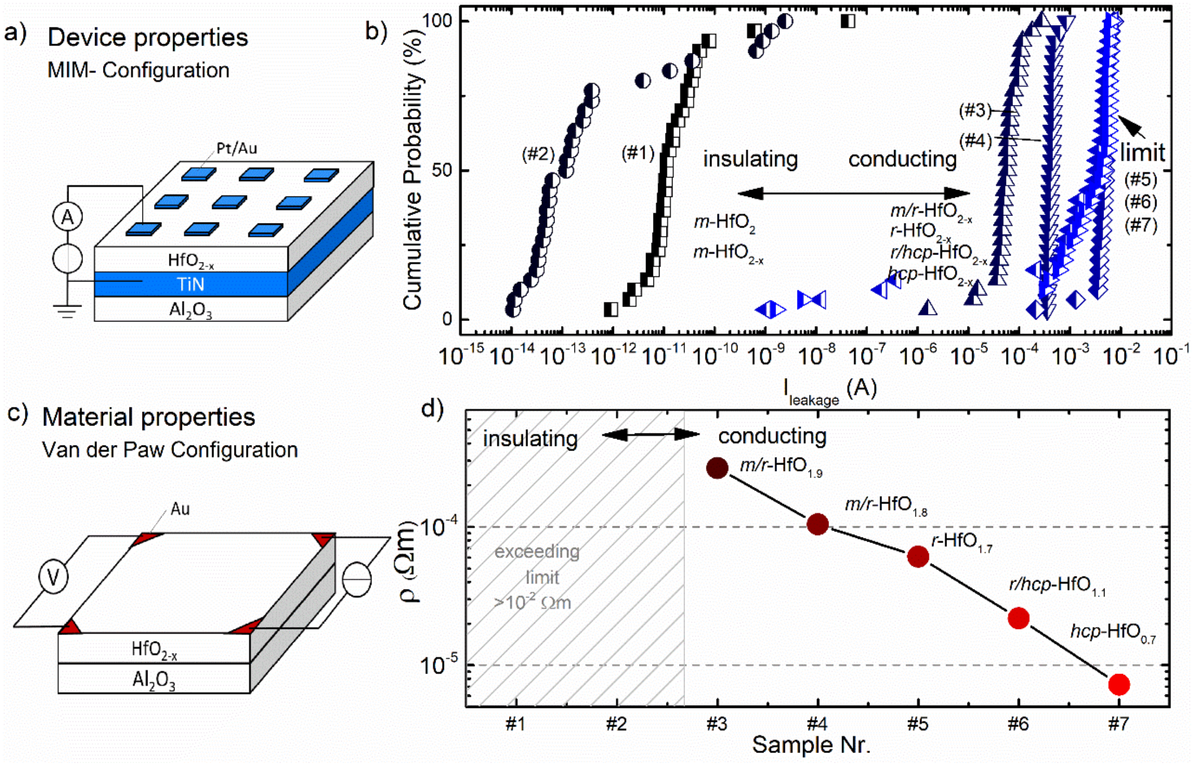

Figure 64: Comparison of leakage measurements from devices a) against Van der Paw resistivity measurements (eliminating contact resistance) obtained directly from hafnium oxide layers c). The results directly compare electrical characteristics from series A and B where the hafnium oxide layers are grown under identical conditions. b) shows the cumulative distribution of leakage currents (V_{read} = 0.2 V) from the device measurements. Note that there is a significant difference between the first two samples #1, #2 which can be considered insulating and the rest #3-#7 which show rather conducting properties. Similarly, for the physical properties, the first two samples could not be measured, but samples #3-#7 show significant electrical conduction in increasing order. Interestingly the limit shown in b) is most likely not determined by the hafnium oxide layer, but by the contact resistance of the sample stack and the measuring setup. Therefore, both series are in good agreement.

This trend does not fully translate in the leakage current statistics of devices in Figure 64 b) as there is a limit at $\sim\ 5 \cdot 10^{-3} A$ for samples *r*-HfO_{2-x} #5 to *hcp*-HfO_{2-x} #7. This limit can be explained by the contact resistance which dominants the resistivity at this value. This argument is supported by two findings. First, by placing the contacts of the Kiteley 4200 semiconductor characterization unit directly next to each other on a metallic layer (250 nm Au + 100nm Pt) the leakage current measurement is only about one order of magnitude higher and therefore close to the limit observed for this series. Second, although samples #5-#7 show statistical scatter in about 50% of the devices, all data points fall on the line at $\sim\ 5 \cdot 10^{-3} A$ after a "forming" step. The data points after such a voltage sweep are displayed in Figure 75 (Supplementary Information). If the hafnium oxide layer would dominate the resistance for samples #5-#7, the leakage measurement after initial "forming" would be expected to deviate from the limiting value. The statistical scattering can therefore most likely be explained by slight oxidation effects which are creeping below the Pt capped HfO_{2-x} layer and are dissolved into the conducting hafnium oxide matrix after "electroforming". Therefore, the limiting value can be assigned to contact resistance of the stack and electrical setup but not the hafnium oxide layer. This example highlights the limitations of "two-point" electrical characterization between top and bottom electrode (which is primarily done form RRAM characterization), where contact resistance can play an important role and needs to be considered for data interpretation. Finally, the electrical characteristics of both series A and B (in device configuration and as plain HfO_{2-x} layer) are in good agreement, confirming the transition from insulating to conducting behavior in the vicinity from *m*-HfO_{2-x} and *r*-HfO_{2-x}.

4.3.6. Conduction Mechanisms in *m*-HfO_2, *r*-$HfO_{1.7}$ and *hcp*-$HfO_{0.7}$ based MIM devices

This chapter discusses the conduction mechanisms observed in devices with hafnium oxide key structures *m*-HfO_2, *r*-$HfO_{1.7}$ and *hcp*-$HfO_{0.7}$ treated in-air and in-vacuo and therefore expands the view on the electrical properties as already discussed in previous chapters 4.3.3 - 4.3.5. Figure 65 gives an overview of the corresponding I-V characteristics in double logarithmic representation. As can be seen for all switching samples a-d) the LRS follows a slope of ~ 1 which corresponds to Ohmic conduction indicating the transport over (thermally excited) free charge carriers. For the HRS shows a slope of ~ 1 for low voltages but ~ 2 for higher voltages for samples a,b) and d).

This finding indicates space charge limited conduction which is related to conduction over crystal defects [185] and is typically constituted of specific portions. [32, 80] At lower voltages the ohmic region dominates with $I_{Ohm} \propto V$, followed by traps filled limited current $I_{TFL} \propto V^2$. At even higher fields the current is typically characterized by a steep increase (when all traps are filled) followed by another square dependence in form of Childs law $I_{Child} \propto V^2$.[80] For the linear portion the thermally exited free charge carriers dominate the current. At the transition to the first square dependence the rate of injected electrons prevents the conservation of (quasi-) charge neutrality in the system. After this point injected charge carriers dominate over thermally excited charge carriers. Once all traps are filled the charge carriers are able to move freely though the dielectric, hence causing the steep increase (or jump) in current. After the steep increase the conduction becomes space charge limited, and at this point the I-V characteristics can be described by Child´s law.

For the SCLC regions of the HRS depicted in Figure 65 only the first transition from ohmic conduction (m ~1) to trap filled limited current (m ~2) are verified as the maximum voltage that has been applied in any case is limited by V_{reset}. There is a significant number of publications which identified SCLC in RRAM. [80] It is also worth noting that for hafnium oxide based RRAM the following conduction mechanisms have been reported besides SCLC [84, 139, 186] : Poole-Frenkel emission [81], Schottky emission [82, 83], Trap assisted tunneling [85, 86] and hopping conduction [87]. This highlights the susceptibility of conduction properties with respect to hafnium oxide quality and selection of electrode materials.

For a significant number of RRAM systems SCLC is found in both, the HRS and LRS.[80] However, there are also many cases in which SCLC is only found in the HRS while ohmic conduction is observed in the LRS. [80] The latter case is also observed for the discussed data in Figure 65. This observation fits well to the classical picture of filament formation where a conducting filament (CF) connects the top to the bottom electrode.

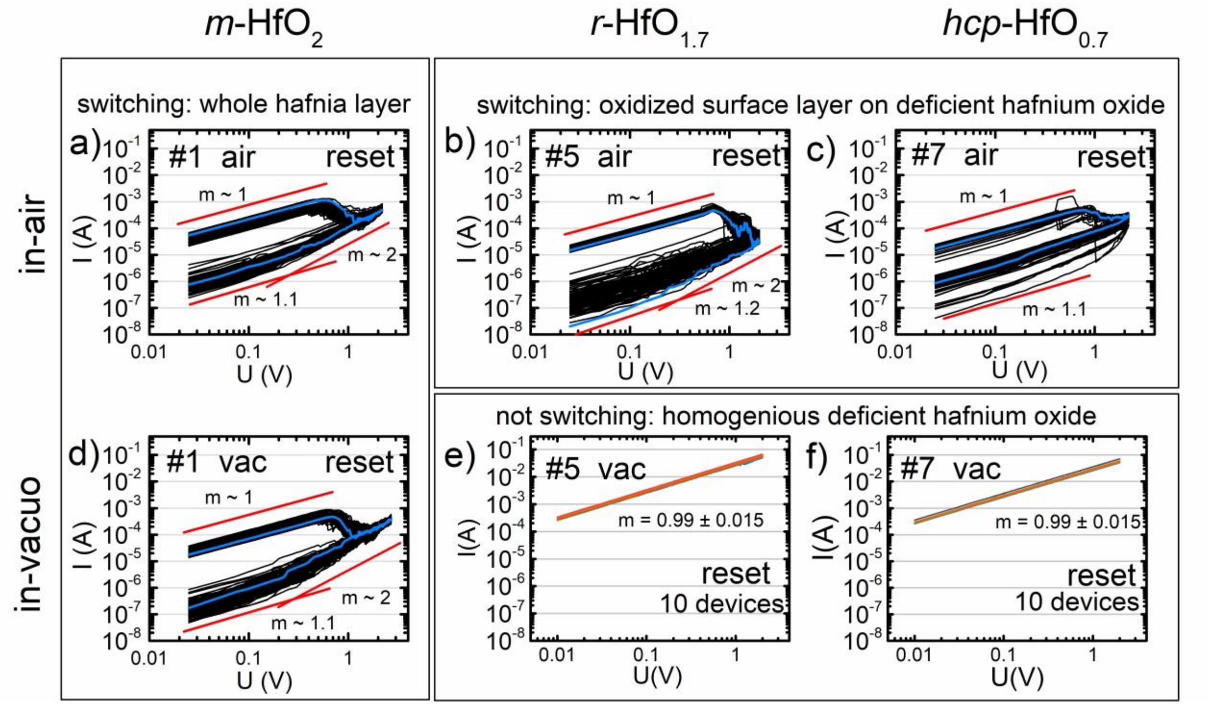

Figure 65: Overview of I-V characteristics in double logarithmic representation for devices with key structures m-HfO_2, r-$HfO_{1.7}$ and hcp-$HfO_{0.7}$ treated in-air and in-vacuo. For all switching samples a)-d) the reset is shown for 100 cycles. Note that the LRS shows a slope of ~1 for all switching devices, which indicates ohmic conduction and therefore conduction over free charge carriers. The HRS generally shows a higher cycle to cycle variability, but corresponds reasonably to space charge limited conduction (SCLC) for a,b,d) as indicated by the transition from a ~ 1 slope to a ~ 2 slope. For the oxygen deficient samples treated in-vacuo 10 devices are shown which only follow a straight line with a slope of ~ 1 indicating ohmic conduction which is in good agreement with the high conductivity of the phases.

In case of ohmic conduction in the LRS it can be assumed that the CF is continuous (or bridges a distance up to the tunneling limit) and shows a significant density of states close to the fermi level. When the conducting filament is locally ruptured as for the HRS, it is sensible to assume that the conduction is also determined by defect states in form of more isolated oxygen vacancies, which fits well to the generally accepted model of SCLC. In this context it is especially interesting that both, in-vacuo treated r-$HfO_{1.7}$ and hcp-$HfO_{0.7}$ show ohmic conduction as can be seen by fitting in Figure 65 e,f). This finding is in good agreement with the significant conduction measured for these phases as discussed in chapter 4.1.4 as well as the observed midgap states in the vicinity of the fermi level as shown in chapters 4.1.5 & 4.2.3. This finding further verifies both phases as potential oxygen deficient conducting filament structures.

4.3.7. OxRAM with Conventional 35nm Compared to 200 nm TiN Bottom Electrodes for Operando TEM

To allow operando TEM measurements on FIB prepared RRAM lamellae, it is crucial that the electrode thicknesses are sufficient to allow for proper contacting on the biasing chip but also to avoid critical buildup of joule heating during switching. Those issues have already been addressed in chapter 3.6 where the fabrication process of a μm thick metallic top electrode for FIB preparation is shown. This chapter is concerned with the more critical growth of an epitaxial TiN bottom electrode (on c-cut sapphire) of several 100 nm thickness which would allow the growth of high crystal quality hafnium oxide on top. However, thicknesses of this magnitude are not easily accessible with MBE. With the optimized growth conditions which allow for highly crystalline TiN growth (0.2 Å/s Ti; 0.6 sccm N_2 340 W) deposition times of multiple hours would be necessary to achieve a minimum thickness of ~ 200 nm which cannot be implemented as a standard routine as the process requires nonstop monitoring and control of the disposition parameters. Further it is reasonable to avoid excessively long deposition times to protect the PVD setup from potential damage due to heat buildup as a consequence of e-beam evaporation but also overly extensive sample rotation and substrate heating. To allow for the faster growth of a thicker bottom electrode, the initial rate was increased to 0.9 Å/s for most of the deposition time up to a QCM measured value of 2000 Å and then reduced down to 0.2 Å/s for additional 350 Å in QCM thickness (about additional 30 nm TiN).

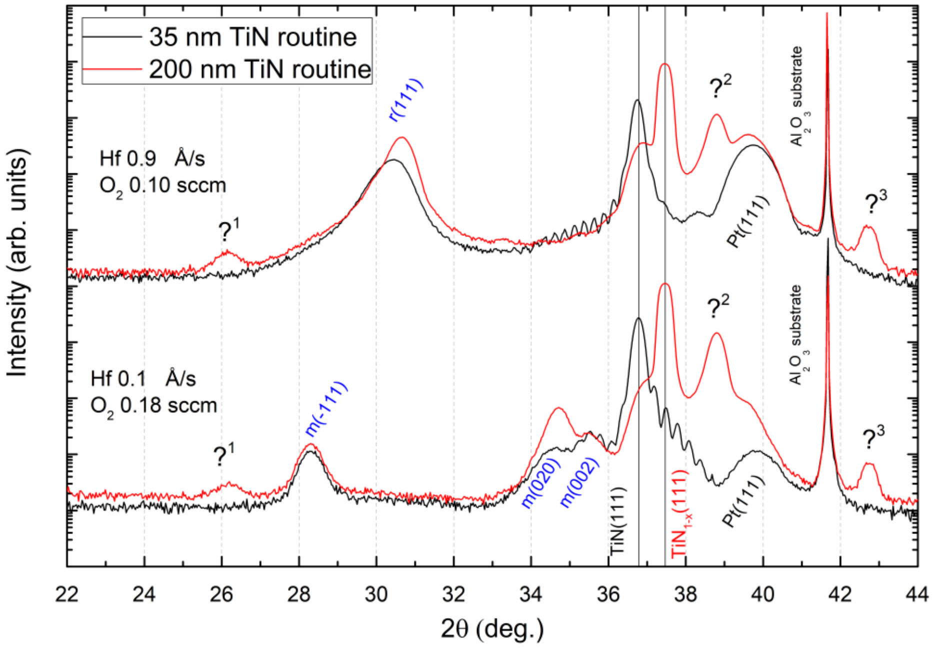

Figure 66: Comparison of crystalline quality for oxygen deficient rhombohedral hafnium oxide and stoichiometric monoclinic hafnium oxide grown on 35 nm TiN and 200 nm TiN respectively. Note that for both hafnium oxide phases at least the same reflection intensities are visible. For the TiN layer a shift to TiN$_{1-x}$ as well as additional reflections can be seen which are likely metallic or subnitride phases which would be expected for the fast growing initial layer for 200nm TiN. ?^{2} corresponds likely to an additional (200) TiN orientation. The additional reflection close to (111) TiN suggests a back-shift to close to stoichiometric TiN for the final 30 nm of deposition.

The goal of this kind of deposition strategy is to first initiate a fast growing layer, which serves as an electrical contact. For this fist layer stoichiometry and film quality is not required to be optimal and the layer should primarily maintain epitaxial conditions. For the last 30 nm the deposition conditions are then changed back to the optimized conditions, to achieve a close to stoichiometric, high crystal quality TiN layer.

Figure 66 compares the crystalline quality for oxygen deficient rhombohedral hafnium oxide and stoichiometric monoclinic hafnium oxide (20 nm in every case) grown on 35 nm TiN and 200 nm TiN respectively. In both cases the intensities of the rhombohedral or monoclinic reflections are comparable, confirming that the crystal quality of hafnium oxides can be maintained also on 200 nm TiN. Nonetheless there are some additional reflections which show up in addition to the well-defined (111) TiN reflection as visible for the 35 nm film (Compare PDF 00-038-1420). First there is a shift of the (111) TiN reflection from 36.8° to 37.4° 2θ which indicates the growth of a nitrogen deficient layer of TiN_{1-x} as expected for the initial layer grown at 0.9 Å/s. Further there are some reflections (indexed $?^1$-$?^3$) which could not unambiguously be identified but are likely metallic or subnitride phases or different TiN orientations. The reflection at 38.89° in 2θ ($?^2$) is close to 38.42° which corresponds to the metallic hexagonal titanium (PDF 00-044-1294) which would be sensible but the larger angle suggests a smaller lattice parameter as compared to a purely metallic system. Further the angle at 42.72° ($?^3$) is close to 42.59° which corresponds to (200) TiN, indicating the appearance of an additional TiN orientation. Especially nitrogen deficient phases such as potential metallic Ti can most likely by assigned to the initial layer grown at a high rate. This is supported by the finding that for both samples with a 200 nm layer a smaller reflection is also present close to (111) TiN, indicating a "back-shift" from (111) TiN_{1-x} after the reduction from 0.9 Å/s to 0.2 Å/s.

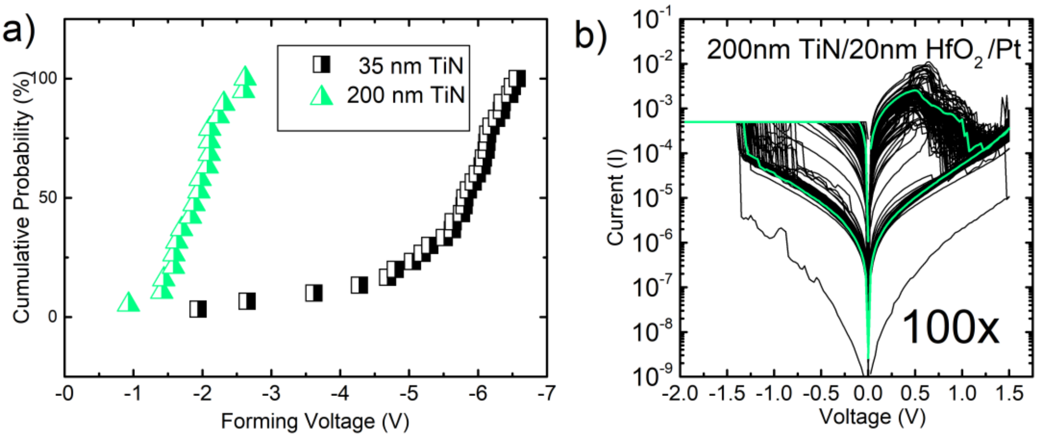

Figure 67: a) Comparison of forming voltages for stoichiometric m-HfO_2 (prepared in-vacuo) on 200 nm TiN and 35 nm TiN. Note that the Forming voltage statistics are significantly reduced for HfO_2 grown on 200 nm TiN which could be due to increased roughness. b) shows 100 cycles of a corresponding RRAM device with thick bottom electrode verifying its applicability for operando TEM.

To further verify the applicability of the growth method for operando TEM, the stoichiometric *m*-HfO_2 samples have been prepared and patterned as TiN/HfO_2/Pt devices for electrical testing. Figure 67 a) shows the corresponding cumulative distribution of forming voltages. While the forming for the samples on 35 nm TiN is in the range of -6 V (as expected for 20 nm of HfO_2) the forming voltages are significantly reduced to about -2 V for the sample with thick bottom electrode. This effect could be due to increased roughness (where the electrical potential is concentrated on local features). Alternatively, the forming voltage could also be reduced due to an oxygen scavenging effect if the top TiN layer would show some strongly nitrogen deficient or metallic inhomogeneity's from the fast growing layer below. Figure 67 b) shows 100 cycles of switching for a corresponding device with thick bottom electrode, verifying the fundamental applicability for operando TEM investigations. While the electroforming statistics indicate that samples grown on 35 nm and 200 nm bottom electrodes do not show identical characteristics, it was shown that the high crystal quality can be reproduced. Further it was demonstrated that such devices can show reliable switching characteristics. Therefore, the applied method proves to be promising to grow about 200 nm and potentially also significantly thicker bottom electrodes for operando TEM investigations. Further analysis by TEM methodology would also help to verify the homogeneity and/or roughness of the TiN top layer.

4.4. Transmission Electron Microscopic Nanoscale Identification of Substoichiometric Hafnium Oxide Phases

The localization of specific phases, their structural and chemical verification on the nanoscale and the identification of their relative arrangement and size of crystalline grains in form of the microstructure allow for a crucial view on thin film properties in particular. In the context of RRAM methods, which are connected to transmission electron microcopy show unique potential, as they allow to correlate nanoscale features such as grain boundaries or interfacial effects with electrical device properties. In filament based RRAM special attention is given to the nanoscale switching mechanism which is characterized by the formation and rupture of a conducting filament. As mentioned in chapter 1.4 in hafnium oxide based OxRAM the conducting filament transports the current between top and bottom electrode and is believed to be formed out of oxygen deficient hafnium oxide. Especially in the last year's relevant progress has been made towards the nanoscale characterization of the nature of conducting filaments in hafnium oxide based devices. Celano et al. performed 3D imaging of a CF region in a Ru/Hf/HfO_2/TiN device stack with a "slice-and-view" c-AFM approach. By this technique the area of the CF was identified to be of a conical shape, narrowing from Hf to TiN with a cross-section around 10 nm^2.[187] Privitera et al. reported for a similar stack of Hf/HfO_2/TiN conical shaped CF with diameters in~1-3 nm on the basis of electron energy loss spectroscopy (EELS) analysis.[188] Kumar et al. used scanning transmission synchrotron X-ray spectromicroscopy (STXM) and describes a radial diffusion of oxygen away from a conductive channel and the formation of a surrounding ring with excess oxygen.[189] Li et al. performed in situ TEM studies utilizing electron holography, in situ low-energy-filtered imaging combined with in situ electrical characterization measurements to monitor the oxygen migration in an AlO_y/HfO_x/TiN stack, where it was concluded that oxygen vacancies are formed at the TiN top interface under positive biasing with an oxygen vacancy channel connecting both electrode sides.[190] Yang et al. was investigating the ion motion with electrostatic force microscopy (EFM) and provided TEM-EDX measurements which support the local oxygen deficiency in a CF region.[191]

While most publications mentioned so far had a primary focus either on scanning probe microscopy (c-AFM, EFM) or spectroscopy based TEM methology (EELS, EDX) more recent publications have shifted the attention more on high resolution imaging of local changes in crystal structure. Yin et al. reported the identification of monoclinic but also orthorhombic structures in RRAM devices.[192] Specifically the orthorhombic phase was assigned to the stoichiometric high pressure phase o-HfO_2. [192] Even more focused on crystalline changes is a publication from Zang et al. where hexagonal structures, assigned to h-$HfO_{0.2}$ and tetragonal structures assigned to the stoichiometric high temperature t-HfO2 phase have been discussed as parts of the conducting filament.[193] In the proposed model, h-$HfO_{0.2}$ should act as the core of the CF while m-HfO_2 and/or t-HfO_2 form a shell, surrounding the conducting, close to metallic h-$HfO_{0.2}$ structure.[193]

It is striking that the phases that are described in the above mentioned publications show a high similarity to the substoichiometric hafnium oxide phases discussed in this thesis. In particular, the high pressure phase of orthorhombic HfO_2 as well as the high temperature phase of tetragonal HfO_2 are both distortions from the cubic fluorite type HfO_2 structure, which in turn was used as a close reference for the here described, oxygen vacancy stabilized rhombohedral $HfO_{1.7}$ (see chapters 4.1.2 & 4.2.2). While the authors assign the orthorhombic or tetragonal structures to their insulating stoichiometric equivalents, it is also conceivable that these phases could also be stabilized by oxygen vacancies (as they are closely related rhombohedral HfO_{2-x}). This circumstance appears reasonable in connection with the formation of conducting filaments, where local oxygen gradients are to be expected. This idea is further supported by findings in bulk synthesis, where cubic or tetragonal HfO_2 structures cannot be quenched from high temperatures.[38] If the structures would be oxygen vacancy stabilized this would further imply that they may contribute to current transport as at least the here discussed *r*-HfO_{2-x} showed considerable midgap states and significant electrical conduction (see chapters 4.1.3, 4.1.4, 4.3.5 & 4.3.6). Further similarities are found between the identified hexagonal structure which was assigned to *h*-$HfO_{0.2}$ [193] and the here discussed *h*-$HfO_{0.7}$ (here denoted *hcp*-$HfO_{0.7}$). This hexagonal structure was proposed as the conducting channel in the corresponding publication which would be in good agreement with the here obtained results on *hcp*-$HfO_{0.7}$ which does not show clear metallic behavior but significant electrical conduction. A final comment is that crystalline transformations likely play an central role in both, amorphous or crystalline pristine devices as Joule heating is generally known to play an important role in filament formation, set and reset.[31]

As can be seen from the previous discussion, the high-resolution characterization of crystalline structures should play a key role in the identification of the conducting filament. Nevertheless, the clear identification of phases and their properties on the nanoscale is not a trivial undertaking. A strategy to maximize the informative value of a nanoscale investigation is to combine structural measurements (HRTEM; HAADF-STEM) with chemical analysis (EDX; EELS) and compare both results with reference measurements on macroscopic samples. For this purpose, various transmission electron microscopic analysis methods were used in collaboration with Alexander Zintler to make reference measurements on the sample series described in this thesis. In the following chapter 4.4.1 the structural identification of the phases *m*-HfO_2, *r*-HfO_{2-x} and *hcp*-HfO_{2-x} is demonstrated by means of HRTEM and HAADF-STEM. In chapter 4.4.2 the STEM-EELS analysis is discussed which allows for effective chemical fingerprinting of the corresponding structures. In the final chapter 4.4.3 the use of Automated crystal orientation mapping demonstrates the automated identification of *m*-HfO_2 against the related *r*-HfO_{2-x} structure.

The thickness optimized TiN bottom electrodes (at least 200 nm) and Pt/Au top electrodes (at least 4 μm) for operando TEM that have been elaborated as part of the collaborative efforts between the advanced thin film technology division ATFT and the advanced electron microscopy division AEM can be found in chapters 3.6 & 4.3.7

4.4.1. HRTEM and HAADF-STEM identification of *m*-HfO_2, *r*-HfO_{2-x} and *hcp*-HfO_{2-x}

This chapter shows the local identification of the phases *m*-HfO_2, *r*-HfO_{2-x} and *hcp*-HfO_{2-x} based on high resolution imaging. Figure 68 specifically demonstrates the HRTEM and HAADF-STEM methodology, both of which are suitable for identifying real space lattice constants. For the purpose of phase identification, the observed lattice planes can be directly compared to e.g. values from powder diffraction databases, or macroscopic XRD measurements. However, to extract reliable length scales with high resolution imaging calibration against a reliable reference must be performed. For this purpose, usually the single crystalline substrate is used for which the lattice constants are known in literature or provided by the supplier. For all samples shown in Figure 68 the measurements are calibrated against the substrates (bright contrast) which are of common c-cut sapphire with (001) orientation.

Figure 68 a-c) shows HRTEM images which are therefore based on phase contrast. In all three cases a) m-HfO_2, b) r-HfO_{2-x} and c) hcp-HfO_{2-x} the hafnium oxide layers appear highly crystalline with the insets showing the out of plane lattice planes with the corresponding lattice parameters being extracted via fast Fourier transformation. As already discussed in chapter 4.1.6 the extracted values are in good agreement to the out of plane lattice constants extracted from XRD measurements. For the samples shown in Figure 68 d,e) the imaging is based on high angle annular dark field in a scanning transmission electron microscopy setup. HAADF is recorded at higher angles than annular dark field (ADF) or Bright field (BF) and known for its susceptibility to Z-contrast. The image shows darkest contrast for TiN, lightest for Pt and the medium contrast for HfO_{2-x}. For Figure 68 d,e) the insets show overlays with corresponding multislice calculations, which allows to identify individual grain orientations. The simulations confirm the m-HfO_2 (010) projection for the grain investigated in Figure 68 d) and the corresponding (01-1) projection for r-HfO_2. It should be noted that the shown simulation for r-HfO_{2-x} was based on a cubic unit cell, which is extremely close to the rhombohedral cell (compare chapters 4.1.2 & 4.2.2).

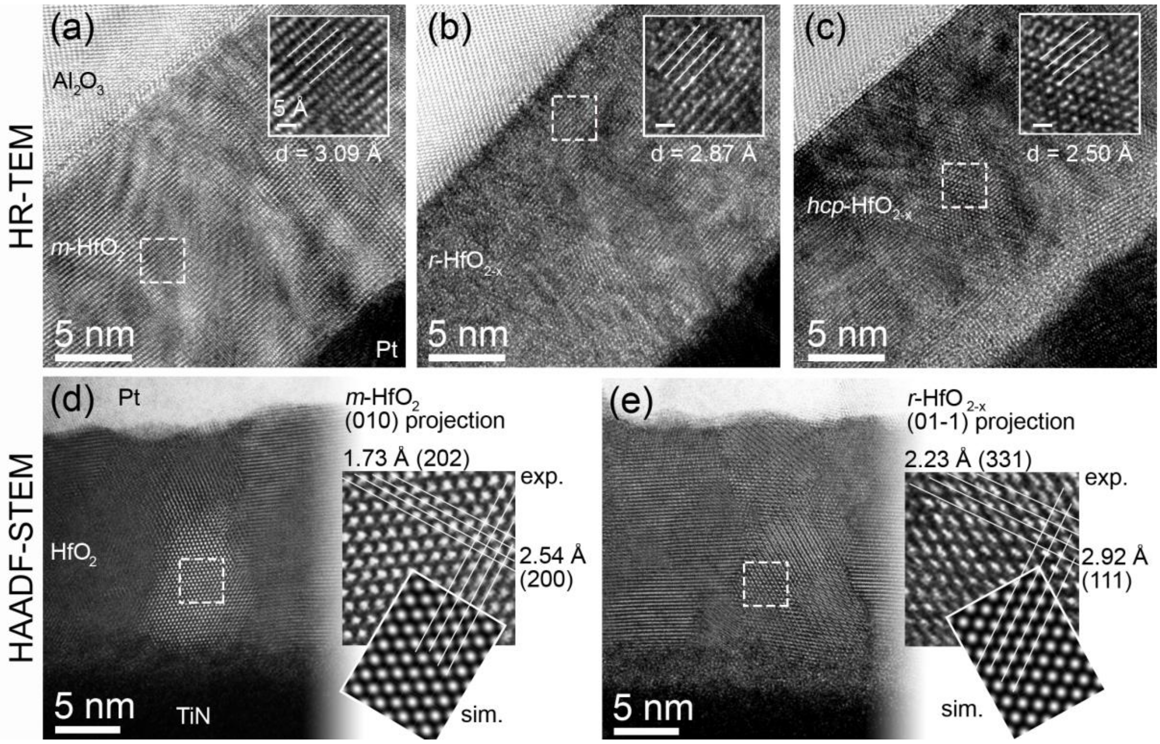

Figure 68: See a comparison between images taken from samples showing the most isolated phases of m-HfO_2 (a,d), r-$HfO_{1.7}$ (b,e) and hcp-$HfO_{0.7}$ (c). The top row shows images resulting from HR-TEM while the lower row corresponds to HAADF-STEM imaging. The top row samples are sandwiched between the sapphire substrate (bright contrast) and platinum for FIB preparation (dark contrast) while for the HAADF images samples are sandwiched between TiN (dark contrast) and Pt (bright contrast). Both methods are suitable for mapping lattice plane distances in real space. The HRTEM images show insets highlighting the of the out of plane lattice parameter while the insets for the HAADF-STEM show different sets of lattice spacing's overlays with multislice simulations. In parts reprinted with permission from reference [146]. https://doi.org/10.1021/acsami.1c09451 Copyright © 2021 American Chemical Society.

Summarizing, it was demonstrated that the observed crystalline structures of m-HfO_2, r-HfO_{2-x} and hcp-HfO_{2-x} can be directly discriminated by high resolution imaging techniques on the nanoscale and shows the high crystallinity of observed hafnium oxide thin films. Since, for example, scanning probe analyses show that the conducting channel in hafnium oxide-based devices is only a few nanometers in diameter, this method is particularly promising for identifying potential structures in the conducting filament region in RRAM.

Nonetheless, as especially *r*-HfO_{2-x} shows strong similarities with stoichiometric hafnia polymorphs such as the cubic and tetragonal high temperature- as well as the orthorhombic high pressure phase (more details are provided in chapter 1.5) the nanoscale identification for the conducting filament identification should be supplemented by chemical analysis in form of EDX or (as discussed in the next chapter) EELS. In this way properties like electrical conduction as measured for oxygen deficient *r*-HfO_{2-x} can be correlated more reliably on the nanoscale.

4.4.2. EELS Fingerprinting of *m*-HfO_2, *r*-HfO_{2-x} and *hcp*-HfO_{2-x}

Electron energy loss spectroscopy (EELS) is an energy-dispersive analysis tool which is often installed in STEM measurement units. While most sensors in STEM are not energy sensitive but primarily count incoming electrons that have been scattered or originate directly from the transmitted incident beam, EELS is able to detect electrons in dependence of their energy lost in the sample. By interacting with the specimen, the electrons may lose energy due to plasmonic or interband excitation.[100] It is possible to probe core electron excitation but also (in some cases) gain information about the bandgap in the low loss region.[100] Therefore, EELS is (comparably to XPS) sensitive for the chemical composition and/or atomic coordination in materials which is of special importance for the here discussed substoichiometric phases of *r*-HfO_{2-x} and *hcp*-HfO_{2-x}.

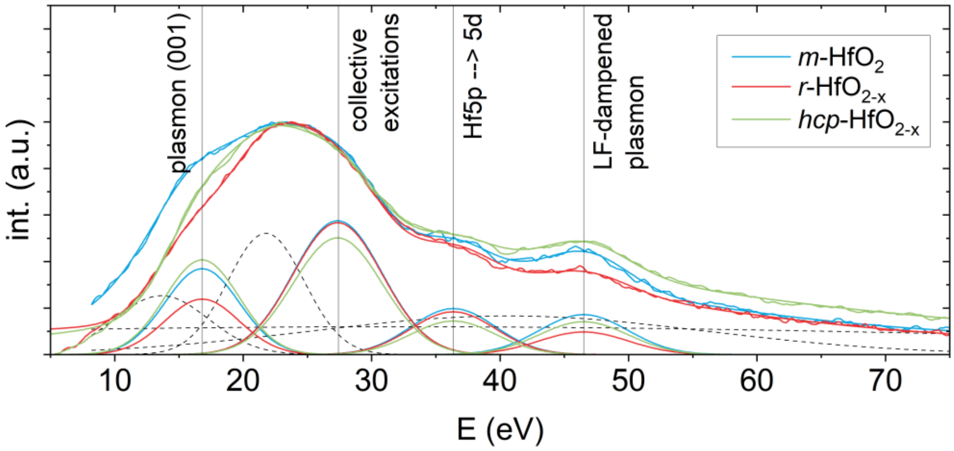

Figure 69: Electron energy loss spectroscopy data of the most isolated phases of *m*-HfO_2, *r*-$HfO_{1.7}$ and *hcp*-$HfO_{0.7}$. The obtained spectra are averaged over the sample growth thickness of ~ 20 nm, scanning the low loss region. All spectra have been normalized after background subtraction. The Graph shows fitting of the main components (vertical lines) where dashed lines correspond to constant contributions.

Figure 69 shows EELS spectra of the samples *m*-HfO_2, *r*-$HfO_{1.7}$ and *hcp*-$HfO_{0.7}$ as presented in the previous chapter. Those spectra were obtained by scanning across the sample growth thickness of 20 nm and by excluding the interface regions by 1 – 2 nm. It should be noted that the spectral response in EELS is dependent on the crystallographic anisotropy of the investigated phase. This effect is specifically described for hafnium oxide by Guedj et al.[194] Therefore, for all samples the obtained spectra can be understood as fingerprints being averaged over different grain orientations. From the main components that are indicated by vertical lines it can be seen that the corresponding phases can be assigned by analyzing the relative intensities of the plasmon (001) and the LF-dampened plasmon which show significant changes in dependence of the measured phase.

Utilizing mapping in inhomogeneous samples or by checking local changes in a conducting filament region, this data can be used to discriminate the recorded phases on the nanoscale. As previously noted, in order to maximize the informative value for definitive phase identification such measurements can be combined with structural analysis. This can be achieved manually by analyzing high resolution images as discussed in the previous chapter or by applying advanced structural analysis in form of automated crystal orientation mapping (ACOM). The corresponding ACOM analysis on the here discussed hafnium oxide structures is given in the next chapter.

4.4.3. Automated Crystal Orientation Mapping for *m*-HfO_2 and *r*-HfO_{2-x} Phase Separation

As already discussed in the previous chapters, the correlation between structural and chemical analysis provides the highest information value with regards to phase identification. In chapter 4.4.1 the classical approach of manual high resolution structural identification was already shown. However, such measurements are not easy when it comes to investigating large areas.

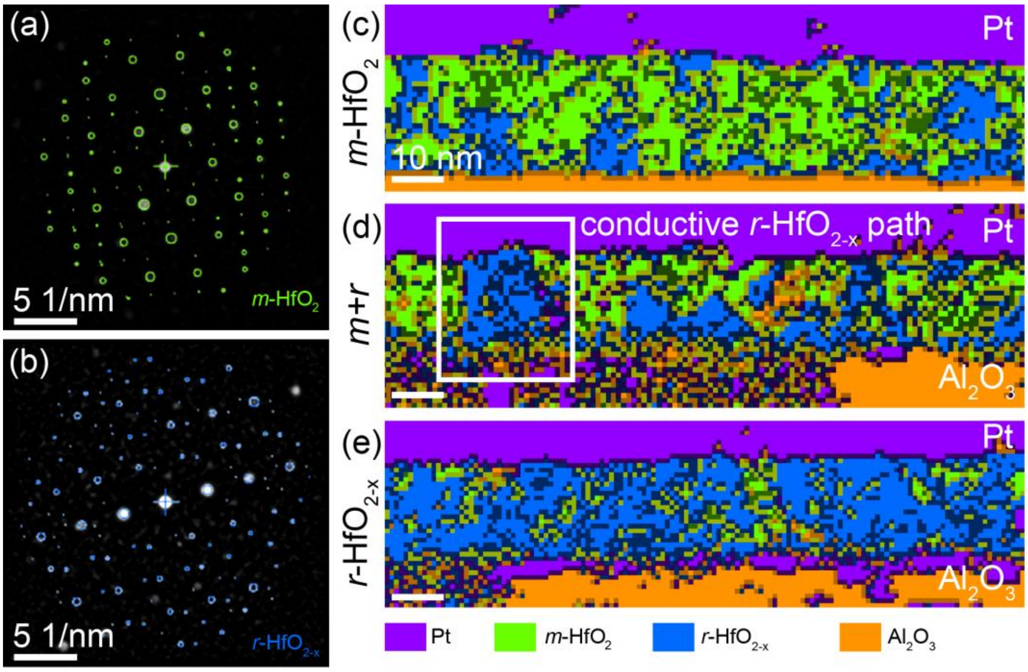

Figure 70: (a,b) Nano beam electron diffraction patterns of hafnium oxide grains which match the corresponding templates for *m*-HfO_2 and *r*-$HfO_{1.7}$. (c-e) 2D ACOM maps of (c) only *m*-HfO_2,(d) mixed m- + *r*-HfO_{2-x} and (e) only *r*-HfO_{2-x}. Note that in (c,e) the majority of pixels are correctly assigned and that in the mixed case (d) both phases are assigned to almost equal portions. Note specifically the continuous *r*-HfO_{2-x} area between the Al_2O_3 substrate and Pt which represents a conducting path due to phase-property correlation.

ACOM significantly expands the area which may be analyzed as it can (once optimized) automatically assign different structures and crystal orientations in the scanned sample. In this way length scales of several hundred nanometers with hundreds of individual grain orientations may be covered. This is achieved by the use of scanning precession electron diffraction in which a ~1nm diameter quasi-parallel electron beam is scanned across the sample. For each pixel in the map with a pixel pitch roughly equaling the electron probe diameter, a diffraction pattern is generated and captured by a 2D sensor.

Figure 70 a,b) shows exemplary diffraction patterns which are matched to the corresponding templates of m-HfO_2 and r-HfO_{2-x} respectively. It should be noted that the matching of r-HfO_{2-x} was done using a cubic cell, which is a good approximation as the rhombohedral cell can be understood as pseudocubic (compare chapters 4.1.2 & 4.2.2). As a 2D diffraction pattern is observed for every point the incident beam is directed to in 2D real space, such kind of analysis is often referred to as 4D STEM. Figure 70 c-e) shows resulting 2D ACOM maps of (c) only m-HfO_2, (d) mixed $m + r$ –HfO_{2-x} and (e) only r-HfO_{2-x}. As can be seen for (c) m-HfO_2 and (e) r-HfO_{2-x} the majority of pixels has been assigned correctly by the software routine. For the mixed case $m + r$ (d) the assigned ratio of m to r appears at close to equal amounts. Note that additional information which can be analyzed like the grain orientations for each phase fraction is not shown here for sake of simplicity. ACOM analysis was also performed for the work of Tobias Vogel et al., who showed similar, if not identical transformation from m-HfO_2 to (presumably) r-HfO_{2-x} through ionic radiation with Au ions, yielding 1.635 GeV at fluencies up to $8*10^{12}$ ions/cm^2.[195, 196] For these studies special attention was also given to transformations in the microstructure. The optimized data analysis for the here discussed thin films shows that it is likely suitable to identify local agglomerations of specific phases as can be seen in Figure 70 d). Here r-HfO_{2-x} is found to connect both interfaces from the Al_2O_3 substrate to Pt deposited for TEM sample preparation. In the context of operando TEM on hafnium oxide based RRAM, this could highlight an area in which a conducting filament may have been formed. If the phase was additionally verified as oxygen deficient, it would serve as a strong indication for a conducting path of r-$HfO_{1.7}$.

4.5. Scanning Probe Microscopy Analysis of Microstructure and Local Conduction

The influence of the microstructure on leakage behavior in high k-dielectrics was investigated in many publications. Results specifically on hafnium oxide are often based on modelling or DFT[85, 197-199] calculations or c-AFM methodology[200-202]. In more recent publications it was shown for RRAM that electroforming in hafnium oxide based microstructures that are defined by highly crystalline growth, combined with a specific subset of grain boundaries, can function as predefined formation path. Electroforming of such devices can result in preferential device characteristics such as low forming voltage and reliable switching statistics.[139, 172] Therefore the investigation of dielectric microstructures via scanning probe microscopy methods yields interesting results especially in the context of RRAM. The investigation of dielectric materials is of cause commonly focused on insulating, low leakage materials. However, the perspective on strongly modified, originally dielectric materials, like strongly doped or oxygen deficient materials allows for a unique viewpoint. Investigating for example strongly oxygen deficient hafnium oxide - as central point of attention in this work - can give specific insights of preferential ways of conduction in dependence of relative grain size, the phase-ratio (e.g. m-HfO_{2-x} against r-HfO_{2-x}) or also with respect to grain boundaries. Those investigations potentially allow to elucidate the role of those microstructural parameters of investigated oxygen deficient phases and their potential role in the electroforming process (compare chapters 4.3.3, 4.3.5 & 4.3.6) or for their use as electrode materials (compare chapters 4.3.3 & 4.3.4).

To answer these open questions, we established collaborative efforts to realize an in vacuo sample transfer from TU Darmstadt to FZ Jülich (Prof. Dittmann, Prof. Waser). In this way oxygen deficient hafnium oxide, as shown in this thesis, can be transported to the scanning probe methods units in Jülich. For this purpose, a custom designed vacuum suitcase from Mantis Deposition Ltd. was used which is equipped with an ion getter pump and a vacuum gauge. The suitcase is capable of holding six samples in a garage (plus one on the manipulator). The suitcase is mounted on a height and angle adjustable frame, which allows the setup to be mounted to all relevant facilities at TU Darmstadt namely to the MBE unit, the ADOMBE system and the Daisy Bat system. Most importantly, the flexible adjustment system also allows the vacuum suitcase to be mounted on the relevant integrated systems in FZ Jülich.

In order to realize the full transfer from sample deposition at TU Darmstadt (by Nico Kaiser) to subsequent SPM analysis in Jülich (by Niclas Schmidt) a custom omicron-type sample holder was collaboratively designed to be compatible with all relevant systems. Special attention was given to the used alloy, which was chosen to be Inconel 718 (commonly used at FZ Jülich and compatible with TU Darmstadt facilities), the clamped sample design, which is a perquisite for some instruments in Jülich, and the thickness of the holder (also considering screws). The thickness of 1.5 mm was chosen to compensate for heat loss during deposition on the clamped holder design. In Darmstadt mostly 2.0 mm thick omicron holders are used in conjunction with silver-glue attachment. Also, the total thickness of the holder including screws is a crucial factor since some tested standard holders with slightly increased thickness did not fit properly into the Darmstadt MBE garage. The final design, which combines all requirements, is referenced in the appendix (Figure 77).

4.5.1. Reproduction of Substoichiometric Hafnium Oxide on Collaborative Sample Holders and Grain Size Effects

This chapter discusses the reproduction of the growth of substoichiometric hafnium oxide on the collaboratively designed sample holders between TU Darmstadt and FZ Jülich (see in the previous chapter and appendix Figure 77). Figure 71 shows the XRD results of two sample series, which cover the range for a transformation from m-HfO_2 to r-$HfO_{1.7}$ with the difference being the calibrated thickness of hafnium oxide with a) 10 nm and b) 20nm. The XRR data of both series have been fitted using a two layer system in order to verify the final film thickness (compare chapter 4.3.1). While the 20 nm series is more comparable to previously synthesized 20 nm series discussed in chapter 4.3.1, the 10 nm series was fabricated in consultation with FZ Jülich to reduce the forming voltages for close to stoichiometric samples.

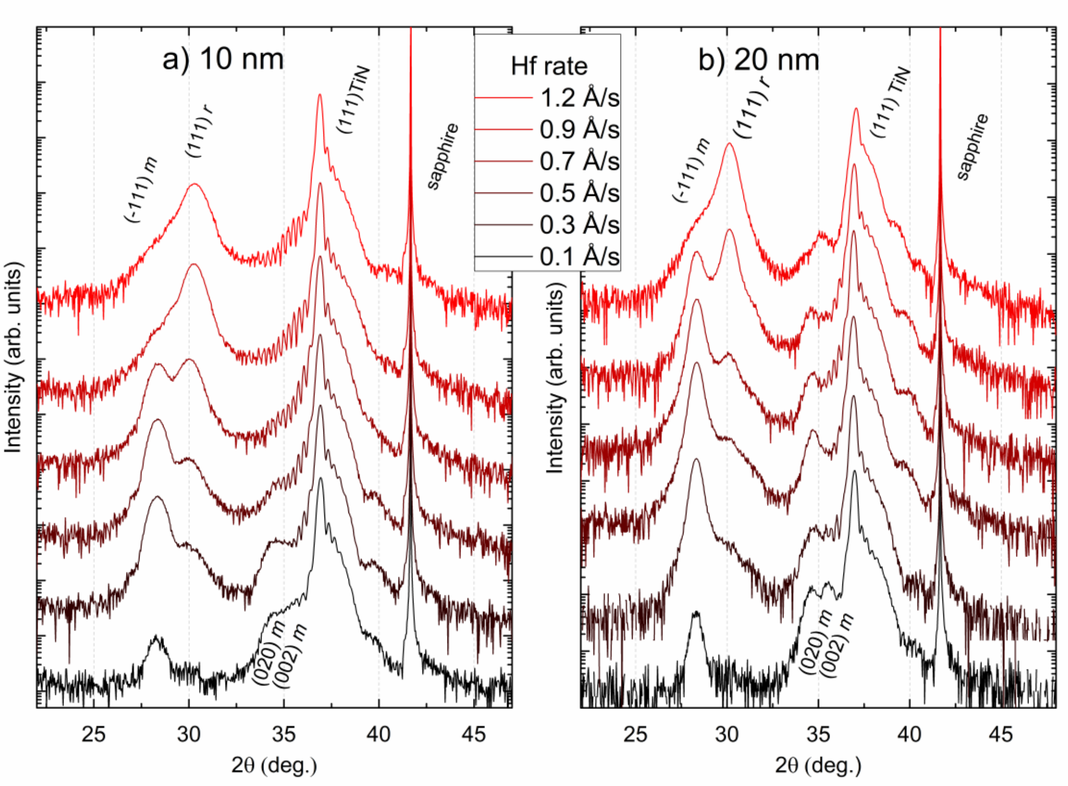

Figure 71: XRD data of two series from m-HfO_2 to r-$HfO_{1.7}$ calibrated to either a) 10 nm and b) 20 nm thickness on collaborative substrate holders. Both, the reproduction of TiN and HfO_{2-x} appears in good quality compared to growth on conventional sample holders. The phase transition from a monoclinic to a rhombohedral structure is best replicated by the 20 nm series, while the 10 nm series shows a tendency towards an overall increased rhombohedral phase fraction. This finding could indicate that the rhombohedral phase favors smaller grain sizes.

TiN was grown in conjunction with previous depositions (compare chapter 4.3.1) with a nitrogen flow of 0.6 sccm, a constant RF plasma power of 340 W and a substrate heating temperature of 800 °C. While for the 20 nm HfO_{2-x} series TiN was grown with a titanium rate of 0.2 Å/s, it was set to 0.3 Å/s for the 10 nm series to reproduce the TiN growth after subsequent cleaning of the N_2-plasma aperture (in boiling aqua regia). Both series have been grown utilizing the collaborative sample holder by using 10 x 10 mm² c-cut sapphire substrates (instead of usually 5 x 5 mm²) and by clamping the samples instead of attaching them via silver glue. First, it can be seen that high quality TiN could be reproduced in both cases as indicated the defined maxima which are close to the bulk value (PDF 00-038-1420) with Laue oscillations (also see chapter 3.3). The reproducibility can be attributed to similar temperature signatures between samples previously grown on both sample holders which have been read out by a front IR sensor in the MBE chamber. One difference to the TiN deposition in chapter 4.3.1 is the small shoulder which appears at higher 2θ angles close to the (111) TiN reflection. This is likely the product of the elevated growth rates right at the beginning of the TiN growth, which is detailed in chapter 3.3.

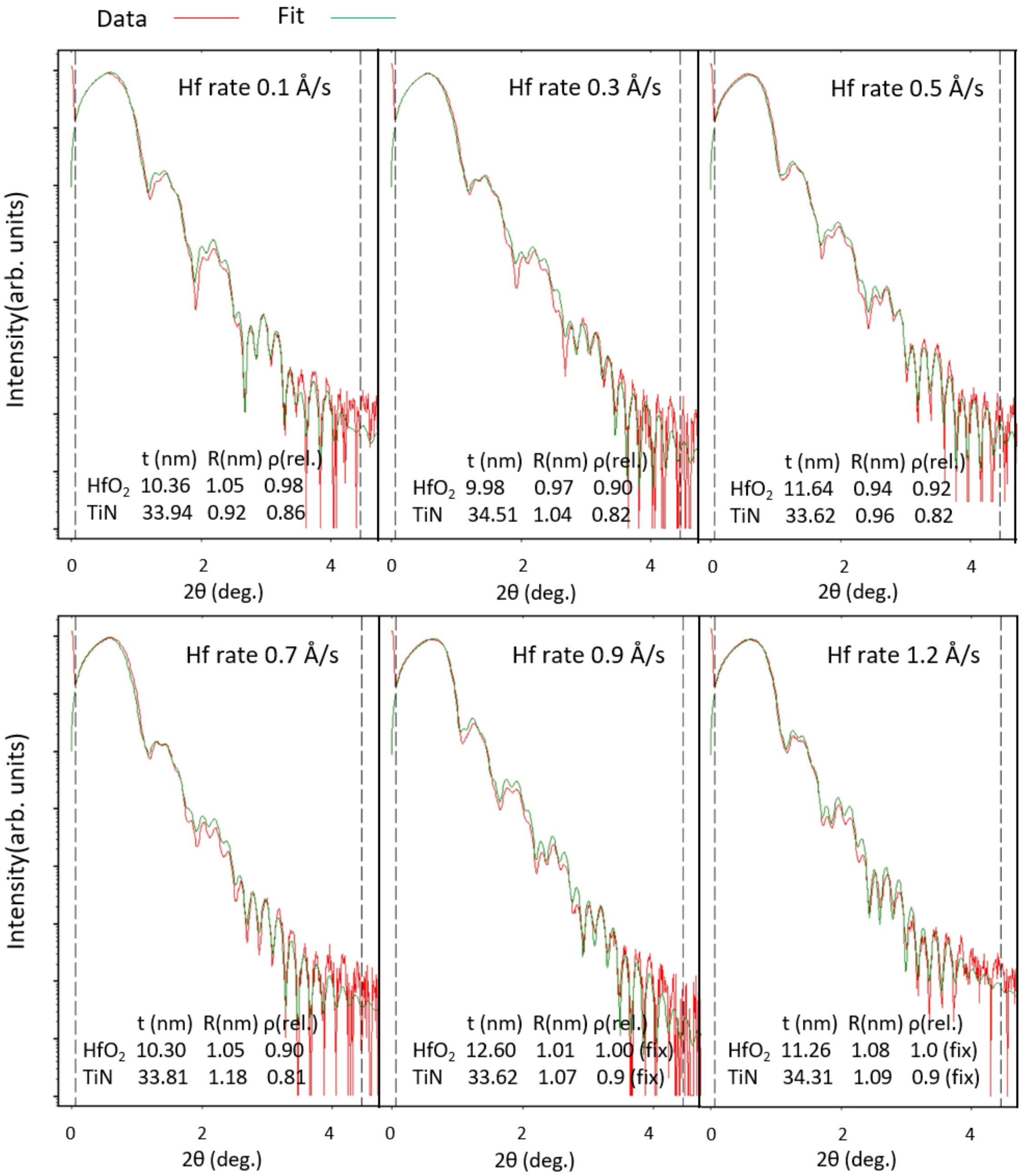

Figure 72: XRR data and corresponding fit via XRR RefSim of all samples of the 10 nm series. Reasonable fitting results could be obtained in any case using a two-layer model of $HfO_2/TiN/Al_2O_3$. The extracted values indicate consistent TiN thicknesses close to 34 nm and HfO_{2-x} thicknesses close to 10 nm throughout the series. Further for all samples the Air/HfO_{2-x} surface as well as the HfO_{2-x}/TiN interface both show a virtually identical roughness close to 1 nm.

The hafnium oxide growth also shows a high level of reproducibility. Note that for the series depicted in Figure 71 all samples have been grown with an identical oxygen flow of 0.18 sccm and a forward plasma power of 200 W. The data demonstrates that the synthesis from monoclinic hafnium oxide to rhombohedral hafnium oxide can be accessed by only changing the hafnium rate from 0.1 Å/s to 1.2 Å/s. The growth conditions are different from previously chosen conditions, where the rate was stopped at 0.9 Å/s with subsequent reduction of the oxygen flow. Nonetheless up to a hafnium rate of 0.9 Å/s the growth conditions are identical to the previously discussed series in chapter 4.3.1 which was grown using conventional substrate holders (and silver glue). Especially the series grown with 20 nm thickness yields a high level of reproducibility in comparison to the series in chapter 4.3.1 as both start out with monoclinic reflections only, and end at 0.9 Å/s, 0.18 sccm O_2 with almost equal intensities for the *m* (-111) and *r* (111). Interestingly, for the 10 nm series, the general trend of a transition from the monoclinic to the rhombohedral phase is conserved, however it seems to more strongly favor the rhombohedral phase fraction. While this observation could be a result of secondary parameter variation during growth, it is known that the grain size can affect the total energy due to surface energy effects.[203] Therefore, the obtained results might serve as in indication that smaller grain sizes favor the rhombohedral over the monoclinic modification.

Figure 72 shows the corresponding XRR data of the 10 nm series being fitted via XRR RefSim.[93] All fitting was done using a two layer model system of HfO_2/TiN/Al_2O_3. By extracting the thicknesses consistent values close to 34 nm for TiN and 10 nm for HfO_{2-x} have been obtained throughout the series. Further, for all samples close to identical roughness values have been obtained for both the Air/HfO_{2-x} surface and the HfO_{2-x}/TiN interface. While such a roughness can be considered small in thin film growth, the roughness at the substrate interface TiN/Al_2O_3 (~ 0.3 nm) are still significantly smaller. As both the HfO_{2-x}/TiN interface and then the Air/HfO_{2-x} surface show the same roughness it is reasonable to assume that the roughness is initiated by the TiN thin film and just transferred onto the HfO_{2-x} layer which itself does not add considerable roughness.

4.5.2. In-Vacuo Scanning Probe Microscopy

While the previous chapters discussed the reproduction of *m*-HfO_2 to *r*-HfO_{2-x} on the collaborative sample holders which are essential for the in-vacuo sample exchange between TU Darmstadt and FZ Jülich, this section is about corresponding scanning probe microscopy measurements. Note that the previously discussed measurements which have been performed at an X-ray goniometer (XRR and XRD) cannot easily be measured in ultra-high vacuum conditions. Therefore, the samples which have been discussed in the previous chapter have all been exposed to air. However, a complementary series using the very same deposition conditions has been reproduced in the same deposition run, and strictly stored and transported in-vacuo using the previously discussed vacuum suit case from Mantis Deposition Ltd. This was necessary as the previously mentioned method of detaching selected samples as from conventional sample holders (see chapter 4.3.2) is not possible with the design of the collaborative sample holder. First, the samples are clamped in (not glued) and second only one 10 x 10 mm^2 substrate can be attached per sample holder. To ensure the applicability of the c-AFM measurements, electrical contact between the sample surface and the sample holder needed to be verified (specifically as the used sapphire substrates are insulating). For this purpose, after TiN deposition on a sample holder, the conductivity was tested via a voltmeter (see appendix Figure 76 a). The transport of in-vacuo stored samples is shown in Figure 76 b) (appendix), where the suitcase is separated from the frame for easy transportation. Also note the 12 V connection which assures a continuous power supply during the transport in a vehicle. Figure 76 c,d) (appendix) shows the vacuum suitcase after successful connection to a central UHV distribution chamber from the division Elektronische Materialien (PGI-7) and transfer of samples from Nico Kaiser (right) to Niclas Schmidt (left) who then performed the SPM measurements which will be discussed in the following.

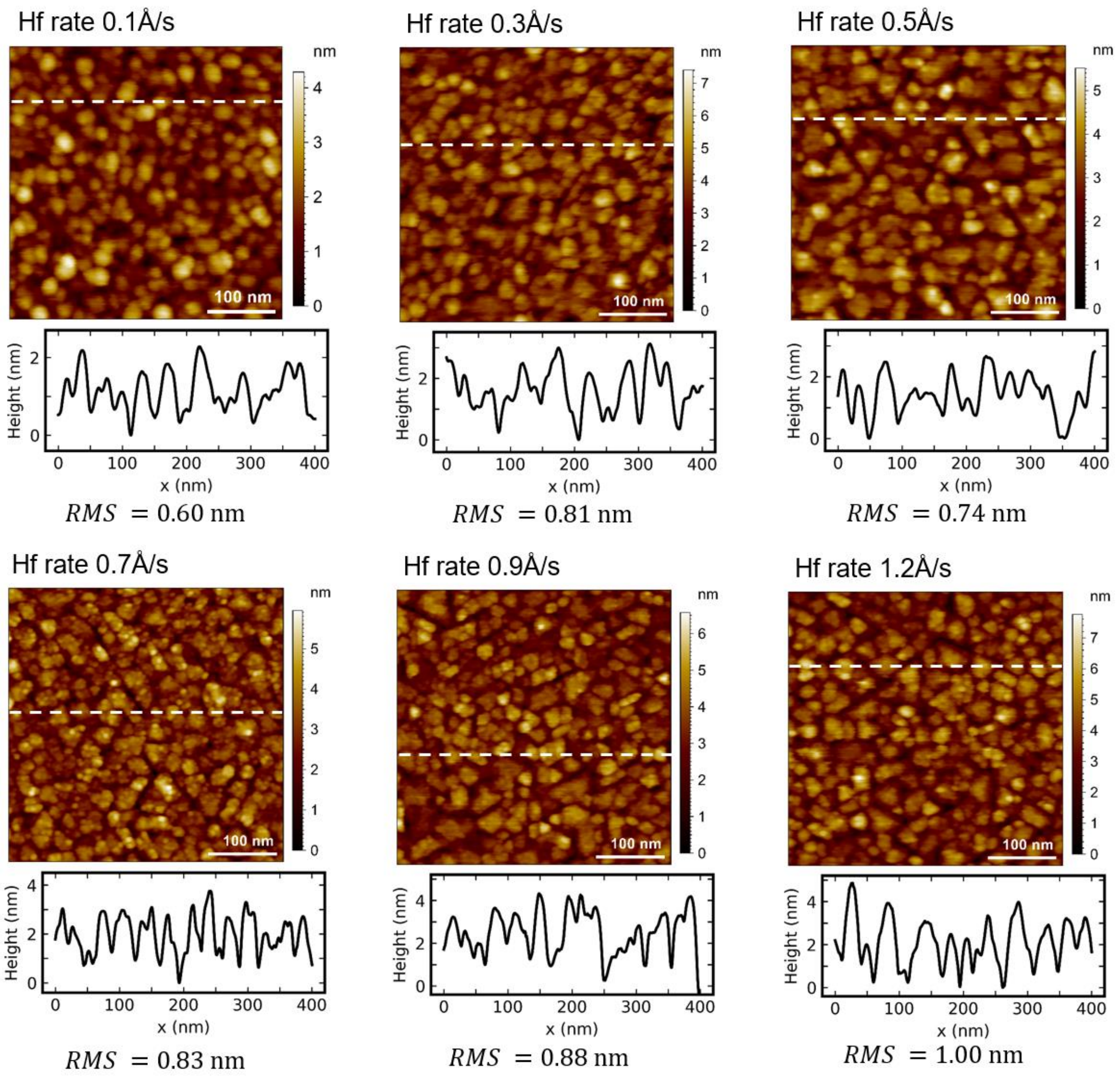

Figure 73: AFM topography of the 10 nm sample series from monoclinic (0.1 Å/s) to rhombohedral (1.2 Å/s) hafnium oxide which was performed in UHV conditions (10^{-9} mbar), using a PtIr-cantilever (r < 25 nm) with a force set point of 1.0 nN. Note that the topography shows lateral grain structures of several 10 nm for all samples. The RMS values vary around 0.9 nm and line scans indicate peak to valley distances between 2 – 4 nm for all samples.

Figure 73 displays the by atomic force microscopy (AFM) acquired topography of the transferred 10 nm samples series from the monoclinic (Hf rate 0.1 Å/s) to the rhombohedral (Hf rate 1.2 Å/s) structure. Those samples have been measured with a PtIr-cantilever (r < 25 nm) applying a force of 1.0 nN. Note that the topographic maps show lateral grain dimensions in the range of several 10 nm with line scans indicating peak to valley distances between approx. 2 – 4 nm for all samples. The extracted root-mean-square roughness shows values around 0.9 nm. Therefore, the extracted roughness is close to the ~ 1.0 nm XRR roughness as stated in the previous section. Following the argument from the previous chapter (from XRR analysis) that the roughness is initiated by the TiN layer and mainly transferred by the HfO_{2-x} interface, the measured “grains” could also be transferred topological features from the underlying layer. In any case, the dimensions of observed grains are in the range of several 10 nm and therefore in good agreement with EM high resolution imaging results on *m*-HfO_2 and *r*-HfO_{2-x} thin films which have been directly grown on c-cut sapphire (compare chapters 4.1.6 & 4.4.1).

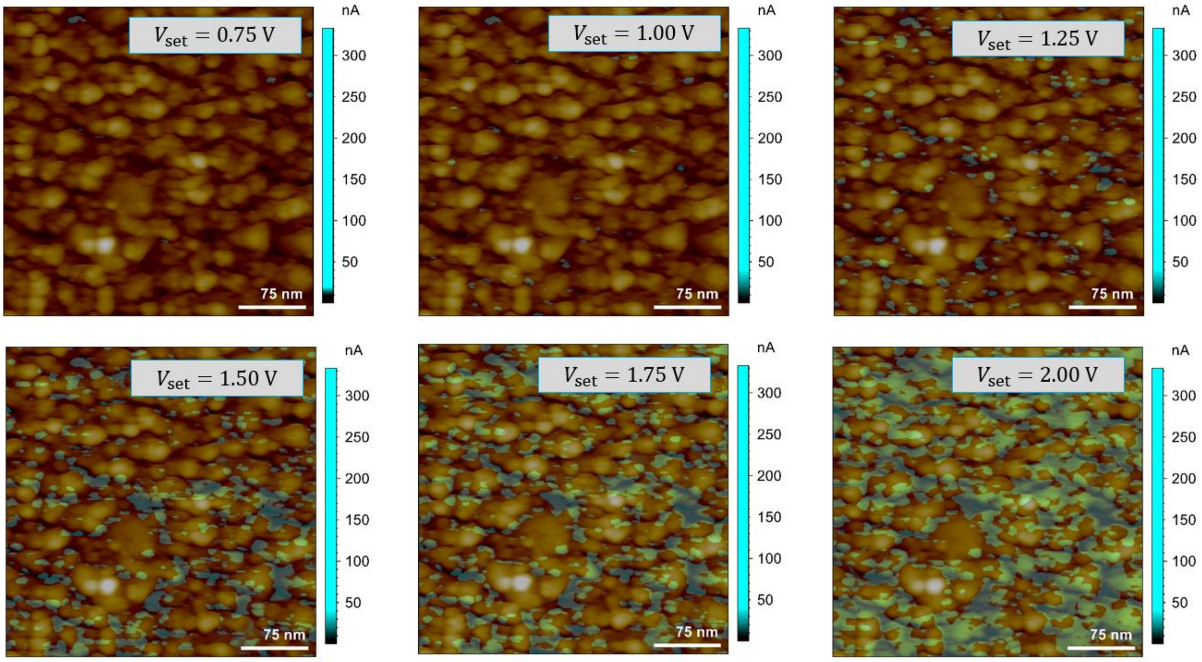

Figure 74: Conductive AFM current maps superimposed over the corresponding topography on oxygen deficient hafnium oxide. The overlay indicates how the formation of preferential conduction paths at different voltages is mediated between supposed grains and therefore at grain boundaries. Current above 10 nA appears cyan.

Figure 74 shows the c-AFM topography of rhombohedral hafnium oxide, grown at a hafnium rate of 1.2 Å/s, superimposed by corresponding current maps at different voltages. Currents below 10 nA are already detected at voltages as low as 0.1 V (not shown). Here, a range of voltages is presented with currents above 10 nA towards the detection limit of the system of 333 nA. As can be seen in the images already at 0.75 V spots of local current above 10 nA are indicated by cyan color. Comparing those results to previous Van der Paw measurements (chapter 4.1), DFT calculations (chapter 4.2) or measurements on macro devices (chapter 4.3) even higher conductive responses would be expected. Nonetheless, for such c-AFM specific contact resistances between cantilever tip and sample surface apply. At the same time, current is detected with high locality since it is confined to the cantilever tip apex. A reduced current measured by c-AFM is therefore expectable compared to currents measured in devices by extended electrodes. Further, through the demanding sample transport, it is conceivable that the samples could have been exposed to slight oxidation effects despite the vacuum transfer. Nonetheless, with detectable currents at low voltage of 0.1 V (not shown), the highly oxygen deficient sample however has to be considered as highly conductive matching the stabilized rhombohedral phase properties. By gradually increasing the voltage, it becomes clear that the current is mediated between the topological heights. Therefore, it is reasonable to assume that the current transport preferentially happens over grain boundary regions. This effect is well known for stoichiometric thin films where the increased defect density in those regions provides favorable leakage paths. More recently it was also proven that grain boundary engineering can lead to reduced forming voltages and preferential switching statistics.[139, 172] The here presented data however reveals that the role of the microstructure and grain boundaries can also be of significant relevance for oxygen deficient hafnium oxide.

The mediation of current along grain boundaries indicates that grain boundary engineering could also be used in such oxygen deficient hafnium oxide layers. While the use as an active layer in RRAM for such highly oxygen deficient layers is out of the question (compare chapter 4.3), it is conceivable that the control of currents given by the microstructure could also be of great benefit in such materials if they are used as RRAM electrode materials as highlighted in chapter 4.3.4. Alternatively, those insights reveal the potential role of the microstructure also for oxygen deprived regions around the conducting filament (compare chapter 4.4).

5. Conclusion & Outlook

In this work, several comprehensive studies were carried out with the aim of gaining a wide-ranging understanding of oxygen-deficient hafnium oxide, its crystal- and electronic structures and other materials properties. Over the course of the investigations, novel rhombohedral (*r*-HfO_{2-x}) and hexagonal (*hcp*-HfO_{2-x}) hafnium oxides with semiconducting characteristics were discovered. The corresponding phases were synthesized by specifically controlling the oxygen content using a Molecular-Beam Epitaxy system and reproduced onto different substrates, in order to either examine physical properties or to characterize the electrical properties such as switching behavior of memory devices in the MIM configuration. Specifically, a band structure model covering the key structures over the whole oxidation range from stochiometric hafnia to metallic hafnium was designed and discussed based on the comprehensive results of the physical properties study. As an important part of this work, the conclusions which were drawn from the experimental results, regarding phase formation, crystal- and valence band structures show excellent agreement with DFT calculations which were produced in collaboration with the theory group of Prof. Valenti (Goethe-Universität in Frankfurt am Main, Germany). The above-mentioned experimental results are mostly acquired by macroscopic measurement techniques such as XRD, XRR, XPS, UV/VIS-transmission spectroscopy, Electrical van der Paw and Hall effect measurements. However, the nanoscale investigation of the discovered electrically conducting hafnium oxides deserves special attention in the quest of capturing the conducting filament in hafnium oxide-based RRAM. Therefore, the identification of synthesized phases through TEM methodology by local structural and chemical analysis, using high-resolution imaging, ACOM and EELS were demonstrated in collaboration with the EM group of Prof. Molina-Luna (TU Darmstadt, Germany). Also, as the role of the microstructure on electrical transport and resistive switching in stochiometric hafnium oxide was recently highlighted in literature, the close collaboration with the group of Prof. Dittmann and Prof. Waser (FZ Jülich, Germany) was brought forward to analyze microstructural implications for current transport in strongly oxygen deficient hafnium oxide.

The following outline is intended to provide an overview of the most important results of this work, followed by perspectives for future studies.

Physical properties of substoichiometric phases of hafnium oxide: By depositing hafnium oxide over a broad range of oxidation conditions via Molecular-Beam Epitaxy two novel structures of rhombohedral *r*-$HfO_{1.7}$ and hexagonal *hcp*-$HfO_{0.7}$ have been identified as the link between stochiometric monoclinic hafnia and metallic hexagonal hafnium. By designated XRD measurements the lattice parameters and symmetry of rhombohedral hafnium oxide was identified with $a = b = c = 5.03$ Å and $\alpha = \beta = \gamma = 89.66°$.

The pseudocubic phase of *r*-$HfO_{1.7}$ was associated with a unique photoelectron spectroscopy fingerprint with Hf^{4+} and Hf^{X+} ($x<4$) states which further allows a distinction of this phase from the high temperature cubic phase of HfO_2 which is associated with Hf^{4+} states only. At the same time, in literature predicted sub oxide configurations like Hf_2O_3 with significantly different valence states, could be ruled out for the investigated phase. The in-vacuo XPS results instead suggested the stabilization of the rhombohedral phase via oxygen defects from the monoclinic structure which relates to ~ 1.2 oxygen vacancies per unit cell.

The oxygen vacancy density which is critical for the stabilization of *r*-$HfO_{1.7}$ was correlated with photoelectron spectroscopic results on the formation of an oxygen vacancy defect band close to the fermi level. This defect band was in turn connected to the significant decline in resistivity from insulating *m*-HfO_2 over ~10^{-4} Ωm for *r*-HfO_{2-x} to ~7.3×10^{-6} Ωm for *hcp*-$HfO_{0.7}$. From Hall effect measurements all conducting samples showed p-type conductivity with estimated charge carrier concentrations from ~ 3.4×10^{21} to 1.8×10^{22} cm^{-3} and low charge carrier mobilities below 0.5 cm^2 V^{-1} s^{-1}.

Also, next to the discovery of *r*-$HfO_{1.7}$ the second identified intermediate phase between stoichiometric hafnia and hexagonal metallic hafnium was found to be of a modified hexagonal structure where oxygen interstitials are expected to occupy octahedral positions. The corresponding XPS composition suggests that the hexagonal lattice is capable of hosting oxygen in at least ~ 70% of its octahedral sites.

Although synthesized substoichiometric hafnium oxide shows a gradual visual darkening with increasing oxygen deficiency, UV-Vis spectroscopic analysis reveals an almost constant bandgap of ~5.6 eV across all samples from stoichiometric monoclinic hafnium oxide towards *hcp*-$HfO_{0.7}$. Photoelectron spectroscopic measurements show that the appearance of midgap states is responsible for optical absorption and significant increase in conductivity. By combining the results of all conducted measurements in this study, a comprehensive band structure model was designed, which describes crystal- and band structure evolution over the whole oxidation range from monoclinic hafnia to metallic hafnium. As important part of this model, the interplay of valence and conduction band orbitals with midgap states in the valence region and their role in the p-type conduction – which is inherent to all conducting samples – is discussed.

Ab-initio simulations on substoichiometric hafnium oxide compared to experimental results: The results show that the transition from stoichiometric monoclinic to the previously discussed rhombohedral phase of hafnium oxide is – also from a theoretical standpoint – mediated by oxygen vacancies. By performing total energy calculations within GGA and HSE06 it was found that rhombohedral hafnium oxide is stabilized beyond a critical composition of $[O]/[Hf] = 1.5$.

The calculated structure of rhombohedral hafnium oxide is of a polar space group, namely $R3m$, showing strong similarities to a recently discovered ferroelectric rhombohedral phase of hafnium zirconium oxide (HZO). This finding suggests that the rhombohedral lattice may be stabilized either through the introduction of oxygen vacancies or cation substitution. As the DFT calculations have been performed without boundary conditions the obtained results show that the rhombohedral phase is not epitaxially induced but may exist as a thermodynamically stable bulk compound.

Further, the comparison between calculated DOS with spectroscopic results from XPS and optical measurements, show excellent agreement. Specifically, the resemblance of experimental and calculated results on the oxygen vacancy induced states further verifies the existence of midgap states as the origin of midgap optical absorption and the electrical conduction of this phase. At last, it was shown how the oxygen vacancy mediated hybridization between hafnium and oxygen orbitals is facilitated by orbital resolved DOSs.

Substoichiometric phases of hafnium oxide as novel electrodes for RRAM applications: In order to investigate the properties of *r*-$HfO_{1.7}$ and *hcp*-$HfO_{0.7}$ in typical MIM configuration, the phases have been grown on epitaxial TiN bottom electrodes (on *c*-cut Sapphire substrates). By using identical growth conditions as for the physical properties study, the observed XRD reflex maxima appear at virtually identical positions, demonstrating a very high level of reproducibility. Platinum was chosen as the chemically inert top electrode since the stack configuration of TiN/HfO_2/Pt is known for its reliable RRAM performance based on a conductive filament composed of oxygen vacancies.

Special attention was given to the investigation of potential oxidation effects at the HfO_{2-x}/Pt interface. For this purpose, simultaneously grown TiN/HfO_{2-x} samples have been processed either in atmosphere or in-vacuo. For oxygen deficient devices of *r*-$HfO_{1.7}$ and *hcp*-$HfO_{0.7}$ which have been prepared without breaking vacuum conditions, a high leakage current with no switching properties was revealed. This finding is in good agreement with the results of both, the physical properties study and the DFT calculations. However, as the final platinum layer was deposited after the hafnium oxide layer was exposed to air, all investigated devices of *r*-$HfO_{1.7}$ and *hcp*-$HfO_{0.7}$ strikingly showed insulating leakage currents and typical bipolar VCM switching behavior up to (at least) 100 cycles each.

This behavior can be explained by an oxidation layer of limited thickness which forms independently of the oxygen content of the hafnium oxide layer from *m*-HfO_{2-x} over *r*-$HfO_{1.7}$ and even *hcp*-$HfO_{0.7}$. This model is confirmed by the virtually identical forming voltage statistics of devices of *r*-$HfO_{1.7}$ and *hcp*-$HfO_{0.7}$. While stoichiometric devices of *m*-HfO_2 show typical forming voltages of ~ 6 V for 20 nm thickness, the oxygen deficient devices of *r*-$HfO_{1.7}$ and *hcp*-$HfO_{0.7}$ both show a reduced forming voltage close to 1.5 V independent of the oxygen content. Forming voltages are typically controlled by the dielectric layer thickness and therefore it is reasonable to assume similar close to stoichiometric oxide layer thicknesses on both substoichiometric phases of *r*-$HfO_{1.7}$ and *hcp*-$HfO_{0.7}$ and therefore for the whole oxidation range of investigated hafnium oxides.

As the formation of an oxide layer is identified as the reason for switching, the electrically conducting layers of *r*-$HfO_{1.7}$ and *hcp*-$HfO_{0.7}$ are understood as the effective bottom electrodes for the investigated devices. This study revealed stable switching behavior for those novel electrode materials. Further, from the physical properties study, it becomes evident that both phases can act as effective oxygen reservoirs. The potential of these novel device structures therefore suggests to further extend endurance and retention studies for both *r*-$HfO_{1.7}$ and *hcp*-$HfO_{0.7}$ electrodes.

Transmission Electron Microscopic nanoscale identification of substoichiometric hafnium oxide phases: To capture the formation, set and reset of a conducting filament in hafnium oxide-based RRAM in operando via high resolution imaging and other techniques is still a long perused goal of many researchers in the field of resistive switching. By comprehensive literature discussion it was highlighted that the precise and undoubted identification of hafnium oxide phases on the nanoscale is far from trivial and requires the combined use of several techniques, including structural and chemical analysis.

To prepare in the best way for this undertaking, it is obvious to pioneer the nanoscale identification of substoichiometric hafnium oxide phases. This work, which deals with the detailed identification of hafnium oxide phases over the entire oxidation range from stoichiometric insulating hafnium to almost metallic hexagonal hafnium, provides the optimal basis for this endeavor. It was shown that the novel conductive phases *r*-$HfO_{1.7}$ and *hcp*-$HfO_{0.7}$ synthesized in this work can be distinguished by different transmission electron microscopic methods.

First it was demonstrated via high resolution imaging through both TEM and HAADF-STEM that all relevant structures, namely m-HfO_2, *r*-$HfO_{1.7}$ and *hcp*-$HfO_{0.7}$ can be distinguished by direct lattice parameter determination on the nanoscale. This is especially relevant if for example an oxygen gradient in and around the conducting filament results in the formation of one or multiple of above discussed phases.

By using EELS methodology, it was shown that all above mentioned phases can also be identified in the low loss region of the electron energy loss spectra. Obtained fingerprints from each phase have been acquired and specific spectral regions for phase identification have been discussed. As previously highlighted, the unambiguous identification of the discussed phases requires the use of multiple analysis techniques. The discussed EELS reference spectra therefore provide another vital component for precise, combined phase identification.

Finally, the structural phase identification was also demonstrated via 4D STEM by ACOM. Therefore, three samples of close to phase pure m-HfO_2 only, *r*-$HfO_{1.7}$ only and mixed m/r-HfO_{2-x} samples have been used. The results show that the predominant areas of the respective phases can be correctly assigned and agglomerations of e.g., *r*-$HfO_{1.7}$ in a m-HfO_2 matrix can be effectively identified. While previously discussed high resolution imaging is an effective tool for in detail structural identification, ACOM allows to map unprecedentedly wide areas of several 100 nm which is crucial for mapping large areas. By applying the proven technique during operando measurements, electron transparent lamellae of hafnium oxide-based RRAM could be mapped along the whole dielectric layer for structural changes during electrical switching.

Scanning probe microscopic analysis of microstructure and local conduction path in substoichiometric hafnium oxide: While the influence of the microstructure on electrical properties is well investigated in stoichiometric hafnium oxide, and recent studies directly underpin the significant relevance for RRAM applications, there is a lack of investigations on oxygen deficient hafnium oxide. The phase transition from insulating monoclinic, to conducting rhombohedral hafnium oxide – as discovered in this work – therefore provides an ideal reference system for microstructural c-AFM analysis.

To realize such measurements in a collaboration with the group Electronic Materials (PGI-7) at Forschungszentrum Jülich, an in-vacuo sample transfer from Darmstadt to Jülich was established. As a product, a custom sample holder design was developed which – together with a designated vacuum suitcase – enabled multiple successful UHV sample transfers between both institutes.

It was shown that using such sample holders allows for the reproduction of the TiN deposition as well as the transition from monoclinic to rhombohedral hafnium oxide with high quality. Since two series have been produced with 20 nm and 10 nm of hafnium oxide, it was additionally found that the formation of *r*-HfO_{2-x} likely promoted for lower film thicknesses.

Interestingly, it was found that the topological microstructure appears unaffected by the phase transition from monoclinic to rhombohedral hafnium oxide, and a potential influence of the TiN layer roughness was discussed. However, by superimposing the topological AFM maps with corresponding current maps at different voltages, it was clearly shown that the current flow is mediated along grain boundaries even in strongly oxygen-deficient rhombohedral hafnium oxide. Finally, some implications for these observations have been discussed, including a potential application where the local formation of the conducting filament in a stoichiometric layer could be mediated through the microstructure of such a conducting, oxygen deficient hafnium oxide electrode. Further this finding implies that the current transport in and around the oxygen deficient conducting filament region might also be determined by changes in the local microstructure.

In summary, the conducted studies highlight the relevance of investigating materials properties in strongly oxygen deficient transition metal oxides such as the crystal- and band structure as well as the electrical properties. The numerous correlations between the hafnium oxide physical properties study and the discussed corresponding DFT study, the devices study, the Electron Microscopy investigations as well as the SPM study underpin the importance of solid physical properties investigations. The numerous perspectives highlight the validity of obtained results and the wide range of their application. Therefore, this thesis provides a comprehensive scientific basis for the understanding of substoichiometric hafnium oxide phases and their role in electronic devices.

Outlook and Future studies:

As demonstrated in this work, the availability of a Molecular-Beam Epitaxy system enables the investigation of metal oxides over an extreme range of oxidation conditions. A next logical step would therefore be to expand comparable physical properties pioneering to other transition metal oxides that are also relevant for next generation non-volatile memory. The system of Yttrium oxide would be an especially interesting example as it is not common in RRAM research yet, but recent publications highlight its applicability for neuromeric computing.

While the comprehensive XRD study was able to identify the unit cell of rhombohedral hafnium oxide, DFT calculations revealed the crystalline ordering of oxygen with a space group of $R3m$. These results could not be verified experimentally so far, as oxygen ordering can hardly be investigated with low intensity X-ray radiation. Therefore, it would be interesting to further investigate the structures oxygen sublattice for example at a research reactor, via neutron diffraction.

As has been shown with DFT calculations, theoretical perspectives could significantly complement the previously experimentally concluded results on hafnium oxide. In the presented work, the focus was laid on the phase transition between the monoclinic and the rhombohedral phase. It would therefore be an interesting step to also conduct calculations for the next phase transition up to the hexagonal structure to complement information on orbital hybridization and phase stability for the whole investigated oxidation range.

As total energy calculations suggested that the rhombohedral phase r-HfO_{2-x} is thermodynamically stable without external constrains, it might exist as a bulk compound. This finding could be experimentally verified via powder diffraction studies. By treating hafnium oxide powders in different atmospheres, pressures or temperatures, the stoichiometric powder could be deprived of oxygen and lead to the potential formation of rhombohedral hafnium oxide in powder form.

The performed device studies on r-HfO_{2-x} and hcp-HfO_{2-x} revealed both phases as effective bottom electrodes for VCM RRAM. Since both phases can be considered as significant oxygen reservoirs, the promising results regarding their performance should be complemented by further extensive endurance and retention measurements.

On the basis of the here demonstrated collaborative work between the ATFT group of Prof. Alff with the EM group of Prof. Molina-Luna (TU Darmstadt) and the “Elektronische Materialien” (PGI-7) department of Prof. Dittmann and Prof. Waser at FZ Jülich a research plan is anticipated which will focus on the comprehensive identification of conducting filament regions in hafnium oxide-based RRAM. The phases synthesized and identified as part of this work over a broad oxidation range are characterized by a transition from insulating to semiconducting behavior. In particular, the electrically conductive structures of rhombohedral and hexagonal hafnium oxide can therefore be considered as potential conducting filament phases. This work has already shown that all participants were able to achieve valuable insights on these oxygen deficient phases through extensive measurements in their respective field of expertise. The intended collaboration goes one step further and aims to investigate the role of substoichiometric phases in hafnium oxide-based RRAM after formation, set and reset and finally even during switching. For this purpose, the RRAM devices will be manufactured by the group of Prof. Alff. Then, utilizing the newly established in-vacuo transport, these devices will be transferred to Jülich to the group of Prof. Dittmann & Prof. Waser. Conductive filament regions will be formed in Jülich via conductive AFM and investigated by comprehensive SPM analysis. From there, the devices will be transported back to Darmstadt, where Prof. Molina Luna's group will examine the local conductive filament regions using the TEM methodology and compare them with the reference measurements already obtained. As a final goal, the local mechanisms during switching are examined in detail in TEM operando measurements and correlated with the expertise of all participating research groups. From this study an unprecedented information value on the atomic switching behavior is to be expected, which promises a key ingredient for the further development of VCM based RRAM.

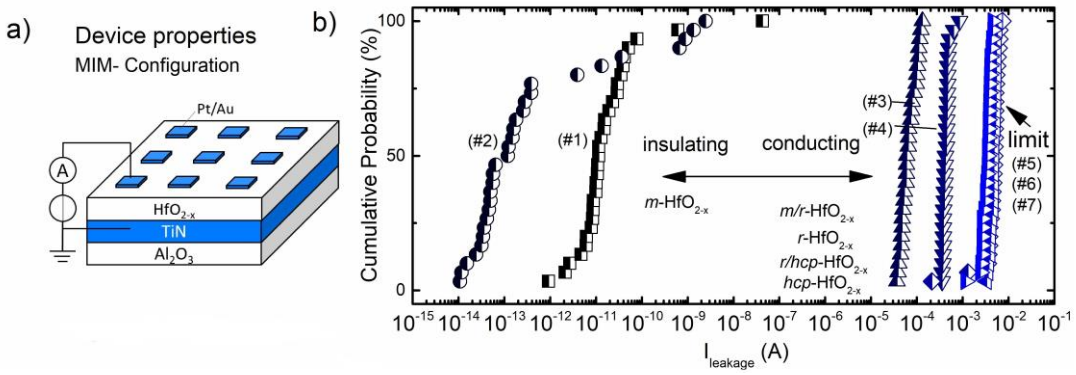

Figure 75: a) hafnium oxide in device configuration b) corresponding leakage measurements after a forming voltage sweep for the most deficient devices that showed some statistical spread from the limit. All devices which showed some deviation from the limit (e.g. for stacks #5- #6) value at 3E-3 A perfectly align to this limit after a high voltage sweep.

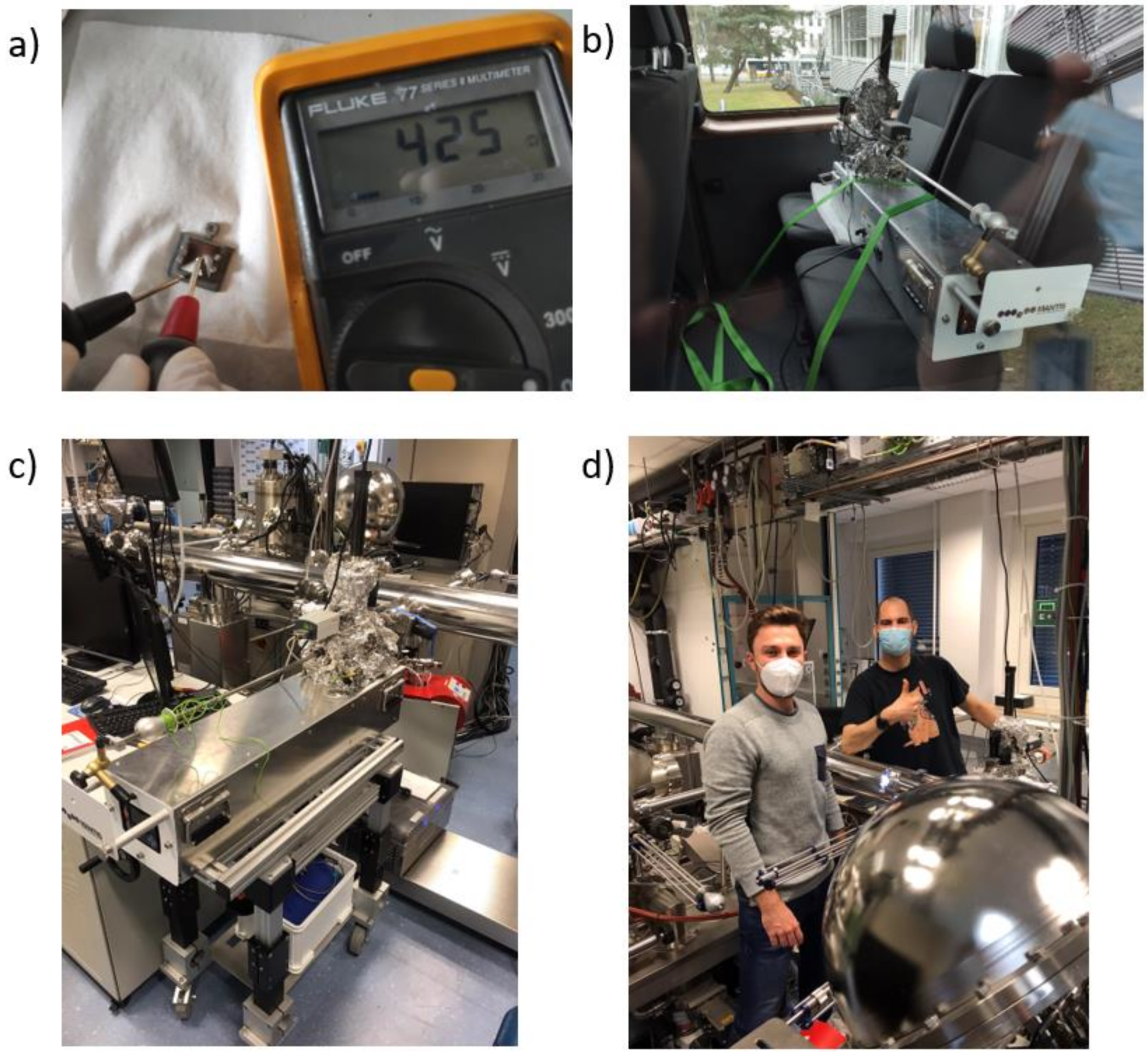

Figure 76: a) Verifying electrical contacts between sample surface and substrate holder after TiN deposition while using insulating sapphire substrates. b) vacuum-suitcase from Mantis Deposition Ltd. detached from the frame and fixed close to the 12V power supply c) vacuum-suitcase on adjustable frame connected to a central distribution system at Elektronische Materialien; PGI-7 in FZ Jülich. d) after successful sample transfer from Nico Kaiser (right) to Niclas Schmidt (left) at FZ Jülich.

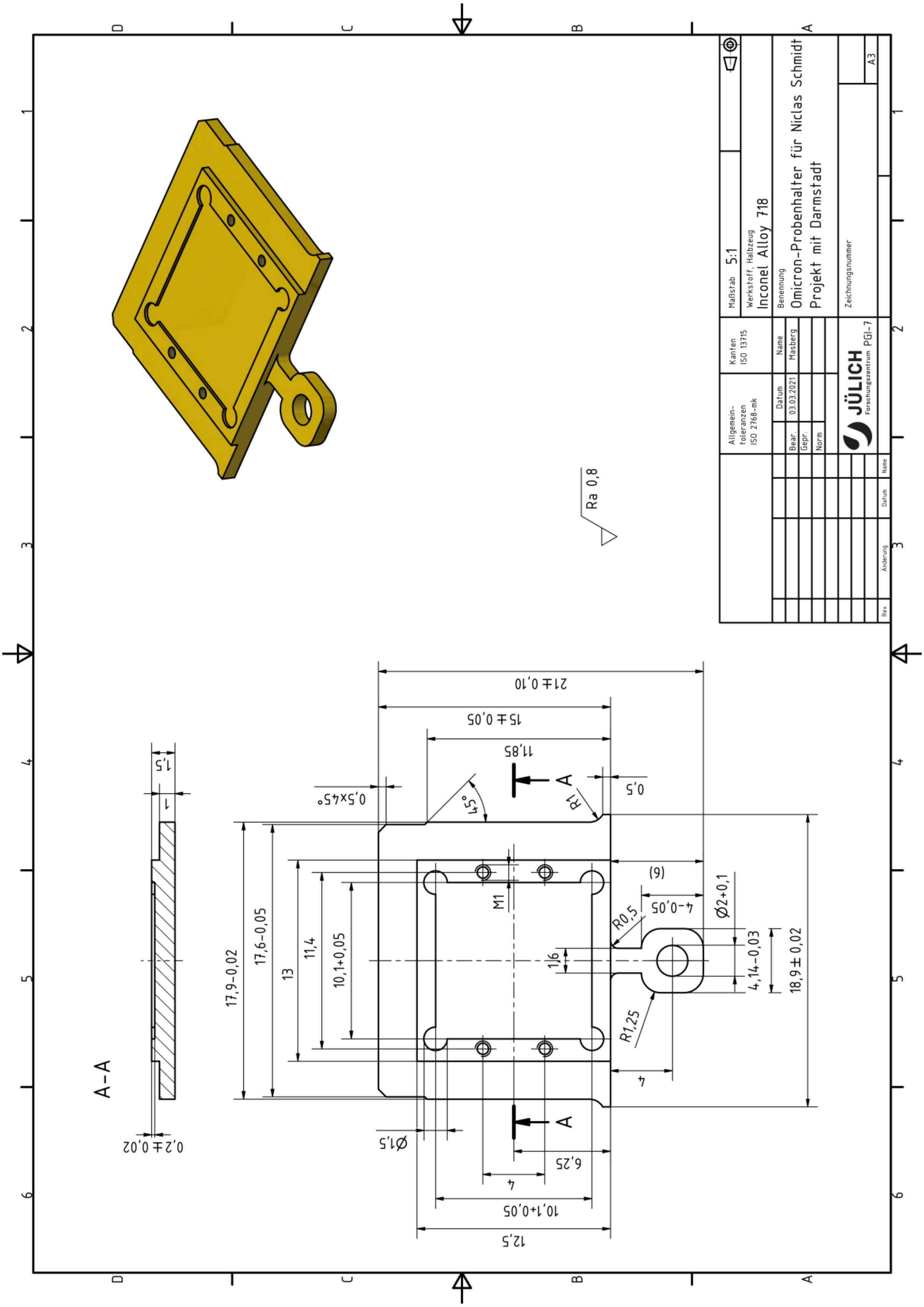

Figure 77: Final design of the sample holder which is compatible with both TU Darmstadt and FZ Jülich facilities between Prof. Alff (ATFT) and Prof. Dittmann/Prof. Waser (Elektronische Materialien; PGI-7).

List of figures

Figure 1: Classical memory hierarchy with fastest memories close to the CPU. The corresponding approximate speed and storage capacities are indicated on the sides of the pyramid and run in opposite directions. Note that the high speed memory types (Registers, Cache and Main Memory) which are shown in blue are all volatile while the storage memory (shown in orange) are the only non-volatile memory types. 1

Figure 2: Categorization of next generation nonvolatile memory by their basic physical principles. Content reprinted from reference [6] https://doi.org/10.1088/1361-6528/ab2084 © IOP Publishing. Reproduced with permission. All rights reserved. 2

Figure 3: Memory technologies and their fundamental architectures with a) SRAM, b) DRAM, c) FLASH, d) STT-MRAM, e) PCRAM, f) Filament based OxRAM, e) CBRAM, h) FeRAM and i) Interface based OxRAM. Content a) - g) reprinted from reference [1] https://doi.org/10.1038/nnano.2015.29 with permission of Springer Nature BV. © 2015 Macmillan Publishers Limited. All rights reserved. Content h) & i) is reprinted from reference [16] https://doi.org/10.1088/1361-6528/ab2084 © IOP Publishing. Reproduced with permission. All rights reserved. 3

Figure 4: Next generation nonvolatile memories and their possible implementation in the memory hierarchy. Reprinted from reference [20] https://doi.org/10.3390/app112311254 which is published under a Creative Commons Attribution 4.0 International License. © 2021 by the authors. Licensee MDPI, Basel, Switzerland. 5

Figure 5: Search results for papers published in the web of science core collection with keywords on RRAM in general (left) and fractions of those publications using keywords regarding the emerging memory fields of “neuromorphic processing” and “In-Memory Computing” (right). Note the steady increase in interest for both emerging fields within the research topic of RRAM. 6

Figure 6: Switching modes of in HfO2-x based RRAM with all switching modes known for OXRAM with a) counter figure eight bipolar switching b) & c) unipolar and threshold switching for stochiometric HfO_2. In oxygen deficient $HfO_{1.5}$ the author could show combined counter figure eight + figure eight switching, e) complementary switching as well as f) figure eight switching. Reprinted after reference [31] https://doi.org/10.1002/adfm.201700432 with permission from John Wiley & Sons – Books. Copyright © 2017 WILEY-VCH Verlag GmbH & Co. KGaA, Weinheim. 7

Figure 7: Experimentally verified polymorphism in stoichiometric HfO_2 showing five distinct phases with the monoclinic structure ($P2_1/c$) as the ambient pressure/temperature phase, the tetragonal ($P4_2/nmc$) and cubic (Fm-3m) structures as high temperature phases and the orthorhombic I (*Pbca*) and orthorhombic II (*Pmnb*) phase. Content reprinted from reference [39] https://doi.org/10.1111/j.1151-2916.2001.tb00843.x with permission of John Wiley & Sons - Books. Copyright © 2004 The American Ceramic Society, all rights reserved. 9

Figure 8: Known and hypothetical hafnium oxide symmetries as proposed by [47]. All verified phases of HfO_2 appear non-polar, while the proposed polar phases yielding the lowest total energy are of orthorhombic symmetry, including the most suggested symmetry $Pca2_1$ for ferroelectric hafnia. Content reprinted from reference [47] https://doi.org/10.1103/physrevb.90.064111 with permission of the American Physical Society. ©2014 American Physical Society. 11

Figure 9: Fitness plot of hafnium oxide structures with different oxygen content predicted via evolutionary algorithm. At low oxygen contents oxygen is found to occupy octahedral positions in the (previously metallic) hexagonal lattice (blue line), the dashed green line shows an crossover of hexagonal and fluorite type structures while the red line indicates fluorite type structures and the doted red line, fluorite type structures with one dimensional vacancy chains [66, 67]. Content

reprinted from reference [67] https://doi.org/10.1039/C8FD00104A with permission of the Royal Society of Chemistry. © The Royal Society of Chemistry 2019. 12

Figure 10: Four cycle with all associated degrees of freedom in θ, ω, ϕ and χ. 15

Figure 11: Typical XRR graph in which different features are correlated with various thin film properties. Content reprinted from reference [89]. 16

Figure 12: Bragg-Law and its geometric relations between $dhkl$, λ and $sin(\theta)$. Content reprinted from reference [88] with permission of Springer. 17

Figure 13: XRD patterns as obtained from powder diffraction files for relevant hafnium oxide and hafnium structures (Compare chapter 1.5). Note that especially the structures of cubic (*Fm*-3*m*), tetragonal ($P4_2/nmc$) and orthorhombic I (*Pbca*) show similar patterns where all structures share an intense reflection at about 30° in 2θ with peak splitting occurring in dependence of symmetry at about 35° 2θ. This highlights how the tetragonal and the orthorhombic phase are distorted from the cubic, fluorite type *Fm-3m* structure. In contrast, the ambient phase of monoclinic hafnia as well as the high-pressure orthorhombic II phase can be easily discerned. Further, the hexagonal phase of metallic hafnium shows significant differences to all hafnium oxides. 18

Figure 14: a) Basic Rocking-curve principle with the 2θ angle being set to a defined lattice plane reflection while the ω angle is scanned in a positive and negative direction with respect to the aligned starting positon. b) Shows how the highly oriented substrate (as shown in a) shows a significantly reduced FWHM as compared to the less oriented thin film. Content reprinted from reference [95] https://doi.org/10.1007/s10832-021-00263-6 with permission of Springer Nature BV. © The Author(s), under exclusive licence to Springer Science+Business Media, LLC, part of Springer Nature 2021. 19

Figure 15: Exemplary pole figure dome showing on an cubic single crystal at which ψ and φ angles the specific lattice planes (100), (110) and (111) show up. For a measurement the 2θ angle is set to a defined value which matches a feature (e.g. the (111) lattice plane) while ψ and φ angles are mapped (covering the displayed dome). The obtained intensity distribution is projected on a 2D plane, showing at which positions the mapped feature shows up. Content reprinted from reference [95] https://doi.org/10.1007/s10832-021-00263-6 with permission of Springer Nature BV. © The Author(s), under exclusive licence to Springer Science+Business Media, LLC, part of Springer Nature 2021. 20

Figure 16: Exemplary EBSD pole figures tracking the (10-11) lattice plane of graphite on (a) Ni substrate and (b)-(e) after transfer to SiO_2/Si showing varying alignment with respect to the substrate in dependence of their growth temperature. Especially the different multi-domain characteristics (yellow and red dotted lines) can easily be identified by the pole figure analysis. (f) Further analysis of the (0001) plane shows its perpendicular alignment to the substrate. Content reprinted from reference [96] https://doi.org/10.1039/C9CE01515A with permission of the Royal Society of Chemistry. © The Royal Society of Chemistry 2020. 21

Figure 17: Simplified beam path and fundamental working principle of a) transmission electron microscopy (TEM) and b) scanning transmission electron microscopy (STEM). Note that for the TEM sketch the incident beam is parallelized before hitting the specimen, while for the STEM configuration a convergent beam is locally directed onto the sample. This convergent beam is consequently scanned across the sample surface. After interaction with the sample, the beam may be recorded by different detectors like the bright field (BF), annular dark field (ADF) or high angle annular dark field detector (HAADF) detector. Alternatively, to BF imaging the beam may be analyzed by electron energy loss spectroscopy (EELS). 22

Figure 18: a) Simulated contrast transfer function (CTF) for TEM in Scherzer focus (blue), covering a broad spectrum of spatial frequencies with rather uniform contrast. The green line shows the CTF at a high defocus value, allowing better contrast for bigger feature sizes, but sacrificing resolution. The more transparent lines show the corresponding CTFs assuming an ideally coherent electron source, while the dampened functions represent CTFs assuming a real electron source. b) Shows simulated optical transfer functions (OTF) which are relevant for STEM. The red line corresponds to the Scherzer focus, offering good contrast at high resolution. The orange line corresponds to a smaller beam convergence, which sacrifices resolution for enhanced depth of focus. Content reprinted from reference [99] https://doi.org/10.1557/mrs.2016.136 with permission of Springer. Copyright © Materials Research Society 2016. 23

Figure 19: Energy scheme for emission and detection in X-ray Photoelectron spectroscopy. Modified after https://de.wikipedia.org/wiki/Datei:XPS_-_Energy_levels_%28schematic%29_DE.svg (2023) which is published under Attribution-ShareAlike 3.0 Unported (CC BY-SA 3.0) Creative-Commons-License. 25

Figure 20: Hf 4f orbital of hafnium metal exposed by a) 8L, b) 40 L and c) 3100 L of oxygen at room temperature showing oxidation dependent Hf^{4+} and Hf^{x+} "suboxide" contributions with clear energy shifts from metallic Hf^0 (Hf^m). Content reprinted from reference [106] https://doi.org/10.1002/sia.740160163 with permission of John Wiley & Sons – Books. Copyright © 1990 John Wiley & Sons Ltd. All rights reserved. 27

Figure 21: Tauc-Plots showing isolated as well as combined spectra of methyl orange (MO) and Titanium Dioxide (TiO_2) for A) mixtures and B) samples that were placed side by side in the spectrometer beam. In both cases the combined spectra lead to an underestimation of the original TiO2 bandgap. This effect is especially prominent in B) and highlights the necessity for appropriate bandgap-correction. Reprinted with permission from reference [114]. https://doi.org/10.1021/acs.jpclett.8b02892 Copyright © 2018 American Chemical Society. 30

Figure 22: Tauc-Plots showing how an appropriate baseline-correction is carried out. The baseline, which is considered to be independent from the investigated bandgap feature should be extrapolated so that it cuts the original bandgap extrapolation. The bandgap estimate is then read from the intercept point. While a baseline extrapolation is always connected to an uncertainty, the method is shown to produce accurate results in many cases and therefore serves as one of the best analysis strategies. Reprinted with permission from reference [114]. https://doi.org/10.1021/acs.jpclett.8b02892 Copyright © 2018 American Chemical Society. 31

Figure 23: Shows the evolution of the double-absorption feature in hafnia thin films in dependence of substrate temperature. Content reprinted from reference [115] https://doi.org/10.1016/j.tsf.2004.01.110 with permission of Elsevier Science & Technology Journals. Copyright © 2004 Elsevier B.V. All rights reserved. 32

Figure 24: Charge carrier densities in dependence of the fermi-level position. The fermi–level position is modified from the intrinsic position (a) a by donor (b) or acceptor (c) type defects. Content reprinted from reference [123] with permission from John Wiley & Sons – Books. Copyright © 2007 John Wiley & Sons, Inc. All rights reserved. 34

Figure 25: Self Consist Field (SCF) Cycle algorithm for eigenvalue determination in DFT. 37

Figure 26: MBE unit featuring e-beam evaporators in an UHV body, corresponding QCM units, radical sources for O* and N* incorporation, a substrate manipulator with a heating unit and a RHEED system for in-situ growth control. 39

Figure 27: Schematic on the plasma intensity in dependence of RF Power and Gas-Flow conditions. Note that a gas flow exceeding a certain threshold will lead to a reduced plasma intensity. Redrawn with information from [134]. 40

Figure 28: a) shows TiN films grown at 800 °C for different conditions shows optima growth conditions (red and blue) while the sample shown in black shows TiN grown under reduced conditions as indicated by the shift of the (111) reflection. The substrate reflection appears different due to different monochromator settings (graphite instead of Ge(220) monochromator). b) shows RHEED patterns of the different stages during growth from 1 to 4. 41

Figure 29 Optical microscope images of 6 x 6 μm^2 and 3 x 3 μm^2 features at three different days on gold, showing high reproducibility. As the cleanroom is not equipped with air conditioning the corresponding humidity is shown for every day respectively. After the Advanced Research Lab from Nitin Malik (supervised by Nico Kaiser) 44

Figure 30: End point detection with a mass spectrometer during IBE procedures for a typical hafnium oxide based RRAM stack. a) complete etching through top electrode materials and hafnium oxide with stop at the HfO_{2-x}/TiN interface b) only etching through the top electrode with stop at the Pt/HfO_{2-x} interface. c) shows the structure of the stack in relation to the mass spectrometer signal above. Note that the actual thicknesses are not true to scale, as e.g. gold (~ 80 nm/min) shows a significantly faster etch rate than platinum (40 nm/min). 46

Figure 31: Leakage current distribution of four Au/Pt/HfO_2/TiN stacks with an identical hafnium oxide layer. The samples are separated in the way the top electrode was deposited (in-vacuo vs. ex-vacuo/after atmospheric exposure) and weather the hafnia layer is etched through or not (etching to BE or to TE/lift-off). Note that etching through the hafnia layer leads to a significant increase in leakage current while the statistical spread is reduced for samples which received the top electrode deposition in-vacuo. 47

Figure 32: Optimal miscopy a) before and b) after sputtering of 4 μm gold on one half of the sample with 30 x 30 μm square electrodes showing that designated devices are still visible for TEM lamellae preparation c) profilometer measurement confirming 4000 nm thickness after 8,000 s (133.3 min) deposition at 30 mA, also showing that the total height of the electrodes ~ 350 nm is still conserved after the significant gold layer deposition. 48

Figure 33: Deposition conditions for the discussed series of 13 samples following a consistent trend in oxidation conditions with most oxidizing conditions for #1 to more and more reduced oxidation conditions to #13. Note that the oxygen flow remains constant for varying hafnium evaporation rate and via versa. Reprinted with permission from reference [146]. https://doi.org/10.1021/acsami.1c09451 Copyright © 2021 American Chemical Society. 52

Figure 34: Oxidation depend evolution of the crystals structures a) and corresponding lattice planes b). The measurements show crystal structures with lattice parameters close to stoichiometric cubic hafnia (*c*-HfO_2) and close to hexagonal metallic hafnia (*hcp*-Hf) as transitional structures between stoichiometric monoclinic hafnia (*m*-HfO_2) and metallic hafnium. The transitional structures are identified as oxygen vacancy stabilized *r*-HfO_{2-x} and oxygen rich metallic hafnium with oxygen interstitials *hcp*-$HfO_{0.7}$ as will be discussed in the following chapters. Reprinted with minor changes with permission from reference [146]. https://doi.org/10.1021/acsami.1c09451 Copyright © 2021 American Chemical Society. 53

Figure 35: a) Increasing critical angle in dependence of decreasing oxidation conditions b) corresponding XRR density as extracted from RCRefSim c) Rocking curve measurements of the most isolated key structures *m*-HfO_2 (#1), *r*-$HfO_{1.7}$ (#9) and *hcp*-$HfO_{0.7}$ (#13). Reprinted with minor changes with permission from reference [146]. https://doi.org/10.1021/acsami.1c09451 Copyright © 2021 American Chemical Society. 54

Figure 36: a) shows the 2θ/ω scan of sample #9 in comparison with PDF references of known HfO_2 structures, highlighting that the out of plane lattice parameter fits all corresponding structures. b) shows a list of lattice planes relevant for phase identification around 35° in 2θ as well as their expected separation in 2θ and in ψ. c) shows the pole figure measurement with peudo-six-fold symmetry at ~ 35.5 ° in 2θ and d), e) and f) confirm that the measured reflection spots show no indications of peak splitting, therefore confirming that the reflections originate from a single (002) lattice plane. As a consequence, the investigated phase corresponds most closely to the cubic reference. The identification is usually further hindered by the effects of peak broadening in thin films as well as the presence of different (usually monoclinic) phase fractions. As already discussed in chapter "Novel Structures *r-HfO2-x* and *hcp-HfO2-x* between Hafnia and Hafnium" 4.1.1, the isolation of an intermediate oxygen deficient phase is only possible in a limited window of growth conditions. Reprinted with permission from reference [146]. https://doi.org/10.1021/acsami.1c09451 Copyright © 2021 American Chemical Society. 56

Figure 37: a), b) and c) show the 2θ scans on the corresponding (111), (-111) and (002) reflections with reference to the geometrical parameters ψ and φ. a) & b) show the peak splitting between (111) and (-111) verifying the rhombohedral nature of the phase. Note that the vertical lines, highlighting the peak maxima in a), b) and c) satisfy the mathematical relation for a rhombohedral structure. d) and e) show the corresbonding pole figures for the (-111) and (002) reflections. The pseudo-sixfold symmetry can be understood by the growth of multiple domains of threefold symmetry (highlighted in black and white) which are offset by 60° in φ. Reprinted with permission from reference [151]. https://doi.org/10.1021/acsaelm.2c01255 Copyright © 2023 American Chemical Society. 57

Figure 38: Pole figure measurements on sample #9 (r-$HfO_{1.7}$) from a) to f) at 2θ values from 31.0° to 33.5° in 0.5° steps. Displayed scans cover ψ = 5 ° to 80 ° and φ = 0 ° to 360 °............................ 59

Figure 39: Pole figure measurements on sample #9 (r-$HfO_{1.7}$) from g) to l) at 2θ values from 34.0° to 36.5° in 0.5° steps. Displayed scans cover ψ = 5 ° to 80 ° and φ = 0 ° to 360 °............................ 60

Figure 40: a) Evidence from survey scans that no Al 2s signal is detected (around 120 eV), ruling out contributions from the substrate b) shows designated scans around the energy window where a C 1s signal would be expected. As can be seen, almost no deviation from the noise can be identified, which shows that besides minimal potential traces no carbon is present in the thin films or even at the surface. While at least carbon adsorbates are a common feature in XPS spectra, these scans highlight the excellent vacuum-conditions for both, synthesis and in-vacuo transfer. 61

Figure 41: XPS surveys on all samples indexed after the Handbook of X-ray Photoelectron Spectroscopy. The orbital emission lines of Hf 4f, Hf 5p, Hf 5s, Hf 4d, Hf 4p as well as O 1s can be clearly identified. Further the auger signals of O KLL and Hf NNN are present in the spectra. Note that all relevant lines are indexed with the expected species of hafnium and oxygen but no additional or unexpected features. 62

Figure 42: In-vacuo XPS spectra of selected oxygen deficient hafnium oxide thin films in dependence of their oxidation conditions over the complete series (from #1 to #13). a) shows the Hf 4f emission lines where sample #1 could be fitted with a single Hf^{4+} doublet showing close to stoichiometric composition. With decreasing oxidation conditions additional Hf^{x+} signals show up while for most deficient samples clear Hf^0 contributions show up. b) shows a O 1s spectra of sample #9 which is representative for the whole series with a clear main contribution from lattice oxygen and a small shoulder indicating traces of surface adsorbates e.g. in form of residual water in the load lock. C) shows the stoichiometry estimate of the corresponding samples as obtained from area matching of the Hf 4f lines and the O 1s lattice contribution. Reprinted with minor changes with permission from reference [146]. https://doi.org/10.1021/acsami.1c09451 Copyright © 2021 American Chemical Society... 64

Figure 43: Van der Paw resistivity of the hafnium oxide series in dependence of oxidation conditions (from most oxidized sample #1 to most deficient sample #13) . Note that the monoclinic samples #1 to #3 grown under most oxidizing conditions could not be measured which is expected for close to stoichiometric hafnia. However, in the vicinity of the phase transition from monoclinic to rhombohedral structure the samples show significant conductivity with a measureable decline of about one order of magnitude between *r*-$HfO_{1.7}$ and *hcp*-$HfO_{0.7}$. Reprinted with minor changes with permission from reference [146]. https://doi.org/10.1021/acsami.1c09451 Copyright © 2021 American Chemical Society. 66

Figure 44: All measured samples show positive Hall coefficients, indicating holes as majority-charge carriers. Note that the measurements reveal consistent trends with oxygen content for both, charge charrier concentrations and mobilities. Reprinted with minor changes with permission from reference [146]. https://doi.org/10.1021/acsami.1c09451 Copyright © 2021 American Chemical Society. 67

Figure 45: Resistivity of the conducting key phases *r*-$HfO_{1.7}$ and *hcp*-$HfO_{0.7}$ measured in dependence of the thin film temperature. Note that both show increasing resistivity at lower temperatures, following semiconducting behavior. The curves do not indicate metallic properties, even for the most deficient *hcp*-$HfO_{0.7}$ phase. Reprinted with minor changes with permission from reference [146]. https://doi.org/10.1021/acsami.1c09451 Copyright © 2021 American Chemical Society. 68

Figure 46: Transmission spectroscopy raw data on the oxidation dependent hafnium oxide series on sapphire with a) showing the complete range, clearly demonstrating a decrease in the overall transmission for lower oxygen content and b) showing the region of interest for occurring absorption slopes. Note of the twofold absorption feature, which appears exclusively in monoclinic hafnia. The measurement is limit to around 190 nm due to atmospheric absorption as indicated by the noise appearing below 200 nm. 69

Figure 47: Bandgap estimation via Tauc plot in representation for a) indirect and b) direct bandgap. Both show similar bandgap values for *m*-HfO_2 as well as *r*-$HfO_{1.7}$ c) shows the gradual visual darkening of the sample series. Reprinted in parts with permission from reference [146]. https://doi.org/10.1021/acsami.1c09451 Copyright © 2021 American Chemical Society. 70

Figure 48: Valence band spectra of the oxidation dependent series with the indicated reference point of E_{VBM}. Note that the conduction band minimum reference E_{CBM} is placed above the E_{VBM} by 5.65 eV consistently with the observed bandgap od rhombohedral hafnium oxide (5.6 eV for monoclinic. Note that while there is a significant increase in midgap DOS over the whole series, the valence band appears almost unchanged from the monoclinic to rhombohedral transformation and only changes significantly towards *hcp*-$HfO_{0.7}$. Reprinted with permission from reference [146]. https://doi.org/10.1021/acsami.1c09451 Copyright © 2021 American Chemical Society. 72

Figure 49: TEM phase contrast images of (a) *m*-HfO_2 #1 , (b) LTP *c*-$HfO_{1.7}$ #9 and (c) *hcp*-$Hf_{0.7}$with atomic resolution showing homogeneous crystallinity for all samples. The bright contrast represents the sapphire substrate, while the dark contrast is a platinum capping layer for TEM preparation. The insets (showing blow ups of the regions marked by dashed boxes) show the FFT extracted lattice parameters of the hafnium oxide thin films which are in good agreement to the XRD measured out of plane lattice constants for any crystal structure respectively. Reprinted with permission from reference [146]. https://doi.org/10.1021/acsami.1c09451 Copyright © 2021 American Chemical Society. 73

Figure 50: Model of the electronic structure for the whole oxidation range, from stoichiometric hafnia to metallic hafnium. As representative phases, the synthesized key structures of *m*-HfO2, *r*-$HfO_{1.7}$, and *hcp*-$HfO_{0.7}$ are shown. The development of a midgap defect band between O 2p and Hf 5d states, mainly below the Fermi level, is revealed as the key mechanism for emergent *p*-type conductivity

throughout the series. Note that the band gaps between the O 2p valence states and the Hf 5d conduction band remain virtually unchanged especially from *m*-HfO_2 to r-$HfO_{1.7}$ and only change dramatically towards *hcp*-Hf. Reprinted with minor changes with permission from reference [146]. Copyright © 2021 https://doi.org/10.1021/acsami.1c09451 American Chemical Society. 74

Figure 51: Comparison of experimental vs theoretical data on the phase transformation from monoclinic to rhombohedral structure. a) shows the phase transformation from 2θ/ω XRD scans with b) the corresponding deposition conditions which result in a consistent trend in the atomic ratio as displayed in c). d) shows the energetic difference between the discussed monoclinic and pseudocubic relaxed structures, confirming a consistent trend with more energetic stability towards the pseudocubic rhombohedral structure. Note that the rhombohedral structure is crossing the energetic threshold for its stabilization over the monoclinic reference at a ratio of [O]/[Hf] = 1.5, which is close to the experimental value of [O]/[Hf] = 1.7 as determined via XPS. E) and f) show the calculated stable structures of *m*-HfO_2 and *r*-$HfO_{1.5}$. Reprinted with permission from reference [151]. https://doi.org/10.1021/acsaelm.2c01255 Copyright © 2023 American Chemical Society. 78

Figure 52: a), b) and c) showing the corresponding (111), (-111) and (002) reflections which are transferred in d) where a comparison between a cubic reference and the calculated rhombohedral phase is shown. Note that the rhombohedral peak splitting between (111) and (-111) is even more pronounced for the calculated as for the measured case. e) displays the corresponding lattice parameters of all discussed phases. f) & g) showing pole figure measurements which reflect the set of (-111) and (002) lattice planes. Note that the lattice planes are represented in white and black, indicating the multi-domain nature of the thin film. h) & i) show a comparison between a stoichiometric cubic phase yielding the highly symmetric *Fm*-3*m* space group and the calculated rhombohedral phase with two oxygen vacancies, yielding a polar *R*3*m* symmetry. j) and k) show the rhombohedral phase in (111) growth direction from the side and top view respectively. Reprinted with permission from reference [151]. https://doi.org/10.1021/acsaelm.2c01255 Copyright © 2023 American Chemical Society. 82

Figure 53: a) and b) compare XPS valence spectra and optical bandgap values to calculated DOS for m-HfO_2 as well as r-$HfO_{1.7}$ from measurement and r-$HfO_{1.5}$ from calculation respectively. c) & d) show the corresponding Tauc plots for bandgap estimation. Note the close resemblance of XPS spectroscopic data with the calculated DOS as well as the close agreement with the optical bandgap between the most pronounced occupied and unoccupied DOS. Reprinted with permission from reference [151]. https://doi.org/10.1021/acsaelm.2c01255 Copyright © 2023 American Chemical Society. 83

Figure 54: Band structure and orbital resolved DOS for the calculated structures of a) stoichiometric monoclinic *m*-HfO_2 and b) deficient rhombohedral *r*-$HfO_{1.5}$. Both predictions show a high level of agreement to the experimental results. Reprinted with permission from reference [151]. https://doi.org/10.1021/acsaelm.2c01255 Copyright © 2023 American Chemical Society. 85

Figure 55: Predicted DOS of all structures as calculated for the energy comparison in chapter 4.1.3. The corresponding lattice parameters and atomic positions are found in Table 5. While $HfO_{1.5}$ is identified as a turning point from monoclinic to rhombohedral transformation, the rhombohedral structure shows more disperse defect states, with a significantly smaller gap to the CBM, therefore indicating higher conductivity as compared to the deficient monoclinic structure. Reprinted with permission from reference [151]. https://doi.org/10.1021/acsaelm.2c01255 Copyright © 2023 American Chemical Society. 86

Figure 56: a-b) 2θ/ω XRD measurements of series A with additional 35 nm TiN layer on the sapphire substrate and of series B on plain sapphire. Note the high similarities of the hafnium oxide phases for both oxygen dependent series and the excellent reproducibility of epitaxial TiN for series A. c)

shows the XPS estimated stoichiometry of series B for reference. d-e) shows the RHEED patterns of the c-cut sapphire substrate and the TiN layer, indicating good surface quality and epitaxial crystallinity. f) deposition conditions for both series in dependence of the sample number. g) comparison of the (-111) *m*-HfO_{2-x}, (111) *r*-HfO_{2-x} and (002) *hcp*-HfO_{2-x} reflections show the high level of agreement between both series also for the relative 2θ positions. 88

Figure 57: XRR data of the key samples a) #1a *m*-HfO_2 , b) #5a *r*-HfO_{2-x} and c) #7a *hcp*-HfO_{2-x} with representative fitting via RCRefSim. Reasonable results could be obtained in any case using a two-layer model of hafnium oxide and titanium nitride on an aluminum oxide substrate. The vertical dashed lines show the range in which the fit is applied to the data. Below the corresponding fitting parameters are shown. 89

Figure 58: XRR thicknesses of the investigated samples HfO_{2-x} and TiN layers as extracted by fitting via RCRefSim. The graph shows uniform thickness of 35 ± 2 nm for the TiN bottom electrode and 20 ± 2 nm for the HfO_{2-x} layers which have been achieved via extensive calibration. 90

Figure 59: Loadlock setup for the removal of individual samples of TiN/HfO_{2-x} before platinum capping. a) Shows how a blade is connected below the sample garage, allowing samples to be detached from the holder, which can then fall into a steel net installed underneath. b) shows the four positions p1-p4 on which 5 x 5 mm substrates are glued on the sample holder. Note that that sample on p4 has already been detached by the blade. c) side view, showing how the blade is attached to the sample garage allowing to control height and rotation. 91

Figure 60: Comparison of the reproducibility of RRAM stacks with monoclinic (top), rhombohedral (middle) and hexagonal (bottom) hafnium oxide phases. Note that for every graph all four samples have been grown with the same settings simultaneously. Generally, the plots show a high level of reproducibility, with the biggest difference being a slight shift and higher signal intensity for the rhombohedral reflex (111). Note that samples at positions p1 and p3 which have been in-vacuo deposited with platinum show a corresponding Pt (111) reflex. 92

Figure 61: Overview of IV-characteristics for TiN/HfO_{2-x}/Pt stacks with the key phases a) *m*-HfO_2 b) *r*-$HfO_{1.7}$ and c) *hcp*-$HfO_{0.7}$. Note that stoichiometric, monoclinic devices d,h) show stable switching for at least 100x cycles independent of their preparation method (in-air or in-vacuo) which is expected. For deficient layers of hafnium oxide however there is a significant difference. For both, *r*-$HfO_{1.7}$ and *hcp*-$HfO_{0.7}$ stable switching can be observed if treated in-air e,f), however, if the same devices are prepared in-vacuo, they show a significant decrease in resistivity and no switching properties. Note that for all cases a G_0 reference is marked as a green line, showing the HRS is below or close to G_0 for all switching samples (as expected). For the conducting samples, the IV curves show even significantly higher conductivity than the LRS of all switching samples (up to the compliance current). k-l) show in-vacuo XPS valence spectra of reference measurements of corresponding hafnium oxide phases which show midgap states in the vicinity of the fermi level which is in good agreement with the observation of conducting, not switching samples if prepared in-vacuo. 93

Figure 62: Forming Voltage characteristics of devices with stoichiometric monoclinic hafnium oxide as well as deficient rhombohedral and hexagonal hafnium oxide as prepared in-air. All forming steps have been performed with negative polarity from the Pt top electrode towards the grounded TiN bottom electrode. Note that the stoichiometric *m*-HfO_2 layers show high forming voltages up to -6.5 V (in-air and in-vacuo) while deficient devices (in-air) of *r*-$HfO_{1.7}$ and *hcp*-$HfO_{0.7}$ show a stoichiometry independent low forming voltage of about -1.5 V. 95

Figure 63: Simplified model of the filament formation in stoichiometric against oxygen deficient hafnium oxide after exposure to air. a) The stoichiometric sample requires the largest formation voltage as the filament forms through the whole hafnium oxide layer. b) and c) for both deficient *r*-$HfO_{1.7}$ and *hcp*-$HfO_{0.7}$ a surface oxidation layer of limited thickness evolves in air. As both *r*-$HfO_{1.7}$ and *hcp*-

$HfO_{0.7}$ show conducting properties they act as the effective bottom electrodes and the formation voltage is only defined by the surface oxidation layers. This results in identical low formation voltages for both, *r*-$HfO_{1.7}$ and *hcp*-$HfO_{0.7}$. 95

Figure 64: Comparison of leakage measurements from devices a) against Van der Paw resistivity measurements (eliminating contact resistance) obtained directly from hafnium oxide layers c). The results directly compare electrical characteristics from series A and B where the hafnium oxide layers are grown under identical conditions. b) shows the cumulative distribution of leakage currents (V_{read} = 0.2 V) from the device measurements. Note that there is a significant difference between the first two samples #1, #2 which can be considered insulating and the rest #3-#7 which show rather conducting properties. Similarly, for the physical properties, the first two samples could not be measured, but samples #3-#7 show significant electrical conduction in increasing order. Interestingly the limit shown in b) is most likely not determined by the hafnium oxide layer, but by the contact resistance of the sample stack and the measuring setup. Therefore, both series are in good agreement. 97

Figure 65: Overview of I-V characteristics in double logarithmic representation for devices with key structures *m*-HfO_2, *r*-$HfO_{1.7}$ and *hcp*-$HfO_{0.7}$ treated in-air and in-vacuo. For all switching samples a)-d) the reset is shown for 100 cycles. Note that the LRS shows a slope of ~1 for all switching devices, which indicates ohmic conduction and therefore conduction over free charge carriers. The HRS generally shows a higher cycle to cycle variability, but corresponds reasonably to space charge limited conduction (SCLC) for a,b,d) as indicated by the transition from a ~ 1 slope to a ~ 2 slope. For the oxygen deficient samples treated in-vacuo 10 devices are shown which only follow a straight line with a slope of ~ 1 indicating ohmic conduction which is in good agreement with the high conductivity of the phases. 99

Figure 66: Comparison of crystalline quality for oxygen deficient rhombohedral hafnium oxide and stoichiometric monoclinic hafnium oxide grown on 35 nm TiN and 200 nm TiN respectively. Note that for both hafnium oxide phases at least the same reflection intensities are visible. For the TiN layer a shift to TiN_{1-x} as well as additional reflections can be seen which are likely metallic or subnitride phases which would be expected for the fast growing initial layer for 200nm TiN. ?^{2} corresponds likely to an additional (200) TiN orientation. The additional reflection close to (111) TiN suggests a back-shift to close to stoichiometric TiN for the final 30 nm of deposition. 100

Figure 67: a) Comparison of forming voltages for stoichiometric m-HfO_2 (prepared in-vacuo) on 200 nm TiN and 35 nm TiN. Note that the Forming voltage statistics are significantly reduced for HfO_2 grown on 200 nm TiN which could be due to increased roughness. b) shows 100 cycles of a corresponding RRAM device with thick bottom electrode verifying its applicability for operando TEM. 101

Figure 68: See a comparison between images taken from samples showing the most isolated phases of *m*-HfO_2 (a,d), *r*-$HfO_{1.7}$ (b,e) and *hcp*-$HfO_{0.7}$ (c). The top row shows images resulting from HR-TEM while the lower row corresponds to HAADF-STEM imaging. The top row samples are sandwiched between the sapphire substrate (bright contrast) and platinum for FIB preparation (dark contrast) while for the HAADF images samples are sandwiched between TiN (dark contrast) and Pt (bright contrast). Both methods are suitable for mapping lattice plane distances in real space. The HRTEM images show insets highlighting the of the out of plane lattice parameter while the insets for the HAADF-STEM show different sets of lattice spacing's overlays with multislice simulations. In parts reprinted with permission from reference [146]. https://doi.org/10.1021/acsami.1c09451 Copyright © 2021 American Chemical Society. 105

Figure 69: Electron energy loss spectroscopy data of the most isolated phases of *m*-HfO_2, *r*-$HfO_{1.7}$ and *hcp*-$HfO_{0.7}$. The obtained spectra are averaged over the sample growth thickness of ~ 20 nm, scanning the low loss region. All spectra have been normalized after background subtraction. The Graph

shows fitting of the main components (vertical lines) where dashed lines correspond to constant contributions. 106

Figure 70: (a,b) Nano beam electron diffraction patterns of hafnium oxide grains which match the corresponding templates for *m*-HfO_2 and *r*-$HfO_{1.7}$. (c-e) 2D ACOM maps of (c) only *m*-HfO_2,(d) mixed m- + *r*-HfO_{2-x} and (e) only *r*-HfO_{2-x}. Note that in (c,e) the majority of pixels are correctly assigned and that in the mixed case (d) both phases are assigned to almost equal portions. Note specifically the continuous *r*-HfO_{2-x} area between the Al_2O_3 substrate and Pt which represents a conducting path due to phase-property correlation. 107

Figure 71: XRD data of two series from *m*-HfO_2 to *r*-$HfO_{1.7}$ calibrated to either a) 10 nm and b) 20 nm thickness on collaborative substrate holders. Both, the reproduction of TiN and HfO_{2-x} appears in good quality compared to growth on conventional sample holders. The phase transition from a monoclinic to a rhombohedral structure is best replicated by the 20 nm series, while the 10 nm series shows a tendency towards an overall increased rhombohedral phase fraction. This finding could indicate that the rhombohedral phase favors smaller grain sizes. 110

Figure 72: XRR data and corresponding fit via XRR RefSim of all samples of the 10 nm series. Reasonable fitting results could be obtained in any case using a two-layer model of HfO_2/TiN/Al_2O_3. The extracted values indicate consistent TiN thicknesses close to 34 nm and HfO_{2-x} thicknesses close to 10 nm throughout the series. Further for all samples the Air/HfO_{2-x} surface as well as the HfO_{2-x}/TiN interface both show a virtually identical roughness close to 1 nm. 111

Figure 73: AFM topography of the 10 nm sample series from monoclinic (0.1 Å/s) to rhombohedral (1.2 Å/s) hafnium oxide which was performed in UHV conditions (10^{-9} mbar), using a PtIr-cantilever (r < 25 nm) with a force set point of 1.0 nN. Note that the topography shows lateral grain structures of several 10 nm for all samples. The RMS values vary around 0.9 nm and line scans indicate peak to valley distances between 2 – 4 nm for all samples. 113

Figure 74: Conductive AFM current maps superimposed over the corresponding topography on oxygen deficient hafnium oxide. The overlay indicates how the formation of preferential conduction paths at different voltages is mediated between supposed grains and therefore at grain boundaries. Current above 10 nA appears cyan. 114

Figure 75: a) hafnium oxide in device configuration b) corresponding leakage measurements after a forming voltage sweep for the most deficient devices that showed some statistical spread from the limit. All devices which showed some deviation from the limit (e.g. for stacks #5- #6) value at 3E-3 A perfectly align to this limit after a high voltage sweep. XVI

Figure 76: a) Verifying electrical contacts between sample surface and substrate holder after TiN deposition while using insulating sapphire substrates. b) vacuum-suitcase from Mantis Deposition Ltd. detached from the frame and fixed close to the 12V power supply c) vacuum-suitcase on adjustable frame connected to a central distribution system at Elektronische Materialien; PGI-7 in FZ Jülich. d) after successful sample transfer from Nico Kaiser (right) to Niclas Schmidt (left) at FZ Jülich. XVI

Figure 77: Final design of the sample holder which is compatible with both TU Darmstadt and FZ Jülich facilities between Prof. Alff (ATFT) and Prof. Dittmann/Prof. Waser (Elektronische Materialien; PGI-7). XVII

List of Tables

Table 1: Survey of relevant conduction mechanisms with corresponding current density expression and electric field and temperature dependency. Adopted after reference [32] https://doi.org/10.3390/electronics4030586 which is published under Attribution 4.0 International (CC BY 4.0) License. 14

Table 2: Optimized lithographic routines for corresponding square features. 43

Table 3: Ion Beam Etching Parameters used for Pt/HfO_{2-x}/TiN stacks. All etching has been performed with liquid nitrogen cooling of the sample holder. 45

Table 4: Crystal structure of *r*-$HfO_{1.7}$ as extracted from the XRD measurements on sample #9 in comparison to the cubic reference (*c*-$HfO_{2;}$ PDF 04-011-9018). Note that the main difference is given by the elongation in [111], resulting in $\alpha = \beta = \gamma = 89.66°$. 58

Table 5: Calculated crystal structures and atomic positions of relaxed stoichiometric and oxygen deficient hafnium oxide structures. Reprinted with permission from reference [151]. https://doi.org/10.1021/acsaelm.2c01255 Copyright © 2023 American Chemical Society. 80

Bibliography

1. Wong, H.-S.P. and S. Salahuddin, *Memory Leads the Way to Better Computing.* Nature nanotechnology, 2015. **10**(3): p. 191-194.
2. Itoh, K., *Vlsi Memory Chip Design*. Vol. 5. 2013: Springer Science & Business Media.
3. Rydning, D.R.-J.G.-J., J. Reinsel, and J. Gantz, *The Digitization of the World from Edge to Core.* Framingham: International Data Corporation, 2018. **16**.
4. Compagnoni, C.M., A. Goda, A.S. Spinelli, P. Feeley, A.L. Lacaita, and A. Visconti, *Reviewing the Evolution of the Nand Flash Technology.* Proceedings of the IEEE, 2017. **105**(9): p. 1609-1633.
5. Compagnoni, C.M. and A.S. Spinelli, *Reliability of Nand Flash Arrays: A Review of What the 2-D–to–3-D Transition Meant.* IEEE Transactions on Electron Devices, 2019. **66**(11): p. 4504-4516.
6. Akinaga, H. and H. Shima, *Resistive Random Access Memory (Reram) Based on Metal Oxides.* Proceedings of the IEEE, 2010. **98**(12): p. 2237-2251.
7. Chen, Y., *Reram: History, Status, and Future.* IEEE Transactions on Electron Devices, 2020. **67**(4): p. 1420-1433.
8. Valov, I., *Interfacial Interactions and Their Impact on Redox-Based Resistive Switching Memories (Rerams).* Semiconductor Science and Technology, 2017. **32**(9): p. 093006.
9. Lai, S. *Current Status of the Phase Change Memory and Its Future*. in *IEEE International Electron Devices Meeting 2003*. 2003. IEEE.
10. Raoux, S., F. Xiong, M. Wuttig, and E. Pop, *Phase Change Materials and Phase Change Memory.* MRS bulletin, 2014. **39**(8): p. 703-710.
11. Wouters, D.J., R. Waser, and M. Wuttig, *Phase-Change and Redox-Based Resistive Switching Memories.* Proceedings of the IEEE, 2015. **103**(8): p. 1274-1288.
12. Tehrani, S., J. Slaughter, E. Chen, M. Durlam, J. Shi, and M. DeHerren, *Progress and Outlook for Mram Technology.* IEEE Transactions on Magnetics, 1999. **35**(5): p. 2814-2819.
13. Apalkov, D., A. Khvalkovskiy, S. Watts, V. Nikitin, X. Tang, D. Lottis, K. Moon, X. Luo, E. Chen, and A. Ong, *Spin-Transfer Torque Magnetic Random Access Memory (Stt-Mram).* ACM Journal on Emerging Technologies in Computing Systems (JETC), 2013. **9**(2): p. 1-35.
14. Francois, T., L. Grenouillet, J. Coignus, P. Blaise, C. Carabasse, N. Vaxelaire, T. Magis, F. Aussenac, V. Loup, and C. Pellissier. *Demonstration of Beol-Compatible Ferroelectric Hf 0.5 Zr 0.5 O 2 Scaled Feram Co-Integrated with 130nm Cmos for Embedded Nvm Applications*. in *2019 IEEE International Electron Devices Meeting (IEDM)*. 2019. IEEE.
15. Mikolajick, T., C. Dehm, W. Hartner, I. Kasko, M. Kastner, N. Nagel, M. Moert, and C. Mazure, *Feram Technology for High Density Applications.* Microelectronics Reliability, 2001. **41**(7): p. 947-950.
16. Slesazeck, S. and T. Mikolajick, *Nanoscale Resistive Switching Memory Devices: A Review.* Nanotechnology, 2019. **30**(35): p. 352003.
17. Lacaze, P.C. and J.C. Lacroix, *State of the Art of Dram, Sram, Flash, Hdd and Mram Electronic Memories.* Non-Volatile Memories, 2014: p. 13-57.
18. Luo, Y., S. Ghose, Y. Cai, E.F. Haratsch, and O. Mutlu, *Improving 3d Nand Flash Memory Lifetime by Tolerating Early Retention Loss and Process Variation.* Proceedings of the ACM on Measurement and Analysis of Computing Systems, 2018. **2**(3): p. 1-48.
19. Pavan, P., R. Bez, P. Olivo, and E. Zanoni, *Flash Memory Cells-an Overview.* Proceedings of the IEEE, 1997. **85**(8): p. 1248-1271.
20. Molas, G. and E. Nowak, *Advances in Emerging Memory Technologies: From Data Storage to Artificial Intelligence.* Applied Sciences, 2021. **11**(23): p. 11254.
21. Zahoor, F., T.Z. Azni Zulkifli, and F.A. Khanday, *Resistive Random Access Memory (Rram): An Overview of Materials, Switching Mechanism, Performance, Multilevel Cell*

(Mlc) Storage, Modeling, and Applications. Nanoscale research letters, 2020. **15**(1): p. 1-26.

22. Kau, D., S. Tang, I.V. Karpov, R. Dodge, B. Klehn, J.A. Kalb, J. Strand, A. Diaz, N. Leung, and J. Wu. *A Stackable Cross Point Phase Change Memory*. in *2009 IEEE International Electron Devices Meeting (IEDM)*. 2009. IEEE.
23. Chen, H.-Y., S. Brivio, C.-C. Chang, J. Frascaroli, T.-H. Hou, B. Hudec, M. Liu, H. Lv, G. Molas, and J. Sohn, *Resistive Random Access Memory (Rram) Technology: From Material, Device, Selector, 3d Integration to Bottom-up Fabrication.* Journal of Electroceramics, 2017. **39**(1-4): p. 21-38.
24. Perrissin, N., G. Gregoire, S. Lequeux, L. Tillie, N. Strelkov, S. Auffret, L. Buda-Prejbeanu, R. Sousa, L. Vila, and B. Dieny, *Perpendicular Shape Anisotropy Spin Transfer Torque Magnetic Random-Access Memory: Towards Sub-10 Nm Devices.* Journal of Physics D: Applied Physics, 2019. **52**(23): p. 234001.
25. Silver, D., A. Huang, C.J. Maddison, A. Guez, L. Sifre, G. Van Den Driessche, J. Schrittwieser, I. Antonoglou, V. Panneershelvam, and M. Lanctot, *Mastering the Game of Go with Deep Neural Networks and Tree Search.* nature, 2016. **529**(7587): p. 484-489.
26. Hart, L.A., *How the Brain Works*. 1975: Basic Books.
27. Drubach, D., *The Brain Explained*. 2000: Pearson.
28. Moon, K., S. Lim, J. Park, C. Sung, S. Oh, J. Woo, J. Lee, and H. Hwang, *Rram-Based Synapse Devices for Neuromorphic Systems.* Faraday discussions, 2019. **213**: p. 421-451.
29. Petzold, S., E. Piros, S.U. Sharath, A. Zintler, E. Hildebrandt, L. Molina-Luna, C. Wenger, and L. Alff, *Gradual Reset and Set Characteristics in Yttrium Oxide Based Resistive Random Access Memory.* Semiconductor Science and Technology, 2019. **34**(7): p. 075008.
30. Petzold, S., E. Piros, R. Eilhardt, A. Zintler, T. Vogel, N. Kaiser, A. Radetinac, P. Komissinskiy, E. Jalaguier, E. Nolot, C. Charpin-Nicolle, C. Wenger, L. Molina-Luna, E. Miranda, and L. Alff, *Tailoring the Switching Dynamics in Yttrium Oxide-Based Rram Devices by Oxygen Engineering: From Digital to Multi-Level Quantization toward Analog Switching.* Advanced Electronic Materials, 2020. **6**(11): p. 2000439.
31. Sharath, S.U., S. Vogel, L. Molina-Luna, E. Hildebrandt, C. Wenger, J. Kurian, M. Duerrschnabel, T. Niermann, G. Niu, P. Calka, M. Lehmann, H.J. Kleebe, T. Schroeder, and L. Alff, *Control of Switching Modes and Conductance Quantization in Oxygen Engineered Hfox Based Memristive Devices.* Advanced Functional Materials, 2017. **27**(32).
32. Lim, E.W. and R. Ismail, *Conduction Mechanism of Valence Change Resistive Switching Memory: A Survey.* Electronics, 2015. **4**(3): p. 586-613.
33. Wang, H. and X. Yan, *Overview of Resistive Random Access Memory (Rram): Materials, Filament Mechanisms, Performance Optimization, and Prospects.* physica status solidi (RRL)–Rapid Research Letters, 2019. **13**(9): p. 1900073.
34. Lee, J.S., S. Lee, and T.W. Noh, *Resistive Switching Phenomena: A Review of Statistical Physics Approaches.* Applied Physics Reviews, 2015. **2**(3): p. 031303.
35. Yang, J.J., D.B. Strukov, and D.R. Stewart, *Memristive Devices for Computing.* Nature nanotechnology, 2013. **8**(1): p. 13-24.
36. Petzold, S., E. Miranda, S. Sharath, J. Muñoz-Gorriz, T. Vogel, E. Piros, N. Kaiser, R. Eilhardt, A. Zintler, L. Molina-Luna, J. Suñé, and L. Alff, *Analysis and Simulation of the Multiple Resistive Switching Modes Occurring in Hfo X-Based Resistive Random Access Memories Using Memdiodes.* Journal of Applied Physics, 2019. **125**(23): p. 234503.
37. Curtis, C., L. Doney, and J. Johnson, *Some Properties of Hafnium Oxide, Hafnium Silicate, Calcium Hafnate, and Hafnium Carbide.* Journal of the American Ceramic Society, 1954. **37**(10): p. 458-465.
38. Wang, J., H.P. Li, and R. Stevens, *Hafnia and Hafnia-Toughened Ceramics.* Journal of Materials Science, 1992. **27**(20): p. 5397-5430.
39. Ohtaka, O., H. Fukui, T. Kunisada, T. Fujisawa, K. Funakoshi, W. Utsumi, T. Irifune, K. Kuroda, and T. Kikegawa, *Phase Relations and Volume Changes of Hafnia under High*

Pressure and High Temperature. Journal of the American Ceramic Society, 2001. **84**(6): p. 1369-1373.

40. Kang, J., E.C. Lee, and K.J. Chang, *First-Principles Study of the Structural Phase Transformation of Hafnia under Pressure.* Physical Review B, 2003. **68**(5): p. 054106.
41. Leger, J.M., A. Atouf, P. Tomaszewski, and A.S. Pereira, *Pressure-Induced Phase Transitions and Volume Changes in Hfo 2 up to 50 Gpa.* Physical Review B, 1993. **48**(1): p. 93.
42. Müller, J., P. Polakowski, S. Mueller, and T. Mikolajick, *Ferroelectric Hafnium Oxide Based Materials and Devices: Assessment of Current Status and Future Prospects.* ECS Journal of Solid State Science and Technology, 2015. **4**(5): p. N30.
43. Böscke, T., J. Müller, D. Bräuhaus, U. Schröder, and U. Böttger, *Ferroelectricity in Hafnium Oxide Thin Films.* Applied Physics Letters, 2011. **99**(10): p. 102903.
44. Mueller, S., J. Mueller, A. Singh, S. Riedel, J. Sundqvist, U. Schroeder, and T. Mikolajick, *Incipient Ferroelectricity in Al-Doped Hfo2 Thin Films.* Advanced Functional Materials, 2012. **22**(11): p. 2412-2417.
45. Schroeder, U., C. Richter, M.H. Park, T. Schenk, M. Pesic, M. Hoffmann, F.P. Fengler, D. Pohl, B. Rellinghaus, and C. Zhou, *Lanthanum-Doped Hafnium Oxide: A Robust Ferroelectric Material.* Inorganic chemistry, 2018. **57**(5): p. 2752-2765.
46. Hoffmann, M., U. Schroeder, T. Schenk, T. Shimizu, H. Funakubo, O. Sakata, D. Pohl, M. Drescher, C. Adelmann, and R. Materlik, *Stabilizing the Ferroelectric Phase in Doped Hafnium Oxide.* Journal of Applied Physics, 2015. **118**(7): p. 072006.
47. Huan, T.D., V. Sharma, G.A. Rossetti, and R. Ramprasad, *Pathways Towards Ferroelectricity in Hafnia.* Physical Review B, 2014. **90**(6): p. 064111.
48. Polakowski, P. and J. Müller, *Ferroelectricity in Undoped Hafnium Oxide.* Applied Physics Letters, 2015. **106**(23): p. 232905.
49. Mittmann, T., M. Materano, P.D. Lomenzo, M.H. Park, I. Stolichnov, M. Cavalieri, C. Zhou, C.C. Chung, J.L. Jones, and T. Szyjka, *Origin of Ferroelectric Phase in Undoped Hfo2 Films Deposited by Sputtering.* Advanced Materials Interfaces, 2019. **6**(11): p. 1900042.
50. Wei, Y., P. Nukala, M. Salverda, S. Matzen, H.J. Zhao, J. Momand, A.S. Everhardt, G. Agnus, G.R. Blake, and P. Lecoeur, *A Rhombohedral Ferroelectric Phase in Epitaxially Strained Hf 0.5 Zr 0.5 O 2 Thin Films.* Nature materials, 2018. **17**(12): p. 1095-1100.
51. Nukala, P., Y.F. Wei, V. de Haas, Q.K. Guo, J. Antoja-Lleonart, and B. Noheda, *Guidelines for the Stabilization of a Polar Rhombohedral Phase in Epitaxial Hf0.5zr0.5o2 Thin Films.* Ferroelectrics, 2020. **569**(1): p. 148-163.
52. Bégon-Lours, L., M. Mulder, P. Nukala, S. De Graaf, Y.A. Birkhölzer, B. Kooi, B. Noheda, G. Koster, and G. Rijnders, *Stabilization of Phase-Pure Rhombohedral Hfzr O 4 in Pulsed Laser Deposited Thin Films.* Physical Review Materials, 2020. **4**(4): p. 043401.
53. Klapper, H. and T. Hahn, *International Tables for Crystallography (2006). Vol. A.* 2006. p. 804-808.
54. Kofstad, P. and D. Ruzicka, *On the Defect Structure of Zro2 and Hfo2.* Journal of The Electrochemical Society, 1963. **110**(3): p. 181.
55. Tallan, N., W. Tripp, and R. Vest, *Electrical Properties and Defect Structure of Hfo2.* Journal of the American Ceramic Society, 1967. **50**(6): p. 279-283.
56. Sarakinos, K., D. Music, S. Mraz, M.T. Baben, K. Jiang, F. Nahif, A. Braun, C. Zilkens, S. Konstantinidis, F. Renaux, D. Cossement, F. Munnik, and J.M. Schneider, *On the Phase Formation of Sputtered Hafnium Oxide and Oxynitride Films.* Journal of Applied Physics, 2010. **108**(1): p. 014904.
57. Ritala, M., M. Leskela, L. Niinisto, T. Prohaska, G. Friedbacher, and M. Grasserbauer, *Development of Crystallinity and Morphology in Hafnium Dioxide Thin-Films Grown by Atomic Layer Epitaxy.* Thin Solid Films, 1994. **250**(1-2): p. 72-80.

58. Xu, X., F.-T. Huang, Y. Qi, S. Singh, K.M. Rabe, D. Obeysekera, J. Yang, M.-W. Chu, and S.-W. Cheong, *Kinetically Stabilized Ferroelectricity in Bulk Single-Crystalline Hfo 2: Y.* Nature Materials, 2021: p. 1-7.
59. Manory, R.R., T. Mori, I. Shimizu, S. Miyake, and G. Kimmel, *Growth and Structure Control of Hfo 2− X Films with Cubic and Tetragonal Structures Obtained by Ion Beam Assisted Deposition.* Journal of Vacuum Science & Technology A: Vacuum, Surfaces, and Films, 2002. **20**(2): p. 549-554.
60. Mori, T., M. Fujiwara, R.R. Manory, I. Shimizu, T. Tanaka, and S. Miyake, *Hfo2 Thin Films Prepared by Ion Beam Assisted Deposition.* Surface and Coatings Technology, 2003. **169**: p. 528-531.
61. Hildebrandt, E., J. Kurian, J. Zimmermann, A. Fleissner, H. von Seggern, and L. Alff, *Hafnium Oxide Thin Films: Effect of Growth Parameters on Oxygen and Hafnium Vacancies.* Journal of Vacuum Science & Technology B: Microelectronics and Nanometer Structures Processing, Measurement, and Phenomena, 2009. **27**(1): p. 325-328.
62. Hildebrandt, E., J. Kurian, M.M. Muller, T. Schroeder, H.J. Kleebe, and L. Alff, *Controlled Oxygen Vacancy Induced P-Type Conductivity in Hfo2-X Thin Films.* Applied Physics Letters, 2011. **99**(11): p. 112902.
63. Hildebrandt, E., J. Kurian, and L. Alff, *Physical Properties and Band Structure of Reactive Molecular Beam Epitaxy Grown Oxygen Engineered Hfo 2±X.* Journal of Applied Physics, 2012. **112**(11): p. 114112.
64. Hirabayashi, M., S. Yamaguchi, T. Arai, H. Asano, and S. Hashimoto, *Interstitial Order-Disorder Transformations in the Zr–O and Hf–O Systems near the Compositions Zro1⁄3 and Hfo1⁄6.* Journal of the Physical Society of Japan, 1972. **32**(4): p. 1157-1157.
65. Hirabayashi, M., S. Yamaguchi, and T. Arai, *Superstructure and Order-Disorder Transformation of Interstitial Oxygen in Hafnium.* Journal of the Physical Society of Japan, 1973. **35**(2): p. 473-481.
66. Rushchanskii, K.Z., S. Blügel, and M. Ležaić, *Routes for Increasing Endurance and Retention in Hfo 2-Based Resistive Switching Memories.* Physical Review Materials, 2018. **2**(11): p. 115002.
67. Rushchanskii, K.Z., S. Blugel, and M. LeZaic, *Ab Initio Phase Diagrams of Hf-O, Zr-O and Y-O: A Comparative Study.* Faraday Discuss, 2019. **213**(0): p. 321-337.
68. Foster, A.S., F.L. Gejo, A. Shluger, and R.M. Nieminen, *Vacancy and Interstitial Defects in Hafnia.* Physical Review B, 2002. **65**(17): p. 174117.
69. Gritsenko, V.A., T.V. Perevalov, and D.R. Islamov, *Electronic Properties of Hafnium Oxide: A Contribution from Defects and Traps.* Physics Reports, 2016. **613**: p. 1-20.
70. Xiong, K., J. Robertson, M. Gibson, and S. Clark, *Defect Energy Levels in Hfo 2 High-Dielectric-Constant Gate Oxide.* Applied physics letters, 2005. **87**(18): p. 183505.
71. Gavartin, J., D. Muñoz Ramo, A. Shluger, G. Bersuker, and B. Lee, *Negative Oxygen Vacancies in Hf O 2 as Charge Traps in High-K Stacks.* Applied Physics Letters, 2006. **89**(8): p. 082908.
72. Broqvist, P. and A. Pasquarello, *Oxygen Vacancy in Monoclinic Hf O 2: A Consistent Interpretation of Trap Assisted Conduction, Direct Electron Injection, and Optical Absorption Experiments.* Applied physics letters, 2006. **89**(26): p. 262904.
73. Wang, B.Z., M. Wang, F.X. Duan, J. Ren, Y. Li, and T.G. Zhou, *First Principles Study of Defects in High-K Hfo2.* Superlattices and Microstructures, 2016. **99**: p. 88-93.
74. McKenna, K.P., *Optimal Stoichiometry for Nucleation and Growth of Conductive Filaments in Hfox.* Modelling and Simulation in Materials Science and Engineering, 2014. **22**(2): p. 025001.
75. Padilha, A. and K. McKenna, *Structure and Properties of a Model Conductive Filament/Host Oxide Interface in Hfo 2-Based Reram.* Physical Review Materials, 2018. **2**(4): p. 045001.

76. Xue, K.-H., P. Blaise, L.R. Fonseca, and Y. Nishi, *Prediction of Semimetallic Tetragonal Hf 2 O 3 and Zr 2 O 3 from First Principles.* Physical review letters, 2013. **110**(6): p. 065502.
77. Li, L.-H., K.-H. Xue, J.-H. Yuan, G.-Q. Mao, and X. Miao, *Hafnia for Analog Memristor: Influence of Stoichiometry and Crystalline Structure.* Physical Review Materials, 2022. **6**(8): p. 084603.
78. Zhang, J., A.R. Oganov, X. Li, K.-H. Xue, Z. Wang, and H. Dong, *Pressure-Induced Novel Compounds in the Hf-O System from First-Principles Calculations.* Physical Review B, 2015. **92**(18): p. 184104.
79. Schmidt, N., K.Z. Rushchanskii, U.k. Trstenjak, R. Dittmann, and S. Karthaüser, *In-Gap States of Hfo2 Nanoislands Driven by Crystal Nucleation: Implications for Resistive Random-Access Memory Devices.* ACS Applied Nano Materials, 2022.
80. Chiu, F.-C., *A Review on Conduction Mechanisms in Dielectric Films.* Advances in Materials Science and Engineering, 2014. **2014**.
81. Mahapatra, R., S. Maji, A. Horsfall, and N. Wright, *Temperature Impact on Switching Characteristics of Resistive Memory Devices with Hfox/Tiox/Hfox Stack Dielectric.* Microelectronic Engineering, 2015. **138**: p. 118-121.
82. Syu, Y.-E., T.-C. Chang, J.-H. Lou, T.-M. Tsai, K.-C. Chang, M.-J. Tsai, Y.-L. Wang, M. Liu, and S.M. Sze, *Atomic-Level Quantized Reaction of Hfox Memristor.* Applied Physics Letters, 2013. **102**(17): p. 172903.
83. Sharath, S.U., S. Vogel, L. Molina-Luna, E. Hildebrandt, C. Wenger, J. Kurian, M. Duerrschnabel, T. Niermann, G. Niu, and P. Calka, *Control of Switching Modes and Conductance Quantization in Oxygen Engineered Hfox Based Memristive Devices.* Advanced Functional Materials, 2017. **27**(32).
84. Lee, H., P. Chen, T. Wu, Y. Chen, C. Wang, P. Tzeng, C. Lin, F. Chen, C. Lien, and M.-J. Tsai. *Low Power and High Speed Bipolar Switching with a Thin Reactive Ti Buffer Layer in Robust Hfo2 Based Rram*. in *2008 IEEE International Electron Devices Meeting*. 2008. IEEE.
85. Bersuker, G., J. Yum, L. Vandelli, A. Padovani, L. Larcher, V. Iglesias, M. Porti, M. Nafria, K. McKenna, A. Shluger, P. Kirsch, and R. Jammy, *Grain Boundary-Driven Leakage Path Formation in Hfo2 Dielectrics.* Solid-State Electronics, 2011. **65-66**: p. 146-150.
86. Long, B., Y. Li, S. Mandal, R. Jha, and K. Leedy, *Switching Dynamics and Charge Transport Studies of Resistive Random Access Memory Devices.* Applied Physics Letters, 2012. **101**(11): p. 113503.
87. Fang, R., W. Chen, L. Gao, W. Yu, and S. Yu, *Low-Temperature Characteristics of Hfo X-Based Resistive Random Access Memory.* IEEE Electron Device Letters, 2015. **36**(6): p. 567-569.
88. Spieß, L., H. Behnken, C. Genzel, R. Schwarzer, and G. Teichert, *Moderne Röntgenbeugung*. Vol. 2. 2009: Springer.
89. Yasaka, M., *X-Ray Thin-Film Measurement Techniques.* The Rigaku Journal, 2010. **26**(2): p. 1-9.
90. Sharath, S., M. Joseph, S. Vogel, E. Hildebrandt, P. Komissinskiy, J. Kurian, T. Schröder, and L. Alff, *Impact of Oxygen Stoichiometry on Electroforming and Multiple Switching Modes in Tin/Tao X/Pt Based Reram.* Applied Physics Letters, 2016. **109**(17): p. 173503.
91. Parratt, L.G., *Surface Studies of Solids by Total Reflection of X-Rays.* Physical review, 1954. **95**(2): p. 359.
92. Blanton, T.N. and C.R. Hoople, *X-Ray Diffraction Analysis of Ultrathin Platinum Silicide Films Deposited on (100) Silicon.* Powder Diffraction, 2002. **17**(1): p. 7-9.
93. Zaumseil, P., *Rcrefsim (Rocking Curve and Reflectivity Simulation).* IHP Frankfurt Oder, 2005.
94. Barabash, R., W. Donner, and H. Dosch, *X-Ray Scattering from Misfit Dislocations in Heteroepitaxial Films: The Case of Nb (110) on Al 2 O 3.* Applied Physics Letters, 2001. **78**(4): p. 443-445.

95. Harrington, G.F. and J. Santiso, *Back-to-Basics Tutorial: X-Ray Diffraction of Thin Films.* Journal of Electroceramics, 2021: p. 1-23.

96. Lu, Z., X. Sun, Y. Xiang, G.-C. Wang, M.A. Washington, and T.-M. Lu, *Large Scale Epitaxial Graphite Grown on Twin Free Nickel (111)/Spinel Substrate.* CrystEngComm, 2020. **22**(1): p. 119-129.

97. Egerton, R.F., *Choice of Operating Voltage for a Transmission Electron Microscope.* Ultramicroscopy, 2014. **145**: p. 85-93.

98. Kirkland, E.J., *Advanced Computing in Electron Microscopy*. Vol. 12. 1998: Springer.

99. Elbaum, M., S.G. Wolf, and L. Houben, *Cryo-Scanning Transmission Electron Tomography of Biological Cells.* MRS Bulletin, 2016. **41**(7): p. 542-548.

100. Egerton, R.F., *Electron Energy-Loss Spectroscopy in the Tem.* Reports on Progress in Physics, 2008. **72**(1): p. 016502.

101. Barth, G., R. Linder, and C. Bryson, *Advances in Charge Neutralization for Xps Measurements of Nonconducting Materials.* Surface and Interface Analysis, 1988. **11**(6-7): p. 307-311.

102. Suzer, S., H. Sezen, G. Ertas, and A. Dâna, *Xps Measurements for Probing Dynamics of Charging.* Journal of Electron Spectroscopy and Related Phenomena, 2010. **176**(1-3): p. 52-57.

103. Baer, D.R., K. Artyushkova, H. Cohen, C.D. Easton, M. Engelhard, T.R. Gengenbach, G. Greczynski, P. Mack, D.J. Morgan, and A. Roberts, *Xps Guide: Charge Neutralization and Binding Energy Referencing for Insulating Samples.* Journal of Vacuum Science & Technology A: Vacuum, Surfaces, and Films, 2020. **38**(3): p. 031204.

104. Barr, T.L. and S. Seal, *Nature of the Use of Adventitious Carbon as a Binding-Energy Standard.* Journal of Vacuum Science & Technology a-Vacuum Surfaces and Films, 1995. **13**(3): p. 1239-1246.

105. Swift, P., *Adventitious Carbon—the Panacea for Energy Referencing?* Surface and Interface Analysis, 1982. **4**(2): p. 47-51.

106. Morant, C., L. Galan, and J. Sanz, *An Xps Study of the Initial Stages of Oxidation of Hafnium.* Surface and interface Analysis, 1990. **16**(1-12): p. 304-308.

107. Seah, M., *The Quantitative Analysis of Surfaces by Xps: A Review.* Surface and Interface Analysis, 1980. **2**(6): p. 222-239.

108. Wagner, C., L. Davis, M. Zeller, J. Taylor, R. Raymond, and L. Gale, *Empirical Atomic Sensitivity Factors for Quantitative Analysis by Electron Spectroscopy for Chemical Analysis.* Surface and interface analysis, 1981. **3**(5): p. 211-225.

109. Shard, A.G., *Practical Guides for X-Ray Photoelectron Spectroscopy: Quantitative Xps.* Journal of Vacuum Science & Technology A: Vacuum, Surfaces, and Films, 2020. **38**(4): p. 041201.

110. Swinehart, D.F., *The Beer-Lambert Law.* Journal of chemical education, 1962. **39**(7): p. 333.

111. Tauc, J., R. Grigorovici, and A. Vancu, *Optical Properties and Electronic Structure of Amorphous Germanium.* physica status solidi (b), 1966. **15**(2): p. 627-637.

112. Coulter, J.B. and D.P. Birnie, *Assessing Tauc Plot Slope Quantification: Zno Thin Films as a Model System.* Physica Status Solidi B-Basic Solid State Physics, 2018. **255**(3): p. 1700393.

113. Viezbicke, B.D., S. Patel, B.E. Davis, and D.P. Birnie, *Evaluation of the Tauc Method for Optical Absorption Edge Determination: Zno Thin Films as a Model System.* Physica Status Solidi B-Basic Solid State Physics, 2015. **252**(8): p. 1700-1710.

114. Makuła, P., M. Pacia, and W. Macyk, *How to Correctly Determine the Band Gap Energy of Modified Semiconductor Photocatalysts Based on Uv–Vis Spectra*. 2018, ACS Publications.

115. Aarik, J., H. Mandar, M. Kirm, and L. Pung, *Optical Characterization of Hfo2 Thin Films Grown by Atomic Layer Deposition.* Thin Solid Films, 2004. **466**(1-2): p. 41-47.

116. Nguyen, N.V., A.V. Davydov, D. Chandler-Horowitz, and M.M. Frank, *Sub-Bandgap Defect States in Polycrystalline Hafnium Oxide and Their Suppression by Admixture of Silicon.* Applied Physics Letters, 2005. **87**(19): p. 192903.
117. Hoppe, E.E., R.S. Sorbello, and C.R. Aita, *Near-Edge Optical Absorption Behavior of Sputter Deposited Hafnium Dioxide.* Journal of Applied Physics, 2007. **101**(12): p. 123534.
118. Balog, M., M. Schieber, M. Michman, and S. Patai, *Chemical Vapor Deposition and Characterization of Hfo2 Films from Organo-Hafnium Compounds.* Thin Solid Films, 1977. **41**(3): p. 247-259.
119. Takeuchi, H., D. Ha, and T.-J. King, *Observation of Bulk Hfo 2 Defects by Spectroscopic Ellipsometry.* Journal of Vacuum Science & Technology A: Vacuum, Surfaces, and Films, 2004. **22**(4): p. 1337-1341.
120. Scopel, W., A.J. Da Silva, W. Orellana, and A. Fazzio, *Comparative Study of Defect Energetics in Hfo 2 and Sio 2.* Applied physics letters, 2004. **84**(9): p. 1492-1494.
121. Jiang, H., R.I. Gomez-Abal, P. Rinke, and M. Scheffler, *Electronic Band Structure of Zirconia and Hafnia Polymorphs from the G W Perspective.* Physical Review B, 2010. **81**(8): p. 085119.
122. Cho, Y.J., N.V. Nguyen, C.A. Richter, J.R. Ehrstein, B.H. Lee, and J.C. Lee, *Spectroscopic Ellipsometry Characterization of High-K Dielectric Hfo 2 Thin Films and the High-Temperature Annealing Effects on Their Optical Properties.* Applied physics letters, 2002. **80**(7): p. 1249-1251.
123. Sze, S.M. and K.K. Ng, *Physics of Semiconductor Devices*. 2006: John wiley & sons.
124. Kohn, W. and L.J. Sham, *Self-Consistent Equations Including Exchange and Correlation Effects.* Physical review, 1965. **140**(4A): p. A1133.
125. Roothaan, C., *Self-Consistent Field Theory for Open Shells of Electronic Systems.* Reviews of modern physics, 1960. **32**(2): p. 179.
126. Blochl, P.E., *Projector Augmented-Wave Method.* Phys Rev B Condens Matter, 1994. **50**(24): p. 17953-17979.
127. Hohenberg, P. and W. Kohn, *Inhomogeneous Electron Gas.* Physical review, 1964. **136**(3B): p. B864.
128. Von Barth, U. and L. Hedin, *A Local Exchange-Correlation Potential for the Spin Polarized Case. I.* Journal of Physics C: Solid State Physics, 1972. **5**(13): p. 1629.
129. Perdew, J.P., K. Burke, and M. Ernzerhof, *Generalized Gradient Approximation Made Simple.* Physical Review Letters, 1996. **77**(18): p. 3865-3868.
130. Perdew, J.P., A. Ruzsinszky, G.I. Csonka, O.A. Vydrov, G.E. Scuseria, L.A. Constantin, X. Zhou, and K. Burke, *Restoring the Density-Gradient Expansion for Exchange in Solids and Surfaces.* Phys Rev Lett, 2008. **100**(13): p. 136406.
131. Lee, C., W. Yang, and R.G. Parr, *Development of the Colle-Salvetti Correlation-Energy Formula into a Functional of the Electron Density.* Physical review B, 1988. **37**(2): p. 785.
132. Heyd, J., G.E. Scuseria, and M. Ernzerhof, *Hybrid Functionals Based on a Screened Coulomb Potential.* The Journal of chemical physics, 2003. **118**(18): p. 8207-8215.
133. Cho, A.Y. and J. Arthur, *Molecular Beam Epitaxy.* Progress in solid state chemistry, 1975. **10**: p. 157-191.
134. OxfordAppliedResearch, *Rf Atom Source Model Oxm1 Serial No. T2010/D5988 Operating and Service Manual*. Crawley Mill, Witney, Oxon OX29 9SP, UK

135. Sharath, S., J. Kurian, P. Komissinskiy, E. Hildebrandt, T. Bertaud, C. Walczyk, P. Calka, T. Schroeder, and L. Alff, *Thickness Independent Reduced Forming Voltage in Oxygen Engineered Hfo2 Based Resistive Switching Memories.* Applied Physics Letters, 2014. **105**(7): p. 073505.

136. Rodriguez-Fernandez, A., J. Muñoz-Gorriz, J. Suñé, and E. Miranda, *A New Method for Estimating the Conductive Filament Temperature in Oxram Devices Based on Escape Rate Theory.* Microelectronics reliability, 2018. **88**: p. 142-146.
137. Hermes, C., R. Bruchhaus, and R. Waser, *Forming-Free Tio2-Based Resistive Switching Devices on Cmos-Compatible W-Plugs.* IEEE electron device letters, 2011. **32**(11): p. 1588-1590.
138. Sharath, S., T. Bertaud, J. Kurian, E. Hildebrandt, C. Walczyk, P. Calka, P. Zaumseil, M. Sowinska, D. Walczyk, and A. Gloskovskii, *Towards Forming-Free Resistive Switching in Oxygen Engineered Hfo2− X.* Applied physics letters, 2014. **104**(6): p. 063502.
139. Petzold, S., A. Zintler, R. Eilhardt, E. Piros, N. Kaiser, S.U. Sharath, T. Vogel, M. Major, K.P. McKenna, L. Molina-Luna, and L. Alff, *Forming-Free Grain Boundary Engineered Hafnium Oxide Resistive Random Access Memory Devices.* Advanced Electronic Materials, 2019. **5**(10): p. 1900484.
140. Banerjee, W., A. Kashir, and S. Kamba, *Hafnium Oxide (Hfo2)–a Multifunctional Oxide: A Review on the Prospect and Challenges of Hafnium Oxide in Resistive Switching and Ferroelectric Memories.* Small, 2022. **18**(23): p. 2107575.
141. Beckmann, K., J. Holt, H. Manem, J. Van Nostrand, and N.C. Cady, *Nanoscale Hafnium Oxide Rram Devices Exhibit Pulse Dependent Behavior and Multi-Level Resistance Capability.* Mrs Advances, 2016. **1**(49): p. 3355-3360.
142. Chen, Y.Y., L. Goux, S. Clima, B. Govoreanu, R. Degraeve, G.S. Kar, A. Fantini, G. Groeseneken, D.J. Wouters, and M. Jurczak, *Endurance/Retention Trade-Off on Hfo 2 / Metal Cap 1t1r Bipolar Rram.* IEEE Transactions on electron devices, 2013. **60**(3): p. 1114-1121.
143. Calka, P., M. Sowinska, T. Bertaud, D. Walczyk, J. Dabrowski, P. Zaumseil, C. Walczyk, A. Gloskovskii, X. Cartoixà, and J. Suñé, *Engineering of the Chemical Reactivity of the Ti/Hfo2 Interface for Rram: Experiment and Theory.* ACS applied materials & interfaces, 2014. **6**(7): p. 5056-5060.
144. Vallée, C., P. Gonon, C. Jorel, F. El Kamel, M. Mougenot, and V. Jousseaume, *High K for Mim and Rram Applications: Impact of the Metallic Electrode and Oxygen Vacancies.* Microelectronic engineering, 2009. **86**(7-9): p. 1774-1776.
145. Piros, E., S. Petzold, A. Zintler, N. Kaiser, T. Vogel, R. Eilhardt, C. Wenger, L. Molina-Luna, and L. Alff, *Enhanced Thermal Stability of Yttrium Oxide-Based Rram Devices with Inhomogeneous Schottky-Barrier.* Applied Physics Letters, 2020. **117**(1): p. 013504.
146. Kaiser, N., T. Vogel, A. Zintler, S. Petzold, A. Arzumanov, E. Piros, R. Eilhardt, L. Molina-Luna, and L. Alff, *Defect-Stabilized Substoichiometric Polymorphs of Hafnium Oxide with Semiconducting Properties.* ACS Appl Mater Interfaces, 2022. **14**(1): p. 1290-1303.
147. Wang, J., H. Li, and R. Stevens, *Hafnia and Hafnia-Toughened Ceramics.* Journal of materials science, 1992. **27**(20): p. 5397-5430.
148. Puurunen, R.L., A. Delabie, S. Van Elshocht, M. Caymax, M.L. Green, B. Brijs, O. Richard, H. Bender, T. Conard, and I. Hoflijk, *Hafnium Oxide Films by Atomic Layer Deposition for High-K Gate Dielectric Applications: Analysis of the Density of Nanometer-Thin Films.* Applied Physics Letters, 2005. **86**(7): p. 073116.
149. Sidhu, S., L. Heaton, and D. Zauberis, *Neutron Diffraction Studies of Hafnium–Hydrogen and Titanium–Hydrogen Systems.* Acta Crystallographica, 1956. **9**(7): p. 607-614.
150. Jaffe, J.E., R.A. Bachorz, and M. Gutowski, *Low-Temperature Polymorphs of Zr O 2 and Hf O 2: A Density-Functional Theory Study.* Physical Review B, 2005. **72**(14): p. 144107.
151. Kaiser, N., Y.-J. Song, T. Vogel, E. Piros, T. Kim, P. Schreyer, S. Petzold, R. Valentí, and L. Alff, *Crystal and Electronic Structure of Oxygen Vacancy Stabilized Rhombohedral Hafnium Oxide.* ACS Applied Electronic Materials, 2023.
152. Suzer, S., S. Sayan, M. Banaszak Holl, E. Garfunkel, Z. Hussain, and N. Hamdan, *Soft X-Ray Photoemission Studies of Hf Oxidation.* Journal of Vacuum Science & Technology A: Vacuum, Surfaces, and Films, 2003. **21**(1): p. 106-109.

153. Kruchinin, V., V.S. Aliev, T. Perevalov, D. Islamov, V. Gritsenko, I. Prosvirin, C.-H. Cheng, and A. Chin, *Nanoscale Potential Fluctuation in Non-Stoichiometric Hfox and Low Resistive Transport in Rram.* Microelectronic Engineering, 2015. **147**: p. 165-167.
154. Zhao, X. and D. Vanderbilt, *First-Principles Study of Structural, Vibrational, and Lattice Dielectric Properties of Hafnium Oxide.* Physical Review B, 2002. **65**(23): p. 233106.
155. Lee, C.-K., E. Cho, H.-S. Lee, C.S. Hwang, and S. Han, *First-Principles Study on Doping and Phase Stability of Hfo 2.* Physical Review B, 2008. **78**(1): p. 012102.
156. Barreca, D., A. Milanov, R.A. Fischer, A. Devi, and E. Tondello, *Hafnium Oxide Thin Film Grown by Ald: An Xps Study.* Surface Science Spectra, 2007. **14**(1): p. 34-40.
157. Hadacek, N., A. Nosov, L. Ranno, P. Strobel, and R.-M. Galéra, *Magnetic Properties of Hfo2 Thin Films.* Journal of Physics: Condensed Matter, 2007. **19**(48): p. 486206.
158. Dietl, T., H. Ohno, F. Matsukura, J. Cibert, and e.D. Ferrand, *Zener Model Description of Ferromagnetism in Zinc-Blende Magnetic Semiconductors.* science, 2000. **287**(5455): p. 1019-1022.
159. White, G. and S. Woods, *Low Temperature Resistivity of Transition Elements: Vanadium, Niobium, and Hafnium.* Canadian Journal of Physics, 1957. **35**(8): p. 892-900.
160. Pinaud, B.A., Z.B. Chen, D.N. Abram, and T.F. Jaramillo, *Thin Films of Sodium Birnessite-Type Mno2: Optical Properties, Electronic Band Structure, and Solar Photoelectrochemistry.* Journal of Physical Chemistry C, 2011. **115**(23): p. 11830-11838.
161. Makuła, P., M. Pacia, and W. Macyk, *How to Correctly Determine the Band Gap Energy of Modified Semiconductor Photocatalysts Based on Uv–Vis Spectra.* The Journal of Physical Chemistry Letters, 2018. **9**(23): p. 6814-6817.
162. Perevalov, T., V.S. Aliev, V. Gritsenko, A. Saraev, and V. Kaichev, *Electronic Structure of Oxygen Vacancies in Hafnium Oxide.* Microelectronic Engineering, 2013. **109**: p. 21-23.
163. Höchst, H., P. Steiner, G. Reiter, and S. Hüfner, *Xps Valence Bands of Ti, Zr, Nb, Mo and Hf.* Zeitschrift für Physik B Condensed Matter, 1981. **42**(3): p. 199-204.
164. Steiner, P., H. Höchst, J. Schneider, S. Hüfner, and C. Politis, *The Xps Valence Band Spectra of Hf Metal and Hfc X N Y O Z Compounds and the Correlation to Their Superconductivity.* Zeitschrift für Physik B Condensed Matter, 1979. **33**(3): p. 241-250.
165. Momma, K. and F. Izumi, *Vesta 3 for Three-Dimensional Visualization of Crystal, Volumetric and Morphology Data.* Journal of applied crystallography, 2011. **44**(6): p. 1272-1276.
166. Yim, K., Y. Youn, M. Lee, D. Yoo, J. Lee, S.H. Cho, and S. Han, *Computational Discovery of P-Type Transparent Oxide Semiconductors Using Hydrogen Descriptor.* npj Computational Materials, 2018. **4**(1): p. 1-7.
167. Hautier, G., A. Miglio, G. Ceder, G.-M. Rignanese, and X. Gonze, *Identification and Design Principles of Low Hole Effective Mass P-Type Transparent Conducting Oxides.* Nature communications, 2013. **4**(1): p. 1-7.
168. Kresse, G. and J. Furthmuller, *Efficient Iterative Schemes for Ab Initio Total-Energy Calculations Using a Plane-Wave Basis Set.* Physical Review B, 1996. **54**(16): p. 11169-11186.
169. Garcia, J.C., A. Lino, L. Scolfaro, J. Leite, V. Freire, G. Farias, and E. da Silva Jr. *Band Structure Derived Properties of Hfo2 from First Principles Calculations*. in *AIP Conference Proceedings*. 2005. American Institute of Physics.
170. Goux, L., P. Czarnecki, Y.Y. Chen, L. Pantisano, X. Wang, R. Degraeve, B. Govoreanu, M. Jurczak, D. Wouters, and L. Altimime, *Evidences of Oxygen-Mediated Resistive-Switching Mechanism in Tin\Hfo 2\Pt Cells.* Applied Physics Letters, 2010. **97**(24): p. 243509.
171. Xu, N., B. Gao, L. Liu, B. Sun, X. Liu, R. Han, J. Kang, and B. Yu. *A Unified Physical Model of Switching Behavior in Oxide-Based Rram*. in *2008 Symposium on VLSI Technology*. 2008. IEEE.

172. Winkler, R., A. Zintler, S. Petzold, E. Piros, N. Kaiser, T. Vogel, D. Nasiou, K.P. McKenna, L. Molina-Luna, and L. Alff, *Controlling the Formation of Conductive Pathways in Memristive Devices.* Advanced Science, 2022: p. 2201806.

173. Milano, G., M. Aono, L. Boarino, U. Celano, T. Hasegawa, M. Kozicki, S. Majumdar, M. Menghini, E. Miranda, and C. Ricciardi, *Quantum Conductance in Memristive Devices: Fundamentals, Developments, and Applications.* Advanced Materials, 2022: p. 2201248.

174. Long, S., X. Lian, C. Cagli, X. Cartoixa, R. Rurali, E. Miranda, D. Jiménez, L. Perniola, M. Liu, and J. Suné, *Quantum-Size Effects in Hafnium-Oxide Resistive Switching.* Applied Physics Letters, 2013. **102**(18): p. 183505.

175. Li, Y., S. Long, Y. Liu, C. Hu, J. Teng, Q. Liu, H. Lv, J. Suñé, and M. Liu, *Conductance Quantization in Resistive Random Access Memory.* Nanoscale research letters, 2015. **10**(1): p. 1-30.

176. O'Hara, A., G. Bersuker, and A.A. Demkov, *Assessing Hafnium on Hafnia as an Oxygen Getter.* Journal of Applied Physics, 2014. **115**(18): p. 183703.

177. Foster, A.S., A. Shluger, and R.M. Nieminen, *Mechanism of Interstitial Oxygen Diffusion in Hafnia.* Physical review letters, 2002. **89**(22): p. 225901.

178. Strachan, J.P., J.J. Yang, R. Münstermann, A. Scholl, G. Medeiros-Ribeiro, D.R. Stewart, and R.S. Williams, *Structural and Chemical Characterization of Tio2 Memristive Devices by Spatially-Resolved Nexafs.* Nanotechnology, 2009. **20**(48): p. 485701.

179. Münstermann, R., J.J. Yang, J.P. Strachan, G. Medeiros-Ribeiro, R. Dittmann, and R. Waser, *Morphological and Electrical Changes in Tio2 Memristive Devices Induced by Electroforming and Switching.* physica status solidi (RRL)–Rapid Research Letters, 2010. **4**(1-2): p. 16-18.

180. Yang, J.J., F. Miao, M.D. Pickett, D.A. Ohlberg, D.R. Stewart, C.N. Lau, and R.S. Williams, *The Mechanism of Electroforming of Metal Oxide Memristive Switches.* Nanotechnology, 2009. **20**(21): p. 215201.

181. Dittmann, R., S. Menzel, and R. Waser, *Nanoionic Memristive Phenomena in Metal Oxides: The Valence Change Mechanism.* Advances in Physics, 2021. **70**(2): p. 155-349.

182. Hensling, F., T. Heisig, N. Raab, C. Baeumer, and R. Dittmann, *Tailoring the Switching Performance of Resistive Switching Srtio3 Devices by Sro Interface Engineering.* Solid state ionics, 2018. **325**: p. 247-250.

183. Baeumer, C., C. Schmitz, A.H. Ramadan, H. Du, K. Skaja, V. Feyer, P. Müller, B. Arndt, C.-L. Jia, and J. Mayer, *Spectromicroscopic Insights for Rational Design of Redox-Based Memristive Devices.* Nature communications, 2015. **6**(1): p. 1-10.

184. Clima, S., B. Govoreanu, M. Jurczak, and G. Pourtois, *Hfox as Rram Material–First Principles Insights on the Working Principles.* Microelectronic Engineering, 2014. **120**: p. 13-18.

185. Rose, A., *Space-Charge-Limited Currents in Solids.* Physical Review, 1955. **97**(6): p. 1538.

186. Kim, T., T. Vogel, E. Piros, D. Nasiou, N. Kaiser, P. Schreyer, R. Winkler, A. Zintler, A. Arzumanov, and S. Petzold, *Oxide Thickness-Dependent Resistive Switching Characteristics of Cu/Hfo2/Pt Ecm Devices.* Applied Physics Letters, 2023. **122**(2): p. 023502.

187. Celano, U., L. Goux, R. Degraeve, A. Fantini, O. Richard, H. Bender, M. Jurczak, and W. Vandervorst, *Imaging the Three-Dimensional Conductive Channel in Filamentary-Based Oxide Resistive Switching Memory.* Nano letters, 2015. **15**(12): p. 7970-7975.

188. Privitera, S., G. Bersuker, S. Lombardo, C. Bongiorno, and D.C. Gilmer, *Conductive Filament Structure in Hfo2 Resistive Switching Memory Devices.* Solid-State Electronics, 2015. **111**: p. 161-165.

189. Kumar, S., Z. Wang, X. Huang, N. Kumari, N. Davila, J.P. Strachan, D. Vine, A.D. Kilcoyne, Y. Nishi, and R.S. Williams, *Conduction Channel Formation and Dissolution Due to Oxygen Thermophoresis/Diffusion in Hafnium Oxide Memristors.* ACS nano, 2016. **10**(12): p. 11205-11210.

190. Li, C., B. Gao, Y. Yao, X. Guan, X. Shen, Y. Wang, P. Huang, L. Liu, X. Liu, J. Li, C. Gu, J. Kang, and R. Yu, *Direct Observations of Nanofilament Evolution in Switching Processes in Hfo2 -Based Resistive Random Access Memory by in Situ Tem Studies.* Adv Mater, 2017. **29**(10): p. 1602976.
191. Yang, Y., X. Zhang, L. Qin, Q. Zeng, X. Qiu, and R. Huang, *Probing Nanoscale Oxygen Ion Motion in Memristive Systems.* Nat Commun, 2017. **8**(1): p. 15173.
192. Yin, J., F. Zeng, Q. Wan, F. Li, Y.M. Sun, Y.D. Hu, J.L. Liu, G.Q. Li, and F. Pan, *Adaptive Crystallite Kinetics in Homogenous Bilayer Oxide Memristor for Emulating Diverse Synaptic Plasticity.* Advanced Functional Materials, 2018. **28**(19): p. 1706927.
193. Zhang, Y., G.-Q. Mao, X. Zhao, Y. Li, M. Zhang, Z. Wu, W. Wu, H. Sun, Y. Guo, and L. Wang, *Evolution of the Conductive Filament System in Hfo2-Based Memristors Observed by Direct Atomic-Scale Imaging.* Nature communications, 2021. **12**(1): p. 1-10.
194. Guedj, C., L. Hung, A. Zobelli, P. Blaise, F. Sottile, and V. Olevano, *Evidence for Anisotropic Dielectric Properties of Monoclinic Hafnia Using Valence Electron Energy-Loss Spectroscopy in High-Resolution Transmission Electron Microscopy and Ab Initio Time-Dependent Density-Functional Theory.* Applied Physics Letters, 2014. **105**(22): p. 222904.
195. Vogel, T., A. Zintler, N. Kaiser, N. Guillaume, G. Lefèvre, M. Lederer, A.L. Serra, E. Piros, T. Kim, and P. Schreyer, *Structural and Electrical Response of Emerging Memories Exposed to Heavy Ion Radiation.* ACS nano, 2022. **16**(9): p. 14463-14478.
196. Vogel, T., N. Kaiser, S. Petzold, E. Piros, N. Guillaume, G. Lefevre, C. Charpin-Nicolle, S. David, C. Vallee, E. Nowak, C. Trautmann, and L. Alff, *Defect-Induced Phase Transition in Hafnium Oxide Thin Films: Comparing Heavy Ion Irradiation and Oxygen-Engineering Effects.* Ieee Transactions on Nuclear Science, 2021. **68**(8): p. 1542-1547.
197. McKenna, K., A. Shluger, V. Iglesias, M. Porti, M. Nafria, M. Lanza, and G. Bersuker, *Grain Boundary Mediated Leakage Current in Polycrystalline Hfo2 Films.* Microelectronic Engineering, 2011. **88**(7): p. 1272-1275.
198. Xue, K.-H., P. Blaise, L. Fonseca, G. Molas, E. Vianello, B. Traore, B. De Salvo, G. Ghibaudo, and Y. Nishi, *Grain Boundary Composition and Conduction in Hfo 2: An Ab Initio Study.* Applied Physics Letters, 2013. **102**(20): p. 201908.
199. Vandelli, L., A. Padovani, L. Larcher, and G. Bersuker, *Microscopic Modeling of Electrical Stress-Induced Breakdown in Poly-Crystalline Hafnium Oxide Dielectrics.* Ieee Transactions on Electron Devices, 2013. **60**(5): p. 1754-1762.
200. Lanza, M., *A Review on Resistive Switching in High-K Dielectrics: A Nanoscale Point of View Using Conductive Atomic Force Microscope.* Materials, 2014. **7**(3): p. 2155-2182.
201. Iglesias, V., M. Porti, M. Nafría, X. Aymerich, P. Dudek, T. Schroeder, and G. Bersuker, *Correlation between the Nanoscale Electrical and Morphological Properties of Crystallized Hafnium Oxide-Based Metal Oxide Semiconductor Structures.* Applied physics letters, 2010. **97**(26): p. 262906.
202. Iglesias, V., M. Porti, M. Nafria, X. Aymerich, P. Dudek, and G. Bersuker, *Dielectric Breakdown in Polycrystalline Hafnium Oxide Gate Dielectrics Investigated by Conductive Atomic Force Microscopy.* Journal of Vacuum Science & Technology B, 2011. **29**(1): p. 01AB02.
203. Batra, R., H.D. Tran, and R. Ramprasad, *Stabilization of Metastable Phases in Hafnia Owing to Surface Energy Effects.* Applied Physics Letters, 2016. **108**(17): p. 172902.

Curriculum Vitae

Personal Information

Name: Nico Kaiser

Date of Birth: 02.10.1989

Place of Birth: Erbach (Odw.)

Nationality: German

Academic Education

02/2018 – 2023	Research assistant and doctoral candidate at Technical University of Darmstadt
Doctoral thesis:	**Substoichiometric phases of hafnium oxide with semiconducting properties**
04/2015 - 11/2017	Master of Science in Materials Science at Technical University of Darmstadt
Master thesis:	**PLD growth investigations on the Na_2O-Al_2O_3 system with focus on sodium-ion conductivity**
10/2010 - 03/2015	Bachelor of Science in Materialwissenschaft (Materials Science) at Technical University of Darmstadt
Bachelor thesis:	**Reproduzierbarkeit des $SrMoO_3$-Schichtwachstums mittels gepulster Laserablation** (Reproducibility of the SrMoO3 layer growth by pulsed laser deposition)

Additional experience:

08/2012 – 09/2012	Internship at the Chung Hua University, Hsinchu, Taiwan in the "Department of Engineering"
Topic:	Investigation of the wetting behavior and the chemical reaction between glass and high-temperature materials

Pre-Academic Education and Service

2009 – 2010	Community service and subsequent voluntary social year at Schule am Drachenfeld, Erbach (Odw.)
2006 – 2009	Allgemeine Hochschulreife at Berufliches Schulzentrum Odenwaldkreis, Michelstadt

List of publications, scientific contributions and supervision of students

Manuscripts in preparation (preliminary title & authorship):

N. Schmidt, **N. Kaiser**, T. Vogel, E. Piros, S. Karthäuser, R. Waser, L. Alff, and R. Dittmann **Spatially Resolved Electrical Analysis of Semiconducting Hafnium Oxide Thin Films**

N. Kaiser*, S. Schreyer*, D. Nasiou, A. Zintler, T. Kim, E. Piros, T. Vogel, L. Molina-Luna, and L. Alff **Substoichiometric Rhombohedral and Hexagonal Hafnium Oxide Phases as novel type of Electrodes in RRAM**

Publications (Listed by year)

2023

N. Kaiser*, Y.-J. Song*, T. Vogel, E. Piros, T. Kim, P. Schreyer, S. Petzold, R. Valentí, and L. Alff **Crystal and Electronic Structure of Oxygen Vacancy Stabilized Rhombohedral Hafnium Oxide** ACS Appl. Electron. Mater. 2023, **5**, 2, 754–763 doi: 10.1021/acsaelm.2c01255

T. Kim, T. Vogel, E. Piros, D. Nasiou, **N. Kaiser**, P. Schreyer, R. Winkler, A. Zintler, A. Arzumanov, S. Petzold, L. Molina-Luna, and L. Alff **Oxide thickness-dependent resistive switching characteristics of Cu/HfO_2/Pt ECM devices** Appl. Phys. Lett. 122, 023502 (2023) doi: 10.1063/5.0124781

2022

F. L. Aguirre, E. Piros, **N. Kaiser**, T. Vogel, S. Petzold, J. Gehrunger, T. Oster, C. Hochberger, J. Suñé, L. Alff and E. Miranda **Fast Fitting of the Dynamic Memdiode Model to the Conduction Characteristics of RRAM Devices Using Convolutional Neural Networks Micromachines**, 13(11), 2002, 2022 doi: 10.3390/mi13112002

T. Vogel, A. Zintler, **N. Kaiser**, N. Guillaume, G. Lefèvre, M. Lederer, A. L. Serra, E. Piros, T. Kim, P. Schreyer, R. Winkler, D. Nasiou, R. R. Olivo, T. Ali, D. Lehninger, A. Arzumanov, C. Charpin-Nicolle, G. Bourgeois, L. Grenouillet, M.-C. Cyrille, G. Navarro, K. Seidel, T. Kämpfe, S. Petzold, C. Trautmann, L. Molina-Luna, L. Alff **Structural and electrical response of emerging memories exposed to heavy ion radiation** ACS Nano (2022) doi: 10.1021/acsnano.2c04841

R. Winkler, A. Zintler, S. Petzold, E. Piros, **N. Kaiser**, T. Vogel, D. Nasiou, K. P. McKenna, L. Molina-Luna, L. Alff **Controlling the Formation of Conductive Pathways in Memristive Devices** Advanced Sciences, 2201806 (2022) doi: 10.1002/advs.202201806

M. Lederer, T. Vogel, T. Kämpfe, **N. Kaiser**, E. Piros, R. Olivo, T. Ali, S. Petzold, D. Lehninger, C. Trautmann, L. Alff, K. Seidel **Heavy ion irradiation induced phase transitions and their impact on the switching behavior of ferroelectric hafnia** Journal of Applied Physics 132, 064102 (2022) doi: 10.1063/5.0098953

T. Vogel, A. Zintler, **N. Kaiser**, N. Guillaume, G. Lefèvre, M. Lederer, A. L. Serra, E. Piros, T. Kim, P. Schreyer, R. Winkler, D. Nasiou, R. R. Olivo, T. Ali, D. Lehninger, A. Arzumanov, C.

Charpin-Nicolle, G. Bourgeois, L. Grenouillet, MC. Cyrille, G. Navarro, K. Seidel, T. Kämpfe, S. Petzold, C. Trautmann, L. Molina-Luna, L. Alff **Integration of labeled 4D-STEM SPED data for confirmation of phase identification** TUdatalib (2022) doi: 10.48328/tudatalib-896

A. Zintler, R. Eilhardt, S. Petzold, S. Ulhas Sharath, E. Bruder, **N. Kaiser**, L. Alff, and L. Molina-Luna Enhanced Conductivity and Microstructure in Highly Textured TiN_{1-x}/*c*-Al_2O_3 Thin Films. ACS Omega 7, 2, 2041–2048 (2022) doi: 10.1021/acsomega.1c05505

N. Kaiser, T. Vogel, A. Zintler, S. Petzold, A. Arzumanov, E. Piros, R. Eilhardt, L. Molina-Luna, and L. Alff **Defect stabilized substoichiometric polymorphs of hafnium oxide with semiconducting properties** ACS Appl. Mater. Interfaces 14, 1, 1290–1303 (2022) doi: 10.1021/acsami.1c09451

2021

T. Vogel, **N. Kaiser**, S. Petzold, E. Piros, N. Guillaume, G. Lefèvre, C. Charpin-Nicolle, S. David, C. Vallée, E. Nowak, C. Trautmann, and L. Alff **Defect-induced phase transition in hafnium oxide thin films: comparing heavyion irradiation and oxygen engineering effects** IEEE Trans Nucl Sci, 68 1542 – 1547 (2021) doi: 10.1109/TNS.2021.3085962

2020

T. Kämpfe, T. Vogel, R. Olivo, M. Lederer, **N. Kaiser**, S. Petzold, T. Ali, D. Lehninger & Seidel, K. **Heavy ion irradiation effects on structural and ferroelectric properties of HfO_2 films.** In 2020 Joint Conference of the IEEE International Frequency Control Symposium and International Symposium on Applications of Ferroelectrics (IFCS-ISAF) (pp. 1-3). IEEE. (2020) doi:10.1109/IFCS-ISAF41089.2020.9234942

L. Serra, T. Vogel, G. Lefèvre, S. Petzold, **N. Kaiser**, G. Bourgeois, M.-C. Cyrille, L. Alff, C. Trautmann, C. Vallée, S. David, C. Charpin-Nicolle, G. Navarro, E. Nowak **Heavy Ions Radiation Effects on 4kb Phase-Change Memory** RADECS 2020, (2020), Virtual Conference, France HAL Id : cea-03086407

S. Petzold, E. Piros, R. Eilhardt, A. Zintler, T. Vogel, **N. Kaiser**, A. Radetinac, P. Komissinskiy, E. Jalaguier, E. Nolot, C. Charpin - Nicolle, C. Wenger, L. Molina - Luna, E. Miranda, L. Alff **Tailoring the Switching Dynamics in Yttrium Oxide - Based RRAM Devices by Oxygen Engineering: From Digital to Multi - Level Quantization toward Analog Switching** Adv. Electron. Mater. **6**, 2000439 (2020) doi: 10.1002/aelm.202000439

E. Piros, M. Lonsky, S. Petzold, A. Zintler, S.U. Sharath, T. Vogel, **N. Kaiser**, R. Eilhardt, L. Molina-Luna, C. Wenger, J. Müller, and L. Alff **Role of Oxygen Defects in Conductive-Filament Formation in Y_2O_3-Based Analog RRAM Devices as Revealed by Fluctuation Spectroscopy** Phys. Rev. Applied **14**, 034029 (2020) doi: 10.1103/PhysRevApplied.14.034029

E. Piros, S. Petzold, A. Zintler, **N. Kaiser**, T. Vogel, R. Eilhardt, C. Wenger, L. Molina-Luna, and L. Alff **Enhanced thermal stability of yttrium oxide-based RRAM devices with inhomogeneous Schottky-barrier** Appl. Phys. Lett. **117**, 013504 (2020) doi: 10.1063/5.0009645

2019

Zintler, R. Eilhardt, S. Petzold, **N. Kaiser**, Sharath Ulhas, L. Alff and L. Molina-Luna **Correlation of Structural Modifications by Multiscale Phase Mapping in Filamentary Type HfO2-based RRAM: Towards a Component Specific in situ TEM Investigation** Microsc. Microanal. **25**, 1842-1843 (2019) doi: 10.1017/S1431927619009942

S. Petzold, A. Zintler, R. Eilhardt, E. Piros, **N. Kaiser**, S. U. Sharath, T. Vogel, M. Major, K. P. McKenna, L. Molina - Luna, L. Alff **Forming - Free Grain Boundary Engineered Hafnium Oxide Resistive Random Access Memory Devices** Adv. Electron. Mater., **5**, 1900484 (2019) doi: 10.1002/aelm.201900484

S. Petzold, E. Miranda, S. U. Sharath,, J. Muñoz-Gorriz, T. Vogel E. Piros, **N. Kaiser**, R. Eilhardt, A. Zintler, L. Molina-Luna, J. Suñé, and L. Alff **Analysis and simulation of the multiple resistive switching modes occurring in HfO_x -based resistive random access memories using memdiodes** J. Appl. Phys. **125**, 234503 (2019) doi: 10.1063/1.5094864

Contributions on Conferences:

This list only shows contributions as first author.

CIMTEC 2022 (Perugia, Italy): “Substoichiometric Hafnium Oxide Polymorphs with Semiconducting Properties” – **N. Kaiser**, T. Vogel, A. Zintler, S. Petzold, A. Arzumanov, E. Piros, R. Eilhardt, L. Molina-Luna, L. Alff; given by Tobias Vogel on behalf of N. Kaiser (due to illness); oral presentation

NANO 2022 (Seville, Spain): “Electrically Conducting Hafnium Oxide Phases” – **N. Kaiser**, T. Vogel, A. Zintler, S. Petzold, A. Arzumanov, E. Piros, R. Eilhardt, L. Molina-Luna, L. Alff; oral presentation

MEMRISYS 2019 (Dresden, Germany): “Structural, Optical and Electronic Properties of Oxygen-Deficient HfO_x Phases Grown by Molecular Beam Epitaxy” - **N. Kaiser**, A. Zintler, S. Petzold, E. Piros, T. Vogel, R. Eilhardt, L. Molina-Luna and L. Alff; poster presentation

Supervision of students & PhD freshmen:

Arash Estiri (Internship program with Grenoble INP) – Photolithography optimization for RRAM applications

Nitin Mallik (Advanced Research Lab) - Optimization of a Contact Mode UV-Photolithography Routine for Square Features with a Side Length of 6 μm to 1.5 μm

Farhan Tanzim (scientific assistant) – Electric Characterization of Oxygen Engineered Hafnium Oxide based RRAM

Patrick Schuldt (Advanced Research Lab) - Electrical Characterization of In-vacuum processed Hafnia based ReRAM with and without Passivation Layer

Patrick Schuldt (Mater Thesis) – Conduction Mechanisms in Substoichiometric Hafnium Oxide based RRAM at Different Temperatures

Also the supervision of PhD freshmen including extensive knowledge transfer, training, support and guidance was provided especially for Phillip Schreyer, Taewook Kim and Giovanni d'Andrea.

PhD training courses attended

International Doctoral School in Functional Materials: Research and Innovation (IDS-FunMat-Inno)

April 8-14, 2018 IDS-FunMat-Inno Spring School (Hirschegg, Austria):

Spring School on Material Selection and Processing & Scientific Communication

- Workshop on Material Selection and Processing
- Poster Session
- Workshop on Scientific Communication

September 24-28, 2018 IDS-FunMat-Inno Autumn School (Bordeaux, France):

Autumn School on Technological Intelligence

- Presentation of the VIA Inno methodologies and the basic architecture of an analysis in technological intelligence
- Workshop on the application of technological intelligence analysis on PhD subjects

April 8-11, 2019 IDS-FunMat-Inno Spring School (Leiden, Netherlands):

Spring School on Circular Economy

- Workshop on Circularity assessment with RaMaScene
- Workshop on Circular Economy Policies
- Workshop on PhD exhance, career counseling and grant writing

Sept 30 – Oct 4, 2019 IDS-FunMat-Inno Autumn School (Bilbao, Spain):

Autumn School on Innovation and Entrepreneurship

- Learn and develop new competencies and skills not covered in the researcher's career. Reflect about their leadership concept to clarify their professional career and goals. Develop personal initiative and personal autonomy. Learn to build and lead teams and projects.
- Innovate and transform a research project into a professional development project. This means to develop a new business line inside an existing company (new product, service or process) or to lead the creation of a new company out of the research outcomes. Participants will design their own professional/personal project.
- Understanding industry challenges. Creating innovations to solve customers' needs.
- Ideate products or services and prototype them using the Lean Start up approach. Ensure that participants are aware of the importance of having a clear business model, taking into account the market needs and the process of customer development.
- Communicate the value proposition of a project according to the targeted market and the customer needs.
- Understanding marketing and customer relationships. Communicate the value proposition of a project taking into account the targeted market and the customer needs.

Acknowledgement

The path of a doctoral student is characterized by countless challenges that lead to incredible growth in both professional, but also personal development. It quickly became apparent that the quality of scientific work is directly related to the ability to exchange ideas and work together with supervisors and colleagues, both within one's own research institute but also in cooperation with partners from other facilities. The success of this work is not only due to the collaboration on the professional level, but also to the many personal moments with colleagues and especially due to the support of my wonderful friends and my fantastic family. This is the right place to express my sincere thanks to all of you.

First of all, I would like to thank my thesis advisor and mentor Prof. Lambert Alff. It has been a long time since I chose you to be my mentor during my studies here at the TU Darmstadt. As luck would have it, my growing interest in physical vapor deposition and functional thin films led me to your group to do my bachelor thesis. Soon I would also earn my Master's degree through the ATFT group. Finally, due to my strong interest in a research project on RRAM that was advertised at the time, I decided to pursue a doctoral degree with you as my supervisor. Through the numerous projects that I was able to participate in as part of this group, through contact with various synthesis and characterization methods and through your supervision in all of the above, I was able to gain a comprehensive understanding of the research field of functional thin films and microelectronics. All this would not have been possible without your continued support and enthusiasm and I would like to thank you heartily for that. I would also like to thank you for your personal commitment to furthering my career goals and especially for your unwavering support and understanding for the challenging live situations outside of academia which accompanied me through my doctorate.

Second I would like to thank Prof. Molina-Luna as my second thesis advisor. I still remember the first time we met was characterized by the enthusiasm for the research project which was designed as a close collaboration between the ATFT and AEM group. Your optimistic attitude often helped to inspire me over the course of joint research projects. I would like to thank you for your readily available support and continuous welcoming atmosphere provided for me and all ATFT members. At this point I also like to thank all members of the EM group for your help and support. Special thanks to Robert Winkler, Despina Nasiou, Oscar Recalde and in particular to my friend and colleague Dr. Alexander Zintler.

I would like to thank Prof. Donner for being part of my committee, but especially for his readiness to teach and discuss about all aspects of structural research with a contagious passion. Through our numerous conversations I was able to learn a lot about X-ray diffraction and structural analysis which was extremely helpful for this work and beyond. For this I like to express my sincere gratitude. Here I also want to thank all current and former members of the structural research group, and specifically Dr. Tom Faske, Dr. Constantin Wansorra, Marcel Urban, Leif Carstensen and David Koch for the scientific exchange and for the long tradition of going to the canteen together.

As the fourth committee member I like to thank Prof. Valentí. Many thanks for the friendly and fruitful collaboration of ours. Special thanks also to Dr. Young-Joon Song for jointly publishing our combined experimental and theoretical research as shared first authors. I was a really nice experience working with your group.

Further I like to thank all collaborative partners from FZ Jülich namely Prof. Waser and Prof. Dittmann, Dr. Karthäuser and Niclas Schmidt. We had the chance to collaborate closely on many levels, including the elaboration of an in-vacuo sample transfer across our institutes, joint research, as well as collaborative proposal and paper writing. Working with you has always been very friendly and effective. As one of my first collaboration partners outside of Darmstadt, you have therefore influenced me in a very positive way and I would like to thank you for that.

Of course I like to thank all members of the ATFT group together with Alumni, some of who already got to know me since the start of my Bachelor Thesis. At the risk of inadvertently omitting one or more important individuals, I try to highlight a few particularly influential colleges. However, it goes without saying that every current and former member deserves a big thank you from me. We all worked together or shared professional or personal thoughts at one point or another. I like to thank Dr. Aldin Radetinac, Dr. Erwin Hildebrandt and Dr. Philipp Komissinskiy accompanying my fist steps in experimental research. Also I especially like to thank my dear friend Dr. Philip Kehne for supervising my master thesis and for our joint endeavor to stay in shape by running some kilometers now and then. Special thanks also to Dr. Stefan Petzold who was a big help in the first years of my doctoral program through knowledge transfer and support. Also thanks to Dr. Marton Major for the nice scientific exchange and support and to Dr. Alexey Arzumanov for help and assistance with electrical measurements and ion beam etching. Thanks to Dr. Juliette Cardoletti, and Dr. Shalini Sharma for our joint coffee-breaks and many laughs and to Benjamin Krah for the right sense of humor. I like to thank Taewook Kim and Philipp Schreyer for being friendly and comradely colleagues who show the right attitude to maintain the success of our groups RRAM research. Thanks also to Gabriele Haindl for her support with CAD drawings and for all of the photos taken on special occasions. Also special thanks to Jürgen Schreeck for the numerous occasions at which you helped to solve technical problems and our many shared lunch breaks. And thanks to Marion Bracke for the universal support and also the always nice personal exchange which I will miss. Also thanks to Angela Dreher for quickly finding your way into and becoming an essential part the group as well as for the many nice conversations.

Special thanks to my colleague Ester Piros. We went on several conferences and the whole PhD school together and quickly became friends. We also worked together on many projects and I have always appreciated that you can be absolutely relied on in all matters. Thank you for your support in all regards.

Also special thanks to my dear friend and colleague Dr. Tobias Vogel, who I got to know through my Master Thesis project. Over the course of our doctorates, we were probably working most closely together as we numerous times fixed the MBE system, planned depositions together, and finally wrote papers together. Thank you for all your help and for becoming a close friend.

I heartily like to thank the students who gave me the chance to supervise them across different projects for their contributions, namely Arash Estiri, Farhan Tanzim, Nitin Mallik and Patrick Schuldt. I learned that to supervise usually means it’s in fact both sides that will learn, not just one. Therefore, thank you very much for our teamwork efforts. Special thanks to Patrick Schuldt for measuring a significant part of the electrical properties of investigated RRAM devices shown in this work.

Thanks to all members of the workshop who were always friendly and ready to help in every regard. Special thanks to Michael Weber for the usually extremely fast and effective help with electronic problems.

Now I like to thank my former fellow students. Without their support I would never have made it this far. Thanks to Dr. Mathias Storch and Thorsten Eisele for accompanying my studies, being there to learn, to have fun and for your support especially in difficult situations. Special thanks to my close friend Dr. Tim Hellmann. It goes without saying that we already became really close friends during our studies. Despite the many changes in our lives, we have remained true to ourselves and I hope that this will remain the case as long as we live. Thank you for your unwavering support in every regard.

Special thanks to my close and longest friend Micha Thiessen. True friendship is revealed when the ice gets thin and you've shown what that means on more than one occasion. Thank you for maintaining our long lasting friendship and for all of your support.

Also special thanks to my close friend René Büttner. You supported me well through the doctoral thesis with your cheering manner and philosophy of life. And thanks to my friend Emil Federbusch for your sociable nature and the joy of shared hobbies.

Also thanks my former schoolmates Felix Friske and Manuel Benz, with whom we recently got in touch again, for the fun we had together as a welcome distraction from work.

I also want to thank my partner Javena Mager. The love and support that you provided over the cause of the last year, which was characterized by many difficult situations, especially in private life, was incredible and I want to thank you for that from the bottom of my heart.

Lastly I want to thank my dear and loving family, which always unwaveringly supported me in my live choices. I want to thank my Sister, Nina Kaiser for the heartfelt relationship and the strong mutual support which we developed especially over the last years. Many thanks also to her fiancée Lukas Benzig who also became truly part of our family. Especially many thanks to my mother Gabi Kaiser and my father Klaus Kaiser for their incredible love and support and for the positive impact you both have cast on my life.

The work leading to this publication has been undertaken in the framework of the projects WAKeMeUP and StorAIge, which received funding from the Electronic Components and Systems for European Leadership Joint Undertaking in collaboration with the European Union’s H2020 Framework Programme (H2020/2014-2020) and National Authorities, under grant agreement nos 783176 and 101007321, respectively. Funding by the Federal Ministry of Education and Research (BMBF) under contract 16ESE0298 and 16MEE0154 is gratefully acknowledged. This work was supported by the Deutscher Akademischer Austauschdienst (DAAD) and the Deutsche Forschungsgemeinschaft under project AL 560/13-2. Also, funding from the DFG grant MO 3010/3-1 and AL 560/21-1 and the European Research Council (ERC) Horizon 2020 Programme under Grant No. 805359-FOXON are gratefully acknowledged.